出藍

SHUTSU RAN

研究報告　第 34 号　2021

PRECISION MACHINING

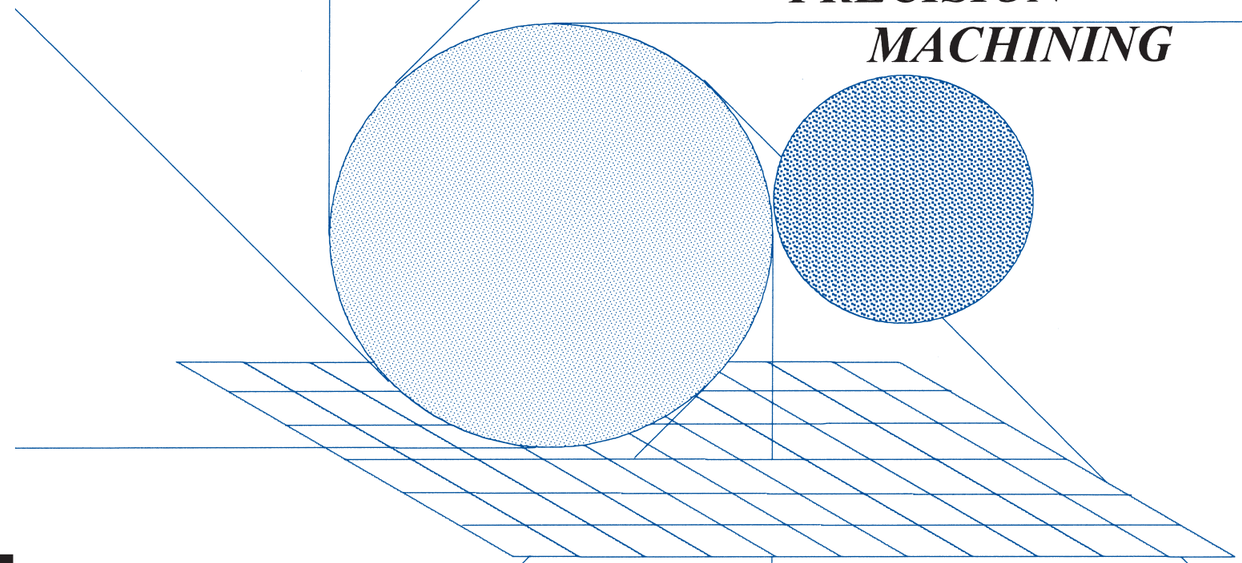

ナノ精度加工学講座

東北大学大学院工学研究科
機械機能創成専攻

出藍　第 34 号

2021 年 5 月

目次

【原著論文（査読有）】

【解説記事・紹介記事】

【国際発表】

【国内発表】

【修士論文】

【原著論文(査読有)】

Nanomanufacturing and Metrology (2020) 3:133–141
https://doi.org/10.1007/s41871-020-00065-4

ORIGINAL ARTICLES

Effects of Topography and Modified Layer by Plasma-Shot Treatment on High-Speed Steel

Yorihito Shibata[1] · Yusuke Sakairi[1] · Keita Shimada[1] · Masayoshi Mizutani[1] · Tsunemoto Kuriyagawa[2]

Received: 13 February 2020 / Revised: 19 March 2020 / Accepted: 2 May 2020 / Published online: 24 May 2020

Abstract
In this study, plasma shot (PS) treatment was applied to high-speed steel (HSS) surfaces using a titanium carbide electrode to confirm the effect of discharge current (I_p) on the formation of a single dimple and analyze a modified layer. The roughness of modified surfaces increased when I_p increased, and energy-dispersive X-ray spectrometry showed an increase in titanium atom density when I_p and electrode consumption volume (V_e) increased. A friction test confirmed that the modified surface's friction was reduced by discharge dimples under low-load conditions. Vickers hardness test confirmed that the hardness of the modified surface was ~ 300–600 HV higher than that of an untreated HSS surface. Moreover, it increased with an increase in I_p. However, application of PS treatment to the edge of surfaces on the workpiece caused shape deterioration. The deterioration size of the edge of the modified layer increased when I_p increased. To solve this issue, we propose a novel method named position-adjusted PS (PA-PS) treatment. PA-PS treatment is used to adjust the end of the electrode in the order of tens of micrometers from the edge of the workpiece to avoid the deterioration of the edge form. Under $I_p = 21$ A, PA-PS formed a modified layer without deteriorating the edge shape of the workpiece, thus confirming the PS characteristics applied to HSS surfaces. Moreover, PA-PS treatment solved the shape deterioration of the edge on modified surfaces via PS treatment.

Keywords Plasma-shot treatment · Electric discharge machining · Surface modification · High-speed steel · Tool wear · Friction

1 Introduction

At present, products that have considerably improved our standard of living are produced by various manufacturing methods. In machine processing, machine parts are accurately produced using machine tools such as lathes, milling machines, drilling machines, and machining centers. The industry depends on the machining process to machine the various shapes of products using cutting tools. High-efficiency cutting has been increasingly demanded for high-mix, low-volume production; however, tool life is a major bottleneck for realizing more efficient manufacturing because cutting tools are exposed to severe environments of high temperatures and pressures at high cutting speeds, which considerably increases the wear rate. To protect such tools from wear, surfaces are treated using conventional surface treatment technology, such as chemical vapor deposition (CVD) and physical vapor deposition (PVD), to form wear proof layers [1]. These surface treatment technologies are important for increasing the machining performance of cutting tools [2]. The disadvantages of these surface treatment technologies include low adhesion of coating and thickness nonuniformity when applied to complex surfaces. However, plasma-shot (PS) treatment can overcome certain disadvantages of the conventional technologies [3].

PS treatment was developed by applying electric discharge machining (EDM). EDM is a manufacturing method that can be used to machine hard materials into complex shapes with high precision [4]. PS treatment is completely the opposite of EDM and transfers electrode materials to the workpiece surface to form modified surfaces. Figure 1 shows the mechanism of PS treatment [5]. In this process, arc discharges occur between the workpiece and the electrode, which partially melts and transfers to the workpiece

✉ Masayoshi Mizutani
masayoshi.mizutani.b6@tohoku.ac.jp

[1] Graduate School of Engineering, Tohoku University, 6-6-01, Aoba, Aramakiaza, Aobaku, Sendaishi, Miyagi, Japan

[2] Graduate School of Biomedical Engineering, Tohoku University, 6-6-01, Aoba, Aramakiaza, Aobaku, Sendaishi, Miyagi, Japan

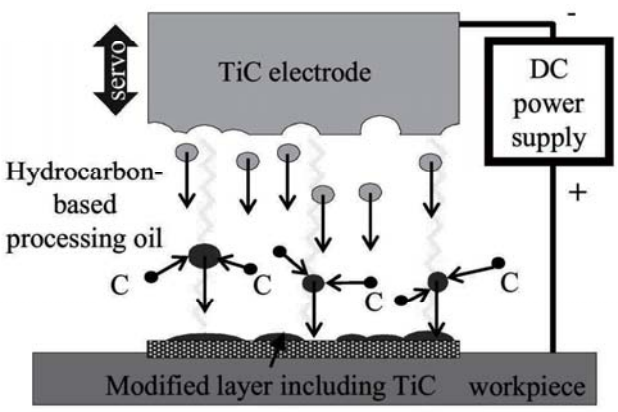

Fig. 1 Mechanism of PS treatment [5]

surface during the discharge. In fact, ~ 10,000 arc discharges occur every second, and the gap between the electrode and workpiece during processing is controlled in the order of tens of micrometers using servo motors [6]. Spectroscopic analysis has confirmed that the temperature of the arc discharge reaches ~ 6000–7000 K [7]. Moreover, the heat flux at > 109 W/m^2 from the arc discharge instantaneously melts and evaporates the electrode. The molten electrode material is laminated in the molten pool on the surface of the workpiece. Usually, the green compact electrode, which is easily consumed, is used to transfer the electrode material to the workpiece surface during processing [8]. The advantages of PS treatment are as follows [5]:

1. The deformation on workpiece surfaces is considerably less because the shrinkage of the workpiece is limited to a shallow range via local pulse discharge during PS treatment.
2. Local treatment is possible by controlling the shape of the electrode material and vibration pattern during processing.
3. The modified layer is highly adhesive because the electrode material is melted by the heat of the arc discharge and mixes with the workpiece material.
4. PS treatment uses appropriate electrode materials to yield various surface characteristics [9]. Previously, a modified layer with high hardness was successfully formed on Fe-based materials using a titanium carbide (TiC) electrode [10].

In conventional research, the detailed characteristics of high-speed steel (HSS) after PS treatment have not been studied [3, 11]. Therefore, to clarify HSS characteristics after PS treatment, we observed and analyzed the shape of a single dimple sample and the modified surface, the amount of transferred titanium (Ti) atoms, and the parameters (e.g., Sa, Sku, and Ssk). Then, we evaluated the mechanical characteristics of modified surfaces by the Vickers hardness (HV) and friction tests. Finally, a new PS treatment was developed that addressed shape deterioration in the cutting edge by adjusting the electrode's position, which is known as position-adjusted PS (PA-PS) treatment. This treatment solves the disadvantage of shape deterioration known as "sagging" on application of PS treatment to the edge of cutting tools.

2 Plasma-Shot Characteristics of HSS Workpiece

2.1 Methodology

The electrode material used in the experiment was TiC, which improved surface wear resistance. The workpiece material was HSS (C: 2.0%, Si: 0.5%, Mn: 0.3%, Cr: 3.8%, Mo: 2.5%, V: 5.1%, W: 14.3%, Co: 11.0%). In this experiment, an electric discharge machine (Mitsubishi Electric Corporation, ES041-A) was used. Moreover, for this process, the workpiece and TiC electrode had positive polarity. Figure 2 and Table 1 show the setup and PS treatment conditions, respectively.

2.2 Observation of a Single Dimple

In this study, scanning electron microscopy (SEM), white light interferometry (WLI), and energy-dispersive X-ray

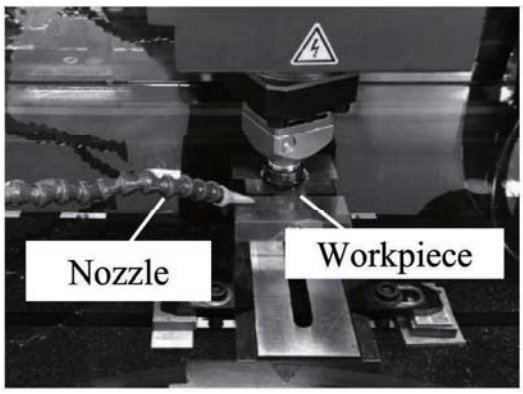

Fig. 2 Setup of PS treatment

Table 1 PS treatment conditions

Voltage	320 V
Pulse duration	8 μs
Pause time	256 μs
Electrode materials	TiC

diffraction (EDX) were used to evaluate the surfaces of the modified layers. A TiC electrode was used to apply PS treatment to HSS surfaces to confirm the effect of discharge current (I_p) on the formation of a single dimple, which was observed using SEM and WLI. Table 1 lists the experimental conditions in which I_p was 1, 3, 10, and 21 A. A single dimple was observed because the modified surface was the outcome of a series of single dimples [12]. Figure 3 shows the SEM images of the single dimple at each I_p. Figure 4 shows the diameter of the single dimple in each I_p measured from Fig. 3. We used the WLI to measure the 3D topography of a single discharge and calculated the average value of the three points where the height of peaks and depth of craters were large for the measurement area of each I_p. Figure 5 shows the roughness of the single dimple of each I_p. The round shape of the single dimple formed in each I_p was confirmed in Fig. 3; the black part in the image was the crater. The shapes of the single dimples were complicated by the effect of the surrounding conditions and the flow of the machining fluid when they were once melted and resolidified. The diameters of the individual dimples increased along with an increase in I_p; however, their growth became saturated after $I_p = 10$ A in Fig. 4. A previous study reported that the capacity of workpiece melting was increased by an increase in discharge current energy [13]. Thus, the diameter of a single dimple increased along with an increase in I_p. On the other hand, dimples with the same diameters were formed under $I_p = 10$ and 21 A. Thus, we confirmed that the height of the peak and the depth of the crater in the discharge dimple increased along with an increase in I_p; however, the height of the peak saturated after $I_p = 10$ A (Fig. 5). This tendency was similar to that of cast iron [11].

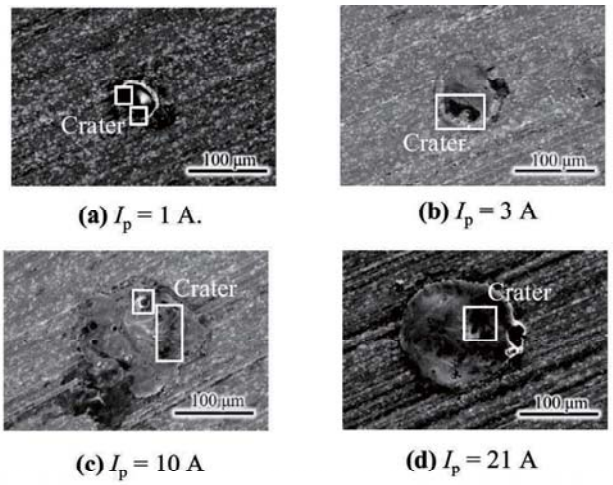

Fig. 3 SEM images of the single dimple on each I_p

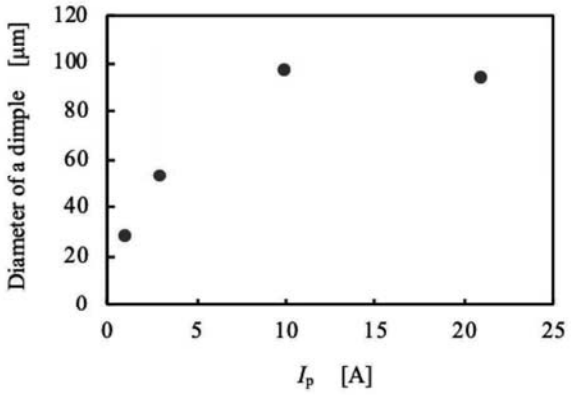

Fig. 4 Relationship between the diameter of a single dimple and I_p when I_p increases

2.3 Observation and Analysis of the Modified Layer

We used SEM to observe the surfaces of modified layers when I_p and the electrode consumption volume (V_e) were varied. The experimental conditions were the same as the ones given in Table 1. The HSS surface was subjected to PS treatment under $I_p = 3$, 10, and 21 A and $V_e = 0.025$, 0.05, and 0.1 mm. The PS treatment time was increased along with an increase in V_e. Figure 6 shows the SEM image of the modified layer when I_p and V_e changed. The modified layer had rough surfaces under each condition, and the size and number of dimples increased when I_p increased under each V_e.

In addition, we used EDX to evaluate the amount of transferred titanium (Ti) atoms from the TiC electrode to the surface on the modified layer when I_p and V_e were varied. Figure 7 shows the change in the Ti atomic number concentration when I_p and V_e changed. An increase in the Ti atomic

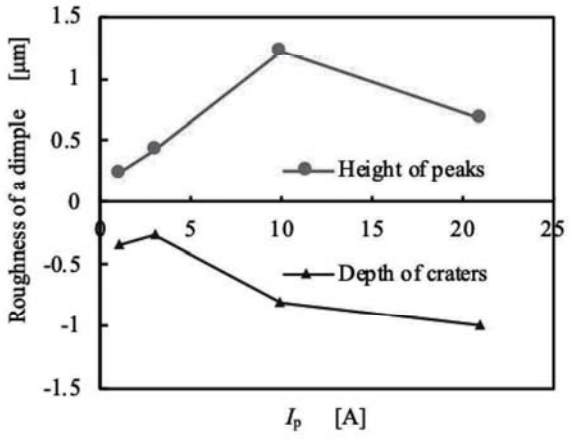

Fig. 5 Relationship between the roughness of a single dimple and I_p when I_p increases

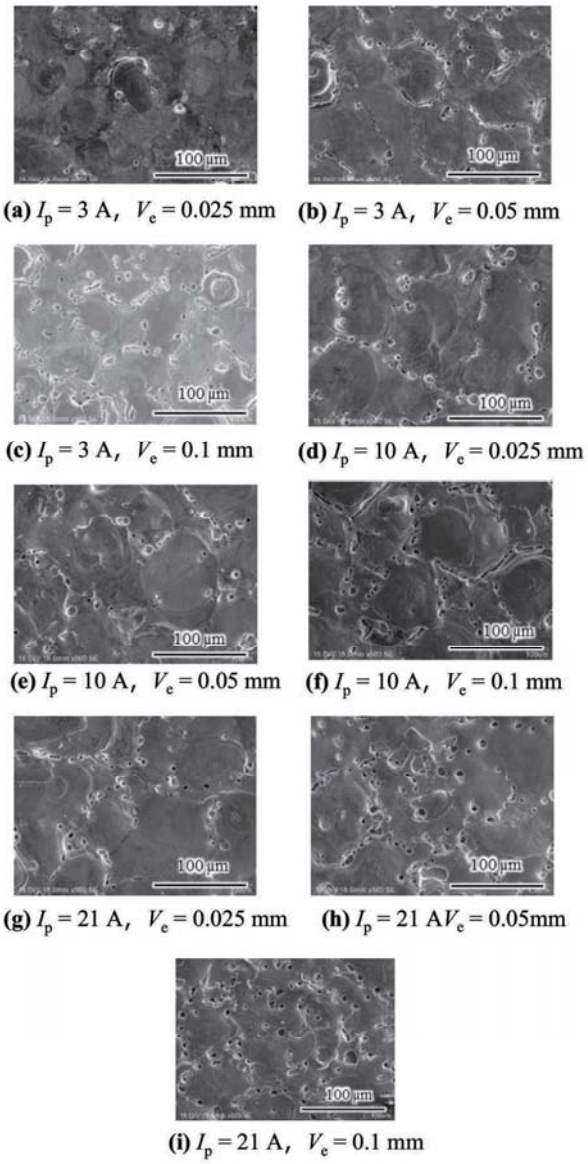

Fig. 6 SEM images of the modified layer when I_p and V_e are varied

number concentration along with an increase in V_e for each I_p was confirmed. The thickness of the TiC-modified layer increased along with an increase in V_e. Moreover, a considerable increase was observed in the Ti atomic number concentration under I_p=3 A and V_e=0.1 mm. This increase was due to the increase in transferred TiC from the electrodes to workpiece surfaces owing to longer treatment time and a decrease in I_p.

2.4 Evaluation of the Modified Surface Topography

The roughness of the modified layer is closely related to the friction of the surface. Therefore, we analyzed the surface

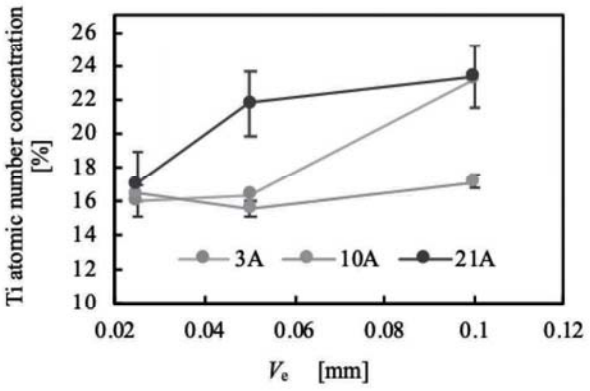

Fig. 7 Change in Ti atomic number concentration when I_p and V_e changed

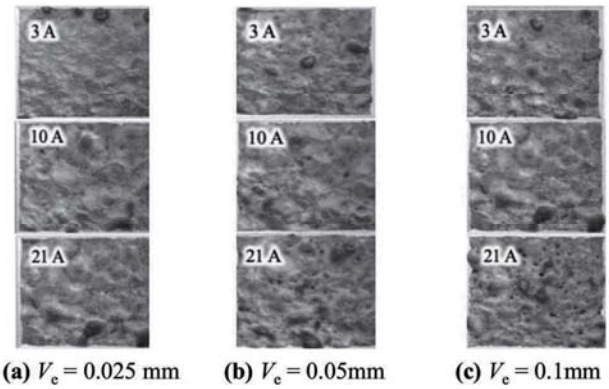

Fig. 8 Topography of modified surfaces when I_p and V_e are varied

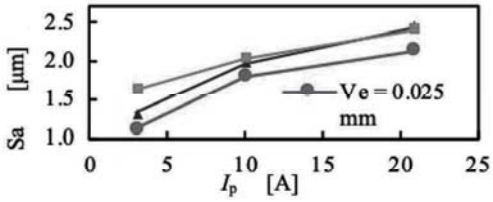

Fig. 9 Relationship between Sa of modified surfaces and I_p when I_p increases on each V_e

and evaluated its parameters (e.g., Sa, Sku, and Ssk) when V_e and I_p were varied. Figure 8 shows the topography of the modified surface evaluated by WLI. The height difference between the top and bottom and roughness of the modified layer increased. The increase in roughness in the single dimple along with an increase in I_p affected this result. The roughness of the modified layer did not change when V_e increased. Figure 9 shows the quantitative evaluation of the Sa increase when I_p increased. The increase in Sa was due

Table 2 Relationship between Sku and the roughness of surfaces

Sku > 3	Surfaces have a sharp roughness
Sku = 3	Height distribution is normal
Sku < 3	Surfaces have a dull roughness

Table 3 Relationship between Ssk and the symmetry of surfaces

Ssk > 0	Surfaces have many mounds
Ssk = 0	Height distribution is symmetrical
Ssk < 0	Surfaces have many craters

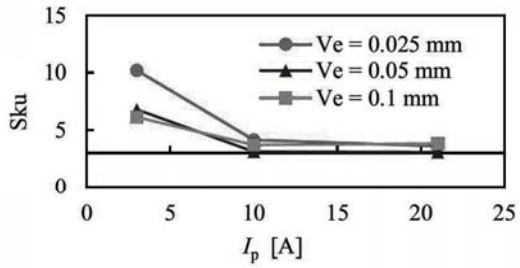

Fig. 10 Relationship between Sku of modified surfaces and I_p when I_p increases on each V_e

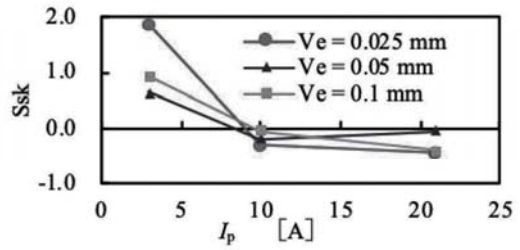

Fig. 11 Relationship between Ssk of modified surfaces and I_p when I_p increases on each V_e

to the high treatment temperature. The change in Sa because of the increase in V_e was not confirmed. Sku is the sharpness of the surface, while Ssk is the symmetry of the surface and characterizes height distribution [14]. Tables 2 and 3 show the relationship between Sku and the sharpness of the surfaces and the relationship between Ssk and the symmetry of the surfaces, respectively. Figures 10 and 11 show Sku and Ssk of the modified layer. Figure 10 shows that the surface treated under $I_p = 3$ A has Sku > 3, which suggests a sharp roughness of shape. The surface treated under $I_p = 10$ A and 21 A has Sku < 3, which indicates a dull roughness of shape. Figure 11 shows that the surface treated under $I_p = 3$ A has Ssk > 0, which shows that the surface has many peaks. The surface treated under $I_p = 10$ and 21 A has Ssk < 0, which

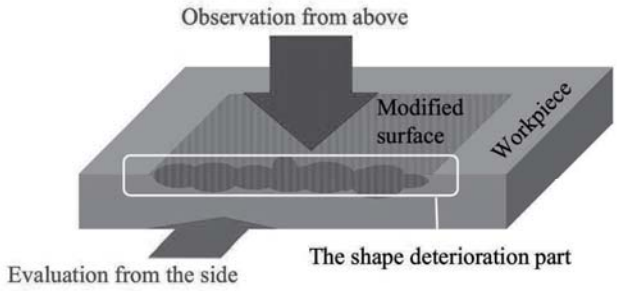

Fig. 12 Schematic of observation and evaluation

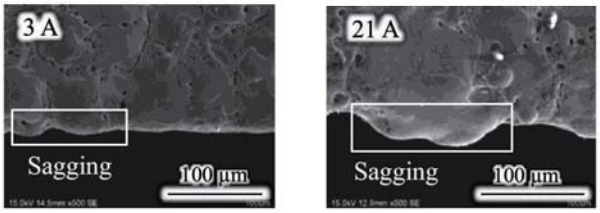

(a) $I_p = 3$ A **(b)** $I_p = 21$ A

Fig. 13 SEM images of the shape deterioration (sagging) on the edge of the workpiece on each I_p

indicates that the surface has multiple craters. The surface treated under $I_p = 10$ and 21 A has low friction because the dimples supply oil to the surfaces because of hydrodynamic lubrication.

2.5 Evaluation of the Edge Shape of Modified Surfaces

We applied PS treatment to the edge of cutting tools to treat the edge of the HSS workpiece. We used SEM and WLI to observe and evaluate the edges of the treated surfaces from above and the side, respectively, to confirm the relationship between the change in I_p and the generation of "sagging." The experimental conditions were the same as those given in Table 1, and $V_e = 0.05$ mm. Figure 12 shows the observation and evaluation methods. Figure 13 shows that the shape deterioration called "sagging" on the edge of the workpiece was generated in each I_p. The size of sagging increased when I_p increased. This result can be attributed to the tendency of the diameter of the dimple and Sa on the surfaces to increase when I_p increases. Figure 14 shows the topography of the edge of workpieces from the side of each I_p. The topography under $I_p = 21$ A shows the partial error of high roughness to the side. The heights of sagging to the side are ~ 8 μm under $I_p = 3$ and ~ 18 μm under $I_p = 21$ A. The tendency of the increase in shape deterioration was the same as that of

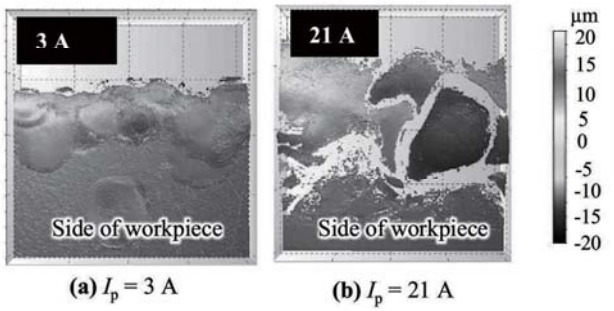

Fig. 14 Topography of the edge of workpieces from the side for each I_p

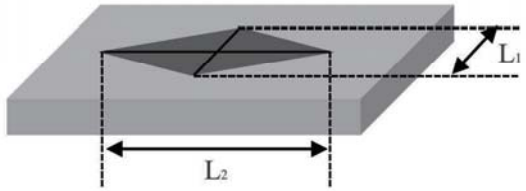

Fig. 15 Image of the generated indentations

the diameter of dimples in Fig. 4. The heights of sagging to the side are smaller than the diameters of dimples at each I_p.

3 Mechanical Characteristics of the Treated Surfaces

We conducted HV and friction tests to evaluate the mechanical characteristics of the treated surfaces by PS treatment. We used the HV test to measure the hardness of the treated surface and investigate the change in HV when I_p was increased. In this test, a microscope was used to determine the analysis area, and an indent was generated by a Vickers indenter. Hardness was measured by dividing the applied load P by the surface area of the generated indentation. Figure 15 shows the generated indentations. The surface area was calculated using L_1 and L_2. The following equation was used for HV:

$$\mathrm{HV} = 189.1 \times 2P/(L_1 + L_2)^2$$

where L_1 and L_2 are the diagonal lengths of the diamond-shaped indentations and P is the load. Table 2 shows the test conditions. We evaluated the HSS workpiece and treated the surfaces in Table 1 for each $V_e = 0.05$ mm when I_p increased. Figure 16 shows HV when I_p increased. The HV test confirmed that the hardness of the modified surface was ~ 300–600 HV larger than that of an untreated HSS surface. Moreover, the hardness increased along with an

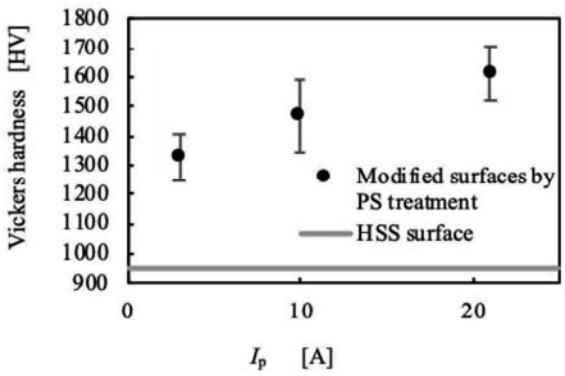

Fig. 16 Relationship between HV and I_p when I_p increases

Table 4 HV test conditions

Indenter type	Vickers
Test load (mN)	1000
Retention time (s)	5
Lens magnification	100 times
Load speed (mN/s)	70.6
Number of indentations	10

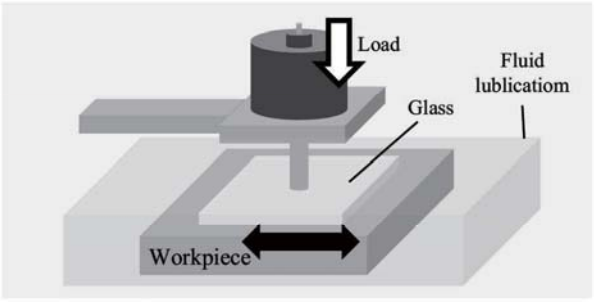

Fig. 17 Schematic of reciprocating friction test with a glass surface under fluid lubrication

increase in I_p, primarily because the thickness of the TiC-modified layer increased along with an increase in the depth of the treated area when I_p increased in the PS treatment process.

We conducted a reciprocating friction test under fluid lubrication to evaluate the friction characteristics of the modified surfaces. Table 3 gives the test conditions, whereas Table 4 gives the lubricating oil specifications. Figure 17 shows the reciprocating friction test with a glass surface under fluid lubrication. The kinematic viscosity of fluid was 8.108 s/mm^2, and the friction test was used to evaluate four types of workpieces: HSS workpieces and modified workpieces by PS treatment under the conditions

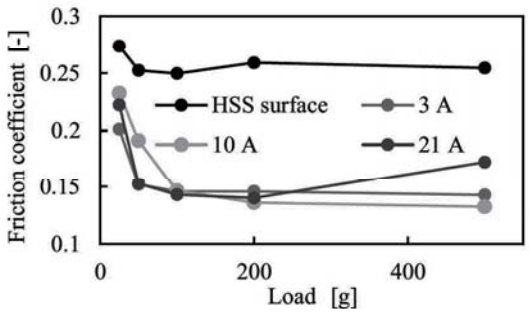

Fig. 18 Relationship between friction coefficient and load at any surface

Table 5 Reciprocating friction test conditions

Load (g)	25, 50, 100, 200, 500
Reciprocating speed (cpm)	180
Linear velocity (mm/s)	30
Reciprocating width (mm)	5
Test time (s)	600

Table 6 Lubrication oil specifications

Kinematic viscosity (s/mm^2)	8.108
Density (g/cm^3)	0.869

of $I_p = 3$, 10, and 21 A and $V_e = 0.1$ mm. The load was increased from 25 to 500 g in the friction test. Figure 18 shows the friction test results. The friction coefficient of the modified surfaces was ~ 0.05–0.10 less than that of the HSS surface in any load. We speculate that dimples on the modified surfaces remained and transferred fluid between the modified surfaces and the glass during the reciprocating movement. Friction reduction by discharge dimples was confirmed, especially under low-load conditions from 25 to 100 g. This reduction was attributed to the wedge effect, generating hydrodynamic pressure in the narrow gaps [15]. However, the friction coefficient at $I_p = 21$ A increased under high-load condition from 200 g, which was attributed to contact between peaks on the modified surfaces and the glass because gaps decreased as the load increased. Therefore, the friction reduction effect owing to hydrodynamic pressure was significant under low load, but the friction increase was generated by the contact between peaks on the modified surfaces and the glass under large load. We concluded that PS treatment improved the friction characteristics of the surface materials arising from a decrease in the friction coefficient under fluid lubrication (Tables 5, 6).

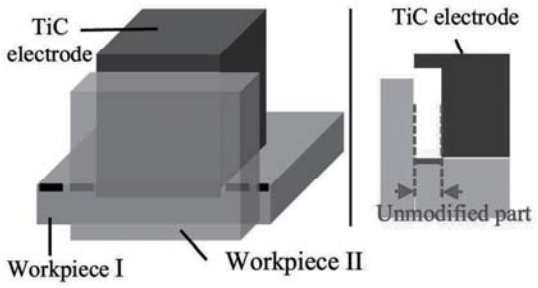

Fig. 19 Position-adjusted PS (PA-PS) treatment

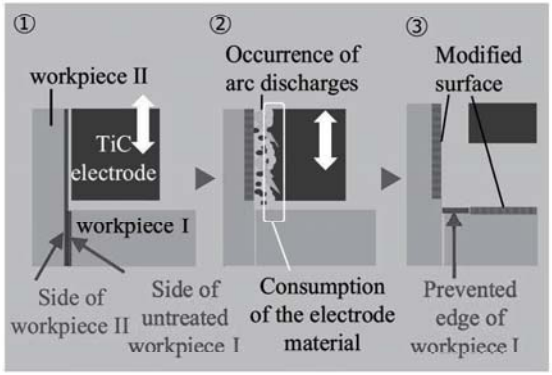

Fig. 20 Process and mechanism of PA-PS treatment

4 Position-Adjusted PS Treatment

We discovered that PS treatment had the disadvantage of causing shape deterioration known as "sagging" when it was applied to the edge of the cutting tools in Sect. 2.5. The size of sagging increased as I_p increased; thus, this study introduces a new PS treatment that addresses shape deterioration in the cutting edge by adjusting the electrode's position, which is known as position-adjusted PS (PA-PS) treatment.

PS treatment was applied to the edge of the HSS workpiece at $I_p = 3$ and 21 A. The experimental conditions were the same as those given in Table 1, and $V_e = 0.05$ mm. Figures 19 and 20 show the appearance and process of PA-PS treatment, respectively. First, this treatment adjusted the side of untreated workpiece I to the side of workpiece II (Fig. 20). Second, the position of the end of the electrode material was adjusted to the edge of workpiece I because of the consumption of the side surface of the electrode material by arc discharges between the side of the electrode material and that of workpiece II during the treatment process. Finally, this treatment prevented the edge of workpiece I from causing shape deterioration because of the adjusted electrode material in the PS process. After the

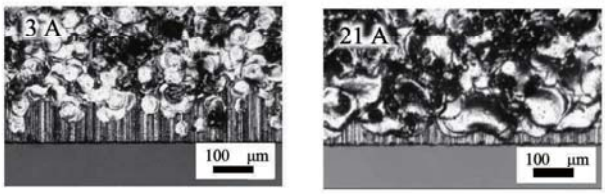

Fig. 21 DM images of the edge of the modified surfaces by PA-PS treatment for each I_p

above process, we used PA-PS treatment to observe and evaluate the edge of the modified surface.

Figure 21 shows the digital microscopy (DM) images of the edge of the modified surfaces using PA-PS treatment. The black and silver parts represent craters and peaks on the modified surfaces in Fig. 21, respectively. The edges of the modified surfaces under $I_p = 3$ and 21 A were successfully prevented from causing shape deterioration (Fig. 21). We used a DM to measure the maximum distance from the edge of the workpiece to the modified surface under I_p to evaluate the appropriate I_p. The measurement results show that the maximum distance from the edge of the workpiece to the modified surface is ~ 150 μm when $I_p = 3$ A and ~ 80 μm when $I_p = 21$ A. This indicates that PA-PS treatment under $I_p = 21$ A can successfully treat the edge of the modified surface. We argue that the distance from the edge of the workpiece to the modified surface was reduced because of an increase in the diameter of a single dimple when I_p increased in Fig. 4. Moreover, the deterioration of the side surface of the electrode material was not generated and the large dimple reached the edge of the modified surface at $I_p = 21$. Therefore, PA-PS treatment at $I_p = 21$ with high hardness was applied to the surface of the cutting tool.

5 Conclusions

In this study, the characteristics of the modified surfaces treated by PS treatment on the HSS workpiece were identified using the TiC electrodes. Based on the experimental results and further discussion, the following conclusions were drawn:

(1) The diameter of a single dimple increases along with an increase in I_p; however, its growth saturates after $I_p = 10$ A.
(2) The height of a peak and the depth of a crater in a discharge dimple increases along with an increase in I_p; however, their growth saturates after $I_p = 10$ A.
(3) The modified layer subjected to PS treatment has rough surfaces, and the roughness of the modified surface increases as I_p increases.
(4) The Ti atomic number concentration in the modified layer increases as V_e increases for each I_p.
(5) The peak shapes on the modified surfaces under $I_p = 3$ A and $I_p = 10$ and 21 A are sharp and dull at any V_e.
(6) The modified surface treated under $I_p = 3$ A has multiple peaks, and the modified surface treated under $I_p = 10$ and 21 A has multiple craters.
(7) The size of "sagging" increases when I_p increases; the heights of "sagging" to the side are ~ 8 μm at $I_p = 3$ A and ~ 18 μm at $I_p = 21$ A.
(8) The hardness of the modified surface is ~ 300–600 HV larger than that of an untreated HSS surface. The hardness increases along with an increase in I_p.
(9) PS treatment improves the friction characteristics of the surfaces of materials because of a decreasing friction coefficient under fluid lubrication.
(10) The maximum distance from the edge of the workpiece to the modified surface is ~ 150 μm when $I_p = 3$ A and ~ 80 μm when $I_p = 21$ A. Moreover, PA-PS treatment under $I_p = 21$ A successfully treated the edge of the modified surface.

References

1. Yamada Y, Ikeda T (1995) Coated cutting tools—drills, endmills. JSPE 61(6):778–782
2. Kıvak T (2014) Optimization of surface roughness and flank wear using the Taguchi method in milling of Hadfield steel with PVD and CVD coated inserts. Measurement 50(1):19–28
3. Sumi N, Goto A, Teramoto H, Yasunaga Y, Nakano Y (2012) Study of improvement of TiC layer by electrical discharge coating—metallographic analyses and characteristics evaluations of improved TiC layer containing Si. JSEME 46(113):133–140
4. Kibria G, Sarkar BR, Pradhan BB, Bhattacharyya B (2010) Comparative study of different dielectrics for micro-EDM performance during microhole machining of Ti–6Al–4V alloy. Int J Adv Manuf Technol 48(5):557–570
5. Mohri N, Saito N (1998) Surface modification by electrical discharge machining. JSPE 64(12):1715–1718
6. Ochiai H, Watanabe M, Arai M, Yoshizawa H (2009) MS coating; useful for life elongation and recovery of parts. IHI Tech Rep 49(4):234–243

7. Hashimoto H, Kunieda M (1997) Spectroscopic analysis of temperature variation of EDM arc plasma. JSEME 31(68):32–40
8. Mohri N, Saitoo N, Tsunekawa Y, Moriyama H, Miyagawa A (1993) Surface modification by electrical discharge machining composite electrode method. JSPE 59(4):625–630
9. Ching-Yuan B, Chun-Hao K (2006) Effects of kerosene or distilled water as dielectric on electrical discharge alloying of superalloy Haynes 230 with Al–Mo composite electrode. Surf Coat Technol 200:4127–4135
10. Moro T, Goto A, Mohri N, Saito N, Matsukawa K, Miyake H (2001) Surface modification process by electrical discharge machining with TiC semi-sintered electrode. JSPE 67(1):114–119
11. Katou C, Egawa A, Kyoizumi T, Sumi N, Xu S, Shimsda K, Mizutani M, Kuriyagawa T (2016) Study on surface treatment by plasma discharge modification Properties evaluation of treated surface under different discharge conditions. In: 2016 JSPE autumn conference, pp 161–162
12. Salonitis K, Stournaras A, Stavropoulos P, Chryssolouris G (2009) Thermal modeling of the material removal rate and surface roughness for die-sinking EDM. Int J Adv Manuf Technol 40:316–323
13. Uno Y, Endo O, Nakajima T (1991) Fundamental aspect of the crater generation mechanism by a single pulse discharge. JSEME 25(49):9–22
14. Yoshida S, Ootake K, Kawanabe K, Kagawa Y, Isono H, Sugibayashi T (2011) Evaluation parameters of surface texture on shot-blasted surfaces. J Jpn Inst Light Met 61(5):187–191
15. Kyoizumi T, Egawa A, Shibata Y, Kato C, Sumi N, Shimada K, Mizutani M, Kuriyagawa T (2018) Low wear/low friction interface generation by plasma-shot treatment and grinding processing. J Jpn Soc Abras Technol 62(7):371–376

Yorihito Shibata is a Master course student at the Department of Mechanical System Engineering, Graduate School of Engineering, Tohoku University. He received the Bachelor's degree at the Department of Mechanical and Aerospace Engineering of Tohoku University in 2018. His research interest is surface texturing with Electric Discharge Machining.

Yusuke Sakairi is a Master course student at the Department of Mechanical System Engineering, Graduate School of Engineering, Tohoku University. He received the Bachelor's degree at the Department of Mechanical and Aerospace Engineering of Tohoku University in 2019. His research interest focus on the development of nano-/micro-hybrid texturing method with Non-conventional machining process.

Keita Shimada is an Assistant Professor at the Department of Mechanical System Engineering, Graduate School of Engineering, Tohoku University. He received his Ph.D. from Tohoku University in 2012. His main research interests focus on the calculation and simulation of mechanical machining process.

Masayoshi Mizutani is an Associate Professor at the Department of Mechanical System Engineering, Graduate School of Engineering, Tohoku University. He received his Ph.D. from Keio University in 2006. His main research interests focus on the applications of nano-/micro-hybrid textured surface and on the creation of the functional interface for bio-medical applications.

Tsunemoto Kuriyagawa is a Professor at the Graduate School of Biomedical Engineering, Tohoku University. He received his Ph.D. from Tohoku University in 1990. His main research interests are Nano-Precision Mechanical Manufacturing, Micro/Meso Mechanical Manufacturing (M4 process) and Powder Jet Deposition.

Paper:

Study on the Creation of Fine Periodic Structure on V-Shaped Groove with Short-Pulsed Laser

Ryohei Takase[*1], Shuhei Kodama[*2], Keita Shimada[*1], Holger Mescheder[*3], Kai Winands[*3], Jan Riepe[*3], Kristian Arntz[*3], Masayoshi Mizutani[*1,†], and Tsunemoto Kuriyagawa[*4]

[*1]Department of Mechanical Systems Engineering, Graduate School of Engineering, Tohoku University
6-6-01 Aramaki Aza-Aoba, Aoba-ku, Sendai, Miyagi 980-8579, Japan
[†]Corresponding author, E-mail: masayoshi.mizutani.b6@tohoku.ac.jp
[*2]Department of Mechanical System Engineering, Graduate School of Engineering, Tokyo University of Agriculture and Technology, Tokyo, Japan
[*3]Department of Non-conventional Manufacturing Processes and Technology Integration,
Fraunhofer Institute for Production Technology IPT, Aachen, Germany
[*4]Graduate School of Biomedical Engineering, Tohoku University, Sendai, Japan
[Received May 19, 2020; accepted May 20, 2020]

Functional surface creation technologies have garnered increasing attention over the years. These technologies can provide various functions to a material by establishing a fine structure on the material surface and responding to the needs of industrial products with distinguished functions or high values. In addition, by creating a "composite fine structure," which is composed of two kinds of structures with different scales, the enhancement of functions and emergence of new functionalities can be expected. Hence, our study combined a micrometer-scale V-shaped groove structure using an ultra-precision cutting and nanometer-scale ultra-fine periodic structure (LIPSS) using a short-pulsed laser. Then, we clarified the creation principle and studied the functionality of the structure, specifically, its wettability. As a result, it was found that optical behavior inside the V-shaped groove changed; therefore, the composite structure changed depending on the groove angle, laser polarization direction, and number of times of irradiation. In addition, it was found that the water wettability changed depending on the type of formed micro-nano composite structures. Moreover, the wettability could be controlled by depending on how the structure is used.

Keywords: short-pulsed laser, ultra-fine periodic structure (LIPSS), composite fine structure, wettability

List of symbols

τ_p:	Pulse width
λ:	Laser wavelength
E_d:	Irradiation energy density
n:	Number of times of irradiation
P:	Pitch width of LIPSS
P_λ:	Pitch width of laser wavelength
P_g:	Pitch width of V-shaped groove

1. Introduction

1.1. Research Background

Currently, the need for industrial products with distinguished functions and values has been increasing, and many researches have attempted to address this concern. In particular, functional surface creation technologies have gathered increasing attention due to their ability to improve the characteristics of conventional materials and provide new functions by creating a fine structure of micro or nanometer scale on material surfaces [1–5]. Examples of functional surfaces are those that have controllable optical properties [6, 7], controllable wettability [8–13], reducible friction and abrasion [14, 15], improvable biocompatibility [16–20], and reducible flow resistance [21–23]. In this study, a fine structure with appropriate shape and dimensions was formed on a material surface to obtain the necessary functions using mechanical and non-conventional processing such as cutting and grinding, and laser processing and electric discharge machining, respectively. When multiple machining processes are combined to create a "composite fine structure," which is a combination of different scales of fine structures, the functions of each structure become integrated to either significantly enhance the functionality of the new structure or create a new function for it. However, studies on composite structures formed by combining multiple processing methods and behaviors of composite material surfaces have not been clarified.

This study focused on the combination process of cutting and laser processing to create a composite fine structure. To obtain a favorable slope of the groove of the micrometer scale formed using ultra-precision cutting technology, a short-pulsed laser (SPL) was irradiated. This was conducted to create a fine periodic structure of the nanometer scale (laser induced periodic surface structure, LIPSS) inside the micrometer scale grooves, which is also known as the micro-nano composite fine structure. We also studied the influence of the groove structure of the

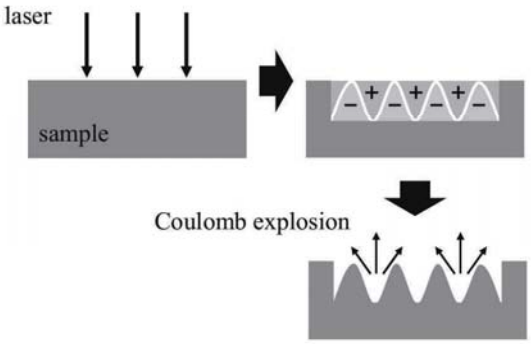

Fig. 1. LIPSS creation process.

surface where SPL was irradiated to create LIPSS. In addition, we produced a composite structure of fine grooves and LIPSS and studied its effect on wettability.

1.2. Principle of Creating LIPSS on Plane

LIPSS is a fine periodic structure formed by irradiating a laser with short pulses of the width τ_p of pico or femto seconds to a material surface. Optical excitations, called Coulomb explosion, directly cut interatomic connections, which remove the material and form the structure [24]. The details of the phenomenon is as follows: when a strong optical electric field, such as ultra-short pulsed laser, is irradiated on a solid surface, electrons involved in the connections of atoms are directly removed and the remaining ions repel each other due to the Coulomb forces and scatter from the surface. In particular, it was reported that the irradiation of a laser with a fluency near the machining threshold results in the self-organization of LIPSS on the surface with a periodicity smaller than the laser wavelength perpendicular to the laser polarization [25–28].

The machining principles of LIPSS currently being studied include a model of interference of the irradiated light with light scattered from the surface and surface radio waves [28] and a surface plasmon model [29]. The pitch width P of LIPSS formed with these models satisfied the following equations, respectively [28, 29].

$$P = \frac{\lambda}{1 \pm \sin\theta}, \quad \ldots\ldots\ldots\ldots\ldots\ldots (1)$$

$$\frac{\lambda}{3} \leq P \leq \lambda. \quad \ldots\ldots\ldots\ldots\ldots\ldots (2)$$

Equation (1) is for the model of interference of the irradiated light with light scattered from the solid surface and surface radio waves. Eq. (2) is for the surface plasmon model. As shown in **Fig. 1**, the electric field strength distribution on the material surface changes with the pitch width, and depending on above equations and Coulomb explosion occurs to create LIPSS. The two models can be used only when the machining target is a plane. However, phenomena occurring on a machining target having a fine structure (unevenness or grooves) have not been clarified. In this study, we studied and discussed how the LIPSS changes and what characteristics the obtained surface would have if the target object to which a laser was irradiated had a fine structure.

Table 1. Laser irradiation conditions.

Laser wavelength λ [nm]	1064
Pulse width τ_p [ps]	20
Frequency f [Hz]	50
Energy density E_d [J/cm^2]	0.036–0.371
Number of times of irradiation n [shots]	1–30

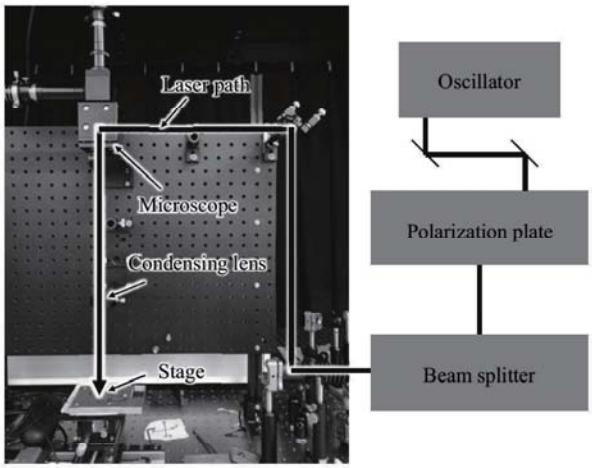

Fig. 2. Optical system of laser used.

2. Experiment on the Irradiation on Slopes of V-Shaped Grooves

We first irradiated a short-pulsed laser to the V-shaped grooves that was produced using an ultra-precision cutting technology and observed an LIPSS creation process.

2.1. Experimental Method

In the study, we used a sample (hereinafter referred simply to Ni-P) formed by plating amorphous nickel phosphorus to a base material of stainless steel (SUS430). We first formed a V-shaped groove structure on the sample using an ultra-precision 5-axis machine (MIC 300, Nagase Integrex Co., Ltd.). The surface was flattened with a diamond R bite and the V-shaped grooves with a depth of 50 μm and a pitch of 500 μm were made using a diamond V bite with an edge angle of 90° and 120°. The machining was conducted in an oil mist environment.

Next, we performed a laser irradiation experiment to the machined sample under the condition shown in **Table 1**. Our laser optical system is shown in **Fig. 2**. As shown in the figure, the optical system was set up in order for the laser to point vertically to the sample on the stage. The thick black line in the figure indicates the optical path of the laser. To study the effect of the V-shaped grooves

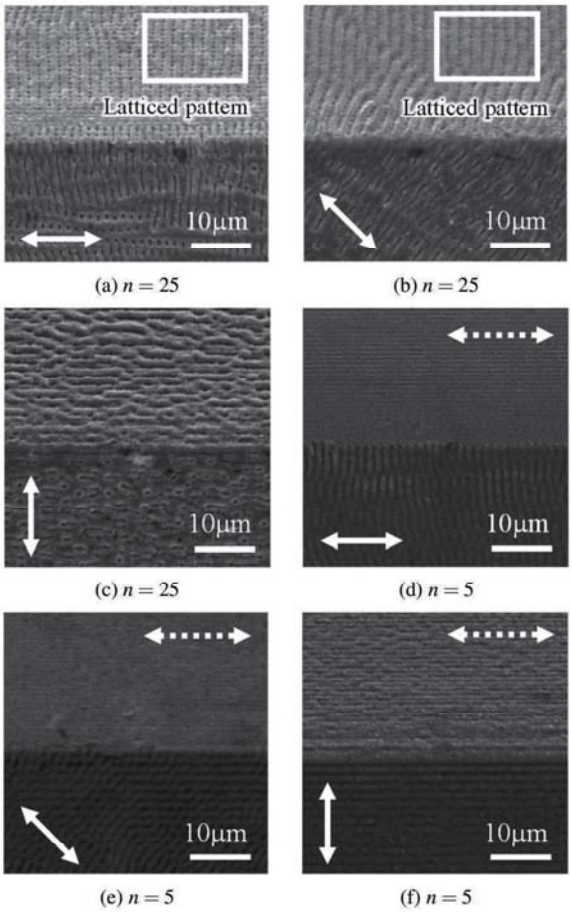

(a) $n = 25$ (b) $n = 25$ (c) $n = 25$ (d) $n = 5$ (e) $n = 5$ (f) $n = 5$

Fig. 3. Result of laser irradiation to 90° V-shaped grooves ($E_d = 0.191$).

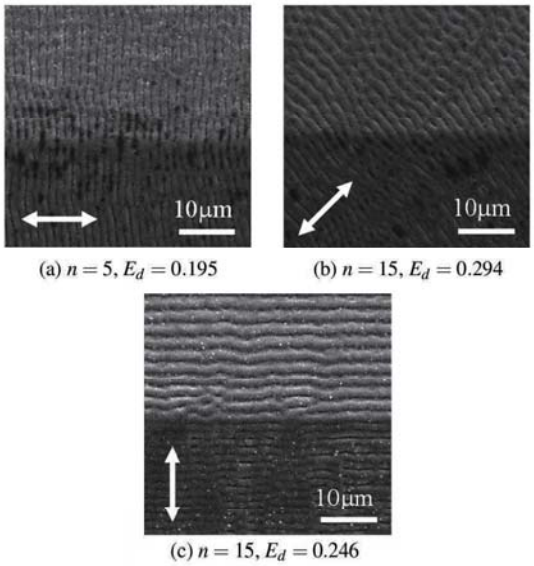

(a) $n = 5$, $E_d = 0.195$ (b) $n = 15$, $E_d = 0.294$ (c) $n = 15$, $E_d = 0.246$

Fig. 4. Result of laser irradiation to 120° V-shaped grooves.

on the creation of LIPSS, we performed the experiment using three polarization angles of the laser. We used 0°, 45°, and 90° against the formed V-shaped grooves. In this study, we defined the polarization direction parallel to the grooves to be 0°. The spot size of the laser slightly changed depending on the irradiation conditions; however, it was always approximately 100–150 μm and had approximately the same width as that of the V-shaped grooves. The irradiation energy density E_d and number of times of irradiation n specified in the irradiation conditions were determined based on the values obtained in a preliminary experiment that irradiated laser to a plane sample and formed an LIPSS. The energy density distribution of the laser used in the experiment was Gaussian distribution. A single laser irradiation was made in the atmosphere with the external air temperature of 296 K.

2.2. Experimental Results

After creating the V-shaped groove on the surface of Ni-P and irradiating a short-pulsed laser to the slope of the grooves, we observed the resulting LIPSS using a scanning electronic microscopy (SEM). The results are shown in **Figs. 3** and **4**. In both figures, the upper side indicates the slope of the V-shaped groove; the lower side shows the plane; and the solid arrows show the polarization direction. The figures indicate that the irradiation of a laser with $n = 25$ to the 90° or 120° V-shaped grooves formed LIPSS in the direction vertical to the polarization of the laser as in the case of irradiation to a plane (**Figs. 3(a)–(c)** and **4**). On the other hand, the irradiation of a laser with $n = 5$ to the 90° V-shaped grooves formed LIPSS on the groove slopes with a pitch width smaller than the laser wavelength parallel to the grooves (indicated by the dotted arrows in **Figs. 3(d)–(f)**), irrespective of the polarization direction of the laser. This LIPSS was called unidirectional narrow pitched LIPSS (UNPL). In **Figs. 3(a)** and **(b)**, the formed LIPSS had a periodicity vertical to the polarization but was observed as a lattice when compared to the ordinary LIPSS formed on a plane.

From the above results, one can consider that the formation of LIPSS on the slopes of the V-shaped grooves follows the principle of LIPSS formation on a plane if a laser were irradiated to 90° V-shaped grooves multiple times or to 120° V-shaped grooves; it follows a different principle if a laser were irradiated to 90° V-shaped grooves at a smaller number of times of irradiation. Therefore, in the next section, we examined the cause for the difference in the LIPSS formation principle between on a slope and on a plane and determined whether the cause comes from the angle or shape of the V-shaped grooves.

3. Laser Irradiation of the Single-Side Slope Experiment

As seen in the previous section, a fine periodic structure, different from the LIPSS formed on a plane, was formed using laser irradiation on the slopes of the V-shaped grooves under a certain condition. To find

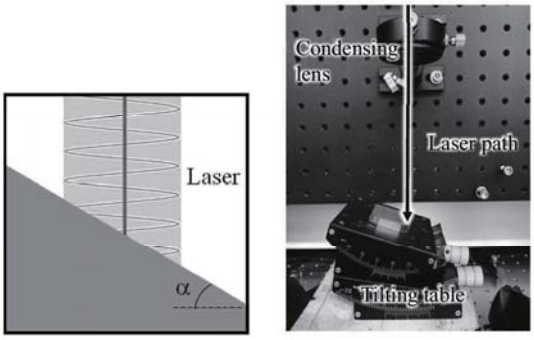

Fig. 5. Laser irradiation to a single slope.

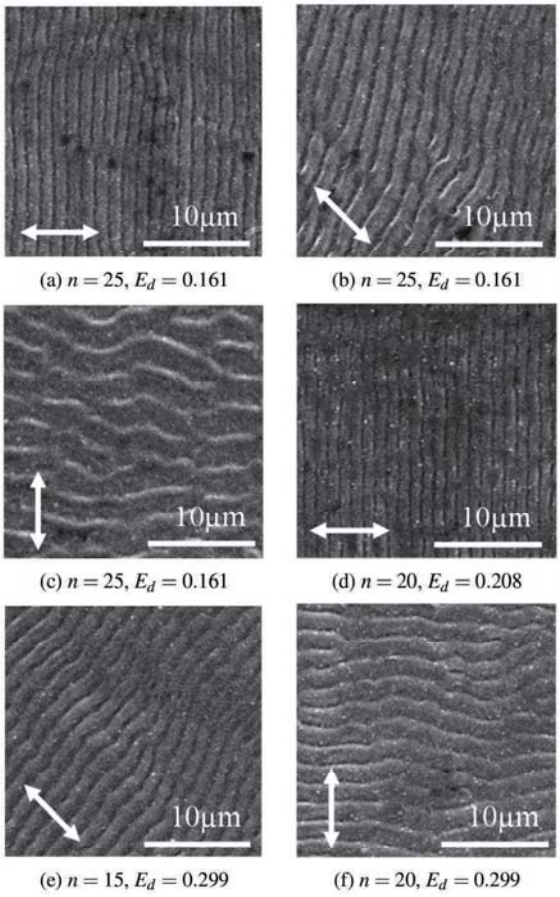

(a) $n = 25$, $E_d = 0.161$ (b) $n = 25$, $E_d = 0.161$

(c) $n = 25$, $E_d = 0.161$ (d) $n = 20$, $E_d = 0.208$

(e) $n = 15$, $E_d = 0.299$ (f) $n = 20$, $E_d = 0.299$

Fig. 6. Result of laser irradiation to a single slope.

whether the structure formation was due to the shape of the grooves, we conducted an experiment of laser irradiation to a single slope which simulated one side of the slopes of the V-shaped grooves as shown in **Fig. 5**. In the experiment, a plane Ni-P sample was placed on a tilted table to simulate the single slope. The tilting angle α was set to the angle of the V-shaped grooves, that is, 45° or 30°. Moreover, we used three conditions for the laser polarization direction in congruence to the V-shaped grooves.

Figure 6 shows the SEM images of the LIPSS formed on the slope. In the figure, $\alpha = 45°$ in **(a)**–**(c)** and $\alpha = 30°$ in **(d)**–**(f)**. As shown in the figure, the laser irradiated to the slope formed the LIPSS in the direction vertical to the laser polarization direction under all the conditions. It was noted that the laser irradiation on the slope did not create LIPSS or UNPL when the number of times of irradiation was small. In **Fig. 6**, the irradiation energy density E_d was different from those used in **Figs. 3** and **4**; however, the result did not change even when the same energy density was used for the laser irradiation on the single slope.

In summary, in this experiment, only the case of a small number of times of laser irradiation to the 90° V-shaped grooves demonstrated a different behavior from the LIPSS creation principle observed on a plane. Therefore, one can consider that the shape and angle of the grooves demonstrated a certain effect to the creation of the UNPL. Because the pitch width of the formed UNLP was evidently smaller than the laser wavelength, we studied the LIPSS creation principle on a slope with respect to the pitch width.

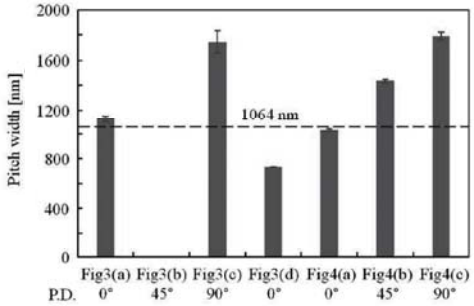

Fig. 7. Pitch width of LIPSS.

4. LIPSS Formation Principle on Slope

4.1. Measurement of LIPSS Pitch Width

In Section 2, the UNPL formed on the slope of the V-shaped grooves when the number of times of laser irradiation was small, as opposed to the principle of the LIPSS formation on a plane. Then, we studied the principle of the LIPSS formation on a slope by measuring the pitch width. The pitch width was calculated by converting the SEM images in **Figs. 3** and **4** to the brightness data and performing fast Fourier transformation (FFT) analysis to the cross-section profiles extracted from the data. The SEM images presented the slope shape projected onto a 2D plane. Therefore, the pitch width calculated from the brightness data was smaller than the actual pitch width of the LIPSS formed on the slope. When necessary, it was divided by cosine to obtain the actual pitch width.

Figure 7 shows the calculated pitch width. The dotted line in the figure indicates the laser wavelength of 1064 nm. In **Fig. 3(b)**, the LIPSS was shallow, and a lattice pattern was formed. Therefore, the cross-section profile and pitch width in the direction could not be extracted and be calculated, respectively, for **Fig. 3(b)**.

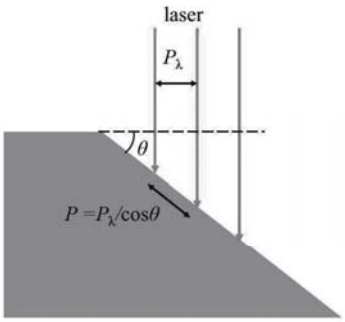

Fig. 8. Laser wavelength on slope.

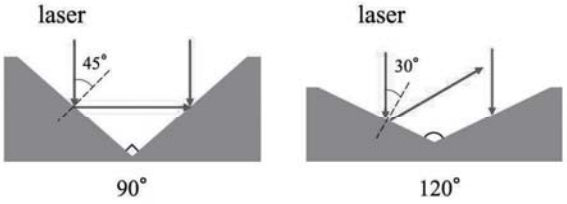

Fig. 9. Laser light behavior inside the V-shaped groove.

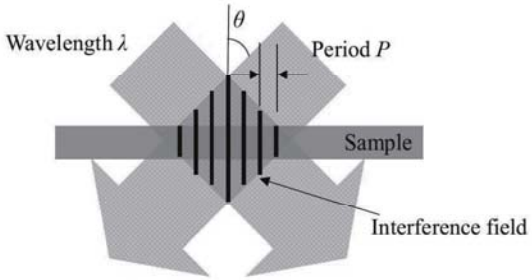

Fig. 10. Schematic diagram of interference exposure method.

In addition, because UNLPs in **Figs. 3(d)–(f)** had approximately equivalent pitches, only the pitch width in **Fig. 3(d)** was presented. From **Fig. 7**, it was found that the pitch width of LIPSS, formed by a laser with a 0° polarization direction on the slope (**Figs. 3(a)** and **4(a)**), was approximately the same as the laser wavelength. On the other hand, the pitch width of the LIPSS formed by a laser with 45° or 90° polarization direction was larger than the laser wavelength. Moreover, the pitch width of the UNLP, formed by a small number of times of irradiation, was smaller than the laser wavelength.

We first determined why the pitch width of the LIPSS on a slope was larger than the laser wavelength. This may have been due to the wider electric field strength distribution of the laser irradiation to a slope than to a plane. If the laser behavior on the slope of the V-shaped groove were equivalent to that on a plane, to which a laser is irradiated obliquely, the pitch width P of LIPSS on the 90° and 120° V-shaped grooves calculated from Eq. (1) was approximately 3632 nm and 2128 nm, respectively. If it were assumed that the laser was irradiated to the slope of the V-shaped groove as shown in **Fig. 8**, the theoretical value of P on the 90° and 120° V-shaped grooves was approximately 1504 nm and 1228 nm, respectively. In other words, the theoretical value of the pitch width of the LIPSS formed on the slope of the V-shaped groove was longer than the laser wavelength. Specifically, the irradiation of a laser with a certain polarization direction to the slope of the V-shaped groove formed an LIPSS with a pitch longer than the wavelength of the laser. However, the measured width was different from that of the theoretical one. This could have been due to the combined effects of the above two factors. This problem is currently under study.

On the other hand, the above theories cannot be applied to the UNPL formed on the slope of the V-shaped groove. Therefore, we studied a UNPL formation principle with respect to the optical interference of irradiated laser on the 90° V-shaped grooves.

4.2. Interference Between the Incident and Reflected Lights

A laser beam irradiated into a V-shaped groove should have an optical path as shown in **Fig. 9**. Specifically, the laser beam reflected from one slope of the 90° V-shaped groove passes through the other slope and interferes with the incident laser beam. On the other hand, the laser beam reflected from one slope of the 120° V-shaped groove goes out of the groove, making no interference. Therefore, in the 90° V-shaped groove, the incident light and light reflected from a slope produced an interference pattern on the slope where the light was periodically enhanced as shown in **Fig. 10**. As a result, the interference pattern formed an LIPSS with a different pitch width from the laser wavelength.

To confirm its validity, we applied an equation of the interference exposure method [30] which could form a pattern with a sub-wavelength period by utilizing the laser beam interference. The pitch width of the interference pattern formed by the interference exposure method is given by the following equation.

$$P = \frac{\lambda}{2\sin\theta}, \quad \ldots\ldots\ldots\ldots\ldots\ldots (3)$$

where λ is the laser wavelength and θ is the incident angle of the laser. Using the actual parameter values ($\lambda = 1064$ nm and $\theta = 45°$) for the laser irradiation on the 90° V-shaped groove, we obtained $P \simeq 752$ nm. The actual pitch width of the UNPL calculated in **Fig. 7** was approximately 731 nm, which is similar to the theoretical value.

4.3. Effect of Interference Using Electric Field Analysis

In Section 4.2, we mentioned that the formation of UNPL on the slope of the V-shaped groove should be related to the interference between the incident and reflected lights from a slope. However, the laser beam observation in an interference pattern on the material surface is difficult to conduct. On the other hand, the for-

Table 2. Analysis conditions.

Laser wavelength λ [nm]	900
Pulse width τ_p [ps]	20
Energy density distribution	Gaussian distribution
Temperature [K]	293

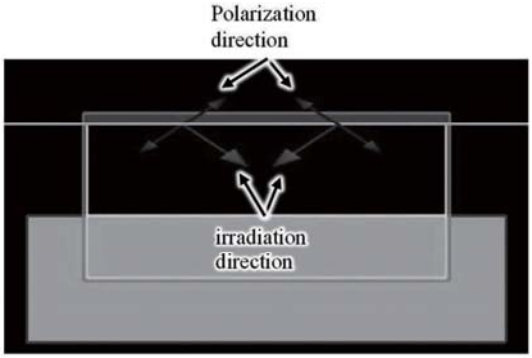

Fig. 11. Analysis model.

mation of the LIPSS is considered to be related to the electric field strength distribution. Moreover, a periodic distribution of the electric field creates a structure with a pitch width corresponding to the periodicity. Therefore, we studied the effect of the laser beam interference on the slope of the V-shaped groove by analyzing the electric field on the laser-irradiated surface. We used the finite-differential-time-domain (FDTD) method and simulation software FDTD solutions (Lumercia) for the electric field analysis [31, 32]. **Table 2** and **Fig. 11** show the analysis conditions and analysis model used, respectively. In the figure, the blue arrows indicate the laser polarization direction, which can be set by changing its angle. The pink arrows indicate the incident direction of the laser. The angle of the V-shaped groove slope can be set by changing the angle of the incident direction. In this model, V-shaped groove slopes was simulated by irradiating a laser from a single direction (single beam) and a laser from two line-symmetric directions (two beams), respectively. The laser polarization direction in **Fig. 11** is set to 90° and we used two angle conditions of 0° and 90°.

The analysis result is shown in **Fig. 12**. From the figure, it can be observed that the oblique irradiation of a single laser beam does not produce a uniform electric field strength distribution but a bias in the distribution in the simulation of a single slope. On the other hand, with the interference of two laser beams in the simulation of V-shaped grooves, a uniform electric field strength distribution can be observed. In addition, the period of the periodically-distributed electric field strength was approximately 660 nm, which is similar to the pitch width of the interference pattern obtained from Eq. (3) with a laser wavelength of 900 nm. The above result analytically indicated that the interference of the laser beams at the slopes of the V-shaped grooves produced an electric

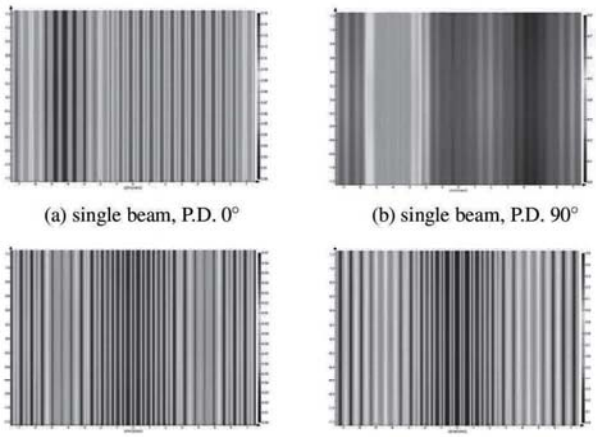

(a) single beam, P.D. 0° (b) single beam, P.D. 90°

(c) two beams, P.D. 0° (d) two beams, P.D. 90°

Fig. 12. Analysis result.

field strength distribution with a smaller pitch width than the laser wavelength. Moreover, the distribution formed a structure (UNPL) with a smaller pitch than the laser wavelength parallel to the grooves. This result was consistent with the experimental results. Therefore, it can be concluded that the UNPL formed on the slopes of the V-shaped grooves under a certain condition was generated by the optical interference of the irradiated laser beams to the V-shaped grooves.

4.4. Change in LIPSS Formation Based on the Number of Times of Irradiation

From the results of the LIPSS formation on the slope obtained in Section 2.2, we explained that a small number of times of laser irradiation to 90° V-shaped grooves made UNPL parallel to the grooves whereas a large number of times of laser irradiation made the periodic LIPSS vertical to the polarization direction. Moreover, we clarified that a latticed LIPSS was formed under a certain condition. In this section, we studied a change in the LIPSS formed on the slopes of 90° V-shaped grooves by changing E_d and n and examining the LIPSS creation principle on the slopes.

Figure 13 shows the fine structures formed on the 90° V-shaped grooves with different values of E_d and n. The polarization directions in **Figs. 13(a)–(c)** were used in the experiments in Section 2, and the angle between the V-shaped groove and polarization direction was as 0° when they were parallel to each other. In **Fig. 13**, the circles and squares indicate the UNPL formed by the interference and LIPSS formed in accordance with the conventional formation principle. Based on the results, it can be observed that the laser interference was dominant and the UNPL parallel to the grooves is formed when E_d or n is small, irrespective of the laser polarization direction, and LIPSS vertical to the laser polarization direction is formed according to the conventional formation principles when E_d or n is large. In other words, the parameters E_d and n change the principle of LIPSS formation on the V-shaped grooves. Hence, it can be considered that

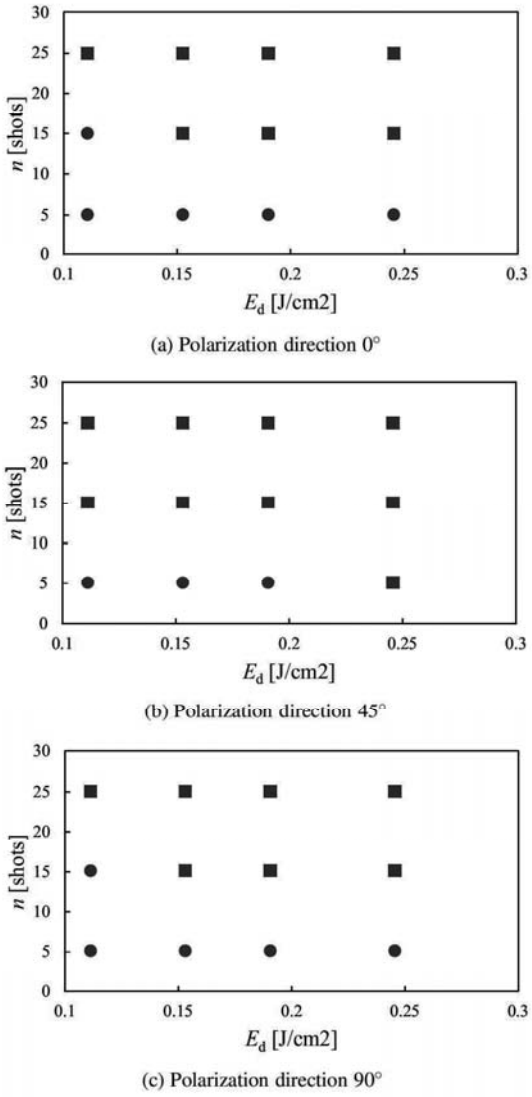

(a) Polarization direction 0°

(b) Polarization direction 45°

(c) Polarization direction 90°

Fig. 13. Fine structures formed at 90° V-shaped grooves under different conditions.

a small number of times of laser irradiation to the 90° V-shaped grooves forms a UNPL parallel to the grooves while a large number of times of laser irradiation forms an LIPPS, overlapped with UNPL, vertical to the polarization direction. The LIPSS observed as latticed structure on the 90° V-shaped grooves was formed in this process.

5. Effect of Micro-Nano Composite Structure on Wettability

In this study, we obtained wettability from various functions because technological innovation on wettability is expected in different industrial fields. It is known that the wetting of material surface is determined by the relationship between its surface and liquid, which changes depending on the microscopic shape of the surface [33]. Specifically, we considered that we could control the wettability by forming the LIPSS on the slopes of the V-shaped grooves to control the liquid entering the V-shaped grooves. In this section, we produced a micro-nano composite structure composed of a V-shaped groove structure and LIPSS. Moreover, we studied the effect of the composite structure on the material surface wetting using a droplet contact angle test.

5.1. Creation of a Composite Structure

Before making a droplet contact angle test, we created a composite structure consisting of V-shaped grooves and LIPSS. We made 90° and 120° V-shaped grooves. They were produced in two types. The first and second types were successive V-shaped grooves with no planes among the grooves and V-shaped grooves where the ratio of the V-shaped groove width to the inter-groove pitch width P_g was 1 : 3, respectively. The groove depth was fixed to 50 μm. A scanning laser was irradiated to the resulting V-shaped groove structures to form the LIPSS on the grooves and plane areas. The scanning speed was set using the following equation:

$$v = \frac{df}{n} \quad \ldots\ldots\ldots\ldots\ldots\ldots (4)$$

where v [μm/s] is the scanning speed; d [μm] is the scanning width; f [Hz] is the laser frequency; and n [shots] is the number of times of laser irradiation. The irradiation energy density was set to the value used in the LIPSS creation experiment in Section 2. The power of the laser used is expressed by a Gaussian distribution and is clearly different in the irradiation center and edge areas. Therefore, we set the scanning width smaller than the laser irradiation diameter in order to allow the edge areas of the irradiation circles to overlap with each other and create a uniform LIPSS. **Figs. 14** and **15** show the SEM images of the created composite structures. The figures on the right are magnified views of those on the left. From the figures, it can be observed that LIPSS could be formed on the slopes of the V-shaped grooves using the scanning laser irradiation.

5.2. Measurement of Contact Angle

To evaluate the wettability, we used a droplet contact angle meter (DM-501, Kyowa Interface Science, Inc.). We measured the contact angle by dropping water on the surface of a sample and using a CCD camera to shoot images from the side. We used purified water for the droplets with volumes of 3 μL. This experiment was made at three points of the sample under the same condition. The obtained results of the contact angle on the different points were averaged. Because the material surface immediately after the laser processing has a high surface energy due to energy flowing during the processing, the surface becomes more hydrophilic. However, the surface reacts with surrounding materials and becomes energetically-stabilized over time. To see the condition of the sample surface after the laser irradiation, we formed the LIPSS on a plane of Ni-P and measured temporal changes in the contact surface. The results are shown in **Fig. 16**. The

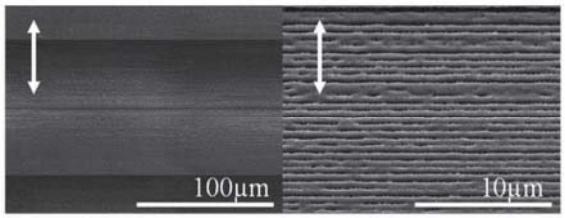

(a) $P_g = 100$, $E_d = 0.113$

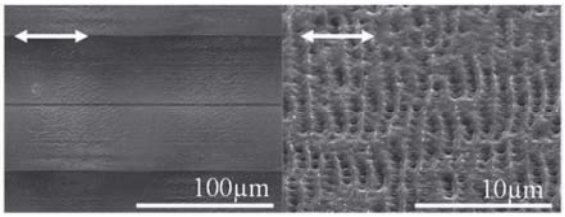

(b) $P_g = 100$, $E_d = 0.157$

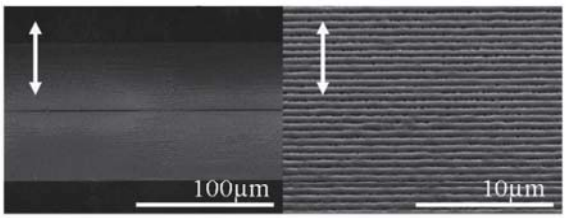

(c) $P_g = 300$, $E_d = 0.113$

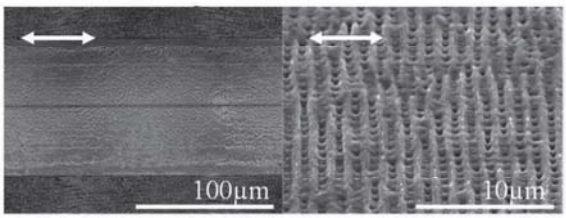

(d) $P_g = 300$, $E_d = 0.180$

Fig. 14. Laser (scanning) irradiation to 90° V-shaped grooves.

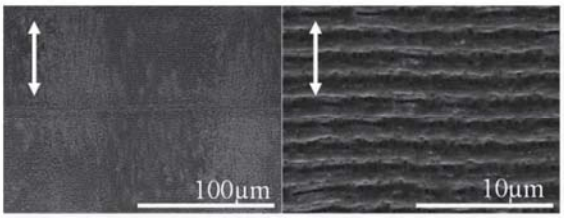

(a) $P_g = 173$, $E_d = 0.335$

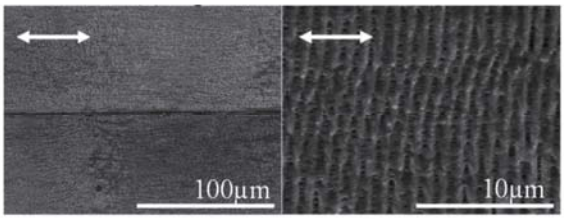

(b) $P_g = 173$, $E_d = 0.260$

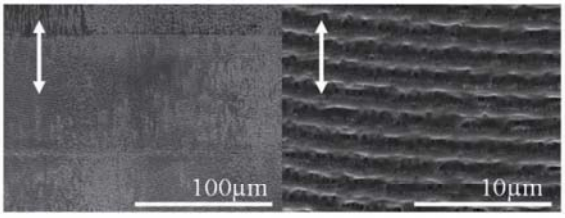

(c) $P_g = 500$, $E_d = 0.335$

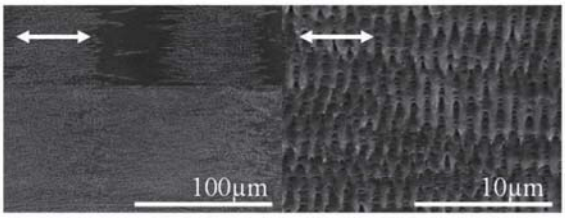

(d) $P_g = 500$, $E_d = 0.260$

Fig. 15. Laser (scanning) irradiation to 120° V-shaped grooves.

contact angle on the Ni-P surface before the creation of the V-shaped grooves was approximately 80°. It can be observed that in four days after the creation of the LIPSS, the contact angle had a stable value of 80°, which was the same angle before the creation of the LIPSS. Therefore, we performed the contact angle measurement experiment five days after the creation of LIPSS, assuming that the angle would be energetically-stabilized.

Figures 17 and **18** show the measurement results of the contact angle. **Fig. 17** shows the contact angles on the composite structure of 90° V-shaped grooves and LIPSS, and **Fig. 18** shows those of the 120° V-shaped grooves and LIPSS. First, let us focus on the data of the V-shaped grooves. The figures indicate that the groove angle or P_g had approximately no effect on the contact angle. Moreover, the data for the composite structure with LIPSS on the 90° V-shaped groove slopes can be observed. The figures show that the contact angle increased after the creation of the LIPSS under all the condition. Lastly, the data for the composite structure with LIPSS on the 120° V-shaped groove slopes show that the contact angle decreased after the creation of LIPSS under all the conditions.

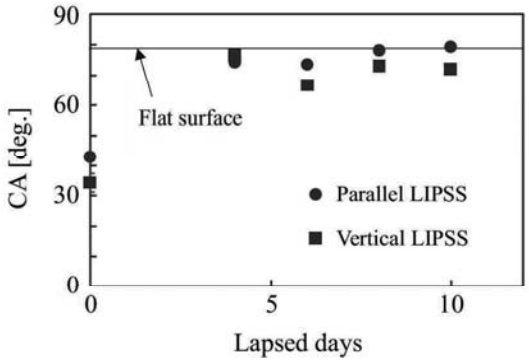

Fig. 16. Temporal change of contact angle on LIPSS surface.

As in the above results, for all the V-shaped groove angles, the V-shaped grooves and composites structure had different contact angles. This could be due to the water droplets entering the grooves. Lee et al. reported two

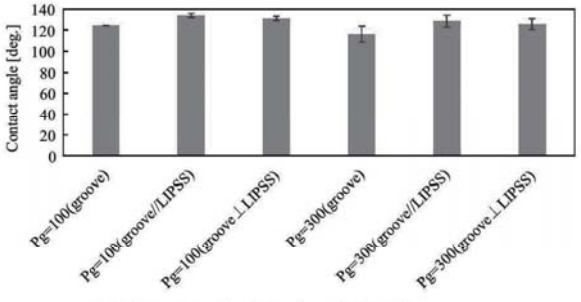

(a) Contact angle viewed parallel to the grooves

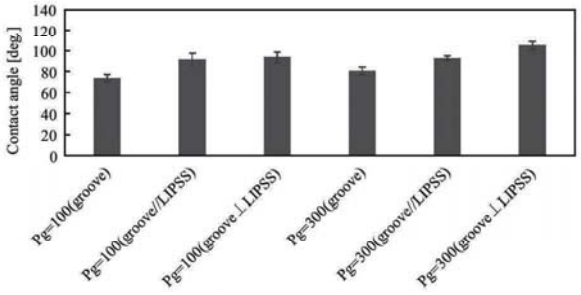

(b) Contact angle viewed vertical to the grooves

Fig. 17. Contact angle of the composite structure consisting of 90° V-shaped grooves and LIPSS.

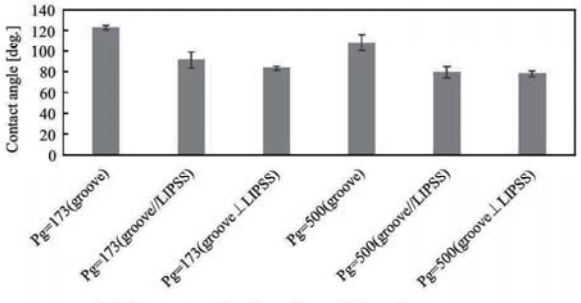

(a) Contact angle viewed parallel to the grooves

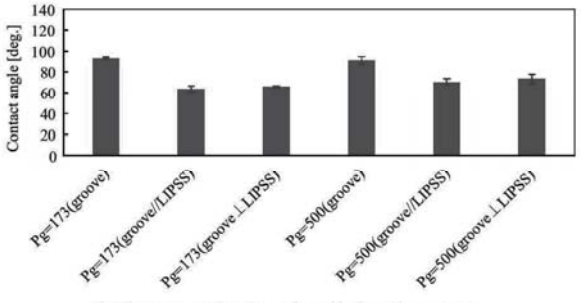

(b) Contact angle viewed vertical to the grooves

Fig. 18. Contact angle of the composite structure consisting of 120° V-shaped grooves and LIPSS.

types of wetting conditions [34]. The first type is the Wenzel state where a liquid completely enters a fine structure while the other type is the Cassie-Baxter state where a liquid does not enter a fine structure because the structure holds air inside. Moreover, they reported that there was an intermediate type of wetting condition where a liquid enters a part of a fine structure. It was also reported that the unevenness of the fine structure changed the wetting condition [34] and that when a liquid entered a fine structure, the contact area between the liquid and material surface gradually increased while the water resistance gradually decreased. In this study, we observed that the contact angle changed when the LIPSS was formed in the V-shaped grooves and that the contact angle change depended on the groove angle. Considering those results, we can see that our wetting condition was not Wenzel or Cassie-Baxter state, but an intermediate state where the liquid entered a part of the V-shaped grooves. Hence, the state changed depending on the groove angle and LIPSS properties.

Compared to the structure with only V-shaped grooves, the composite structure with LIPSS in the grooves had different contact angles depending on the groove angle. The composite structure with LIPSS in 90° V-shaped grooves had a larger contact angle than that of the V-shaped grooves without LIPSS. In this case, LIPSS could prevent the droplets from entering the grooves. On the contrary, the composite structure with LIPSS on the 120° V-shaped grooves had a smaller contact angle than that of the V-shaped grooves without LIPSS. In this case, LIPSS could promote the droplets to enter the grooves. In the experiment, we did not see a significant difference in the contact angle for different directions of the LIPSS. This could be because the aspect ratio of the formed LIPSS was small to prevent spreading of droplets sufficiently.

We could thus confirm that the surface wettability was significantly affected by the micro-nano composite structure, consisting of a fine structure of nanometer scale in a groove structure of a micrometer scale. In particular, it can be expected that the wettability could be controlled by changing the pitch width and height of the LIPSS and the angle and depth of the V-shaped grooves. In future, we aim to clarify the behavior of droplets entering the V-shaped grooves.

6. Conclusions

In this study, we developed a V-shaped groove structure using an ultra-precision cutting technology and irradiated short-pulsed laser to the grooves in order to create a nanometer fine periodic structure (LIPSS) on the slopes of the grooves. Then, we studied and discussed the principle of the LIPSS formation. In addition, we focused on the wettability of material surface and examined the effect of the composite structure on the wettability. The obtained knowledge is given below.

1. As observed in irradiation on a plane, the laser irradiation on the 90° V-shaped grooves produced LIPSS in vertical to the laser polarization when the number of times of irradiation was large. If it were small, the LIPSS (UNPL) with the pitch width smaller than the laser wavelength was formed parallel to the grooves and independent of the polarization direction.

2. Laser was irradiated to the 120° V-shaped grooves and a single slope. In either case, the LIPSS was formed vertical to the laser polarization, as observed in laser irradiation to a plane.
3. LIPSS pitch width measurement and electric field analysis showed that the formation of the UNPL on the slopes of the 90° V-shaped grooves by a small number of times of laser irradiation was due to interference between the incident laser and reflected beams from the slopes.
4. It was clarified that the principle of LIPSS creation on the slopes of V-shaped grooves followed the laser beam interference theory and principle of LIPSS creation on a plane when the number of times of irradiation was small and large, respectively.
5. A contact angle measurement was performed on a micro-nano composite structure consisting of V-shaped grooves and LIPSS. The composite structure was found to affect the wettability, which indicated potential controllability of the wettability.

Acknowledgements

This study was supported in part by JSPS KAKENHI Grant Numbers JP17K06074 and JP17KK0126.

References:

[1] A. A. G. Bruzzone, H. L. Costa, P. M. Lonardo, and D. A. Lucca, "Advances in engineered surface for functional performance," CIRP Annals – Manufacturing Technology, Vol.57, No.2, pp. 750-769, 2008.
[2] M. Mizutani, S. Xu, K. Shimada, and T. Kuriyagawa, "Micro-/Nano-texturing by Ultrasonic-Assisted Grinding," J. Yan (Ed.), "Micro and Nano Fabrication Technology," Springer, pp. 1-55, 2018.
[3] S. Kodama, S. Suzuki, K. Hayashibe, K. Shimada, M. Mizutani, and T. Kuriyagawa, "Control of short-pulsed laser induced periodic surface structure with machining – Picosecond laser micro/nanotexturing with ultraprecision cutting –," Precision Engineering, Vol.55, pp. 433-438, 2019.
[4] S. Kodama, H. Yamaguchi, K. Shimada, M. Mizutani, and T. Kuriyagawa, "Control of short-pulsed laser induced periodic surface structures with machining – picosecond laser nanotexturing with magnetic abrasive finishing –," Precision Engineering, Vol.60, pp. 428-436, 2019.
[5] U. Hermens, M. Pothen, K. Winands, K. Arntz, and F. Klocke, "Automated polarization control for the precise alignment of laser-induced self-organized nanostructures," Optics and Lasers in Engineering, Vol.101, pp. 44-50, 2018.
[6] Y. Tanaka, "Fabrication of Anti-reflective Structures using Glass Molding," New Glass, Vol.23, No.4, pp. 32-38, 2008.
[7] S. Bolotov, R. Kobayashi, K. Shimada, M. Mizutani, and T. Kuriyagawa, "Fabrication of Precision Micrograting on Resin Substrate Utilizing Ultrasonic-Assisted Molding," Int. J. Automation Technol., Vol.9, No.1, pp. 43-50, 2015.
[8] S. Shamsudin, M. K. Ahmad, A. N. Aziz, R. Fuhriah, F. Mohamad, N. Ahmad, N. Nafarizal, C. F. Soon, A. S. Ameruddin, A. B. Faridah, M. Shimomura, and K. Murakami, "Hydrophobic Rutile Phase TiO_2 Nanostructure and Its Properties for Self-Cleaning Application," AIP Conf. Proc., Vol.1883, No.2, pp. 1-9, 2017.
[9] K. Asakura and J. Yan, "Water Repellency Control of Oxgen-Free Copper Surface by Diamond-Cut Micro Grooves," Int. J. Automation Technol., Vol.9, No.4, pp. 396-402, 2015.
[10] S. Imabayashi, "Effect of surface roughness on wettability of solid surfaces," Review of Polarography, Vol.54, No.2, pp. 115-121, 2008.
[11] S. Xu, K. Shimada, M. Mizutani, and T. Kuriyagawa, "Analysis of Machinable Structures and Their Wettability of Rotary Ultrasonic Texturing Method," Chinese J. of Mechanical Engineering, Vol.29, No.6, pp. 1187-1192, 2016.
[12] K. Shimada, T. Hirai, M. Mizutani, and T. Kuriyagawa, "Unidirectional Wetting Surface Fabrication by Ultrasonic-Assisted Cutting," Int. J. Automation Technol., Vol.13, No.2, pp. 191-198, 2019.
[13] S. Kirner, U. Hermens, A. Mimidis, E. Skoulas, C. Florian, F. Hischen, C. Plamadeala, W. Baumgartner, K. Winands, H. Mescheder, J. Krüger, J. Solis, J. Siegel, E. Stratakis, and J. Bonse, "Mimicking bug-like surface structures and their fluid transport produced by ultrashort pulse irradiation of steel," Applied Physics A, Vol.123, No.12, pp. 1-13, 2017.
[14] S. Ma, Y. Liu, Z. Wang, Z. Wang, R. Huang, and J. Xu, "The Effect of Honing Angle and Roughness Height on The Tribological Performance of CuNiCr Iron Liner," Metals, Vol.9, No.5, p. 487, 2019.
[15] N. Sumi, C. Kato, K. Shimada, M. Mizutani, and T. Kuriyagawa, "Influence of Workpiece Materials on the Characteristics of the Layers by Electrical Discharge Coating," Int. J. Automation Technol., Vol.10, No.5, pp. 773-779, 2016.
[16] J. Lu, M. P. Rao, N. C. MacDonald, C. Khang, and T. J. Webster, "Improved endothelial cell adhesion and proliferation on patterned titanium surface with rationally designed, micrometer to nanometer features," Acta Biomaterialia, Vol.4, pp. 192-201, 2008.
[17] M. Mizutani, R. Honda, Y. Kurashima, J. Komotori, and H. Ohmori, "Improved Cytocompatibility of Nanosecond-Pulsed Laser-Treated Commercially Pure Ti Surface," Int. J. Automation Technol., Vol.8, No.1, pp. 102-109, 2014.
[18] Y. Fukayo, T. Amemiya, K. Nakaoka, M. Mizutani, J. Komotori, Y. Hamada, and T. Hayakawa, "Bone and Gingival Connective Tissue Responses Nanosecond-Pulsed Laser-Treated Titanium Implants," J. of Hard Tissue Biology, Vol.25, No.2, pp. 181-194, 2016.
[19] Y. Kurashina, A. Ezura, R. Murakami, M. Mizutani, and J. Komotori, "Effect of Hydroxy Group and Micro-Topography Generated by a Nanosecond-Pulsed Laser on Pure Ti Surfaces," J. of Materials Science: Materials in Medicine, Vol.30, No.5, 57, 2019.
[20] M. Hirota, T. Harai, S. Ishibashi, M. Mizutani, and T. Hayakawa, "Cortical bone response toward nanosecond-pulsed laser-treated zirconia implant surfaces," Dental Materials J., Vol.38, No.3, pp. 444-451, 2019.
[21] Y. F. Fu, C. Q. Yuan, and X. Q. Bai, "Marine drag reduction of shark skin inspired riblet surface," Biosurface and Biotribology, Vol.3, No.1, pp. 11-24, 2017.
[22] Y. Sun, S. Xu, T. Kyoizumi, K. Shimada, M. Mizutani, and T. Kuriyagawa, "CFD Analysis of Friction-Reduction Effect of Micro-Textured Surfaces in Lubricant," Int. J. Automation Technol., Vol.12, No.2, pp. 206-214, 2018.
[23] Y. Sun, K. Shimada, S. Xu, M. Mizutani, and T. Kuriyagawa, "Friction Reduction by Micro-Textured Surfaces in Lubrication," Int. J. Automation Technol., Vol.12, No.4, pp. 603-610, 2018.
[24] S. Kodama, S. Suzuki, A. Shibata, K. Shimada, M. Mizutani, and T. Kuriyagawa, "Effect of Crystal Structure on Fabrication of Fine Periodic Surface Structure with Short Pulsed Laser," Int. J. Automation Technol., Vol.12, No.6, pp. 868-875, 2018.
[25] T. Tomita, "Laser Ablation: From the Viewpoint of Solid State Physics," J. Plasma Fusion Res., Vol.89, No.7, pp. 493-499, 2013.
[26] M. Tsukamoto and M. Hashida, "Material Processing of Metal with Femtosecond Laser," J. of Japan Welding Society, Vol.72, No.8, pp. 22-25, 2003.
[27] F. Coatache, M. Henyk, and J. Reif, "Surface patterning on insulators upon femtosecond laser ablation," Applied Surface Science, Vols.208-209, No.15, pp. 486-491, 2003.
[28] H. Sawada, K. Kawahara, T. Ninomiya, K. Kurosawa, and A. Yokotani, "Precise Periodic Structuring with Femtosecond-laser," J. of Japan Society for Precision Engineering, Vol.69, No.4, pp. 554-558, 2003.
[29] M. Hashida, "Nanostructure fabrication by femtosecond processing," Laser Cross. No.181, pp. 1-3, 2003.
[30] J. Amako and D. Sawaki, "Deep-UV laser-based Manufacturing Process for Sub-wavelength structures – Interference Exposure for Resist Patterning –," J. of Japan Society for Precision Engineering, Vol.74, No.8, pp. 789-794, 2008.
[31] K. S. Yee, "Numerical Solution of Initial Boundary Value Problems Involving Maxwell's Equations in Isotropic Media," IEEE Trans. on Antennas and Propagation, Vol.14, No.3, pp. 302-307, 1996.
[32] O. Hashimoto, "Finite Difference Time Domain Method," Morikita Publishing Co., Ltd., 2006 (in Japanese).
[33] R. Blossey, "Self-cleaning surface – virtual realities," Nature Materials, Vol.2, pp. 301-306, 2003.
[34] J. B. Lee, H. R. Gwon, S. H. Lee, and M. Cho, "Wetting Transition Characteristics on Microstructured Hydrophobic Surface," Materials Trans., Vol.51, No.9, pp. 1709-1711, 2010.

Name:
Ryohei Takase

Affiliation:
Master Course Student, Department of Mechanical System Engineering, Graduate School of Engineering, Tohoku University

Address:
6-6-01 Aramaki Aza-Aoba, Aoba-ku, Sendai, Miyagi 980-8579, Japan

Brief Biographical History:
2018 Received Bachelor degree from Tohoku University
2018- Master Course Student, Graduate School of Engineering, Tohoku University

Name:
Shuhei Kodama

Affiliation:
Assistant Professor, Department of Mechanical Systems Engineering, Graduate School of Engineering, Tokyo University of Agriculture and Technology

Address:
6-311, 2-24-16 Nakacho, Koganei, Tokyo 184-0012, Japan

Brief Biographical History:
2016 Received M.E. from Tohoku University
2019 Received Ph.D. from Tohoku University
2019- Assistant Professor, Graduate School of Engineering, Tokyo University of Agriculture and Technology

Main Works:
- S. Kodama, H. Yamaguchi, K. Shimada, M. Mizutani, and T. Kuriyagawa, "Control of Short-Pulsed Laser Induced Periodic Surface Structures with Machining – Picosecond Laser Nanotexturing with Magnetic Abrasive Finishing –," Precision Engineering, Vol.60, pp. 428-436, 2019.
- S. Kodama, S. Suzuki, K. Hayashibe, K. Shimada, M. Mizutani, and T. Kuriyagawa, "Control of Short-Pulsed Laser Induced Periodic Surface Structures with Machining – Picosecond Laser Micro/Nanotexturing with Ultraprecision Cutting –," Precision Engineering, Vol.55, pp. 433-438, 2019.
- S. Kodama, A. Shibata, S. Suzuki, K. Shimada, M. Mizutani, and T. Kuriyagawa, "Fabrication and control of fine periodic surface structures by short pulsed laser," Int. J. Automation Technol., Vol.10, No.4, pp. 639-646, 2017.

Membership in Academic Societies:
- Japan Society of Mechanical Engineers (JSME)
- Japan Society for Precision Engineering (JSPE)
- Japan Society of Electrical-Machining Engineers (JSEME)

Name:
Keita Shimada

Affiliation:
Assistant Professor, Department of Mechanical Systems Engineering, Graduate School of Engineering, Tohoku University

Address:
6-6-01 Aramaki Aza-Aoba, Aoba-ku, Sendai, Miyagi 980-8579, Japan

Brief Biographical History:
2009 Received M.E. from Tohoku University
2012 Received Ph.D. from Tohoku University
2012- Assistant Professor, Graduate School of Engineering, Tohoku University

Main Works:
- K. Shimada, N. Yoshihara, J. Yan, T. Kuriyagawa, Y. Sueishi, and H. Tezuka, "Ultrasonic-assisted Grinding of Ultra-High Purity SUS 316," Int. J. Automation Technol., Vol.5, No.3, pp. 427-432, 2011.
- K. Shimada, P. J. Liew, T. Zhou, J. Yan, and T. Kuriyagawa, "Statistical Approach Optimizing Slant Feed Grinding," J. Adv. Mech. Design, Systems and Manu., Vol.6, No.6, pp. 898-907, 2012.
- K. Shimada, C.-I. Kuo, M. Mizutani, and T. Kuriyagawa, "Statistical Analysis for Evaluating Surface Roughness of Plane Honing," Int. J. Automation Technol., Vol.8, No.4, pp. 576-583, 2014.

Membership in Academic Societies:
- Japan Society of Mechanical Engineers (JSME)
- Japan Society for Precision Engineering (JSPE)
- Japan Society for Abrasive Technology (JSAT)

Name:
Holger Mescheder

Affiliation:
Research Associate, Fraunhofer Institute for Production Technology IPT

Address:
Steinbachstraße 17, Aachen 52074, Germany

Brief Biographical History:
2006 Received Diploma in Architecture from Dortmund University of Applied Sciences and Arts
2006-2014 Department of CAx-Technologies, Fraunhofer IPT
2014-2020 Department of Non-conventional Manufacturing Processes, Fraunhofer IPT
2020- Department of Directed Energy Manufacturing, Fraunhofer IPT

Main Works:
- P. Comanns, K. Winands, M. Pothen, and H. Mescheder, "Bionisch funktionalisierte Oberflächen durch laserbasierte Nachbildung der Schuppenstruktur feuchtigkeitserntender Echsen 'BioLas.exe'," Shaker Verlag, 2019.
- H. Mescheder and U. Hermens, "Design and function for freeform surfaces. How to texture 3D parts with micro- and nanostructures automated and distortion-free," Laser-Technik-J., Vol.15, No.1, pp. 29-31, 2018.
- S. V. Kirner, U. Hermens, W. Baumgartner, K. Winands, H. Mescheder, E. Stratakis, and J. Bonse, "Mimicking bug-like surface structures and their fluid transport produced by ultrashort laser pulse irradiation of steel," Applied Physics A, Vol.123, 754, 2017.

Name:
Kai Winands

Affiliation:
Head of Competence Field of Additive Manufacturing, Fraunhofer Institute for Production Technology IPT

Address:
Steinbachstraße 17, Aachen 52074, Germany

Brief Biographical History:
2009 Received Diplom-Ingenieur from RWTH Aachen University
2009-2015 Research Scientist, Field of Laser Surface Functionalization, Fraunhofer IPT
2015-2018 Group Manager, Field of Laser Materials Processing, Fraunhofer IPT
2018- Head of Competence, Field of Additive Manufacturing, Fraunhofer IPT

Main Works:
• Laser surface functionalization by laser texturing with pulsed nano- and picosecond laser sources, laser powder bed fusion of stainless steel 316L

Membership in Academic Societies:
• Association of German Engineers (VDI)

Name:
Jan Riepe

Affiliation:
Manager, Group of Laser Material Processing, Fraunhofer Institute for Production Technology IPT

Address:
Steinbachstraße 17, Aachen 52074, Germany

Brief Biographical History:
2011 Received Diplom-Ingenieur from RWTH Aachen
2011- Research Scientist, ForWind (Center for Wind Energy Research), University of Oldenburg
2013- Project Engineer, Hamburg Energie
2016- Research Scientist, Fraunhofer Institute for Production Technology IPT
2018- Manager of Laser Material Processing Group, Fraunhofer Institute for Production Technology IPT

Main Works:
• Laser metal deposition with wire, directed energy deposition, cam-module, process control, Inconel 718, titanium, H11

Name:
Kristian Arntz

Affiliation:
Manager, Department of Technology Organisation, Fraunhofer Institute for Production Technology IPT

Address:
Steinbachstraße 17, Aachen 52074, Germany

Brief Biographical History:
2003 Graduated from RWTH Aachen University (Mechanical Engineering and Materials Engineering)
2003- Scientist, Department of High Performance Machining, Fraunhofer IPT
2009- Chief Engineer, Fraunhofer IPT
2010- Manager, R&D, WBA Aachener Werkzeugbau Akademie GmbH
2013 Received Ph.D. in Mechanical Engineering from RWTH Aachen University
2016- Managing Director, ACAM Aachen Center for Additive Manufacturing GmbH

Main Works:
• Process chain development in manufacturing, additive manufacturing, CAx process chains, laser materials processing, tool and die making, digitalisation in manufacturing

Membership in Academic Societies:
• Association of German Engineers (VDI)

Name:
Masayoshi Mizutani

Affiliation:
Associate Professor, Department of Mechanical Systems Engineering, Graduate School of Engineering, Tohoku University

Address:
6-6-01 Aramaki Aza-Aoba, Aoba-ku, Sendai, Miyagi 980-8579, Japan

Brief Biographical History:
2003 Received M.E. from Integrated Design Engineering, Graduate School of Science and Technology, Keio University
2004- Junior Research Associate, Ohmori Materials Fabrication Laboratory, RIKEN
2006 Received Ph.D. from Integrated Design Engineering, Graduate School of Science and Technology, Keio University
2006- Collaboration Researcher, Advanced Development and Supporting Center, RIKEN
2007- Collaboration Researcher, Ohmori Materials Fabrication Laboratory, RIKEN
2009- Special Postdoctoral Researcher, Ohmori Materials Fabrication Laboratory, RIKEN
2011- External Collaborative Researcher, Sophia University
2012- Collaboration Researcher, Ohmori Materials Fabrication Laboratory, RIKEN
2012- Associate Professor, Department of Mechanical Systems and Design, Tohoku University

Main Works:
• Micro/meso mechanical manufacturing (M4 process), laser process, powder jet deposition (PJD), functional interface, biomaterials, bio-medical applications, biomimetic surface

Membership in Academic Societies:
• Japan Society of Mechanical Engineers (JSME)
• Japan Society for Precision Engineering (JSPE)
• Japan Society for Abrasive Technology (JSAT)

Name:
Tsunemoto Kuriyagawa

Affiliation:
Professor, Bio-Medical Interface Fabrication Laboratory, Graduate School of Biomedical Engineering, Tohoku University

Address:
6-6-01 Aramaki Aza-Aoba, Aoba-ku, Sendai, Miyagi 980-8579, Japan

Brief Biographical History:
1984-1990 Research Associate, Tohoku University
1990-1992 Assistant Professor, Tohoku University
1991-1992 Visiting Professor, University of Connecticut
1992-2002 Associate Professor, Tohoku University
2003- Professor, Tohoku University

Main Works:
• Nano-precision mechanical manufacturing, micro/meso mechanical manufacturing (M4 process), powder jet deposition, and creation of functional interface

Membership in Academic Societies:
• Science Council of Japan (SCJ)
• International Committee for Abrasive Technology (ICAT)
• International Society for Nanomanufacturing (ISNM)
• Japan Society of Mechanical Engineers (JSME)
• Japan Society for Precision Engineering (JSPE)
• Japan Society for Abrasive Technology (JSAT)

Paper:

Porosity and Tensile Properties of Rhizoid Porous Structure Fabricated Using Selective Laser Melting

Shinji Ishibashi[*1], Keita Shimada[*1], Hiroyasu Kanetaka[*2,*3], Masaki Tsukuda[*1], Takumi Mizoi[*1], Masataka Chuzenji[*1], Shoichi Kikuchi[*4], Masayoshi Mizutani[*1,†], and Tsunemoto Kuriyagawa[*3]

[*1]Graduate School of Engineering, Tohoku University
6-6-01 Aramaki Aza-Aoba, Aoba-ku, Sendai, Miyagi 980-8579, Japan
[†]Corresponding author, E-mail: masayoshi.mizutani.b6@tohoku.ac.jp
[*2]Graduate School of Dentistry, Tohoku University, Sendai, Japan
[*3]Graduate School of Biomedical Engineering, Tohoku University, Sendai, Japan
[*4]Department of Mechanical Engineering, Faculty of Engineering, Shizuoka University, Hamamatsu, Japan
[Received February 3, 2020; accepted May 9, 2020]

The reduced density of the autogenous bone around metal medical implants forces joint replacement patients to undergo revision surgery. The loss of bone density is caused by a significant difference in the elastic modulus between implants and autogenous bone. Various studies have attempted to reduce the elastic modulus of the implant to close the large gap in the two moduli. Porous metal is a promising material for reducing the elastic modulus of implants, but it is difficult to fabricate a closed-cell structure like bone using conventional porous metal fabrication methods. In this study, porous Ti-6Al-4V was prepared by selective laser melting, then its porosity was evaluated by X-ray computed tomography. Additionally, tensile test specimens of the porous structure were prepared and the effect of pores on the tensile properties was evaluated. Depending on the energy density, the structure of the porous body was found to form both closed- and open-cell structures. In the tensile specimens that showed the most favorable results, the elastic modulus was reduced by approximately 90%, and the tensile strength exceeded that of the annealed material. This indicates that a metal implant that has a low elastic modulus while maintaining strength can be obtained.

Keywords: porous metal, selective laser melting, X-ray computed tomography, tensile strength, Ti-6Al-4V

1. Introduction

Healthy life expectancy (HALE) was defined by the World Health Organization (WHO) in 2000 as the "average number of years that a person can expect to live in 'full health' by taking into account years lived in less than full health due to disease and/or injury." HALE is becoming more important each year as the global average life expectancy increases [1]. The WHO reported high life expectancy and HALE in Japan in 2018 and pointed out the large difference between the two [2]. Cerebrovascular disease, fractures and falls accounted for 16.6%, 12.1%, and arthritis 10.2% of the causes of support and long-term care in Japan [3]. Additionally, the incidence of cerebral infarction, a cerebrovascular disease, tends to decrease with increased daily walking and exercise time [4]. Thus, the prolongation of HALE requires recovery of the body so that it can walk and exercise, even after the development of fractures and arthritis.

More than 140,000 operations are performed annually in Japan to replace inflamed or dysfunctional joints with prostheses [5]. Although a prosthesis should ideally be stable and anchored in the body throughout the lifetime without damaging the surrounding biological tissue, the autogenous bone around the implant may fracture and require revision surgery. One of the causes of fractures is the loss of bone density due to stress shielding [6, 7]. Stress shielding is a mechanical phenomenon in which metal implants interfere with the transmission of daily stress to the bone. A large gap between the elasticities of the metal implant and bone causes the shielding phenomenon. Continued stress shielding prevents the bone around the implant from receiving the stimulation necessary for bone growth, leading to a gradual decrease in bone density and eventually to fracture. Various studies have attempted to fabricate implants that can transfer the appropriate stresses to the autogenous bone by forming bone-like porous structures in metal [8–10]. Additive manufacturing (AM), which can produce complex shapes such as lattice structures and is attracting attention as a method for the fabrication of tailor-made implants in the medical field, is a promising candidate for the fabrication of porous structures [11]. The elastic modulus of a lattice object (E^*) is expressed by Eq. (1) using the elastic modulus of the dense material (E_S), porosity (ε), and proportion coefficient (C) [12].

$$\frac{E^*}{E_S} = C(1-\varepsilon)^2 \quad \ldots\ldots\ldots\ldots\ldots (1)$$

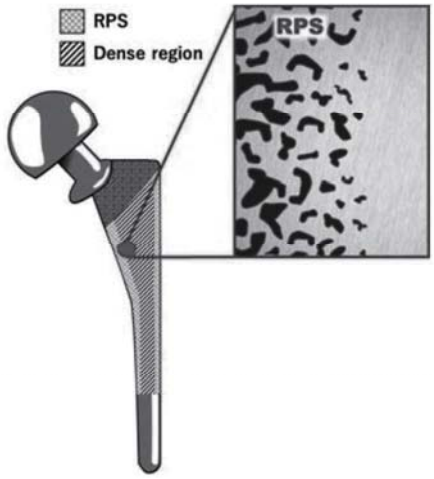

Fig. 1. Conceptual model of a proposed implant fabricated with RPS.

Although the lattice structure can reduce the elastic modulus of the structure, it cannot continuously change the porosity from the porous to the dense part [13]. Stress concentration occurs at the interface where the porosity varies discontinuously because different porosities have different deformation responses to stress [14]. Thus, it is important for the porous and dense parts of an implant to change continuously to prevent the loss of strength of the porous implant. To solve these problems, we propose a new method of fabricating a rhizoid porous structure (RPS), with the possibility of changing the porosity gradient using selective laser melting (SLM).

2. Proposed Metal Medical Implant with RPS Structure

Figure 1 shows a conceptual image of an implant that includes an RPS. This implant has a gradient structure that includes both dense and porous parts. The dense part maintains the strength of the implant, and the porous part decreases the elastic modulus. To realize this structure, we attempted to control the number of pores generated during the SLM melting and solidification process by changing the shaping conditions. Since the goal of this method is to control the morphology of the pores, such as their size, distribution, and shape, the relationship between randomly occurring pores and the shaping conditions must be clarified. In this study, we focused on porosity above the other pore properties because it significantly affects the elastic modulus according to Eq. (1). Additionally, the RPS needs to have the appropriate mechanical properties for an implant.

The pores of RPS cubes fabricated under various laser conditions were visualized using X-ray computed tomography (CT), and the porosity was evaluated. Based on the porosity results, tensile specimens of RPS material were prepared and their tensile properties were evaluated.

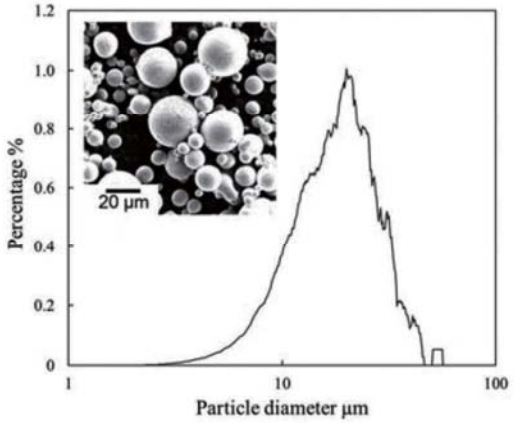

Fig. 2. EM image and volume-based particle size distribution of Ti-6Al-4V powder.

Table 1. Shaping conditions of cube specimens.

Equipment	ProX 100 (3D systems)
Laser scan speed	100, 150, 240, 260, 280, 300, 340, 370, 400, 430 mm/s
Laser scan hatch spacing	40, 70 μm
Laser type	Yb-fiber laser
Laser spot diameter	80 μm
Laser wavelength	1074 nm
Laser power	50 W
Layer thickness	45 μm
Chamber atmosphere	Argon

3. Experimental Conditions

3.1. Material and Shaping Conditions

Figure 2 shows the scanning electron microscope (SEM) image and particle size distribution of the Ti-6Al-4V powders used to fabricate all specimens in this study (TILOP64-45, Osaka Titanium Technologies Co., Ltd.). The particle size distribution was measured by automated static image analysis (Morphologi g3, Malvern Panalytical Ltd.). The volume-based median diameter was 18 μm.

The porosity of a conventional SLM specimen depends on the energy density E_d [J/mm^3], which indicates the input energy per unit volume into the metal powder bed [15–17]. The energy density is expressed as shown in Eq. (1) using the power of the heat source p [W], the layering thickness t [mm], the scan hatch spacing d [mm], and the scan speed s [mm/s]. Since the porosity of SLM specimens, including RPS, should be affected by E_d, this study aimed to clarify the relationship between E_d and porosity.

$$E_d = \frac{p}{tds} \quad \ldots\ldots\ldots\ldots\ldots\ldots \quad (2)$$

Cubes with side lengths of 7 mm were fabricated according to the conditions shown in **Table 1**. Ten laser

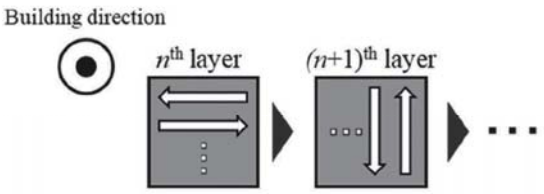

Fig. 3. Laser strategy.

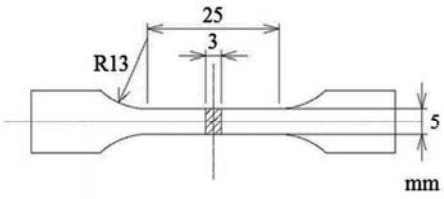

Fig. 4. Schematic diagram of the tensile test specimen.

Table 2. X-ray CT scan conditions.

Equipment	ScanXmate-D160TSS105 (Comscantecno Co., Ltd.)
Tube current	170 kV
Tube voltage	200 μA
Magnification	22×
Spatial resolution	5.7 μm/pixel

Table 3. EBSD conditions.

Analysis sample	S260-D70, S400-D70
Step size	0.3 μm
Material	Titanium (α), Titanium (β)
Confidence index	> 0.1

speeds (S) and two laser scan hatch spacings (D) were set for each cube. Hereinafter, the test pieces are referred to using symbols and numbers, for example, S150-D70. **Fig. 3** shows a schematic diagram of the laser strategy.

Note that the thermal effect from adjacent laser irradiation is negligible on pore generation because the estimated cooling rate of the sintered part of the SLM, 1.0×10^2–10^6 K/s [18, 19], is high enough.

3.2. Pore Morphology and Microstructural Analysis

Since the pores of the SLM specimens are three-dimensional (3D) and non-uniformly distributed, 3D evaluation is necessary to understand the pore morphology. X-ray CT scan analysis, which is used to evaluate casting nests [20], was adopted to evaluate the internal structure of the SLM specimens in three dimensions. The conditions of the X-ray CT scan are shown in **Table 2**.

Since metal microstructure also affects tensile properties, the microstructure of the SLM specimens was evaluated by electrical backscatter diffraction (EBSD) analysis under the conditions shown in **Table 3**. The microstructure of the Ti-6Al-4V specimens prepared by conventional SLM consists of fine acicular grains of the α-phase, which do not change significantly with energy density [21–23]. Although the specimens in this study are likely to show similar results, few studies have observed the microstructure of SLM specimens fabricated at low energy densities; thus, two RPS cubes fabricated at high and low energy densities have been analyzed.

Table 4. Shaping conditions of the tensile test specimen and tensile test conditions.

Laser scan speed	150, 240, 300, 340, 400, 430 mm/s
Laser scan hatch spacing	70 μm
Loading speed	1.5 mm/min
Sample size	2

3.3. Tensile Test Conditions

Tensile test specimens were cut to the shape shown in **Fig. 4** from $70 \times 12 \times 3$ mm^3 SLM-ed objects using a wire electric discharge machine. They were SLM-ed and tested under the conditions listed in **Table 4**. Hereinafter, the test piece is referred to as TT-S150, using the scan speed symbol S and the tensile test symbol TT.

4. Results

4.1. Effects of Scan Speed on Porosity and Cell Structure

The pores were visualized, and the porosity was calculated from X-ray CT sequence images using 3D image analysis software. In the pore visualization image shown in **Fig. 5**, the red region represents the largest single pore in the measured volume, the yellow region represents the second to tenth, the green region the eleventh to one hundredth, the light blue region the 101st to 1000th, and the blue region represents all pores smaller than the one-thousandth pore. Under low-speed laser conditions, the blue pores are distributed throughout the RPS cubes, while at high speeds, the red pores occupy the entire cube. These results indicate that as the scan speed increased, the independent pores connected with each other and merged into a single pore. In other words, the RPS method can generate both closed-cell structures consisting of independent pores and open-cell structures consisting of connected pores by controlling the scan speed. The cross-sectional views of the pores in S150-D70 and S430-D70 (**Fig. 6**) show that the pores in S150-D70 are independent and those in S430-D70 are connected like plant roots. The pores have an awkward angular shape.

The relationship between porosity and energy density (**Fig. 7**) indicates that the porosity gradually decreased with increasing energy density but never fell below 5%.

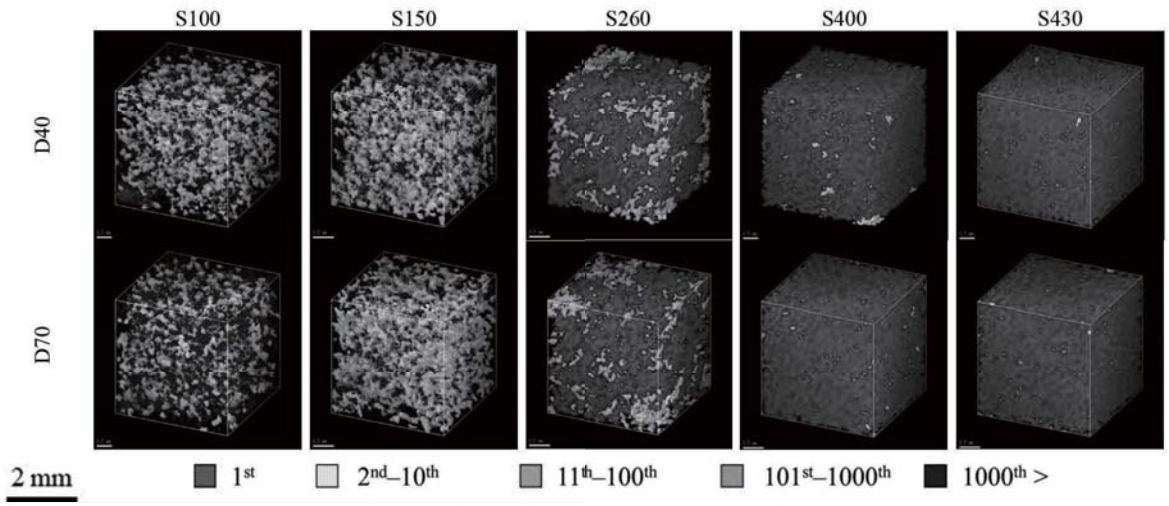

Fig. 5. Visualization of pores inside SLM specimens.

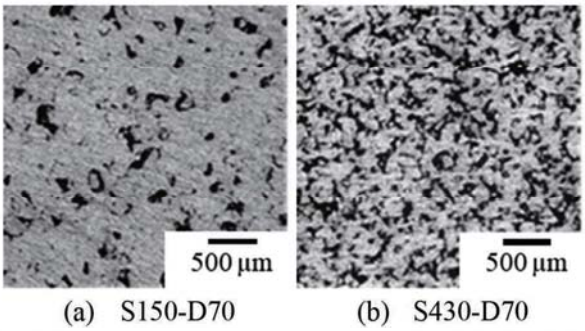

Fig. 6. Cross-sectional views of S150-D70 and S430-D70.

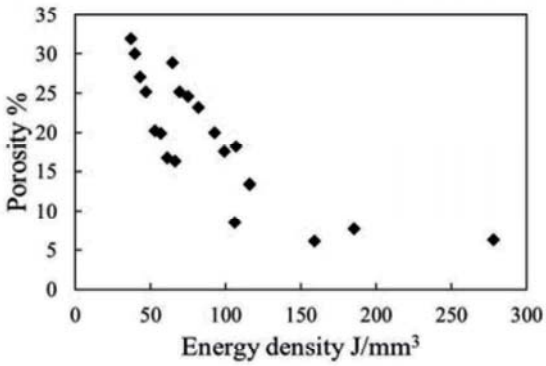

Fig. 7. Energy density vs. porosity.

The highest porosity was 31.3% for S430-D70.

From the relationship between the scan speed and the porosity (**Fig. 8**), the scan speed had a greater effect on the porosity than did the scan hatch spacing. Focusing on the difference in the scan hatch spacing, the difference in porosity is at most 5% under the same scan speed conditions, and the effect of the scan hatch spacing on the porosity is small. In the SEM images of the top surfaces of

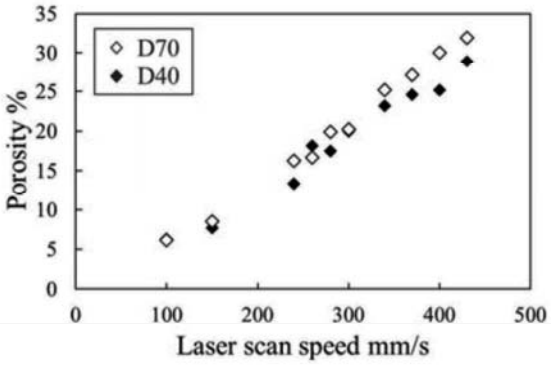

Fig. 8. Laser scan speed vs. porosity.

S150 and S430 (**Fig. 9**), the red dashed lines indicate the boundaries between lasers, and the yellow dashed lines surround areas with a lack of fusion. The images show that the laser molten marks are wider and there are more areas lacking fusion under the 70-μm scan hatch spacing.

4.2. Effect of Energy Density on the Crystal Structure

Figure 10 shows the inverse pole figure (IPF) maps and phasc maps obtaincd from thc EBSD analysis. Thc analysis areas of the IPF map and the phase map are the same. Based on the figures, the metal microstructure of the RPS had α-phase acicular grains, and the difference in energy densities had little effect on the metal microstructure. The width and length of the acicular grains were approximately 1 μm and 20–50 μm, respectively. The crystal orientation was isotropic and β-phase grains were rare.

4.3. Effect of Scan Speed on the Tensile Properties

The stress-strain diagram (**Fig. 11**) obtained from the tensile test results shows that the ultimate tensile

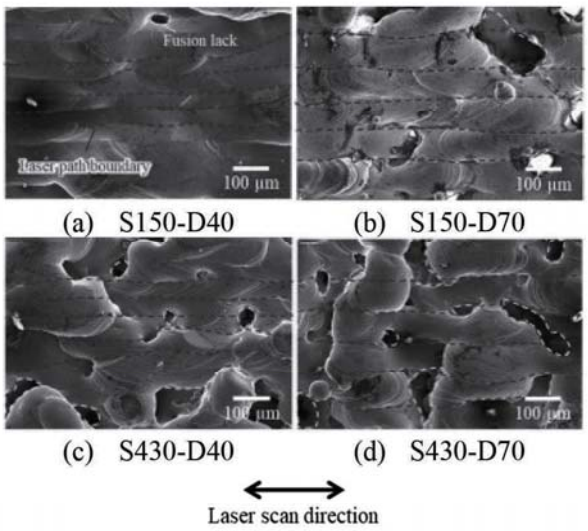

Fig. 9. SEM images of top surfaces of RPS cubes.

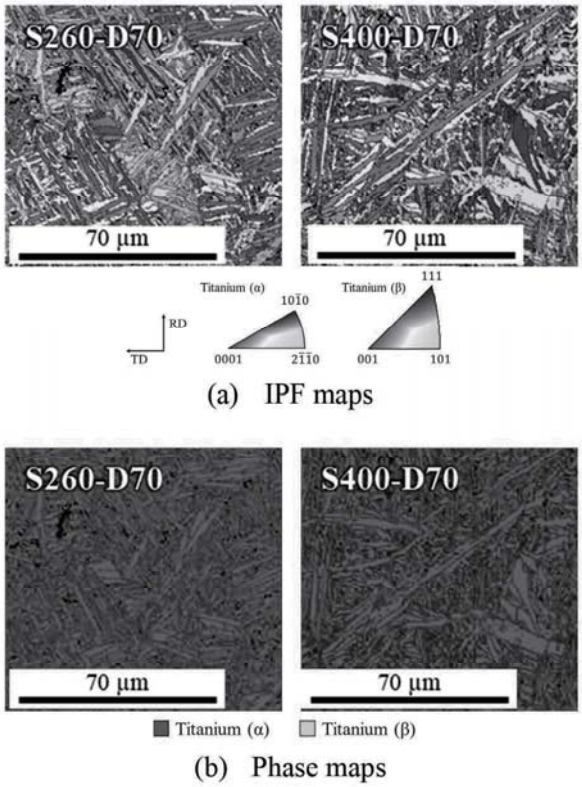

Fig. 10. IPF maps and phase maps of the side surfaces of RPS cubes.

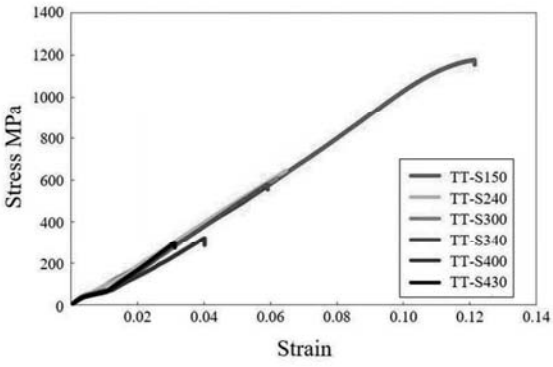

Fig. 11. Stress-strain diagram of RPS specimens.

Fig. 12. Specimen TT-S150 after the tensile test.

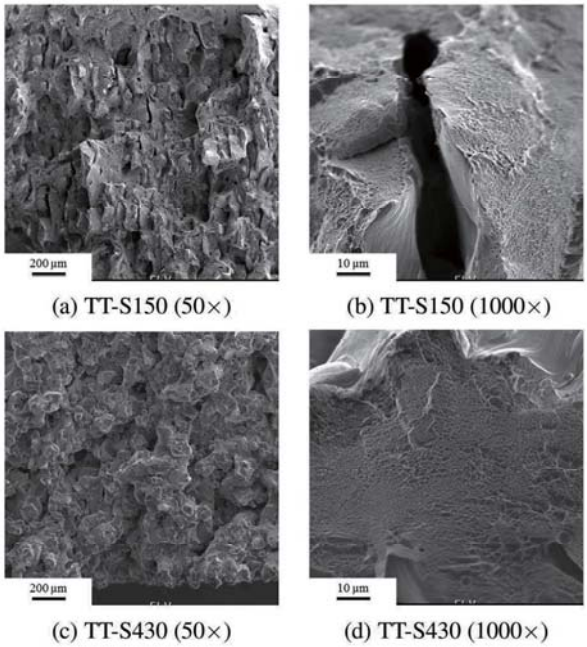

Fig. 13. SEM images of the fracture surfaces of TT-S150 and TT-S430.

strength (UTS) and the maximum strain decreased with increasing laser scan speed. The deformation of the RPS-containing tensile specimens was ductile, and the stress varied linearly with the strain until fracture. There is no clear yield point in the diagram.

The tensile specimens broke perpendicular to the tensile direction; the crack propagation path was zigzagged, as shown in **Fig. 12**. **Fig. 13** shows SEM images of the fracture surfaces of TT-S150 and TT-S430. At low magnification, the surface of TT-S150 showed peeled-off surfaces, and the surface of TT-S430 showed pore surfaces. At high magnification, both specimens showed equiaxed dimple patterns on the fracture surface.

Table 5 summarizes the UTS, maximum strain, 0.2% proof stress, and elastic modulus of each specimen and annealed Ti-6Al-4V. Annealed Ti-6Al-4V is a biomaterial suitable for medical implants [24]. Only the UTS of

Table 5. Tensile properties (values in parentheses indicate standard deviation).

	UTS [MPa]	Maximum strain [%]	0.2% proof stress [MPa]	Elastic modulus [GPa]
TT-S150	1144 (34)	12.3 (1.2)	26.5 (0.1)	13.3
TT-S240	644 (38)	6.5 (0.2)	24.1 (0.8)	12.1
TT-S300	608 (51)	6.2 (0.3)	22.3 (1.8)	11.2
TT-S340	580 (15)	5.9 (0.6)	23.9 (0.7)	12.0
TT-S400	321 (162)	4.0 (0.8)	21.0 (3.2)	10.5
TT-S430	299 (98)	3.1 (0.8)	23.3 (0.2)	11.7
Ti-6Al-4V (annealed)	895–930	N/A	825–869	110–114

TT-S150 was greater than that of the annealed material. The UTS decreased with increasing scan speed; the smallest value was 299 MPa (TT-S430). As with the UTS, the maximum strain of TT-S150 was approximately twice as large as that of the other test pieces. The 0.2% proof stress of each test piece was approximately 25 MPa, which was one-fortieth of that of the annealed material. The elastic modulus of each RPS test piece was approximately 10 GPa, which was approximately one-tenth of that of the annealed material. From these results, the behavior and values of the tensile properties of the RPS differed significantly from those of the conventional material.

5. Discussion

5.1. Effect of Scan Speed on the Porosity and Cell Structure

Kyogoku et al. [25] classified the pore defects of SLM-ed products into three categories, based on the pore morphology: lack of fusion pores (LFPs), micropores, and microcracks. Micropores have small spherical shapes, microcracks have linear shapes, and LFPs have awkward angular shapes. **Fig. 6** shows that the RPS is derived from LFPs.

The size, distribution, shape, and connectivity of LFPs should be affected by the size of the melt pools generated in the sintering zone during the melting and solidification process. Ikeshoji [26] showed analytically that melt pools form a teardrop shape. Dilip et al. [27] showed that the width and depth of the melt pool decreased with the acceleration of the scan speed when the laser was irradiated to the titanium plate. In other words, LFPs may be more likely to form at the edge of the melt pool where lack of fusion is likely to occur, and they may become larger as the melt pool becomes smaller with increasing scan speed. At low laser scan speeds, LFPs tend to be independent because the melt pools overlap significantly in both the width and depth directions. At high laser scan speeds, LFPs may be more likely to connect with each other as the melt pool shrinks. Therefore, the RPS at low laser scan speed became a closed-cell structure in which small independent pores were distributed throughout the specimens, while at high laser scan speed the RPS became an open-cell structure in which the pores connected with each other. This suggests that the porosity of an SLM product can be gradually changed by setting the scan speed in steps. Furthermore, the cell structure could also be changed from a closed-cell structure to an open-cell structure.

Figure 9 suggests that the amount of lack of fusion increases as the scan width increases, but the scan width had little effect on the porosity under these scan speed conditions. Since the melt pool becomes narrower as the scan speed increases, further acceleration of the laser scan speed may increase the lack of fusion and porosity of the SLM specimens.

The reason the porosity did not fall below 5% was probably that the excess energy density caused sputtering and gas encapsulation. Sputtering degrades the sintered surface and gas encapsulation forms microscopic pores; this makes it difficult to produce a fully dense SLM object under excessive energy density conditions [18].

5.2. Effect of Scan Speed on the Tensile Strength

As with the cubic specimens, the porosity of the RPS tensile specimens should increase with the acceleration of the laser scan speed. The reason for the decrease in the UTS in RPS specimens should be the decrease in the effective sectional area (ESA) with the increase in porosity [28]. The ESA of the RPS tensile specimens can be calculated from the porosity of the RPS cubes, which was described in the previous section. Thus, the results of the comparison between the ESA-considered UTS (σ_{Bt}), the original UTS (σ_B), and the annealed Ti-6Al-4V are shown in **Fig. 14**. The figure shows that the σ_{Bt} was greater than σ_B for all specimens, and the UTS of the annealed material was higher than the σ_{Bt} of all the specimens except for TT-S150. Therefore there must be other reasons for the decline in the UTS besides the decline in ESA. Focusing on the fracture mode of the RPS specimens, **Fig. 12** shows that TT-S150 broke perpendicular to the tensile direction and had a zigzagged crack propagation. This fracture is similar to the cleavage fracture commonly seen in brittle materials, but the RPS specimens exhibited ductile deformation, as shown in **Fig. 9**. **Fig. 13** clearly shows that the RPS tensile specimens broke with local ductile fracture and formed equiaxed dimples. Equiaxed dimples

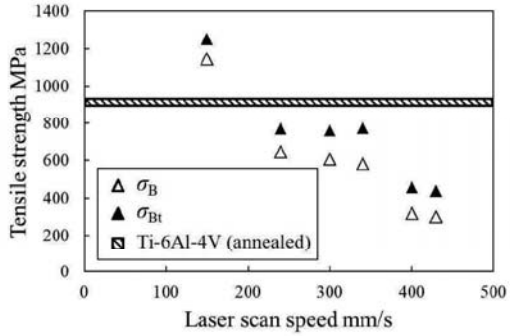

Fig. 14. Comparison of σ_{Bt} and σ_B.

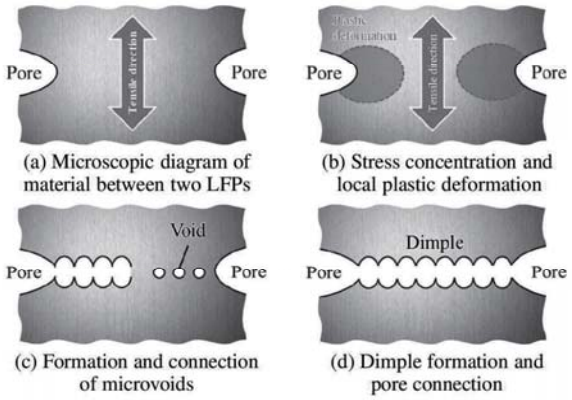

Fig. 15. Fracture model of RPS under tensile stress.

refer to microvoids that occur in a fractured surface when a ductile metal breaks with necking [29].

From these results, a fracture model for RPS under tensile stress is proposed in **Fig. 15**. Microscopically, the two LFPs under tensile stress can be regarded as necking tensile specimens (**Fig. 15(a)**). Since the LFPs have corners, stress concentration and local plastic deformation should occur at the corners in the early deformation stage (**Fig. 15(b)**). Then, microvoids may be formed and connected between the LFPs (**Fig. 15(c)**), and the dimples and the pore surfaces are exposed as the LFPs are connected (**Fig. 15(d)**). The stress concentration at the corners of the pores reduced the UTS more than the reduction of the ESA did. Additionally, because the pores were distributed throughout the specimens, the specimens also deformed plastically at the early deformation phase. Then the 0.2% proof stress and elastic modulus decreased.

The reason that only the UTS of TT-S150 exceeded the UTS of the annealed material may be the influence of metal microstructure. Whereas the metal microstructure of the annealed Ti-6Al-4V has fine α-phase equiaxed crystals and β-phase lamellar structures [30], that of the RPS cubes is dominated by fine acicular α-phase grains. This structure is similar to the metal microstructure formed in conventional SLM objects composed of Ti-6Al-4V, which has a higher tensile strength than that of the annealed material [31, 32]. Because the metal microstructure between the LFPs also reinforces the tensile strength, pore connection is difficult if the pores are far from each other. Since TT-S150 had a low porosity of 8.6% and little exposure of the pore surface, the strength reduction due to LFPs may be negligible.

Therefore, the strength of RPS should be affected by both the weakening of the LFPs and the hardening of the metal microstructure.

6. Conclusions

RPS cubes and tensile test specimens were fabricated using SLM. The porosity and tensile property results, along with further discussion, led to the following conclusions.

1. Appropriate control of the energy density allowed successful fabrication of both closed-cell structures with fine independent pores and complex open-cell structures that looked like plant roots.
2. The relationship between scan speed and porosity suggests that the porosity can be inclined, and the cell structure can be controlled depending on the scan speed.
3. A model of the deformation and fracture behavior of the RPS was proposed based on the results of the tensile test.
4. The tensile properties of the RPS were significantly different from those of the annealed material due to the increase in porosity and stress concentration at the pore corners.
5. While there was no clear difference in the metal structure of the RPS cubes based on the energy density, the structure was significantly different from that of the annealed material. Since the metal structure had excellent tensile strength, the low porosity specimen showed higher UTS than the annealed material.

References:

[1] World Health Organization, "World Health Report 2000: Health Systems: Improving Performance," 2000. https://www.who.int/whr/2000/en/whr00_en.pdf [Accessed December 25, 2019]
[2] World Health Organization, "World Health Statistics 2018: Monitoring health for the SDGs," 2018. https://apps.who.int/iris/bitstream/handle/10665/272596/9789241565585-eng.pdf [Accessed December 25, 2019]
[3] Ministry of Healthy, Labour and Welfare, "Comprehensive Survey of Living Conditions 2016," 2016. https://www.mhlw.go.jp/toukei/saikin/hw/k-tyosa/k-tyosa16/dl/05.pdf [Accessed December 25, 2019]
[4] H. Noda, H. Iso, H. Toyoshima, C. Date, A. Yamamoto, S. Kikuchi, A. Koizumi, T. Kondo, Y. Watanabe, Y. Wada, Y. Inaba, and A. Tamakoshi, "Walking and Sports Participation and Mortality From Coronary Heart Disease and Stroke," J. Am. Coll. Cardiol., Vol.46, No.9, pp. 1761-1767, 2005.
[5] Ministry of Healthy, Labour and Welfare, "4th NDB Open Data Japan," 2019. https://www.mhlw.go.jp/content/12400000/000539648.pdf [Accessed December 25, 2019]
[6] Y. Noyama, T. Miura, T. Ishimoto, N. Ikeo, M. Niinomi, and T. Nakano, "Bone Loss and Degradation of Bone Quality in the Human Femur after Total Hip Arthroplasty under Stress-Shielding by Titanium-Based Implant," J. Japan Inst. Metals, Vol.76, No.7, pp. 468-473, 2012.

[7] H. Lindahl, "Epidemiology of periprosthetic femur fracture around a total hip arthroplasty," Injury, Vol.38, pp. 651-654, 2007.
[8] C. E. Wen, Y. Yamada, K. Shimojima, Y. Chino, T. Asahina, and M. Mabuchi, "Processing and mechanical properties of autogenous titanium implant materials," J. Mater. Sci-Mater. M., Vol.13, pp. 397-401, 2002.
[9] S. Fujibayashi, M. Neo, H. M. Kim, T. Kokubo, and T. Nakamura, "Osteoinduction of porous bioactive titanium metal," Biomaterials, Vol.25, No.3, pp. 443-450, 2004.
[10] T. Nakamoto, N. Shirakawa, N. Shinomiya, and H. Inui, "Selective Laser Melting of Biomaterial (Pure Titanium) with High-Power Laser," J. of Japan Society for Laser Surgery and Medicine, Vol.33, No.2, pp. 166-174, 2012.
[11] D. A. Hollander, M. V. Walter, T. Wirtz, R. Sellei, B. S. Rohlfing, O. Paar, and H. Erli, "Structural, mechanical and in-vitro characterization of individually structured Ti-6Al-4V produced by direct laser forming," Biomaterials, Vol.27, No.7, pp. 955-963, 2006.
[12] L. J. Gibson and M. F. Ashby, "Cellular Solids: structure and properties," Pergamon Press, 1988.
[13] R. Goodall and A. Mortensen, "Porous Metals," Physical Metallurgy, pp. 2399-2595, 2014.
[14] T. Shibutani, "Evaluation of Crack Initiation at Interfacial Edge on the Basis of Fracture Mechanics Concept and Application to Electronics Devices," J. JIEP, Vol.7, No.7, pp. 639-644, 2004.
[15] A. Simchi and H. Pohl, "Effects of laser sintering processing parameters on the microstructure and densification of iron powder," Mater. Sci. Eng. A, Vol.359, Nos.1-2, pp. 119-128, 2003.
[16] D. Dai, D. Gu, H. Zhang, J. Xiong, C. Ma, C. Hong, and R. Poprawe, "Influence of scan strategy and molten pool configuration on microstructures and tensile properties of selective laser melting additive manufactured aluminum based parts," Opt. Laser Technol., Vol.99, No.1, pp. 91-100, 2018.
[17] H. Gu, H. Gong, D. Pal, K. Rafi, T. J. J. Starr, and B. E. Stucker, "Influences of Energy Density on Porosity and Microstructure of Selective Laser Melted 17-4PH Stainless Steel," Proc. of Annual Int. Solid Freeform Fabrication Symp., pp. 474-489, 2013.
[18] C. Meier, R. W. Penny, Y. Zou, J. S. Gibbs, and A. J. Hart, "Thermophysical Phenomena in Metal Additive Manufacturing by Selective Laser Melting: Fundamentals, Modeling, Simulation and Experimentation," Annu. Rev. Heat Trans., Vol.20, pp. 241-316, 2018.
[19] H. Attar, S. E. Haghighi, D. Kent, X. Wu, and M. S. Dargusch, "Comparative study of commercially pure titanium produced by laser engineered net shaping, selective laser melting and casting processes," Mater. Sci. Eng. A, Vol.705, pp. 385-393, 2017.
[20] Y. Hangai, I. Akuzawa, S. Kitahara, O. Kuwazuru, N. Yoshikawa, and S. Amada, "Influence of Compression Process on Amount and Morphology of Porosity in Aluminum Alloy ADC12 Die-casting Products," J. JFS, Vol.78, No.11, pp. 551-556, 2006.
[21] M. Simonelli, Y. Y. Tse, and C. Tuck, "On the Texture Formation of Selective Laser Melted Ti-6Al-4V," Metall. Mater. Trans. A, Vol.45, No.6, pp. 2863-2872, 2014.
[22] T. Morita, C. Tsuda, H. Sakai, and N. Higuchi, "Fundamental Properties of Ti-6Al-4V Alloy Produced by Selective Laser Melting Method," Mater. Trans., Vol.58, No.10, pp. 1397-1403, 2017.
[23] E. W. Lui, W. Xu, A. Pateras, M. Qian, and M. Brandt, "New Development in Selective Laser Melting of Ti-6Al-4V: A Wider Processing Window for the Achievement of Fully Lamellar $\alpha+\beta$ Microstructures," JOM, Vol.69, pp. 2679-2683, 2017.
[24] M. Niinomi, "Mechanical properties of biomedical titanium alloys," Mater. Sci. Eng. A, Vol.243, Nos.1-2, pp. 231-236, 1998.
[25] H. Kyogoku and T. Ikeshoji, "A review of metal additive manufacturing technologies: Mechanism of defects formation and simulation of melting and solidification phenomena in laser powder bed fusion process," Mech. Eng. Rev., Vol.7, No.1, pp. 1-19, 2020.
[26] T. Ikeshoji, "Liquidation and Solidification Phenomena During Laser Powder Bed Fusion Process," J. Smart Process., Vol.6, No.3, pp. 109-114, 2017.
[27] J. J. S. Dilip, S. Zhang, C. Teng, K. Zeng, C. Robinson, D. Pal, and B. Stucker, "Influence of processing parameters on the evolution of melt pool, porosity, and microstructures in Ti-6Al-4V alloy parts fabricated by selective laser melting," Progress in Additive Manufacturing, Vol.2, pp. 157-167, 2017.
[28] M. Okayasu, K. Kanazawa, and N. Nishi, "Effects of Internal Defects on Tensile Properties of ADC10 Die Casting," J. JFS, Vol.70, No.11, pp. 779-785, 1998.
[29] T. L. Anderson, "Fracture mechanics: Fundamentals and applications (3rd ed.)," Taylor and Francis, pp. 219-232, 2011.
[30] C. Ouchi, "Thermomechanical Processing in Titanium Alloys," Bulletin of the Japan Inst. of Metals, Vol.25, No.8, pp. 672-679, 1986.
[31] T. Vilaro, C. Colin, and J. D. Bartout, "As-Fabricated and Heat-Treated Microstructures of the Ti-6Al-4V Alloy Processed by Selective Laser Melting," Metall. Mater. Trans. A, Vol.42, No.10, pp. 3190-3199, 2011.
[32] H. K. Rafi, J. V. Karthik, H. Gong, T. L. Starr, and B. E. Stucker, "Microstructures and Mechanical Properties of TI6Al4V Parts Fabricated by Selective Laser Melting and Electron Beam Melting," J. Mater. Eng. Perform., Vol.22, No.12, pp. 3872-3883, 2013.

Name:
Shinji Ishibashi

Affiliation:
Doctoral Course Student, Department of Mechanical Systems Engineering, Graduate School of Engineering, Tohoku University

Address:
6-6-01 Aramaki Aza-Aoba, Aoba-ku, Sendai, Miyagi 980-8579, Japan

Brief Biographical History:
2017 Received Master's degree (Engineering) from Tohoku University
2017- Doctoral Course Student, Graduate School of Engineering, Tohoku University

Membership in Academic Societies:
- Japan Society for Precision Engineering (JSPE)
- Society of Materials Science, Japan (JSMS)
- Japan Institute of Metals and Materials (JIM)
- Japanese Society for Strength and Fracture of Materials (JSFM)

Name:
Keita Shimada

Affiliation:
Assistant Professor, Department of Mechanical Systems Engineering, Graduate School of Engineering, Tohoku University

Address:
6-6-01 Aramaki Aza-Aoba, Aoba-ku, Sendai, Miyagi 980-8579, Japan

Brief Biographical History:
2009 Received M.E. degree from Tohoku University
2012 Received Ph.D. from Tohoku University
2012- Assistant Professor, Department of Mechanical Systems and Design, Tohoku University

Main Works:
- K. Shimada, N. Yoshihara, J. Yan, T. Kuriyagawa, Y. Sueishi, and H. Tezuka, "Ultrasonic-assisted Grinding of Ultra-High Purity SUS 316," Int. J. Automation Technol., Vol.5, No.3, pp. 427-432, 2011.
- K. Shimada, P. J. Liew, T. Zhou, J. Yan, and T. Kuriyagawa, "Statistical Approach Optimizing Slant Feed Grinding," J. Adv. Mech. Design, Systems and Manu., Vol.6, No.6, pp. 898-907, 2012.
- K. Shimada, C. I. Kuo, M. Mizutani, and T. Kuriyagawa, "Statistical Analysis for Evaluating Surface Roughness of Plane Honing," Int. J. Automation Technol., Vol.8, No.4, pp. 576-583, 2014.

Membership in Academic Societies:
- Japan Society of Mechanical Engineers (JSME)
- Japan Society for Precision Engineering (JSPE)
- Japan Society for Abrasive Technology (JSAT)

Name:
Hiroyasu Kanetaka

Affiliation:
Associate Professor, Graduate School of Dentistry, Tohoku University
Graduate School of Biomedical Engineering, Tohoku University

Address:
4-1 Seiryo-machi, Aoba-ku, Sendai, Miyagi 980-8575, Japan
6-6-01 Aramaki Aza-Aoba, Aoba-ku, Sendai, Miyagi 980-8579, Japan

Brief Biographical History:
1997- Assistant Professor, School of Dentistry, Tohoku University
2002- Visiting Scholar, University of Illinois at Chicago
2007- Associate Professor, Tohoku University

Main Works:
• "In vitro evaluation of biocompatibility of Ti-Mo-Sn-Zr superelastic alloy," J. Biomater. Appl., Vol.30, No.1, pp. 119-130, 2015.

Membership in Academic Societies:
• Japanese Orthodontic Society (JOS)
• Japanese Society of Dysphagia Rehabilitation (JSDR)
• Japan Institute of Metals and Materials (JIM)

Name:
Masaki Tsukuda

Affiliation:
Nissan Motor Co., Ltd.

Address:
1-1-1 Takashima, Nishi-ku, Yokohama-shi, Kanagawa 220-8686, Japan

Brief Biographical History:
2018 Received Master's degree from Graduate School of Engineering, Tohoku University
2018- Nissan Motor Co., Ltd.

Name:
Takumi Mizoi

Affiliation:
Hitachi, Ltd.

Address:
1-6-6 Marunouchi, Chiyoda-ku, Tokyo 100-8280, Japan

Brief Biographical History:
2019 Received Master's degree from Graduate School of Engineering, Tohoku University
2019- Hitachi, Ltd.

Name:
Masataka Chuzenji

Affiliation:
Master Course Student, Department of Mechanical Systems Engineering, Graduate School of Engineering, Tohoku University

Address:
6-6-01 Aramaki Aza-Aoba, Aoba-ku, Sendai, Miyagi 980-8579, Japan

Brief Biographical History:
2019 Received Bachelor's degree from Undergraduate School of Engineering, Tohoku University
2019- Master Course Student, Graduate School of Engineering, Tohoku University

Name:
Shoichi Kikuchi

Affiliation:
Department of Mechanical Engineering, Faculty of Engineering, Shizuoka University

Address:
3-5-1 Johoku, Naka-ku, Hamamatsu, Shizuoka 432-8561, Japan

Brief Biographical History:
2008- GCOE Researcher, Keio University
2010- Assistant Professor, Ritsumeikan University
2013- Visiting Researcher, University of Kaiserslautern
2014- Assistant Professor, Kobe University
2018- Associate Professor, Shizuoka University

Main Works:
• S. Kikuchi, T. Imai, H. Kubozono, Y. Nakai, M. Ota, A. Ueno, and K. Ameyama, "Effect of harmonic structure design with bimodal grain size distribution on near-threshold fatigue crack propagation in Ti-6Al-4V Alloy," Int. J. of Fatigue, Vol.92, pp. 616-622, 2016.

Membership in Academic Societies:
• Society of Materials Science, Japan (JSMS)
• Japan Society of Mechanical Engineers (JSME)
• Japan Institute of Metals and Materials (JIM)
• Japan Society for Abrasive Technology (JSAT)

Name:
Masayoshi Mizutani

Affiliation:
Associate Professor, Department of Mechanical Systems Engineering, Graduate School of Engineering, Tohoku University

Address:
6-6-01 Aramaki Aza-Aoba, Aoba-ku, Sendai, Miyagi 980-8579, Japan

Brief Biographical History:
2003 Received M.E. from Integrated Design Engineering, Graduate School of Science and Technology, Keio University
2004- Junior Research Associate, Ohmori Materials Fabrication Laboratory, RIKEN
2006 Received Ph.D. from Integrated Design Engineering, Graduate School of Science and Technology, Keio University
2006- Collaboration Researcher, Advanced Development and Supporting Center, RIKEN
2007- Collaboration Researcher, Ohmori Materials Fabrication Laboratory, RIKEN
2009- Special Postdoctoral Researcher, Ohmori Materials Fabrication Laboratory, RIKEN
2011- External Collaborative Researcher, Sophia University
2012- Collaboration Researcher, Ohmori Materials Fabrication Laboratory, RIKEN
2012- Associate Professor, Department of Mechanical Systems and Design, Tohoku University

Main Works:
• Micro/meso mechanical manufacturing (M4 process), laser process, powder jet deposition (PJD), functional interface, biomaterials, bio-medical applications, biomimetic surface

Membership in Academic Societies:
• Japan Society of Mechanical Engineers (JSME)
• Japan Society for Precision Engineering (JSPE)
• Japan Society for Abrasive Technology (JSAT)

Name:
Tsunemoto Kuriyagawa

Affiliation:
Professor, Bio-Medical Interface Fabrication Laboratory, Graduate School of Biomedical Engineering, Tohoku University

Address:
6-6-01 Aramaki Aza-Aoba, Aoba-ku, Sendai, Miyagi 980-8579, Japan

Brief Biographical History:
1984-1990 Research Associate, Tohoku University
1990-1992 Assistant Professor, Tohoku University
1991-1992 Visiting Professor, University of Connecticut
1992-2002 Associate Professor, Tohoku University
2003- Professor, Tohoku University

Main Works:
• Nano-precision mechanical manufacturing, micro/meso mechanical manufacturing (M4 process), powder jet deposition, and creation of functional interface

Membership in Academic Societies:
• Science Council of Japan (SCJ)
• International Committee for Abrasive Technology (ICAT)
• International Society for Nanomanufacturing (ISNM)
• Japan Society of Mechanical Engineers (JSME)
• Japan Society for Precision Engineering (JSPE)
• Japan Society for Abrasive Technology (JSAT)

Paper:

Effects of Pulse Duration and Heat on Laser-Induced Periodic Surface Structures

Shuhei Kodama*,†, Keita Shimada, Masayoshi Mizutani**, and Tsunemoto Kuriyagawa****

*Tokyo University of Agriculture and Technology
2-24-16 Nakacho, Koganei, Tokyo 184-0012, Japan
†Corresponding author, E-mail: shuhei-kodama@go.tuat.ac.jp
**Tohoku University, Sendai, Japan
[Received December 27, 2019; accepted April 3, 2020]

Compared with traditional nanotexturing methods, an ultrashort-pulsed laser is an efficient technology of fabricating nanostructures called laser-induced periodic surface structures (LIPSS) on material surfaces. LIPSS are easily fabricated when the pulse duration is shorter than collisional relaxation time (CRT). Accordingly, ultrashort-pulsed lasers have been mainly used to study LIPSS, but they unstably irradiate while requiring high costs. Although long-pulsed lasers have low cost and high stability, the phenomena (such as the effect of pulse duration, laser wavelength, and heat) of the LIPSS fabricated using short-pulsed lasers with the pulse duration close to the maximum CRT, which is greater than femtosecond, have not been clarified. However, the nanosecond pulse laser has been reported to produce LIPSS, but those were unclear and ununiform. In this study, the short-pulsed laser with the pulse duration of 20 ps, which is close to the maximum CRT, was employed to clarify the effects of pulse duration and heat on the fabrication of LIPSS and to solve problems associated with ultrashort-pulsed lasers. First, a finite-difference time-domain simulation was developed at 20-ps pulse duration to investigate the effects of irradiation conditions on the electric-field-intensity distribution. Subsequently, experiments were conducted using the 20-ps pulse laser by varying conditions. The aspect ratio of the LIPSS obtained was greater than that of the LIPSS fabricated using ultrashort-pulsed lasers, but LIPSS were not fabricated at 355- and 266-nm laser wavelength. In addition, the short-pulsed laser experienced thermal influences and a cooling material was effective for the fabrication of LIPSS with high-aspect-ratio. This demonstrates the effects of pulse duration close to the CRT and heat on the fabrication of LIPSS.

Keywords: short-pulsed laser, 20-ps pulse duration, electric field, laser wavelength, material temperature

1. Introduction

Micro/nanostructures can be used to alter the material-surface functionalities such as tribology [1, 2], wettability [3], optical properties [4], and bioaffinity [5]. Compared with traditional methods, the ultrashort-pulsed laser is more appropriate method of fabricating fine structures, and it is used to fabricate fine periodic structures called laser-induced periodic surface structures (LIPSS). In addition, LIPSS offered functionalities such as the friction reduction [6], water repellency [7], anti-reflection [8], and bioaffinity [9]. Notably, LIPSS are easily fabricated when the pulse duration is shorter than the collisional relaxation time (CRT) from a few ps to approximately 20 ps, as thermal effects occur after CRT [10]. Accordingly, an ultrashort-pulsed laser with the pulse duration of less than 10 ps has been mainly used to study LIPSS, although the lasers with longer pulse duration have lower cost and higher stability [11–13].

Theoretically, it is difficult to fabricate LIPSS by using the nanosecond pulse laser with the wavelength of 1064 nm because of thermal effects and low intensity, however, it produced unclear LIPSS partially [14]. In addition, it has been unclear whether a short-pulsed laser with short laser wavelength can be used to fabricate LIPSS, while an ultrashort-pulsed laser with short laser wavelength can be used to fabricate LIPSS [15–17]. Moreover, LIPSS fabricated at higher temperature had low roughness and threshold. In addition, laser irradiation at high material temperature facilitated the fabrication of LIPSS depending on the material, owing to the increase in the initial carrier density, laser absorption and electron scattering [14, 18–21], although non-thermal processing is effective for fabrication of LIPSS [10]. However, the phenomena associated with the LIPSS fabricated using a short-pulsed laser with pulse duration close to CRT have not been clarified.

The objective of this study is to verify the effects of the pulse duration that is close to CRT, and also analyze the effects of heat on the fabrication of LIPSS, by using a short-pulsed laser with the pulse duration of 20 ps, which is close to the maximum CRT. We also aim to stably fabricate uniform LIPSS on the entire irradiated surface at low cost. First, a finite-difference time-domain (FDTD) simu-

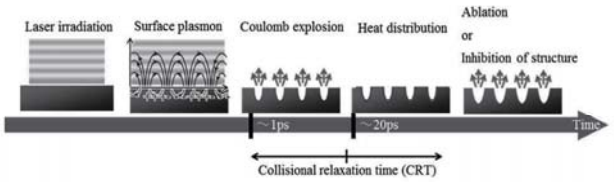

Source: IJAT, Vol.12, No.6 [27], Precision Engineering, Vol.55 [28]

Fig. 1. Processing model of a short-pulsed laser.

lation was conducted with the pulse duration of 20 ps by using a 304 stainless steel material (SUS304, classified by Japanese Industrial Standards), which is a commonly used industrial material, to investigate the effects of conditions on the electric-field-intensity distribution and the geometry of LIPSS when the pulse duration was 20 ps, as laser fluence and wavelength change the electric-field-intensity distribution and electron density related to the pitch length and height of LIPSS [22, 23]. Subsequently, experiments were conducted using the short-pulsed laser with the pulse duration of 20 ps by irradiating on SUS304 substrates while varying the laser energy density, pulse, laser wavelength, and material temperature to investigate the effects of the pulse duration of 20 ps and material temperature on the fabrication and geometry (e.g., pitch length and height) of LIPSS, compared with ultrashort pulsed lasers.

2. Principle

The incident light is divided into plasma waves and scattered lights via protrusions on a surface based on the parametric decay [14, 24–26]. The interference between the incident light and plasma waves induced surface plasmons, resulted in periodic Coulomb explosions on the surface, as depicted in **Fig. 1** [27, 28]. After varying the CRT from a few ps to approximately 20 ps, thermal effects induced the ablation or inhibition of structures, and LIPSS were fabricated. The pitch length of LIPSS on metals is approximately 0.5–0.85 times as long as the laser wavelength and increases upon increasing the laser energy density. Because a laser with pulse duration shorter than CRT can be used to fabricate LIPSS without thermal effects [29], a short-pulsed laser with the pulse duration of 20 ps was employed in this study, as 20 ps is close to the maximum CRT and, therefore, it may induce thermal effects to clarify the effects of 20-ps pulse duration and heat on the fabrication of LIPSS and to stabilize laser irradiation at low cost.

3. FDTD

The principle stated that the pitch length of LIPSS mainly depends on the laser wavelength and that it expands upon increasing the energy density. The electromagnetic field analysis using the FDTD method was performed with various laser intensities and wavelengths to investigate the effects of laser-irradiation conditions (e.g., laser intensity and wavelength) on the electric-field-intensity distribution related to the geometry of resultant LIPSS in the case of the laser with the pulse duration of 20 ps. The 20-ps pulsed laser has thermal effects, which results in the melting and oxidation of the irradiated material surface because of the pulse duration being close to CRT. Notably, CRT expands by lowering the material temperature because the electron-phonon interactions are suppressed. Therefore, laser irradiation with a cooling material was proposed to suppress the thermal effects and easily fabricate sharp LIPSS, which were similar to those fabricated using the femtosecond laser. In addition, the FDTD simulation was performed by varying the material temperature to investigate the effects of material temperature on the electric-field-intensity distribution and fabrication of LIPSS.

3.1. Method

The FDTD simulation is used to indicate electric-field-intensity distribution. The electromagnetic-field intensity is calculated by solving the time-dependent Maxwell's equations, introduced by Yee in 1966 [30, 31]. The time arrangement is determined using Eqs. (1) and (2) as follows:

$$E^n = \frac{1-\frac{\sigma\Delta t}{2\varepsilon}}{1+\frac{\sigma\Delta t}{2\varepsilon}}E^{n-1} + \frac{\frac{\Delta t}{\varepsilon}}{1+\frac{\sigma\Delta t}{2\varepsilon}}\nabla\times H^{n-\frac{1}{2}} \quad . \quad (1)$$

$$H^{n+\frac{1}{2}} = H^{n-\frac{1}{2}} - \frac{\Delta t}{\mu}\nabla\times E^n \quad . \quad . \quad . \quad . \quad . \quad . \quad . \quad (2)$$

E denotes the electric field, H the magnetic field, μ the permeability, ε the permittivity, σ the conductivity, superscript n the time steps, and Δt the time increment.

3.2. Analytical Setup and Conditions

Electromagnetic-field analysis with an FDTD simulation (nanophotonic FDTD simulation software from Lumerical Inc.) was performed to investigate the changes in the electric-field-intensity distribution by varying the laser intensity, laser wavelength, and material temperature, depending on the refractive index and extinction coefficient of material, and also to investigate the effects of 20-ps pulse duration and heat on LIPSS fabrication. In **Fig. 2**, we depict the analytical model: the analysis area is the inside of the rectangle represented using the thick line; the monitor area is the inside of a square represented using the thin line; the direction of the incident light is denoted by the arrow, and the direction of the laser polarization is denoted by the double-headed arrow. The surface with grooves was prepared to imitate the case of fabricating LIPSS, as the electric field was homogeneously distributed on the flat surface, meaning the entire surface is removed. The analytical conditions are listed in **Table 1**. The refractive index and extinction coefficient of

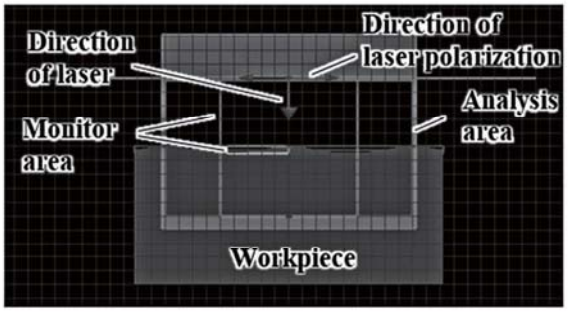

Fig. 2. Analytical model.

Table 1. Analytical conditions.

Laser wavelength	900, 532, 355, 266 nm
Pulse duration	20 ps
Material	SUS304
Pitch length P_g	100–900 nm
Depth	50 nm
Relative intensity	1.0, 2.0, 3.0, 4.0
Material temperature	293, 373 K

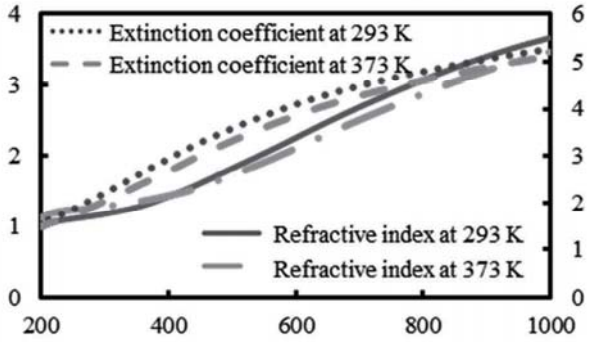

Fig. 3. Refractive index and extinction coefficient of SUS304.

SUS304 were preliminarily measured using an ellipsometer from the wavelength of 200 to 1000 nm at 293 K and 373 K, as depicted in **Fig. 3**. First, the laser wavelength and laser-pulse duration were set to 900 nm and 20 ps, respectively. The depth and pitch length of the grooves were set to 50 and 850 nm, respectively, as the pitch length of LIPSS was close to the laser wavelength. The relative intensities were set to 1.0, 2.0, 3.0, and 4.0. Next, the laser wavelengths were set to 900, 532, 355, and 266 nm, and the pitch lengths of the grooves were set to 700–900, 400–500, 250–350, and 150–250 nm, respectively. Subsequently, the pitch lengths of the grooves were set to 850, 400, 300, and 150 nm for the cases of 900, 532, 355, and 266 nm laser wavelength, respectively. The material temperatures were set to 293 K and 373 K, and the changes in the electric-field intensity were investigated by decreasing the temperature.

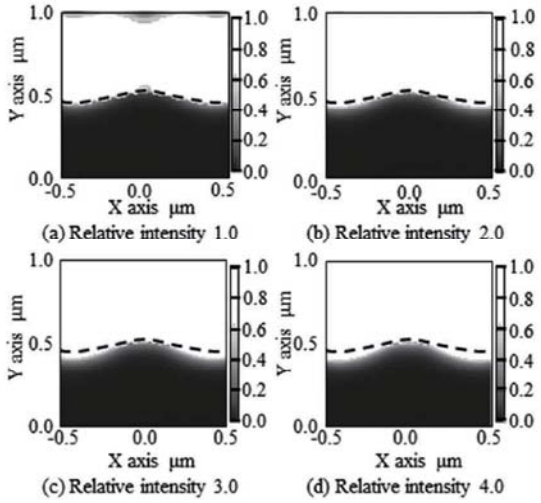

Fig. 4. Electric field distribution at different intensity.

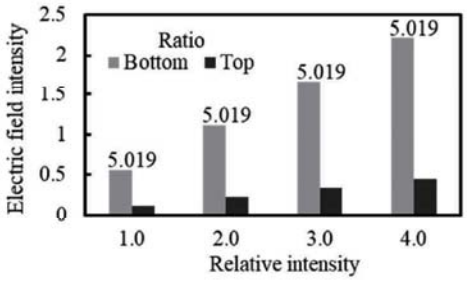

Fig. 5. Relationship between relative intensity and electric field intensity (the number in the figure is the ratio of the electric-field intensity at the bottom of the groove to that at the top of the groove).

3.3. Analytical Results

3.3.1. Simulation with Various Intensities

In **Fig. 4**, we depict the analytical results of electric-field distribution at different intensity with the same scale of electric-field intensity. The upper and lower regions divided using the dotted lines represent the atmosphere and material, respectively. Ablation might occur at the region with large electric-field intensity because of the Coulomb explosion. In the case wherein the penetration depth of the electric field is higher at the bottoms of the grooves than that at the tops of grooves, the bottoms of the grooves might be removed, thereby resulting in LIPSS. The penetration becomes deeper upon increasing the relative intensity, and the electric-field distribution was homogeneously observed on the entire surface at high relative intensity, removing the entire surface. In **Fig. 5**, we depict the changes in the electric-field intensity of top and bottom of the grooves and the ratio of the electric-field intensity at the bottom of groove to that at the top of groove for each relative intensity. The electric-field intensity at the bottoms of grooves slightly increased upon increasing the relative intensity without change in the ratio of the

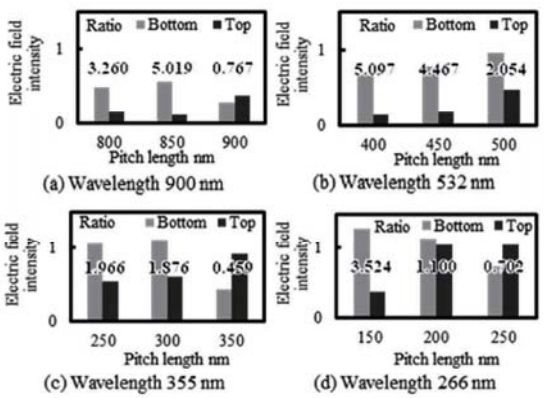

Fig. 6. Relationship between laser wavelength and electric field intensity (the number in the figure is the ratio of the electric-field intensity at the bottom of the groove to that at the top of the groove).

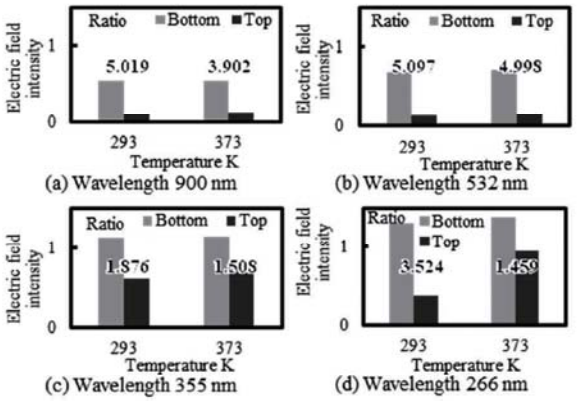

Fig. 7. Relationship between the material temperature and electric-field intensity (number in the figure is the ratio of the electric-field intensity at the bottom of groove to that at the top of groove).

electric-field intensity. The pitch length of the grooves with high ratio was extended with increase in the relative intensity; i.e., the increase in the energy density extends the pitch length of LIPSS, in accordance with the principle of extending the pitch length upon increasing the energy density related to the electric field.

3.3.2. Simulation with Various Laser Wavelengths

In **Fig. 6**, we depict the changes in the electric-field intensity for each laser wavelength. The ratio of the electric-field intensity at the top of the grooves to that at the bottoms of the grooves for the pitch lengths of 850, 400, 300, and 150 nm were large for the laser wavelengths of 900, 532, 355, and 266 nm, respectively, indicating that the laser wavelength mainly determines the pitch length of LIPSS. Moreover, the electric-field intensity increased at both the top and the bottom of the groove upon decreasing the laser wavelength, indicating that shorter-wavelength lasers require lower energy density to fabricate LIPSS, owing to the removal of the entire irradiated surface because of high intensity.

3.3.3. Simulation with Various Material Temperatures

In **Fig. 7**, we depict the changes in the electric-field intensity for each laser wavelength and material temperature. High electric-field intensity was observed on the workpiece surface, especially at the top of the groove, at high material temperature. This indicates that although the threshold decreases, yet the fabrication of LIPSS is difficult at high temperatures because of the removal of the entire irradiated surface. However, the ratio of the electric-field intensity at the bottom of the groove to that at the top of the groove increased for lower material temperatures, indicating that it is easy to fabricate LIPSS with higher aspect ratio (i.e., the height of LIPSS divided by the pitch length thereof) at lower temperatures.

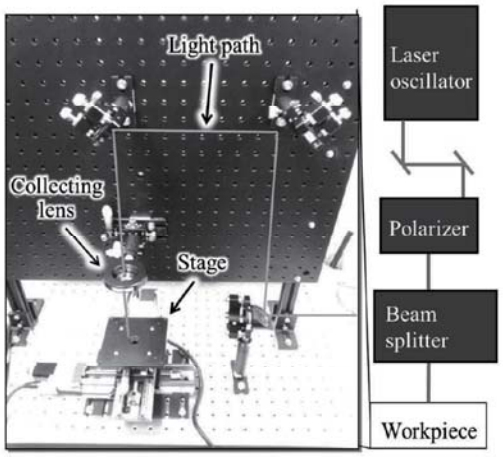

Fig. 8. Processing model of a short-pulsed laser.

4. Experiments

From the FDTD simulation results, we predicted the geometry of LIPSS at 20-ps pulse duration depending on the laser energy density and wavelength, and the low-temperature environment facilitated the fabrication of LIPSS with high aspect ratio. The experiments were then conducted to confirm the effects of both the pulse duration close to CRT and heat on the fabrication and geometry of LIPSS with the 20-ps pulsed laser while varying the laser-irradiation conditions.

4.1. Experimental Conditions

SUS304 substrates with mirror surfaces were prepared. Laser irradiation-experiments on the mirror surfaces were conducted using a picosecond-pulse laser oscillator (Ekspla, PL2250-50P20) with 20-ps pulse duration. The experimental setup is depicted in **Fig. 8**, including a polarizer, beam splitter, and collecting lens with the focusing range of 150 mm.

Table 2. Experimental conditions.

Wavelength	1064, 532, 355, 266 nm
Pulse duration	20 ps
Frequency	50 Hz
Pulse n	1–1000 pulse(s)
Energy density E_d	0.0034–4.47 J/cm^2
Temperature	223, 293 K
Workpiece	SUS304

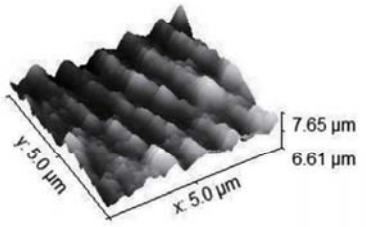

Fig. 9. AFM image of LIPSS at 1064-nm laser wavelength.

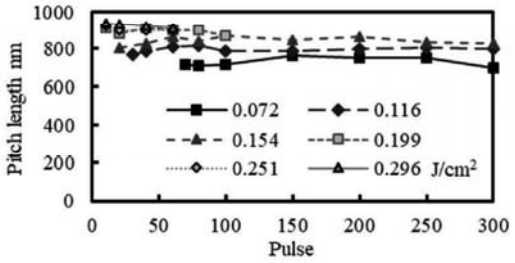

Fig. 10. Pitch length of LIPSS at 1064-nm wavelength.

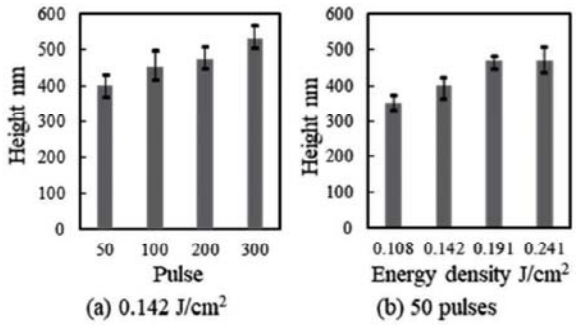

Fig. 11. Height of LIPSS at 1064-nm wavelength.

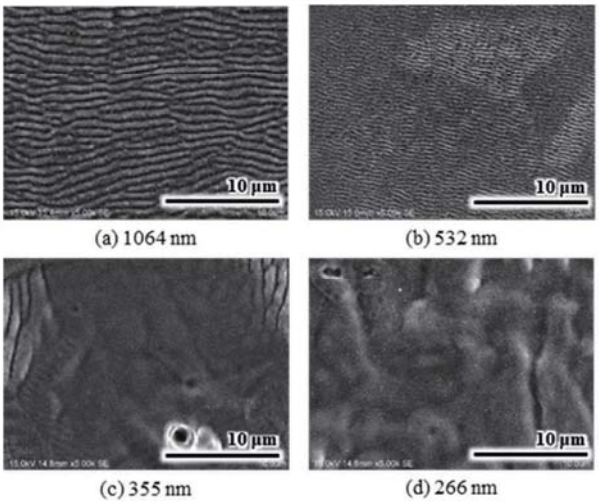

Fig. 12. SEM images of irradiated regions at different laser wavelength.

The laser-irradiation conditions are listed in **Table 2**. The laser with the Gaussian beam profile was irradiated on the substrate without scanning. The pulses and energy density were varied, and the laser wavelengths were set to 1064, 532, 355, and 266 nm. The material temperatures were set to 223 K and 293 K using a thermal controller for microscopy (Collet Kogyo Co., Ltd.). The workpiece was refrigerated on the holder in the controller, where liquid nitrogen flowed, and the laser was irradiated through a window in the vacuum. The central parts of the laser-irradiated regions were observed using a scanning electron microscope (SEM), a transmission electron microscope (TEM), and an atomic force microscope (AFM).

4.2. Experimental Results

4.2.1. Experiments with Various Energy Densities and Pulses at 1064-nm Laser Wavelength

In **Fig. 9**, we depict an example of the AFM image of LIPSS. In **Fig. 10**, we depict changes in the pitch length of LIPSS for various pulses and energy densities. The pitch length was approximately 700–900 nm and slightly increased upon increasing the energy density irrespective of pulses, as attributed to the parametric decay. In **Fig. 11**, we depict the changes in the height of LIPSS. The height of LIPSS was approximately 350–550 nm and slightly increased upon increasing the pulses and energy density. Overall, the pitch length and height of the LIPSS fabricated on SUS304 using the short-pulsed laser are approximately 700–900 and 350–550 nm, respectively. The aspect ratio of LIPSS (i.e., the height of LIPSS divided by the pitch length thereof) with the 20-ps pulsed laser is greater than that of LIPSS with ultrashort-pulsed lasers that, in the case of with the wavelength of 800 nm, fabricated LIPSS with approximately pitch length of 600 nm, height of 150–250 nm and aspect ratio of 0.25–0.42 on stainless steel surfaces [32–35] due to removal of convex parts with high intensity [13].

4.2.2. Experiments with Various Laser Wavelengths

In **Fig. 12**, we depict the SEM images of the laser-irradiated regions by using various laser wavelengths. The 1064- and 532-nm-wavelength lasers fabricated LIPSS, but the 355- and 266-nm-wavelength lasers did not fabricate LIPSS, while the ultrashort-pulsed laser with 370-fs pulse duration at 257-nm wavelength fabricated LIPSS [17]. It is considered that significant nonperiodic

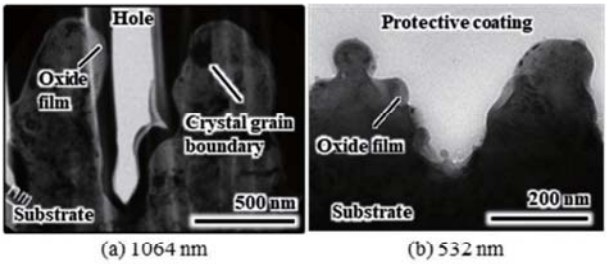

Fig. 13. TEM images of irradiated regions at 1064 and 532 nm laser wavelength.

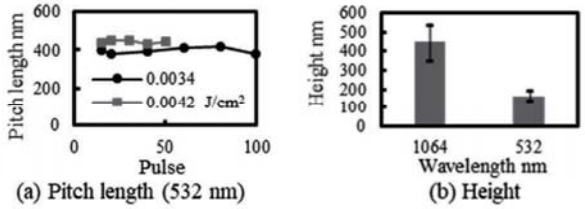

Fig. 14. Geometry of LIPSS at 532- and 1064-nm laser wavelength.

absorption, as mentioned in Section 3.3.2, occurs deeper in the case of 355- and 266-nm-wavelength lasers compared with the ultrashort pulsed laser, and the entire irradiated surface is removed. Additionally, the 532-nm-wavelength laser required lower energy density to fabricate LIPSS compared with the 1064-nm-wavelength laser, as the short-wavelength laser is absorbed deeper into the substrate.

In **Fig. 13**, we depict the TEM images of the cross sections of the LIPSS fabricated using the 1064- and 532-nm-wavelength lasers, respectively. The LIPSS with 10-μm thick oxide films were larger at 1064-nm laser wavelength than that at 532-nm laser wavelength. In **Fig. 14**, we depict the changes in the pitch length and height of LIPSS for each laser-irradiation condition, respectively. The pitch length and height of the 532-nm-wavelength laser fabricated LIPSS were initially approximately 400 nm and 200 nm, respectively. Both of them slightly increased upon increasing the energy density, as is the case of the LIPSS fabricated using the 1064-nm-wavelength laser.

4.2.3. Experiments with Various Material Temperatures

In **Fig. 15**, we depict the SEM images of the irradiated regions for low material temperature. The 1064- and 532-nm-wavelength lasers fabricated LIPSS, but 355- and 266-nm-wavelength lasers could not fabricate LIPSS even if the material temperature decreased. In **Fig. 16**, we depict the TEM images of LIPSS at 1064-nm wavelength and various temperatures. The LIPSS were sharp at 223 K, while they were roundish at 293 K. In **Fig. 17**, we depict the element mappings detected via energy dispersive X-ray spectrometry of the TEM images. The laser irradiation at low material temperature suppressed

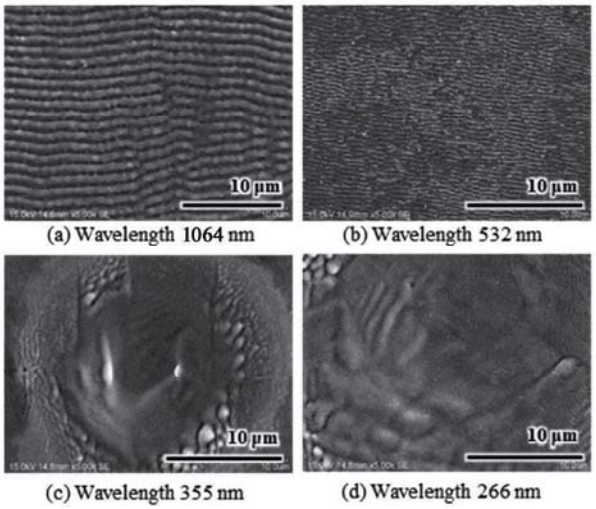

Fig. 15. SEM images of irradiated regions at 223 K.

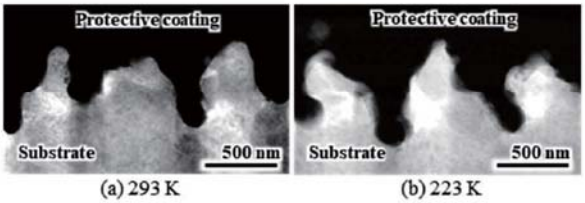

Fig. 16. TEM images of LIPSS at 1064-nm laser wavelength and various temperatures.

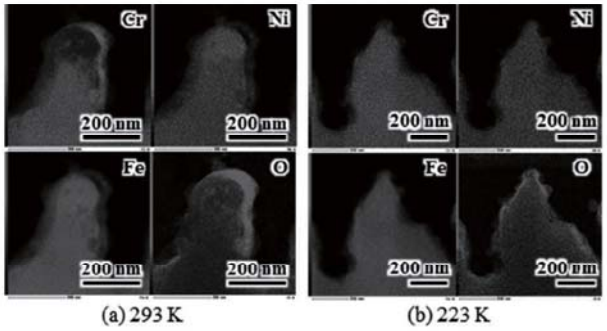

Fig. 17. Element mappings of TEM images LIPSS at 1064-nm laser wavelength and various temperatures.

the growth of an oxide film without changing the other elements such as chromium, nickel, and iron, namely, the short-pulsed laser with 20-ps pulse duration exerted thermal influence for the fabrication of LIPSS, melting and producing roundish LIPSS. In **Fig. 18**, we depict the changes in the pitch length of LIPSS at 223 K. Similar to the case at 293 K, the pitch length of LIPSS at 223 K was approximately 800–1000 and 400 nm with the 1064- and 532-nm-wavelength lasers, respectively, while the LIPSS fabricated at higher temperature had longer pitch length [19, 21], as the change of 50 K was insufficiently small to change the pitch length of LIPSS. In **Fig. 19**,

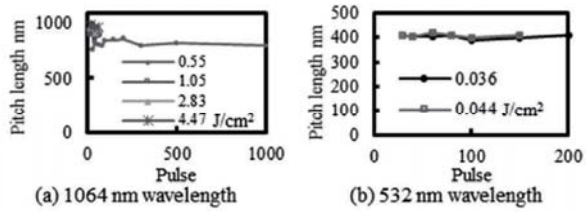

Fig. 18. Pitch length of LIPSS at 223 K.

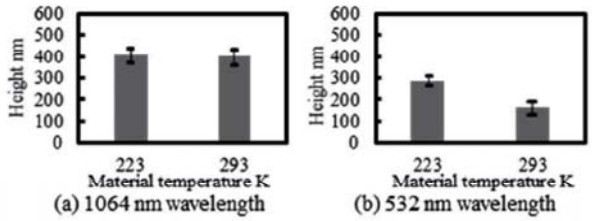

Fig. 19. Height of LIPSS for each material temperature.

we depict the changes in the height of LIPSS for each material temperature. The height of LIPSS at 223 K was greater than that at 293 K, as cooling material easily propagated surface plasmons and increased the ratio of the electric-field intensity at the bottom of groove to that at the top of groove. Accordingly, these results demonstrated the effects of pulse duration close to CRT and heat on the fabrication and geometry of LIPSS using the 20-ps pulsed laser. In addition, the results verified the efficiency of the short-pulsed laser and low-temperature environment to fabricate stably uniform LIPSS with high aspect ratio on the entire irradiated surface at low cost compared with the ultrashort pulsed laser, owing to the prevention of the removal of the convex parts of LIPSS because of low intensity of the 20-ps pulsed laser and to the extension of the CRT and the reduction of thermal effects by cooling material, causing dominant optical behavior.

5. Conclusions

We studied the effects of 20-ps pulse duration and heat on the electric-field-intensity distribution and resultant LIPSS to stably and effectively fabricate LIPSS on the entire irradiated surface. The following are the results of simulations and experiments performed using the 20-ps pulsed laser.

1. The pitch length and the height of the LIPSS fabricated on SUS304 using the short-pulsed laser at 1064-nm wavelength are 700–900 and 350–550 nm, respectively. The aspect ratio of LIPSS is approximately 0.5, which is greater than 0.2–0.4 of LIPSS fabricated using ultrashort-pulsed lasers.

2. The 355- and 266-nm-wavelength lasers could not fabricate LIPSS, as the electric-field intensity was high at both the top and bottom of the groove, following which significant nonperiodic absorption occurred deeper compared with the ultrashort pulsed laser, and, therefore, the entire irradiated surface was removed.

3. Compared with the ultrashort pulsed laser, the short pulsed laser experienced thermal influences, thereby producing roundish LIPSS with thick oxide films. The low-temperature environment suppressed the growth of oxide films and promoted the fabrication of LIPSS with high aspect-ratio because of the resultant extension of CRT, thereby facilitating the propagation of surface plasma waves and increasing the ratio of the electric-field intensity at the bottom of groove to that at the top of groove.

Acknowledgements

The authors would like to express their gratitude to the Kuriyagawa/Mizutani Laboratory at Tohoku University for supporting this research. This study was supported in part by JSPS KAKENHI under Grant Numbers JP17K06074 and JP17KK0126.

References:

[1] S. Mitrovic, D. Adamovic, F. Zivic, D. Dzunic, and M. Pantic, "Friction and wear behavior of shot peened surfaces of 36CrNiMo4 and 36NiCrMo16 alloyed steels under dry and lubricated contact conditions," Applied Surface Science, Vol.290, pp. 223-232, 2014.

[2] E. S. Kim, S. M. Kim, and Y. Z. Lee, "The effect of plateau honing on the friction and wear of cylinder liners," Wear, Vol.400, No.401, pp. 207-212, 2018.

[3] S. Shamsudin, M. Ahmad, A. Aziz, R. Fakhriah, F. Mohamad, N. Ahmad, N. Nafarizal, C. Soon, A. Ameruddin, A. Faridah, M. Shimomura, and K. Murakami, "Hydrophobic rutile phase TiO2nanostructure and its properties for self-cleaning application," AIP Conf. Proc., Vol.1883, 020030, 2017.

[4] Y. Tanaka, "Fabrication of Anti-reflective Structures Using Glass Molding," New Glass, Vol.23, No.4, pp. 32-38, 2008.

[5] J. Lu, M. P. Rao, N. C. MacDonald, D. Khang, and T. J. Webster, "Improved endothelial cell adhesion and proliferation on patterned titanium surfaces with rationally designed, micrometer to nanometer features," Acta Biomaterialia, Vol.4, pp. 192-201, 2008.

[6] K. Nakamura, Y. Nishitani, and T. Kitano, "Frictional properties of plants-derived polyamide against surface microstructures of metal counterpart fabricated by femtosecond laser," AIP Conf. Proc., Vol.1914, 200002, 2017.

[7] D. Chu, K. Yin, X. Dong, Z. Luo, and J. Duan, "Femtosecond laser fabrication of robust underwater superoleophobic and anti-oil surface on sapphire," AIP Advances, Vol.7, 115224, 2017.

[8] A. Y. Vorobyev and C. Guo, "Antireflection effect of femtosecond laserinduced periodic surface structures on silicon," Optics Express, Vol.19, No.5, pp. 1031-1036, 2011.

[9] T. Shinonaga, S. Kinoshita, Y. Okamoto, M. Tsukamoto, and A. Okada, "Formation of Periodic Nanostructures with Femtosecond Laser for Creation of New Functional Biomaterials," Procedia CIRP, Vol.42, pp. 57-61, 2016.

[10] M. Hashida, A. Semerok, O. Gobert, G. Petite, Y. Izawa, and J. Wagner, "Ablation threshold dependence on pulse duration for copper," Applied Surface Science, Vol.197, No.198, pp. 862-867, 2002.

[11] J. Yang, L. Pabst, W. Perrie, O. Allegre, G. Dearden, and S. P. Edwardson, "Advanced Laser Patterning for Security Marking of High Value Metal Components," Procedia Engineering, Vol.183, pp. 363-368, 2017.

[12] R. Harzic, D. Breitling, M. Weikert, S. Sommer, C. Föhl, S. Valette, C. Donnet, E. Audouard, and F. Dausinger, "Pulse width and energy influence on laser micromachining of metals in a range of 100 fs to 5 ps," Applied Surface Science, Vol.249, pp. 322-331, 2005.

[13] S. Kinoshita, T. Shinonaga, Y. Okamoto, and A. Okada, "Study on Shape Variation of Periodic Surface Nanostructures Produced with Ultrashort Pulse Laser for Control of Cell Spreading Direction," Proc. of Int. Conf. on Leading Edge Manufacturing in 21st Century (LEM21), 014, 2017.

[14] K. Mikami, S. Motokoshi, M. Fujita, T. Somekawa, T. Jitsuno, and K. Tanaka, "Temperature Dependences of Laser Induced Plasma Thresholds and Periodic Structures by Nanosecond Infrared Laser for Copper, Iron, and Chrome," Applied Physics Express, Vol.5, No.6, 062701, 2012.
[15] M. Hashida, Y. Ikuta, Y. Miyasaka, S. Tokita, and S. Sakabe, "Simple formula for the interspaces of periodic grating structures self-organized on metal surfaces by femtosecond laser ablation," Applied Physics Letters, Vol.102, 174106, 2013.
[16] T. Shinonaga, M. Tsukamoto, and G. Miyaji, "Periodic nanostructures on titanium dioxide film produced using femtosecond laser with wavelengths of 388 nm and 775 nm," Optics Express, Vol.22, No.12, pp. 14696-14704, 2014.
[17] F. Fraggelakis, G. Mincuzzi, I. Manek-Hönninger, J. Lopez, and R. Kling, "Rainer Generation of micro- and nano-morphologies on a stainless steel surface irradiated with 257 nm femtosecond laser pulses," RSC Advances, Vol.8, No.29, pp. 82-87, 2018.
[18] G. Deng, G. Feng, and S. Zhou, "Experimental and FDTD study of silicon surface morphology induced by femtosecond laser irradiation at a high substrate temperature," Optics Express, Vol.25, No.7, pp. 7818-7827, 2017.
[19] S. Gräf, C. Kunz, S. Engel, T. Derrien, and F. Müller, "Femtosecond Laser-Induced Periodic Surface Structures on Fused Silica: The Impact of the Initial Substrate Temperature," Materials, Vol.11, No.8, 1340, 2018.
[20] Y. Li, Q. Wu, M. Yang, Q. Li, Z. Chen, C. Zhang, J. Sun, J. Yao, and J. Xu, "Uniform deep-subwavelength ripples produced on temperature controlled LiNbO 3: Fe crystal surface via femtosecond laser ablation," Applied Surface Science, Vol.478, pp. 779-783, 2019.
[21] M. Mezera, J. Bonse, and G. Römer, "Influence of Bulk Temperature on Laser-Induced Periodic Surface Structures on Polycarbonate," Polymers, Vol.11, No.12, 1947, 2019.
[22] C. Wang, L. Jiang, F. Wang, X. Li, Y. Yuan, H. Xiao, H. Tsai, and Y. Lu, "First-principles electron dynamics control simulation of diamond under femtosecond laser pulse train irradiation," J. of Physics: Condensed Matter, Vol.24, No.27, 275801, 2012.
[23] M. Lebugle, N. Sanner, O. Utéza, and M. Sentis, "Guidelines for efficient direct ablation of dielectrics with single femtosecond pulses," Applied Physics A: Materials Science and Processing, Vol.114, pp. 129-142, 2014.
[24] S. Maruo, O. Nakamura, and S. Kawata, "Evanescent-wave holography by use of surface-plasmon resonance," Applied Optics, Vol.36, No.11, pp. 2343-2346, 1997.
[25] S. Sakabe, M. Hashida, S. Tokita, S. Namba, and K. Okamuro, "Mechanism for self-formation of periodic grating structures on a metal surface by a femtosecond laser pulse," Physical Review B, Vol.79, No.3, 033409, 2009.
[26] L. Gemini, M. Hashida, Y. Miyasaka, S. Inoue, J. Limpouch, T. Mocek, and S. Sakabe, "Periodic surface structures on titanium self-organized upon double femtosecond pulse exposures," Applied Surface Science, Vol.336, pp. 349-353, 2015.
[27] S. Kodama, S. Suzuki, A. Shibata, K. Shimada, M. Mizutani, and T. Kuriyagawa, "Effect of Crystal Structure on Fabrication of Fine Periodic Surface Structures with Short Pulsed Laser," Int. J. Automation Technol., Vol.12, No.6, pp. 868-875, 2018.
[28] S. Kodama, S. Suzuki, K. Hayashibe, K. Shimada, M. Mizutani, and T. Kuriyagawa, "Control of Short-Pulsed Laser Induced Periodic Surface Structures with Machining – Picosecond Laser Micro/Nanotexturing with Ultraprecision Cutting –," Precision Engineering, Vol.55, pp. 433-438, 2019.
[29] G. Miyaji and K. Miyazaki, "Ultrafast Dynamic Processes for Periodic Surface Nanostructure Formation lnduced with Femtosecond Laser Pulses," Laser Original, Vol.41, No.10, pp. 816-820, 2013.
[30] K. S. Yee, "Numerical solution of initial boundary value problems involving maxwell's equations in isotropic media," IEEE Trans. Antenna Propagation, Vol.14, No.3, pp. 302-307, 1966.
[31] O. Hashimoto, "Finite Difference Time Domain Method," Morikita Publishing, 2006.
[32] L. Qi, K. Nishii, and Y. Namba, "Regular subwavelength surface structures induced by femtosecond laser pulses on stainless steel," Opt. Lett., Vol.34, No.12, pp. 6-8, 2009.
[33] K. Kawahara and H. Sawada, "Coverage ratio increase of fluorine coatings on stainless steel by ultrashort pulse laser irradiation," JSPE Autumn Meeting, pp. 237-238, 2016.
[34] M. Martínez-Calderon, A. Rodríguez, A. Dias-Pontea, M. C. Morant-Minana, M. Gómez-Aranzadi, and S. M. Olaizola, "Femtosecond laser fabrication of highly hydrophobic stainless steel surface with hierarchical structures fabricated by combining ordered microstructures and LIPSS," Applied Surface Science, Vol.374, pp. 81-89, 2016.
[35] M. Martínez-Calderon, M. Manso-Silván, A. Rodríguez, M. Gómez-Aranzadi, J. P. García-Ruiz, S. M. Olaizola, and R. J. Martín-Palma, "Surface micro- and nano-texturing of stainless steel by femtosecond laser for the control of cell migration," Scientific Reports, Vol.6, No.1, 36296, 2016.

Name:
Shuhei Kodama

Affiliation:
Assistant Professor, Department of Mechanical Systems Engineering, Graduate School of Engineering, Tokyo University of Agriculture and Technology

Address:
6-311, 2-24-16 Nakacho, Koganei, Tokyo 184-0012, Japan

Name:
Keita Shimada

Affiliation:
Assistant Professor, Department of Mechanical Systems Engineering, Graduate School of Engineering, Tohoku University

Address:
6-6-01 Aramaki Aza-Aoba, Aoba-ku, Sendai, Miyagi 980-8579, Japan

Name:
Masayoshi Mizutani

Affiliation:
Associate Professor, Department of Mechanical Systems Engineering, Graduate School of Engineering, Tohoku University

Address:
6-6-01 Aramaki Aza-Aoba, Aoba-ku, Sendai, Miyagi 980-8579, Japan

Name:
Tsunemoto Kuriyagawa

Affiliation:
Professor, Bio-Medical Interface Fabrication Laboratory, Graduate School of Biomedical Engineering, Tohoku University

Address:
6-6-01 Aramaki Aza-Aoba, Aoba-ku, Sendai, Miyagi 980-8579, Japan

Journal of Manufacturing Processes 60 (2020) 644–653

Contents lists available at ScienceDirect

Journal of Manufacturing Processes

journal homepage: www.elsevier.com/locate/manpro

Surface defect inhibition mechanisms of laser assisted microcutting on Ni-P amorphous alloy

Pei Qiu [a], Shohei Teraoka [b], Qingrui Gong [a], Shaolin Xu [a,*], Keita Shimada [b], Masayoshi Mizutani [b], Tsunemoto Kuriyagawa [b]

[a] Department of Mechanical and Energy Engineering, Southern University of Science and Technology, Shenzhen, China
[b] Department of Mechanical Systems Engineering, Graduate School of Engineering, Tohoku University, Sendai, Japan

ARTICLE INFO

Keywords:
Microstructures
Laser assisted microcutting
Amorphous alloy
Surface defect

ABSTRACT

Laser-assisted microcutting (LAMC) is a feasible technique for precision machining of amorphous alloys. However, due to the significant difference in deformation characteristics between amorphous and crystalline alloys, the research on LAMC of crystalline alloys cannot be directly used to explain the phenomenon of amorphous alloys. This paper studies the surface defect generation process in ultraprecision machining of Ni-P amorphous alloy by stepped microcutting. It is found that LAMC can greatly reduce the accumulation of elastic potential energy and the deformation zone, thus suppressing the generation of in-plane chipping and edge chipping. LAMC experiments of Ni-P amorphous alloy with different laser irradiation power show that the laser assisted temperature should be controlled around T_g.

Introduction

Molding method is a key manufacturing technology for fabricating microstructures on glass and polymer surfaces. To improve molds' life time and optical components' form accuracy, high strength and hardness are essential for the mold materials. Electroless nickel phosphorus (Ni-P) plating with an amorphous structure is one of the most commonly used mold materials. The amorphous structure imparts unique mechanical, chemical, and physical properties to the amorphous alloy, such as high strength, hardness, elastic limit, and wear/corrosion resistance [1]. Structured Ni-P molds have been widely utilized for manufacturing of microstructured optical products including light guide plates and microlens arrays. In the processing of Ni-P mold, diamond cutting is widely used due to its high flexibility and high productivity [2]. However, in ultra-precision cutting of microstructures on a Ni-P plating layer, chippings and burrs are generally formed simultaneously at the surfaces of microstructures, which always deteriorate the form accuracy. Fig. 1 demonstrates an example of the surface defects in ultra-precision microcutting of microstructures on Ni-P plating layer.

Unfortunately, due to the special deformation characteristics of amorphous alloys, these obvious defects shown in Fig. 1 are hard to avoid in conventional mechanical microcutting, especially the chippings that are rarely found in machining of typical crystal metals, such as aluminum alloys, stainless steel and copper. Due to periodic arrangement of atoms and their long-range translation order, the plastic deformation of crystalline metals can be carried out by the slip of dislocations at lower energy or stress states [3]. However, the flow of atoms in amorphous alloys under external force is collective movement in nano-scale space [4]. The basic unit of plastic deformation of an amorphous alloy is a partial rearrangement of atomic groups capable of carrying shear deformation [5]. Therefore, amorphous alloys lack plastic deformation capacity at room temperature compared with ordinary crystalline metals. To reduce defects, the deformation characteristics of amorphous alloys need to be controlled.

Previously, laser irradiation was proved to be a good way to adjust the mechanical properties of amorphous alloys due to its temperature sensibility. In particular, residual stress induced by laser irradiation is beneficial for improving the bending plasticity of BMG [6]. Also, by comparing the depth curve fluctuation in indentation experiment of Zr-based amorphous alloy before and after laser irradiation, it is found that nanosecond pulsed laser irradiation can soften the irradiated regions and improve the plasticity of the material [7]. Therefore, some researchers tried to control the deformation characteristics of amorphous alloys and improve its microcutting quality by laser-assisted micromachining. For example, Xu et al. firstly demonstrated that laser-assisted microcutting (LAMC) can effectively inhibit surface

* Corresponding author.
E-mail address: xusl@sustech.edu.cn (S. Xu).

https://doi.org/10.1016/j.jmapro.2020.11.005
Received 4 September 2019; Received in revised form 29 October 2020; Accepted 2 November 2020
Available online 13 November 2020

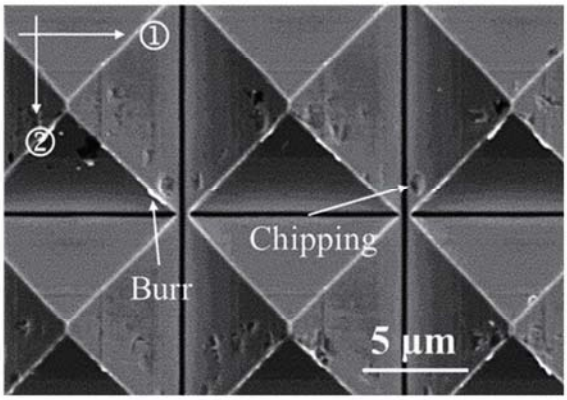

Fig. 1. SEM images of the defect examples on micropyramid fabricated by microcutting; the numbers and the arrows show the cutting orders and directions, respectively.

chippings when machining Ni-P amorphous alloy [8]. To improve thermal efficiency, Park et al. proposed a direct laser assisted machining (DLAM) technique. In the processing with DLAM, the Zr-BMG workpiece is irradiated by a laser directly passing through the sapphire cutting tool [9]. In this way, the workpiece machinability is improved by decreasing the cutting force. Meanwhile, a better surface finish is obtained.

However, in the previous studies, the surface defects generation mechanism in microcutting and the mechanism of using laser irradiation to reduce surface defects are not clarified. This limits the performance of LAMC of amorphous alloys in practical applications. Therefore, by considering the unique deformation mechanisms of amorphous alloys with shear deformation theory [10] and elastic potential energy theory [11], the present research studied the surface defect generation process in ultra-precision cutting of amorphous alloys and the effect of LAMC on surface defect inhibition.

Experimental design

A Ni-P layer with amorphous structure coated on a stainless-steel substrate (JIS SUS 304) by an electroless plating method was selected as workpieces. Diamond planing with a 1-mm-radius round nose

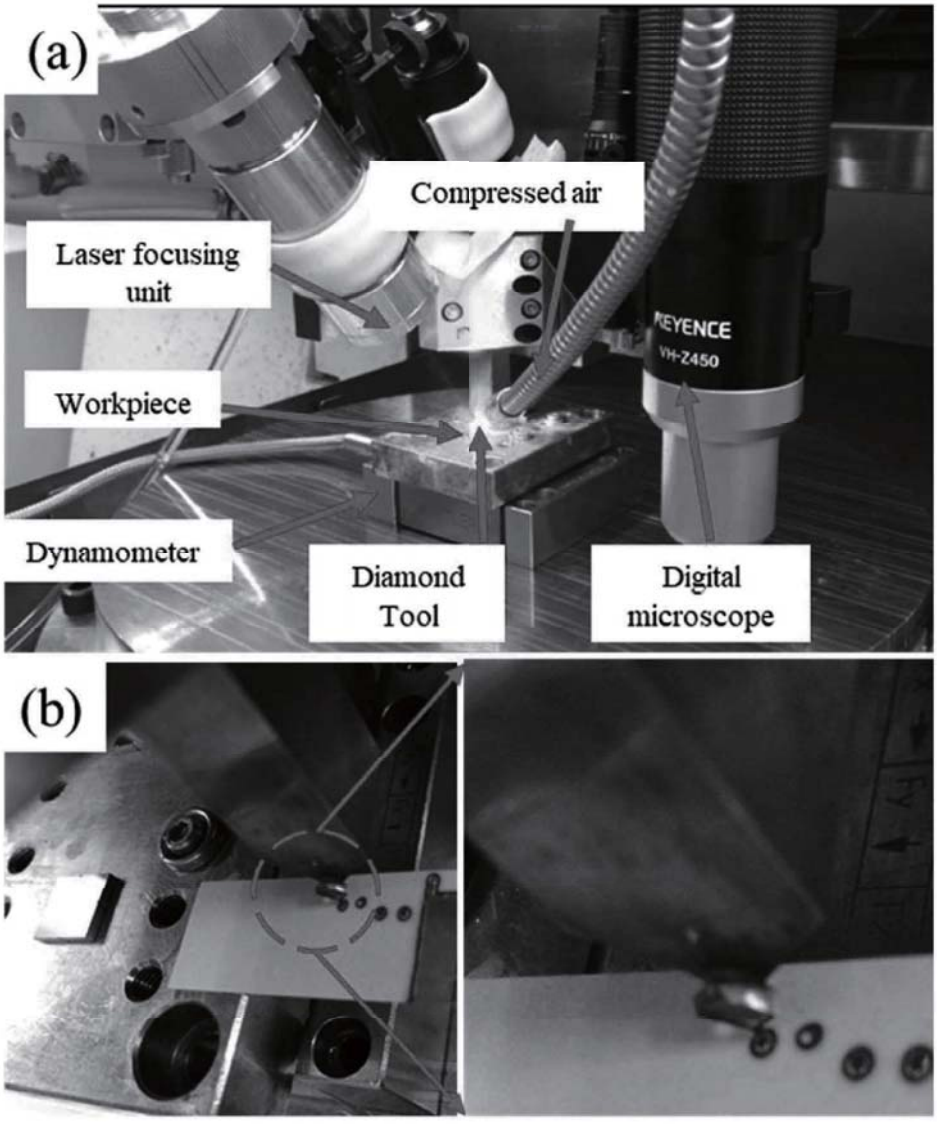

Fig. 2. (a) Overview of the laser assisted microcutting equipment and (b) a top view of laser focusing position.

Table 1
Conditions of laser irradiation.

Parameters	Values		
Laser average power (P)	1.2 W	2.0 W	3.4 W
Pulse width (τ)	75 ns	60 ns	45 ns
Repetition rate (f)	60 kHz	40 kHz	20 kHz
Wavelength	532 nm		
Spot diameter w_x, w_y	520 μm, 500 μm		
Irradiation angle	40°		

Table 2
Cutting conditions of LAMC experiments.

Workpiece	Ni-P plating (P- 10 % (w/w))
Thickness of Ni-P plating	150 μm
Environmental condition	Dry cutting
Cutting speed	1000 mm/min
Ambient Temperature	23 °C
Rake angle	0°
Relief angle	8°

diamond tool was pre-performed to flatten the Ni-P plated surface before machining microstructures. As shown in Fig. 2, the LAMC equipment is composed of an ultra-precision machine (Nagase Integrex Corporation,

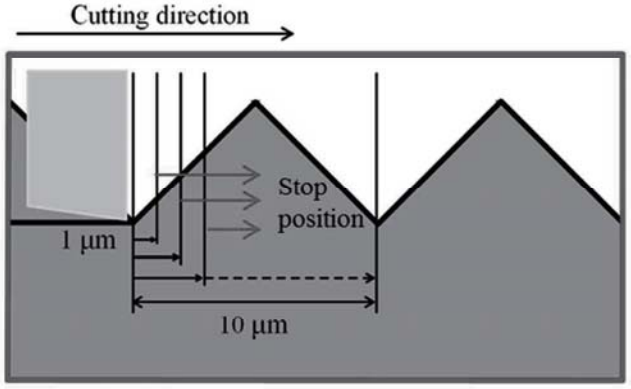

Fig. 3. Schematic of stepped microcutting.

MIC-300) and a laser irradiation system (Precitec Corporation, Navigator J40-X30SC). A digital microscope as shown in Fig. 2**(a)** was used to observe the spot position in real time. Additionally, the laser ablation trace on the surface of a thin plastic film as shown in Fig. 2**(b)** was used to double check the real laser spot position. The laser spot was set to be tangent to tool rake face in the experiments. Therefore, the distance between laser beam and tool rake face is the half diameter of laser spot

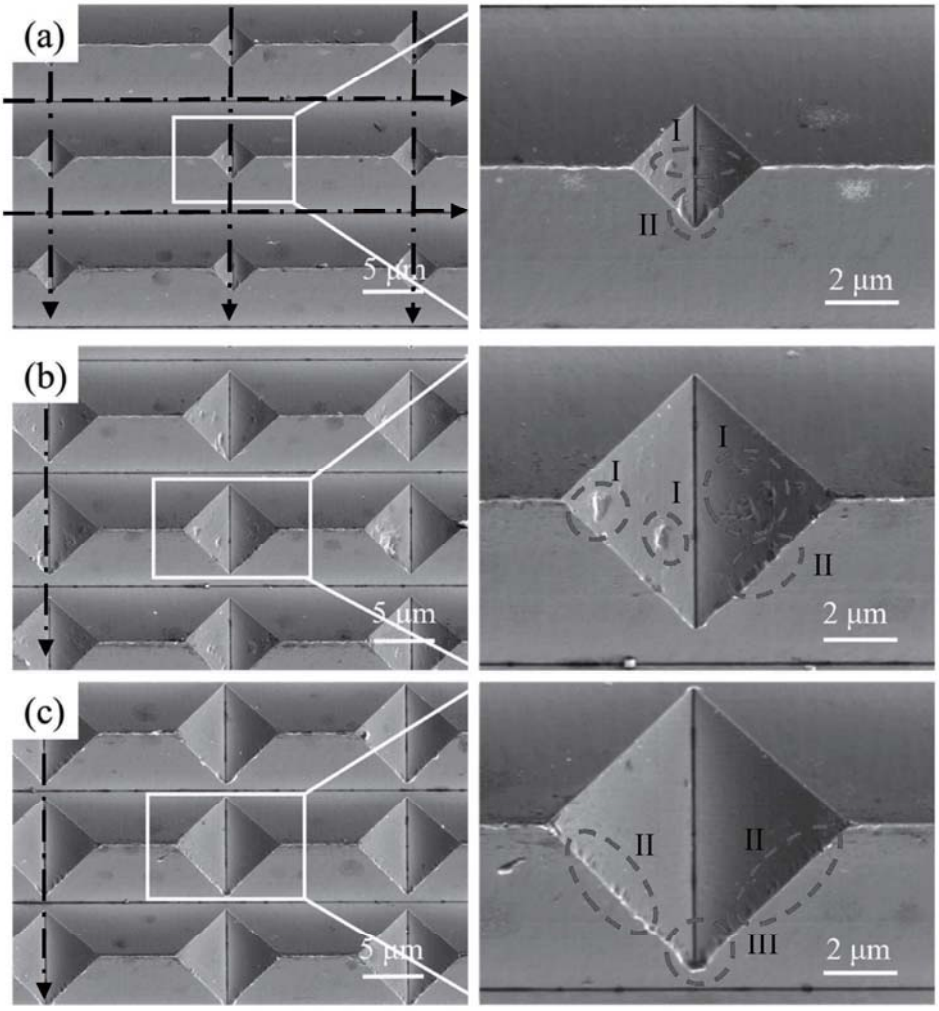

Fig. 4. Microgrooves machined without laser assistance (a) the first cut (the cutting depth $d = 2.4$ μm); (b) the second cut ($d = 2.3$ μm); (c) the third cut ($d = 0.3$ μm). Defects are marked in the red circle (For interpretation of the references to colour in this figure legend, the reader is referred to the web version of this article).

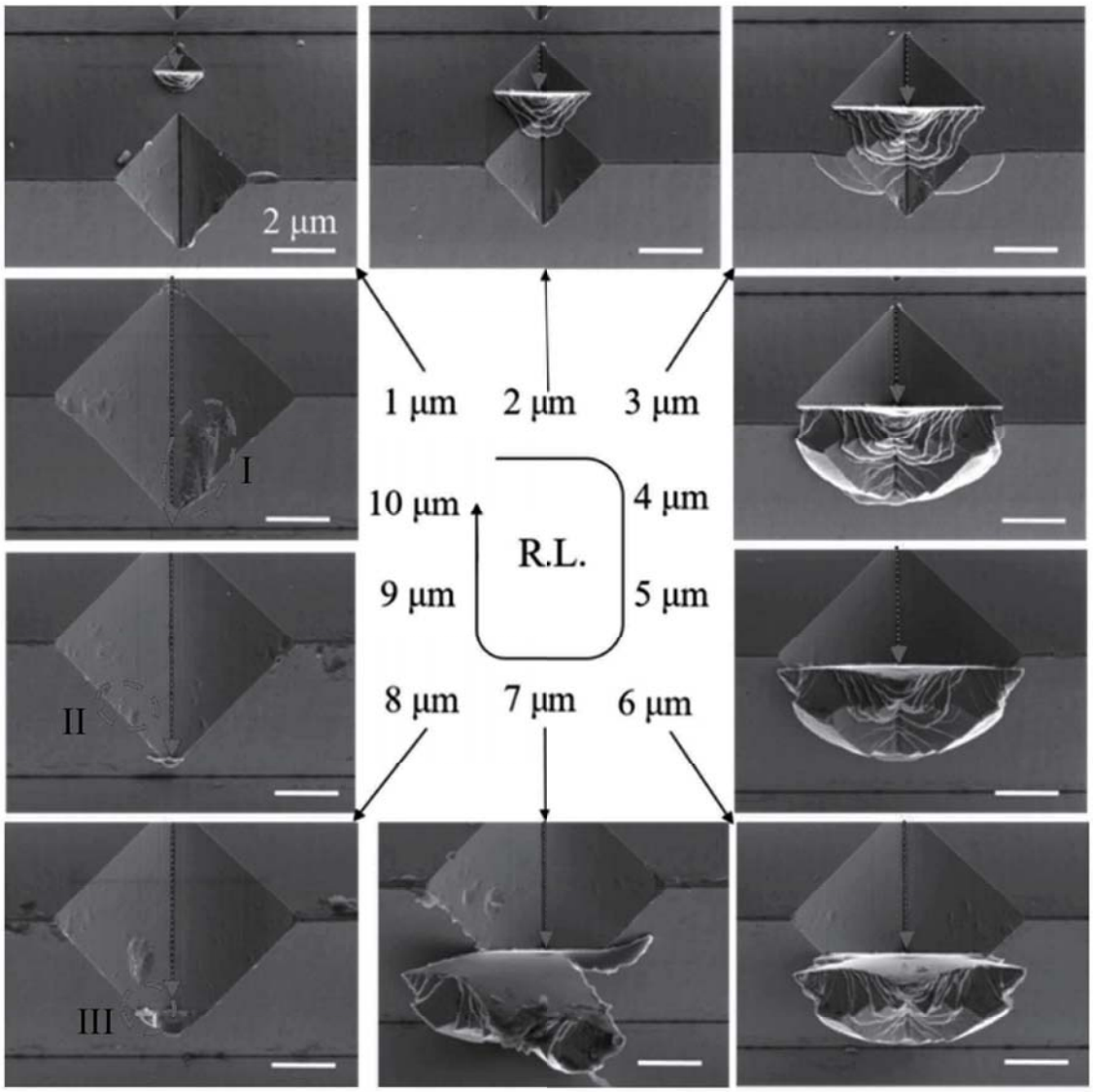

Fig. 5. SEM images of stepped microcutting at the second cut of orthogonal microgrooves without laser irradiation (R.L. is relative cutting length). The scale bar in the first one is applied to all these images.

(around 260 μm). The ultra-precision machine enables its table to move under five-axis (XYZBC) numerical control at a step resolution of 1 nm at XYZ axes. The laser beam can be well focused to the position in front of the diamond cutting edge by a laser focusing unit composed of a collimating lens and a collecting lens. Laser parameters are presented in Table 1.

The micropyramid cutting experiments were conducted as follows: first a microgroove array was fabricated, then microgrooves orthogonal to the microgroove array were carved. The orthogonal microcutting conditions are listed in Table 2. A repeated cutting process is adopted to study the material removal mechanisms: first microgrooves were fabricated with 2.4 μm at depths, the second cut were added to the first microgrooves at 2.3 μm depth, the third cut were added to the second microgrooves at 0.3 μm (total depth of cut = 2.4 μm + 2.3 μm + 0.3 μm = 5.0 μm). Orthogonal crossed microgrooves were fabricated to observe the occurrence of the defects at the edges of micropyramids.

To further observe the propagation of surface defects at tool exit regions, stepped microcutting was carried out as schematically shown in Fig. 3. It disperses the continuous cutting process into one micrometer feed at one time, which is helpful to observe the deformation of materials in the process of microcutting. The deformation of amorphous alloys is usually related to the potential energy accumulation, so the stepped microcutting experiment is also helpful to analysis the potential energy accumulation process in the microcutting. Hence, this method is conducted on both conventional and laser-assisted microcutting.

The machined surfaces were observed with a field emission scanning electron microscope (SM-71010, JEOL Corporation) and a scanning electron microscope (SU1510, Hitachi). A three-axis dynamometer (MiniDyn 9256a2, Kistler) was mounted under the workpiece to measure the cutting force.

Results and discussion

Conventional microcutting

Fig. 4 shows SEM images of microgrooves fabricated by conventional microcutting (CMC). There are three kinds of defects on the micropyramid, i.e. in-plane chipping (I), edge chipping (II) and burrs (III). As shown in Fig. 4, the first cutting mainly produces type I and type II defects, and the second cutting produces three types of defects with the

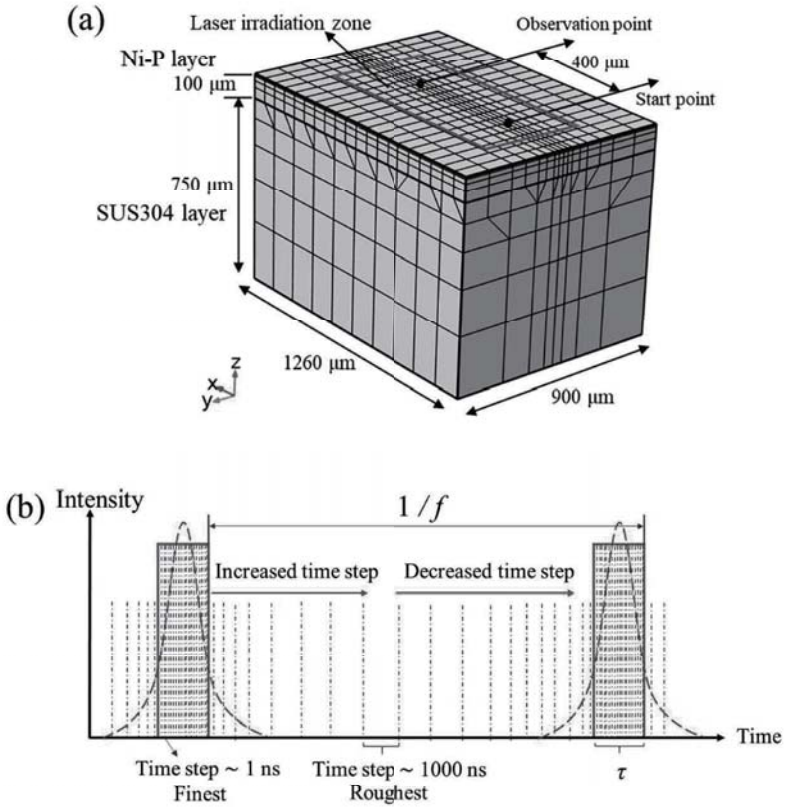

Fig. 6. (a) 3D simulation model of laser irradiation (b) schematic diagram of time step division.

largest number and volume. After the third cutting, type II and type III defects are the main defects. Therefore, it can be judged that the type I defect has a great relationship with the cutting depth. The material removal mode of the third cutting changes from unstable plastic removal to stable plastic removal showing a better plastic deformation ability, and thus the in-plane chipping was greatly reduced. This deformation process is similar to that of hard and brittle materials, which have a brittle-ductile transition depth.

Furthermore, it can be concluded from Fig. 4 that as the cutting volume increases, the number of defects increases. To deeply investigate the defect generation mechanisms of amorphous alloy in microcutting process, stepped microcutting was carried out in the above mentioned second cut process. Fig. 5 shows surface morphology of the stepped microcutting as the relative cutting length (R.L.) increasing from 1 to 10 μm. The whole cutting process can be generally divided into three stages by the plastic deformation characteristics of amorphous Ni-P layer:

Stage 1: The accumulation and the propagation of shear bands as shown in Fig. 5 when R.L. changes from 1 to 4 μm.

At the initial stage, the material deformation is caused by extrusion. This initial deformation is relatively small. However, a large deformation begins to occur at the exit when R.L. is 3 μm.

It has been proposed that the shear deformation process of amorphous alloys mainly involves elastic-plastic shearing process [12]. With the feed of tool, the material in front of tool is subjected to shear stress. The accumulated elastic potential energy is mainly dissipated by the generation and propagation of single shear band caused by the extension of the shear deformation zone under shear stress. Hence, the shear band needs to propagate over a long distance to dissipate the rapidly increasing energy. The large amount of deformation as shown in Fig. 5 (R.L. = 3–4 μm) indicates that lots of elastic potential energy have been released rapidly. Meanwhile, the shear transformation zone along the direction of the maximum principal stress has been activated.

As the shear band expansion, its stability decreases gradually with the increase of the propagation distance. Some shear bands may propagate underneath the processing path and produce micro-voids [13,14]. When the tool moves to the position of micro-voids, the shear band is easier to deflect. Meanwhile, more shear bands are generated to consume energy in the shear band quickly [15]. At this time, shear fracture will occur in the material, resulting in in-plane chipping.

Stage 2: The shear fracture as shown in Fig. 5 (R.L. = 5–7 μm).

The unstable propagation of the shear band at the exit of the cutting path may cause chipping at the exit. In addition, it can be seen from Fig. 5 (R.L. = 5–7 μm) that when the tool approaches the edge, the bending of the chip will lead chips to bear tensile stress. The existence of tensile stress will weaken the plastic deformation ability of the undeformed part, and the shear deformation process will be more inclined to brittle shear fracture, which will lead to the edge chipping.

Stage3: The chip sheared off as shown in Fig. 5 (R.L. = 8–10 μm).

Chipping and burrs are formed at the edges of groove when the chip sheared off at the end. These small defects may be removed by finishing cuts if the chipping is small as shown in Fig. 4(c), but the large chipping as shown in Fig. 5 (R.L. = 10 μm) is difficult to be removed and also impossible to be repaired. Therefore, new techniques should be

Table 3
The variables used in simulation.

Variables	Implications	Values	Ref.
ρ	Material density g/(cm^3)	Ni-P: 7.9; SUS304: 8.03	[8]
C_p	Specific heat capacity J/(g K)	Ni-P: 0.48; SUS304: 0.502	[8]
k	Thermal conductivity W/(m K)	Ni-P: 5.02; SUS304: 15.0	[8]
ε	Absorptivity of the surface	0.536	
w_x, w_y	Laser beam diameter (μm)	500, 520	
v	Scan velocity (m/s)	1/60	
α	Absorption coefficient (1/m)	6.37×10^7	
T	Temperature	–	
t	Time (s)	–	
Q_{in}	Laser beam power density (W/m^2)	–	

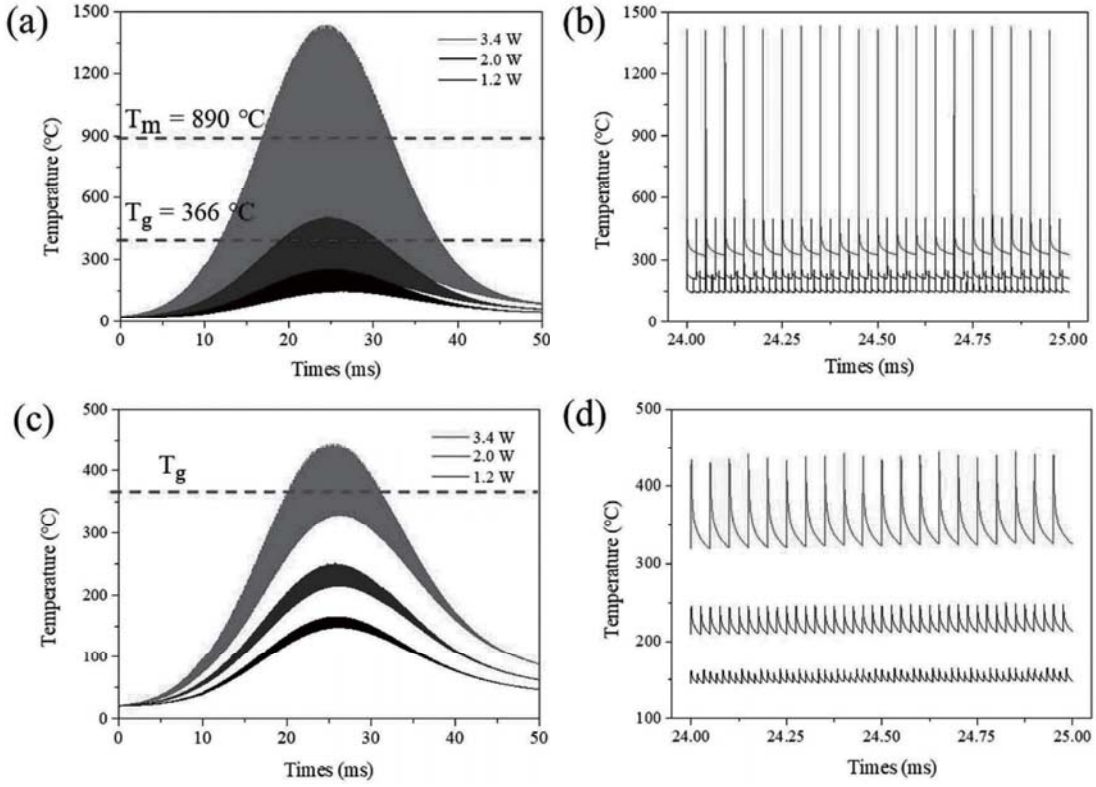

Fig. 7. Temporal change in temperature under each average laser power (a)(b) the top surface (c)(d) 1 μm under the top surface.

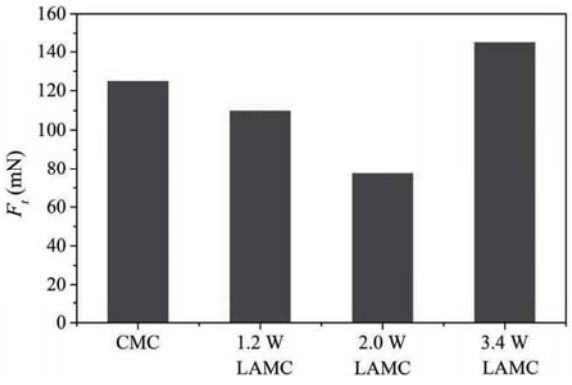

Fig. 8. Transverse force of parallel microgrooving in CMC and LAMC (d = 5 μm).

proposed to suppress these defects in the microgrooves cutting processes.

Overall, the main reason for the defects generation in the cutting process is that the excessive accumulation of elastic potential energy leads to the instability of the cutting process. The extension of shear band provides a preliminary impetus for the generation of defects. Based on the causes of defects, the mechanism of laser suppressing defects is explored below.

Laser assisted microcutting

Laser-assisted microcutting was carried out to attempt to inhibit surface defects in microcutting. In this section, we firstly used the commercial software COMSOL Multiphysics® to simulate the temperature distribution under laser irradiation at different powers to determine the operating temperature of LAMC, and then compared the results of LAMC at different laser powers to study the effect of laser irradiation on the processing performance.

Simulation of the temperature distribution

As shown in Fig. 4, the thermal simulation under laser irradiation with a model based on a grooved surface would be more accurate. However, if the grooved structure is used, it is necessary to refine the grid to make the element length less than the edge radius of groove. This will largely prolong the calculation time and also involve the heat transfer at nanoscale. Therefore, in our study we used the simulation on a flat surface to predict the temperature distribution under laser irradiation with different powers, and the reliability of simulation was further judged by comparing the simulation results and experimental results at melting point by referring to the method proposed in reference [16]. A 3D cuboid simulation domain with a flat surface as shown in Fig. 6**(a)** is established. The laser beam sweeps from the start point to the observation point, and for the sake of the accurate calculation of temperature, the meshes are refined in the laser irradiation zone. In order to shorten the simulation time and ensure the calculation accuracy, the time step of the simulation process is correlated with the pulse width. As shown in Fig. 6**(b)**, the closer to the pulse, the smaller the time step. The minimum time step in pulse duration is 1 ns, while the maximum time step in interval time is 1000 ns. The simulation parameters were set as the same as the experimental conditions. The corresponding variables, their implications, and their initial values used in simulation are shown in Table 3.

Laser irradiation is considered as a heat flux imposed on the top surface of Ni-P, and convective heat transfer occurs on the top surface, while the bottom and lateral surface are set to the thermal insulation boundary. The governing equations utilized to determine the temperature distribution by pulse laser irradiation are as follows:

$$g(t) = \begin{cases} 1, & 0 \le t - T \times [t/T] \le \tau \\ 0, & Others \end{cases} \quad (1)$$

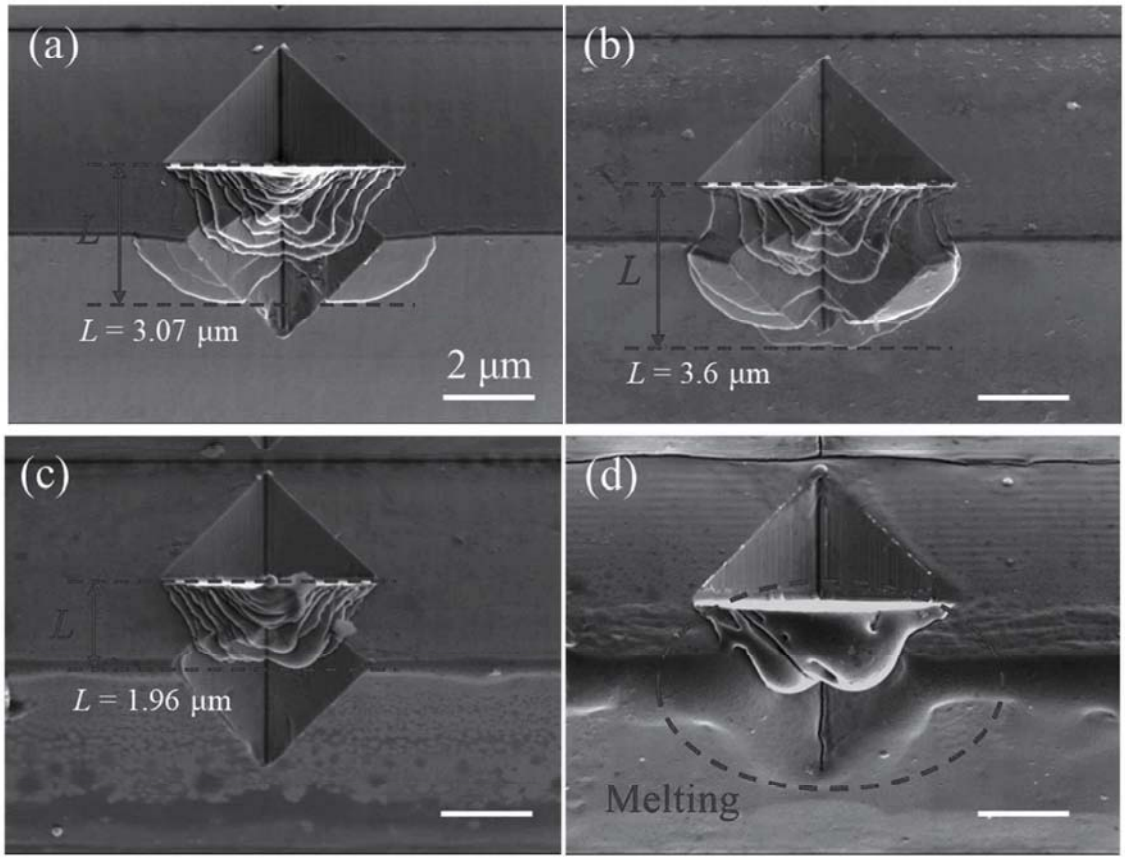

Fig. 9. Morphology of stepped microgrooves cutting experiments: (a) CMC; (b) LAMC with $P = 1.2$ W ($< T_g$); (c) LAMC with $P = 2.0$ W (around T_g); (d) LAMC with $P = 3.4$ W (around T_m).

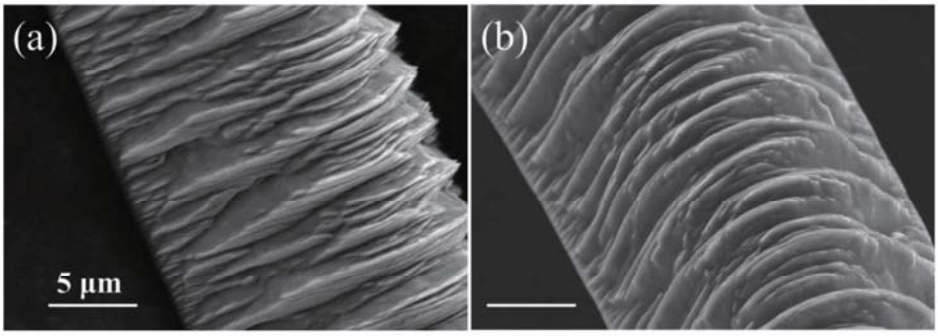

Fig. 10. Morphology of chips generated by (a) CMC (b) LAMC.

$$Q_{in} = \frac{8\varepsilon}{\pi w_x w_y}\frac{P\tau}{f}g(t)\exp\left\{-8\left[\left(\frac{x-vt}{w_x^2}\right)^2+\left(\frac{y}{w_y^2}\right)^2\right]\right\}\exp(-\alpha z) \quad (2)$$

$$\rho C_p\frac{\partial T}{\partial t} = k\left(\frac{\partial^2 T}{\partial x^2}+\frac{\partial^2 T}{\partial y^2}+\frac{\partial^2 T}{\partial z^2}\right)+Q_{in} \quad (3)$$

where x, y and z are the coordinates of the simulation domain.

Fig. 7 shows the temperature distribution of the monitored point of workpiece under three different laser power. The maximum temperature ranges from 150 ℃ to 1500 ℃, covering the glass transition temperature T_g (366 ℃) and the melting temperature T_m (890 ℃) of Ni-P amorphous alloy. Basically, when $P = 2.0$ W, the temperature of laser irradiation is around T_g, and when $P = 3.4$ W, the temperature of laser irradiation is around T_m. Therefore, the influence of laser power on the micromaching of Ni-P can be investigated well.

Experiment results of laser assisted microcutting

Firstly, transverse force (F_t) of parallel microgrooving in different conditions was investigated. As shown in Fig. 8, F_t decreased by 12 % and 38 % for LAMC with laser power of 1.2 and 2.0 W compared to that of CMC attributing to the thermal softening of Ni-P amorphous alloy under laser irradiation. However, F_t increased largely when the laser power was set to be 3.4 W. Fig. 7**(a)** shows that the temperature of workpiece exceeds the glass transition temperature under this condition. Thus the molten amorphous alloy is in a supercooled liquid region, which leads to a large viscous resistance against tool feed [17]. The experimental results indicate that LAMC with an appropriate laser condition can reduce the deformation activation energy of amorphous

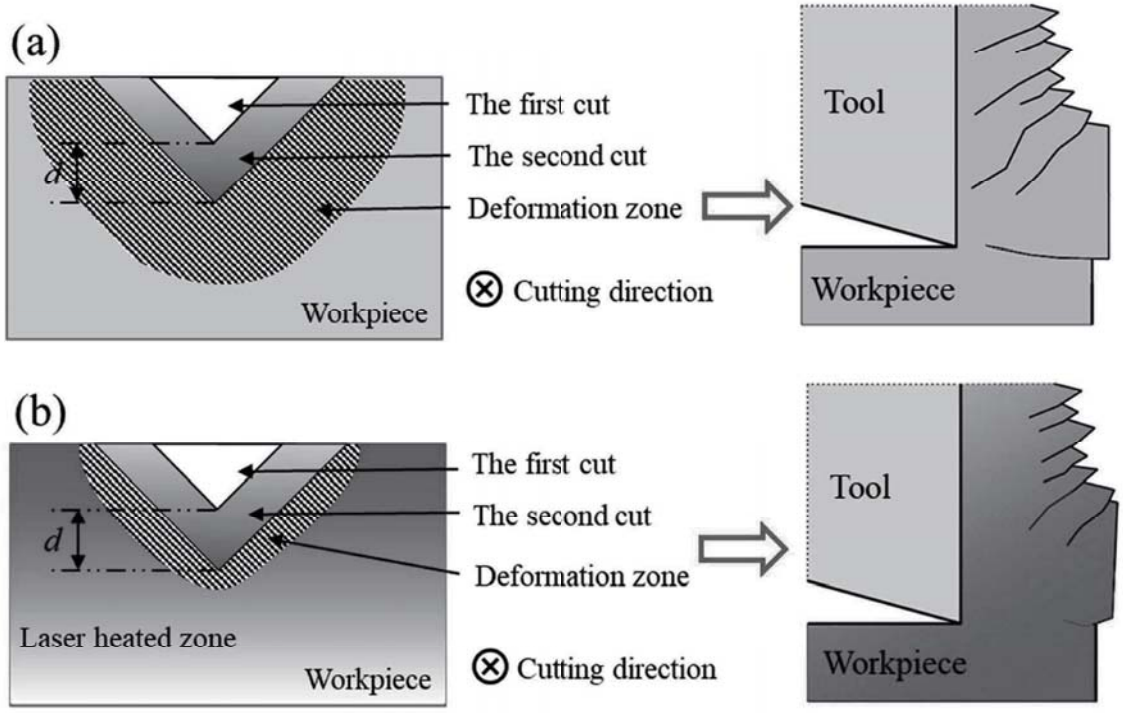

Fig. 11. Schematic of chipping generation process in (a) CMC (b) LAMC.

alloy and make it prone to plastic deformation.

Fig. 5 indicates that the shear band expands rapidly at R.L. = 3 μm, so the effect of different laser powers on the deformation region is studied at this condition. Fig. 9 shows the SEM images of stepped microcutting under different laser irradiation conditions listed in Table 1. The effect of laser-assisted microcutting on material deformation is mainly shown in three aspects: (1) The size of the deformation zone in the tool feeding direction, or the propagation distance of the shear band (L) at $P = 1.2$ W ($< T_g$) is basically the same as that in CMC; (2) L significantly reduces and the shear band density (number of shear bands per unit length) increases during LAMC at $P = 2.0$ W (around T_g); (3) The groove edges melted in LAMC with $P = 3.4$ W (around T_m), which is also consistent with the simulation results shown in Fig. 7.

These phenomena reflect the deformation characteristics of amorphous alloys during cutting, and the influence of laser power on surface quality.

Firstly, at $P = 1.2$ W ($< T_g$), laser irradiation has little effect on the deformation characteristics of amorphous alloys, so it also has little effect on reducing defects.

Secondly, at $P = 3.4$ W (around T_m), the temperature of laser irradiation is too high to melt the amorphous alloys, and the shape of the materials can be changed directly.

Finally, at $P = 2.0$ W (around T_g), the increase of shear band density reflects the increase of plasticity of amorphous alloys. The plasticity of amorphous alloys can be improved when the deformation is no longer confined to a few shear bands. In this way, the volume fraction of amorphous phase involved in plastic deformation increases and dissipates more elastic energy, which leads to better plasticity [18]. And a Zr-based amorphous alloy with super-large compressive plasticity caused by high density shear band at room temperature has been reported [19]. Therefore, it can be considered that the intensive shear band in Fig. 9**(c)** is a performance of good plasticity.

On the other hand, at $P = 2.0$ W (T_g), the shear band propagation is steady, which has close relationship with the reduction of chippings, and this can be reflected by the morphology of chips. Fig. 10 shows a comparison of chip morphology produced by CMC and laser-assisted microcutting. It can be seen that serrated profile of the chips becomes smoother under laser irradiation. Fig. 11 is a schematic comparison of chipping generation process in the cutting of Ni-P amorphous alloy without and with laser irradiation. Under the same cutting depth, the deformation zone of workpiece is smaller with higher temperature of workpiece. Therefore, as shown in Fig. 11, large chipping will appear when the deformation zone is bigger than the cutting depth in CMC process. In LAMC experiments, the plastic deformation will be concentrated in smaller area, thus inhibiting the chipping phenomenon.

In summary, at $P = 2.0$ W (around T_g), the shear band expands steadily and the heat affected zone is small, so that the defects can be reduced, the shape accuracy can be also maintained, and the machining quality can be well improved.

Finally, Fig. 12 shows the morphology of micropyramid machined by CMC and LAMC of different laser powers. In Fig. 12**(a) (b)**, the chipping at the exit edge exceeds 1 μm. Burrs appear in almost every tool exit of Fig. 12**(a)**, while burrs in the exit of Fig. 12**(b)** decrease. When $P = 2.0$ W and 3.4 W, the chipping almost disappears at the surface of microgrooves. However, the sharpness of the edges and vertices of the microarray decreases when $P = 3.4$ W, which is the result of thermal distortion. It can be concluded that the propagation process of shear zones is directly related to the surface defect generation. LAMC can significantly improve plastic deformation ability of amorphous alloys under an appropriate temperature, and thus help to inhibit the surface defects.

However, LAMC has also created a new problem. The thermal effect of laser melted the edge burrs, resulting in small recasting dots as shown in Fig. 11**(b)**, which need to be further studied by optimizing laser irradiation conditions or removed by post-processing.

Conclusions

In this study, laser assisted microcutting was proposed to reduce defects at the surface of microstructures in ultraprecision cutting of Ni-P amorphous alloy. The defect inhibition mechanisms are studied by stepped microcutting experiments. Main conclusions drawn from the

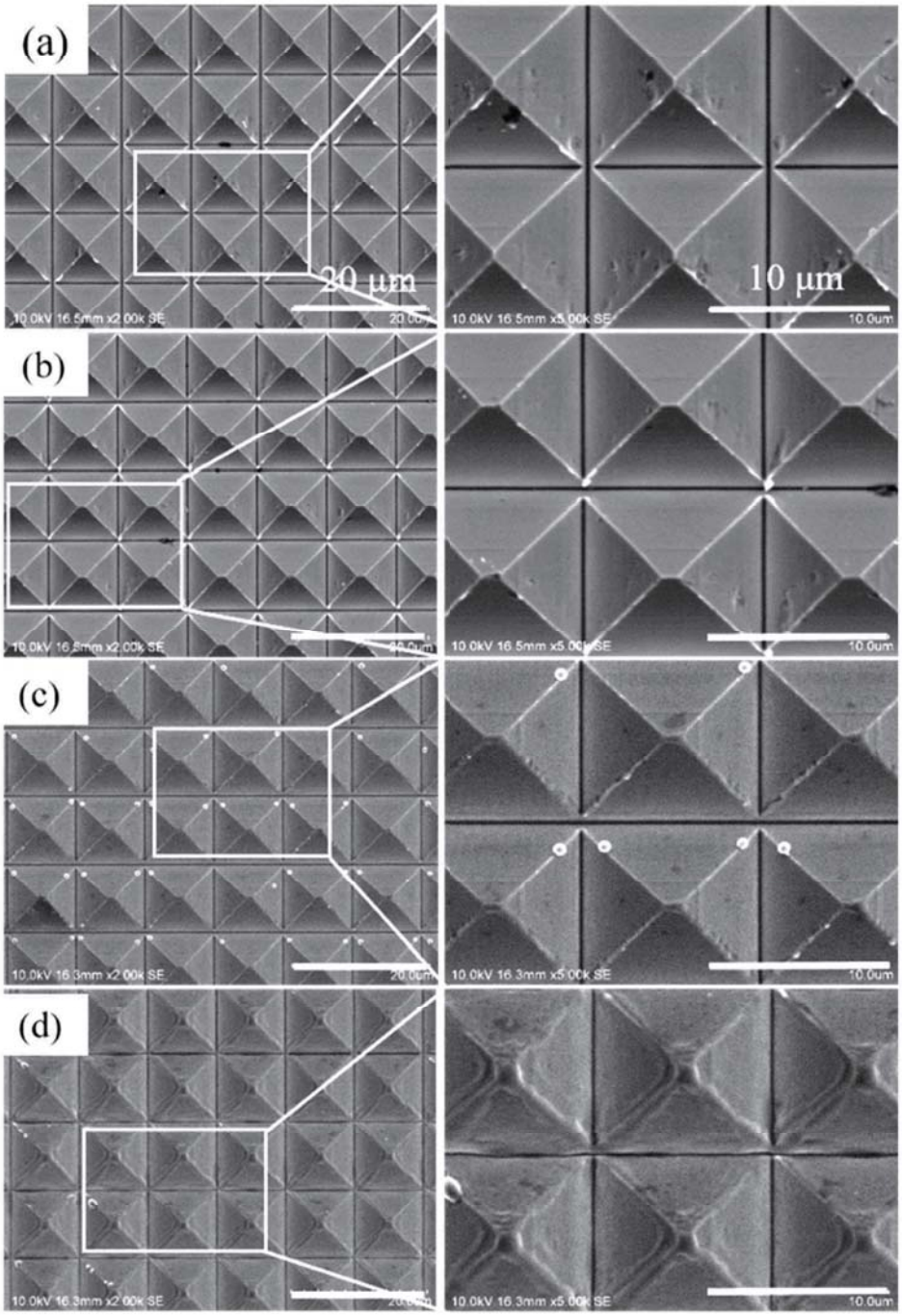

Fig. 12. Results of the micropyramid experiments: (a) CMC; (b) LAMC with P = 1.2 W; (c) LAMC with P = 2.0 W; (d) LAMC with P = 3.4 W.

present study can be summarized as follows:

(1) In-plane chipping has a great relationship with the cutting depth. The smaller the undeformed chip thickness, the fewer in-plane defects.
(2) Excessive accumulation of elastic potential energy makes the cutting process unstable, resulting in the expansion of the shear band and the formation of in-plane chipping.
(3) The increase of temperature will lead to the decrease of the processing stress, thus reducing the accumulation of elastic potential energy. LAMC under the appropriate temperature can significantly reduce the in-plane chipping and edge chipping produced in the Ni-P microcutting.
(4) Since the thermal deformation of the amorphous alloy Ni-P is irreversible during the heating process, when the temperature is too high, the shape accuracy deteriorates. In order to ensure a certain surface accuracy and suppress the occurrence of burrs and defects, the laser assisted temperature should be controlled around glass transition temperature (T_g).

Declaration of Competing Interest

The authors declare that they have no known competing financial

interests or personal relationships that could have appeared to influence the work reported in this paper.

Acknowledgments

This work was supported by the National Natural Science Foundation of China (Grant No. 51705233) and the Shenzhen Science and Technology Programs (Grant No. GJHZ20190820151801786, KQTD20170810110250357).

References

[1] Trexler MM, Thadhani NN. Mechanical properties of bulk metallic glasses. Prog Mater Sci 2010;55:759–839. https://doi.org/10.1016/j.pmatsci.2010.04.002.
[2] Chavoshi SZ, Goel S, Morantz P. Current trends and future of sequential micro-machining processes on a single machine tool. Mater Des 2017;127:37–53. https://doi.org/10.1016/j.matdes.2017.04.057.
[3] Davoudi KM, Vlassak JJ. Dislocation evolution during plastic deformation: equations vs. Discrete dislocation dynamics study. J Appl Phys 2018;123. https://doi.org/10.1063/1.5013213.
[4] Steif PS, Spaepen F, Hutchinson JW. Strain localization in amorphous metals. Acta Metall 1982;30:447–55. https://doi.org/10.1016/0001-6160(82)90225-5.
[5] Maloney C, Lemaître A. Subextensive scaling in the athermal, quasistatic limit of amorphous matter in plastic shear flow. Phys Rev Lett 2004;93. https://doi.org/10.1103/PhysRevLett.93.016001. 016001–1.
[6] Chen B, Li Y, Yi M, Li R, Pang S, Zhang T. Optimization of mechanical properties of bulk metallic glasses by residual stress adjustment using laser surface melting. Scr Mater 2012;66:1057–60. https://doi.org/10.1016/j.scriptamat.2012.02.046.
[7] Huang H, Jiang M, Yan J. Softening of Zr-based metallic glass induced by nanosecond pulsed laser irradiation. J Alloys Compd 2018;754:215–21. https://doi.org/10.1016/j.jallcom.2018.04.278.
[8] Xu S, Osawa S, Kobayashi R, Shimada K, Mizutani M, Kuriyagawa T. Minimizing burrs and defects on microstructures with laser assisted micromachining technology. Int J Automot Technol Manag 2016;10:891–8. https://doi.org/10.20965/ijat.2016.p0891.
[9] Park SS, Wei Y, Jin XL. Direct laser assisted machining with a sapphire tool for bulk metallic glass. CIRP Ann Manuf Technol 2018:1–4. https://doi.org/10.1016/j.cirp.2018.04.070.
[10] Jiang F, Jiang MQ, Wang HF, Zhao YL, He L, Sun J. Shear transformation zone volume determining ductile-brittle transition of bulk metallic glasses. Acta Mater 2011;59:2057–68. https://doi.org/10.1016/j.actamat.2010.12.006.
[11] Wang WH. Correlation between relaxations and plastic deformation, and elastic model of flow in metallic glasses and glass-forming liquids. J Appl Phys 2011;110. https://doi.org/10.1063/1.3632972.
[12] Jiang MQ, Dai LH. Formation mechanism of lamellar chips during machining of bulk metallic glass. Acta Mater 2009;57:2730–8. https://doi.org/10.1016/j.actamat.2009.02.031.
[13] Chang HJ, Kim SY, Moon WJ, Kim YM, Park ES, Kim DH. Probing structural changes during ductile fracture in metallic glasses via in situ straining inside a MeV transmission electron microscope. Intermetallics 2018;102:94–100. https://doi.org/10.1016/j.intermet.2018.08.012.
[14] Ye JC, Lu J, Yang Y, Liaw PK. Study of the intrinsic ductile to brittle transition mechanism of metallic glasses. Acta Mater 2009;57:6037–46. https://doi.org/10.1016/j.actamat.2009.08.029.
[15] He Q, Shang JK, Ma E, Xu J. Crack-resistance curve of a Zr-Ti-Cu-Al bulk metallic glass with extraordinary fracture toughness. Acta Mater 2012;60:4940–9. https://doi.org/10.1016/j.actamat.2012.05.028.
[16] Liu FR, Han XX, Bai N, Zhao JJ, Chen JM, Lin X. Numerical simulation on the temperature field induced by a nanosecond pulsed excimer laser in the phase-change film. Thin Solid Films 2014;551:102–9. https://doi.org/10.1016/j.tsf.2013.11.092.
[17] Xiong J, Wang H, Zhang G, Chen Y, Ma J, Mo R. Machinability and surface generation of $Pd_{40}Ni_{10}Cu_{30}P_{20}$ bulk metallic glass in single-point diamond turning. Micromachines 2020;11. https://doi.org/10.3390/mi11010004.
[18] Hays CC, Kim CP, Johnson WL. Microstructure controlled shear band pattern formation and enhanced plasticity of bulk metallic glasses containing in situ formed ductile phase dendrite dispersions. Phys Rev Lett 2000:696–716. https://doi.org/10.1103/PhysRevLett.84.2901.
[19] Liu YH, Wang G, Wang RJ, Zhao DQ, Pan MX, Wang WH. Super plastic bulk metallic glasses at room temperature. Science 2007;315:1385–8. https://doi.org/10.1126/science.1136726.

論　文

粒子タブレット切削方式による歯科用パウダージェットデポジションハンドピースの開発

冨江瑛彦*1, 山本浩己*2, 本郷那美*2, 森田隆輝*2, 久慈千栄子*2,
嶋田慶太*2, 水谷正義*2, 泉田一賢*3, 佐々木啓一*3, 厨川常元*1

Development of dental powder jet deposition handpiece utilizing particle feed mechanism of tablet cutting

Akihiko TOMIE, Hiroki YAMAMOTO, Nami HONGO, Ryuki MORITA, Chieko KUJI,
Keita SHIMADA, Masayoshi MIZUTANI, Kuniyuki IZUMITA, Keiichi SASAKI and Tsunemoto KURIYAGAWA

パウダージェットデポジション(PJD)は常温大気圧環境下で適用可能な成膜法である. 筆者らは本手法を用いてハイドロキシアパタイト(HA)膜を歯質上に形成する歯科治療法を推進している. PJD に供するミクロンオーダの HA 粒子は凝集性が高いため, 粒子タンクからハンドピースまでの搬送配管内壁に粒子が残留することが課題となっていた. 本研究ではこの欠点を解決するため, 配管による粒子搬送を用いない粒子タブレット切削方式の歯科用 PJD ハンドピースを開発した. その結果, 配管内への粒子残留がなく, HA 膜の形成が可能であることを示した.

Key words : powder jet deposition, hydroxyapatite, dental treatment, handpiece, particle dispersion

1. 序　論

パウダージェット加工(Powder Jet Processing)は常温大気圧環境下で材料粒子を対象物に噴射・衝突させるプロセスである [1]. 本手法の加工現象として, 粒子が対象物に付着するパウダージェットデポジション(PJD:Powder Jet Deposition), あるいは対象物が除去されるアブレイシブジェット加工(AJM:Abrasive Jet Machining)のいずれかが発現する. 加工現象が遷移する条件としては粒子径と衝突速度の関係が報告されており, 5μm 以下の粒子が亜音速から遷音速程度で衝突する場合は PJD が支配的になる [2)-4)].

PJD による成膜層は衝突のエネルギによって創成される化学的活性な多結晶体が粒子から剥離し, それらが再結合することで形成される [5]. そのため, セラミックスなどの高融点材料にも適用可能であり, 材料選択の自由度が高い.

この特性を利用し, 筆者ら [6)-8)] はバイオセラミックスの1つであるハイドロキシアパタイト(HA:Hydroxyapatite)を PJD に適用することを提唱している. HA は歯のエナメル質や骨などの生体硬組織の主成分であり, 生体親和性材料として知られている [9]. アプリケーションとしては歯科分野を想定しており, 口腔内で歯質上に HA 膜を形成する治療法の開発を進めている. 本手法では歯科用接着剤などの生体異種材料を用いずに歯質の再構築が可能であり, 例えば変色歯の色調を回復する審美歯科 [10] や, 抗菌性 HA 粒子を用いた予防歯科への適用が検討されている.

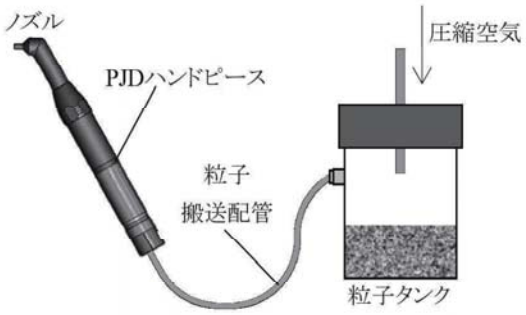

図1　従来の歯科用PJDハンドピースの構成

先行研究 [4] では**図 1** に示す PJD ハンドピースを開発し, 抜去歯への成膜実験を行った. 本装置は HA 粒子を充填した粒子タンクに圧縮空気を供給することでエアロゾル化し, 搬送配管を通してノズルから噴射する構造である. 検討の結果, 膜厚 10μm 程度の成膜層が形成されており, PJD による歯科治療法の実現可能性が示されている.

一方, 粒径がミクロンオーダの HA 粒子は凝集性が極めて高く, 流動性が悪い. そのため, 搬送配管内壁には多量の粒子が残留し, 投入粒子量に対する噴射効率に改善の余地を残している. また, PJD において粒子の凝集状態は加工現象に大きく影響することが予想される.

そこで本研究では配管による搬送を用いない粒子供給方法を提案し, 上述した課題の解消を試みた. さらにハンドピース内の内部流路を複数試作し, ハンドピース内部形状と粒子分散特性および成膜特性との関係について検討した.

*1　東北大学大学院医工学研究科:〒980-8579 宮城県仙台市青葉区荒巻字青葉6-6-01
Graduate School of Biomedical Engineering, Tohoku University
*2　東北大学大学院工学研究科:〒980-8579 宮城県仙台市青葉区荒巻字青葉6-6-01
Graduate School of Engineering, Tohoku University
*3　東北大学大学院歯学研究科:〒980-8575 宮城県仙台市青葉区星陵町4-1
Graduate School of Dentistry, Tohoku University
〈学会受付日:2020年6月30日〉
〈採録決定日:2020年8月31日〉

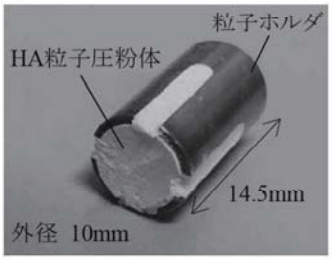

図2 HA粒子タブレット外観

2. 粒子タブレット切削式歯科用PJDハンドピースの開発

2. 1 実験装置の構成

配管を用いない粒子供給方法として筆者らは**図2**に示す専用のホルダ（以降，粒子ホルダ）にHA粒子を圧入してタブレット化し，ハンドピース内部に装着する構成を考案した．装着したタブレットを小径回転工具で切削して切りくずを生成し，それを噴射粒子として供給するものである．

図3に試作した粒子タブレット切削式歯科用PJDハンドピースの構成を示す．図3(a)に示すように，本装置は圧縮空気を供給するコンプレッサと圧縮空気の圧力制御器，および切削ユニットとノズルユニットからなるPJDハンドピースで構成される．図3(b)に切削ユニットの外観を示す．本ユニットでは回転工具を同図(a)の-Z方向に送りながらノズルユニットに固定されたタブレットを切削する．タブレットは低硬度であり，容易に切削され，HAの組成には影響がないと考えられる[7]．また，ユニット内部には圧縮空気の流路が備えられており，生成粒子をノズルユニットに供給する．本構成ではHA粒子はハンドピース内部でのみ発生するため，配管内部の粒子残留は原理的に生じない．次に図3(c)にノズルユニットの詳細を示す．ノズルユニットは粒子ホルダを固定し，タブレット切削を行うタブレット切削部とテーパ状の搬送流路部および先端のノズル部から構成される．ノズル部は搬送流路部に締結されており，交換が可能である．

2. 2 供試ノズル

気相中における凝集体の分散メカニズムとして，高速気流への投入，気流の加速[11]，障害物への衝突[12]などが知られている．本研究ではこれらの原理を適用した5種類のノズル（A, B, C, D, E）を作製し，HA粒子の分散特性と成膜特性を比較する．**図4**に作製したノズルの内部流路の断面図を示す．また主要寸法を**表1**に示す．各ノズルはステンレス筐体にアルミナ製の中空パイプを差し込み，接着固定することで作製した．まず，ノズルAは流路の長さL_1を24mm，内径d_1を1mmとしたものである．本ノズルを用いて小径流路に粒子が供給され，高速で運動することによる分散特性を確認する．ノズルBはL_1をノズルAの3倍にしたものであり，粒子の高速移動区間の長さと分散の関係を評価する．ノズルCには流路内径を中間位置でd_2(=1.5d_1)に拡大することで急峻な速度変化が生じる機能を設けた．なお，内径がd_2となる部分の流路の長さをL_2で表す．ノズルDはノズルAと同一寸法の直線流路先端に内径d_2の90°屈曲させた流路を接続したものである．本ノズルでは屈曲部に粒子が衝突することによる分散特性を評価する．ノズルEはノズルDのL_1の区間を3倍にしたうえで屈曲部に衝突させる構造である．

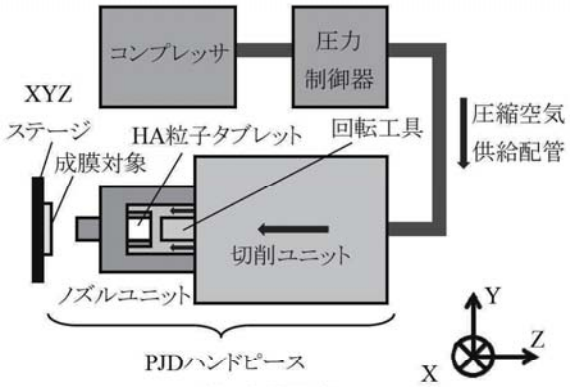

(a) 全体構成

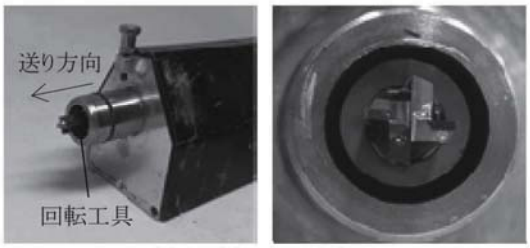

(b) 切削ユニット外観図
(左：ユニット全体図，右：工具拡大図)

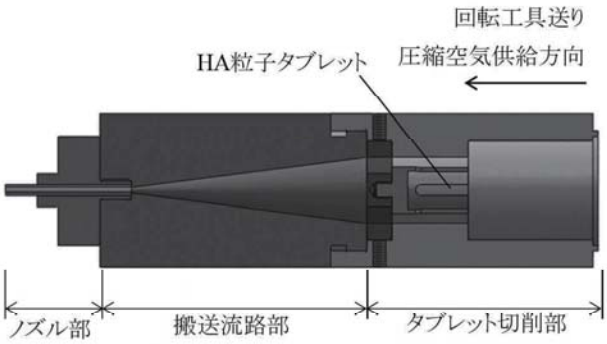

※図4(a)のノズルA装着時

(c) ノズルユニット詳細図

図3 粒子タブレット切削式歯科用PJDハンドピースの構成

3. 数値流体解析による粒子速度評価

3. 1 解析モデル

各ノズルでは圧力損失や流れ場が異なることにより，同一圧力の圧縮空気を供給した場合でも噴射される粒子の衝突速度は異なることが予想される．流路形状による分散特性および成膜特性の違いのみ抽出するためには，一定の衝突速度で実験を行うことが望ましい．そこで，各ノズルの圧縮空気の圧力と粒子速度の関係を数値流体解析によって求め，粒子が同一速度で衝突する圧力を算出した．**表2**に解析条件を示す．本研究では解析ソフトウェアとしてANSYS FLUENTを用いた．先行研究[13]ではPJDノズルの噴流はキャリヤガスの圧力によって100～300m/sの範囲で変化することを粒子画像流速測定法（PIV法）によって示している．空気の流れでは流

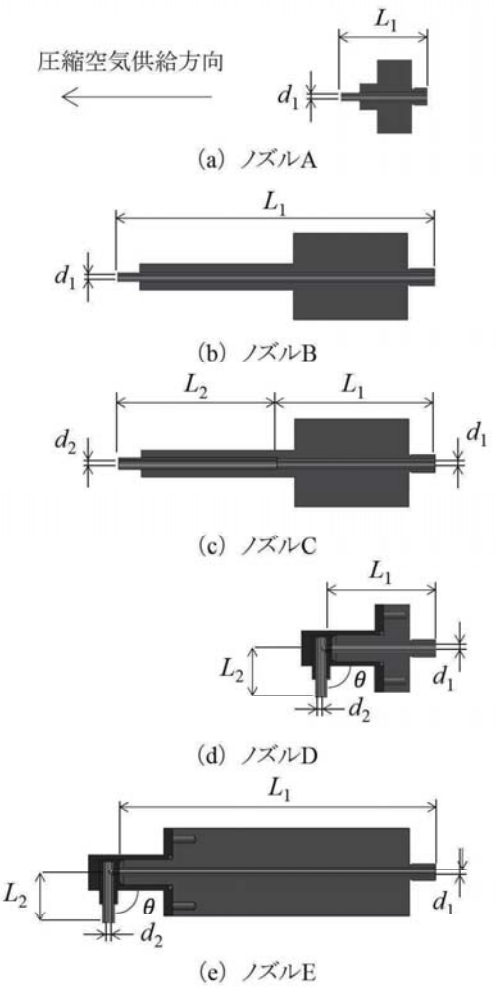

図4　ノズル部の断面構造

表1　ノズル主要寸法　(単位:mm　角度除く)

ノズル	L_1	L_2	d_1	d_2	θ
A	24	-	1.0	-	0°
B	72	-	1.0	-	0°
C	36	36	1.0	1.5	0°
D	24	11.5	1.0	1.5	90°
E	72	11.5	1.0	1.5	90°

速が100m/s以上である場合，流体密度が圧力に依存して変化する圧縮流れとなる[14]．本研究で開発したノズルでも同様の速度の流れ場が発生することを想定し，圧縮流れに関する基礎方程式を解析に適用した．また，乱流のモデルとしてはRealizable k-εモデルを用いた．本モデルで求めた流れ場に粒子を供給し，成膜対象である平面基板への衝突速度を求めた．粒子は粒径2μmのHA粒子を仮定し，ノズル・基板間距離を5mm，ノズルと基板がなす角は90°とした．圧縮空気の圧力は0.1MPaから0.5MPaまでの5条件で変化させた．

3．2　解析結果

図5に粒子がノズルから噴射され，基板に衝突する粒子軌跡の一例を示す．得られた粒子軌跡から，基板に到達した全

表2　解析条件

解析ソフトウェア	ANSYS FLUENT	
乱流モデル	Realizable k-ε	
キャリヤガス	圧縮空気	
圧力 MPa	0.1, 0.2, 0.3, 0.4, 0.5	
粒子	材料	HA
	粒径 μm	2
ノズル・基板間距離 mm	5	
ノズル・基板角度 °	90	

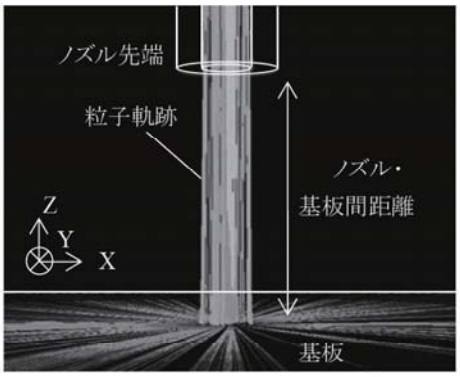

図5　粒子軌跡解析結果の一例

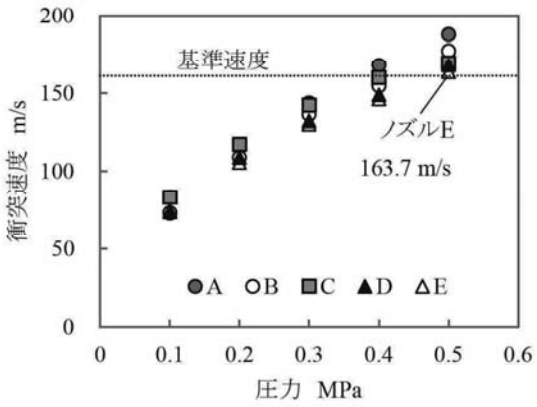

図6　圧力と衝突速度の関係

粒子の基板近傍の速度の平均値を衝突速度として定義した．圧縮空気の圧力と衝突速度の関係を**図6**に示す．衝突速度はいずれのノズルについても圧力に対して直線的に増加する傾向が認められた．最大圧力0.5MPaのもとでの衝突速度を比較すると，ノズルAが最も大きな速度を示し，ノズルEが最も小さい163.7m/sを示した．ノズルAは5種類のノズルの中で流路の長さが最も短く，かつ内径の変化や屈曲も設けていない構造であるため，ノズル内部での圧力損失が小さい．一方で，ノズルEは流路長が大きいことによる損失と，先端部の屈曲部に粒子が衝突することによる減速によって最も小さな値を示したと考えられる．

この結果から，0.5MPaにおけるノズルEの衝突速度を基準衝突速度として定め，その他のノズルが同一の衝突速度を示す圧力を線形近似することで求めた．求めた圧力を**表3**に示

表3　噴射実験における各ノズルの設定圧力

ノズル	設定圧力 MPa
A	0.39
B	0.43
C	0.44
D	0.46
E	0.50

す．次節で行う噴射実験では，表中の圧力を圧力制御器に入力する．

4．粒子生成・噴射実験

4．1　実験手順

はじめに，各条件で生成された粒子の凝集状態を確認するために粒度分布の比較を行った．比較対象は粒子ホルダ圧入前の原料粒子，タブレット切削による生成粒子および切削後に5種類のノズルから噴射された粒子の7条件である．まず，圧縮空気を供給しない状態でタブレット切削を行い，生成粒子を回収した．原料粒子と切削の条件を**表4**に示す．切削条件は予備実験で最も分散の良い条件を採用した．次に表3に示した設定圧力のもとで，容積が十分大きい容器中に噴射した粒子を回収した．得られた各粒子の粒度分布を湿式粒度分布計（FPIA-3000S，シスメックス）によって測定した．なお，原料粒子の測定のみ，粒子を懸濁した溶液に超音波振動で加振し，凝集の解砕を促進した状態で行った．凝集体を含まない1次粒子の粒度分布と切削・噴射を経て生成された粒子の分布を比較することで各条件の分散特性を評価した．また，再現性の確認のために各測定は3回ずつ実施した．

次に，HA基板を対象とした噴射実験を行った．本基板は人工的に合成したHAを研磨処理によって平滑化したものである．本基板を図3に示すXYZステージに取り付け，ノズル・基板間距離を5.0mmの位置に固定した状態で投入粒子全量が切削されるまで噴射を行った．得られた噴射面をレーザプローブ式3次元形状計測機（NH-3T，三鷹光器）によって測定し，形状と断面プロファイルを確認した．

4．2　回収粒子の評価

図7に原料粒子の粒度分布の一例を示す．図中に示すようにモード径（最頻度粒子径）は1.1μm，D_{50}（体積積算50%径）は5.8μmである．次にタブレット切削によって生成された粒子の粒度分布の一例を**図8**に示す．凝集状態の評価方法として本実験ではD_{50}に着目する．同図より生成粒子のD_{50}は9.0μmを示し，原料粒子よりも大粒径側にシフトしている．原料粒子の粒度分布（図7）から9.0μm以上の粒子比率はおよそ20%であるため，この場合，生成粒子の30%は9.0μm以上の凝集体であるといえる．したがって，1次粒子に分散するには切削のみでは不十分であり，ノズルの分散作用を併用することが必要となる．

次に，5種類のノズルによって噴射されたあとに回収した粒子の粒度分布の一例を**図9**に示す．流路長L_1が短いノズルA，

表4　実験条件

試供粒子	材料	HA
	モード径 μm	1.1
	D_{50} μm	5.9
	投入粒子量 g	0.7
タブレット切削条件	回転速度 rpm	1000
	送り速度 mm/min	5.0
成膜対象	HA 基板	
ノズル・基板間距離 mm	5.0	
キャリヤガス	圧縮空気	

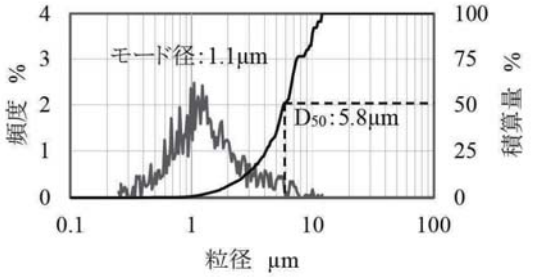

図7　原料粒子の粒度分布

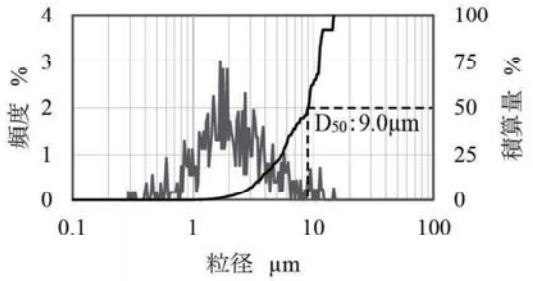

図8　タブレット切削後生成粒子の粒度分布

およびノズルDではD_{50}がそれぞれ5.7μm，5.6μmを示し1次粒子と同水準の値を示した．よって，D_{50}より大粒径側の凝集体は1次粒子に解砕されているとみなせる．それに対して，流路が長いノズルBおよびEのD_{50}はそれぞれ11.4μmと14.0μmであり，多量の凝集体が確認された．よって，内径d_1=1mmの区間長さL_1は粒子分散に対して負の相関が認められた．一方，流路全長が長い場合でもノズルCのようにノズル内部で流路内径をd_2=1.5mmに拡大させる場合はD_{50}が切削後生成粒子よりも小さく，分散作用が認められた．したがって，流路面積拡大による速度変化が凝集体の解砕に有効な手段であると考えられる．また，90°の屈曲部についてはノズルDとEの分布の比較からノズル長さの影響がより支配的であり，また，ノズルAとDの比較から粒子衝突による分散効果は限定的であると考えられる．最後に3回計測したD_{50}の平均値をまとめたものを**図10**に示す．ここで，エラーバーは計測された最大・最小値と平均値の差分である．同図から，上述したノズルA，C，Dの分散特性が複数回再現されることを確認した．

4．3 噴射面の比較

図11にHA基板上に形成された噴射面の形状とX軸，Y軸方向の断面プロファイルを示す．ここで，図中に示す座標は図3と同様であり，断面は噴射面の中心を通る位置で切断する面とした．同図より全てのノズルで加工高さが正方向であり，本装置でPJDによる成膜層が形成されていることが確認された．つづいて，各ノズルによって形成された成膜層の特徴について，断面曲線を比較して考察する．

図11(a)(c)(d)に示すノズルA，C，Dによる成膜層はそれぞれ形状に違いはあるが，いずれも滑らかな曲線を示している．一方で，ノズルBによる成膜層は図11(b)に示すように膜の外周部に成膜層が除去された剥離痕があり，同図(e)のノズルEによる成膜層においても中心部に剥離痕が確認された．前述したようにノズルB，Eからの噴射粒子には多量の凝集体が含まれている．そのため，大粒径の凝集体が成膜層に衝突することで除去加工(＝アブレイシブジェット加工)が生じ，成膜層が部分的に剥離したと考えられる．すなわち，1次粒子で判別した場合に粒度分布と衝突速度が付着条件であっても，凝集体が形成されて除去加工条件となった場合，付着と除去が混在した加工現象が発現すると考えられる．

次に，成膜層の形状について比較する．図11(a)および(b)より断面積がノズルの全区間でd_1=1mmで一定であるノズルA，Bで形成された膜は中心付近の膜厚が大きい．特にノズルBは5種類のノズルの中で最大の60.3μmを示した．それに対して同図(c)(d)(e)より，ノズル内部で断面積がd_2=1.5mmに拡大されるノズルC，D，Eによって形成された成膜層は中心部の膜厚は相対的に小さいが，成膜層の面積はノズルA，Bよりも大きい．また，ノズルの全長が短いノズルA，Dによって形成される成膜層のプロファイルは偏りがある形状となっているのに対して，ノズルの全長が長いノズルB，C，Eによる成膜層のプロファイルでは偏りが小さく中心付近を頂点とした凸型のプロファイルを示した．この2点から，ノズル先端の流路面積は成膜層の広がりに寄与し，ノズルの全長を大きくするほど成膜層の形状が均質化されることが明らかになった．以上より，ノズルの形状とHA粒子の分散特性および成膜特性の相関について知見が得られた．

この結果から，歯科治療に適したノズルの条件を検討する．審美歯科の場合，膜厚が均一な成膜層を形成し色むらを抑制することが好ましい．また，歯質の除去を防止するためには凝集体を解砕した状態で成膜を行う必要があることが明らかとなった．今回の検討の場合，ノズルCに備えた流路面積拡大が粒子分散と成膜層の均質化の両立に有効である．

5．結　論

本研究の結論を以下に記す．

(1) 粒子搬送配管を備えない粒子タブレット切削式歯科用PJDハンドピースを開発した．本装置によって配管内粒子残留の解消とHA膜形成が可能であることを示した．

(2) 粒子衝突速度が同一条件でもノズル形状によって分散特性が異なることを明らかにした．また，凝集体を含む場合は成膜層の部分的な剥離が生じることを確認した．

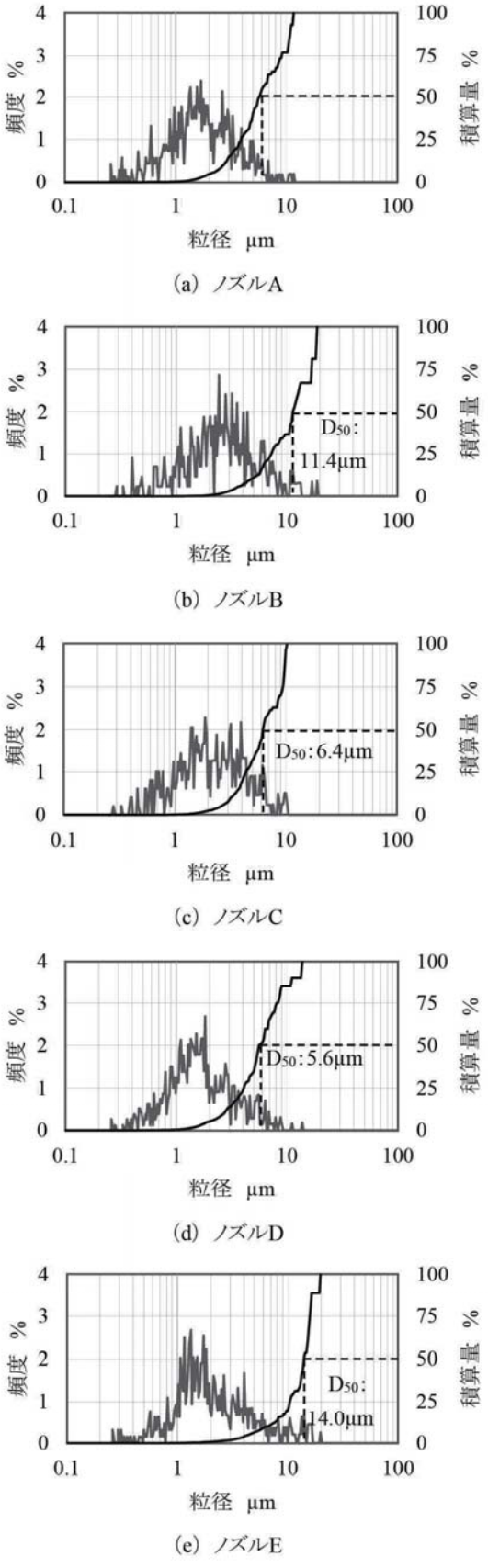

図9 ノズルから噴射後の粒度分布

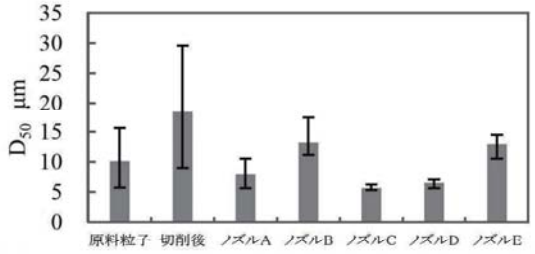

図10 各条件のD_{50}平均値

(3) ノズル先端の流路面積と成膜層の面積は正の関係があり，ノズル全長を大きくすると成膜層が凸型の均質化された形状に近づく傾向を確認した．

(4) ノズル内での流路面積拡大が粒子分散と成膜層の形状均質化の両立に有効である．

謝辞

本研究は平成28年度新エネルギー・産業技術総合開発機構戦略的基盤技術高度化支援事業（プロジェクト委託型）の助成を受けたものである．

6. 参考文献

1) C. Nishikawa, N. Mizukuchi, A. Tomie, K. Shimada, M. Mizutani and T. Kuriyagawa: Characteristics of Thick Film Deposition in Powder Jet Machining, Int. J. of Automation Technology, 7, 6 (2013) 630.
2) C. Nishikawa, K. Sato, T. Hagiwara, K. Mizutani, K. Shimada and T. Kuriyagawa: Substrate fracture by particle impact Study of the mechanism of power jet machining. Journal of the Japan Society for Abrasive Technology, 57 ,3 (2013) 174 (in Japanese).
3) C. Nishikawa, K. Mizutani, T. F. Zhou, J. W. Yan and T. Kuriyagawa: Investigation of Particle Impact Phenomena in Powder Jet Deposition Process, Key Engineering Materials, 523, (2012) 184.
4) K. Sato, C. Nishikawa, T. Hagiwara, K. Shimada, W. Horiuchi, K. Matsumura, R. Akatsuka, K. Sasaki, T. Ishizaki, M. Arakawa, K. Ohta, M. Mizutani and T. Kuriyagawa: Creation of hydroxyapatite film on human enamel utilized powder jet deposition. Transaction of the Japan Society of Mechanical Engineers, Series C, 79, 808 (2013) 109 (in Japanese).
5) M. Mizutani, C. Kuji, H. Ohisa, S. Nishimura, K. Mizutani, R. Akatsuka, K. Sasaki, S. Xu, K. Shimada and T. Kuriyagawa: Particle fracture behavior and deposition mechanism in powder jet deposition (PJD), Journal of the Japan Society for Abrasive Technology, 61, 1 (2017) 28 (in Japanese).
6) A. Tomie, C. Kuji., N. Mizukuchi , C. Nishikawa, K. Shimada, K. Izumita, R. Akatsuka, K. Sasaki, M. Mizutani and T. Kuriyagawa: Deposition of hydroxyapatite film within a cavity dental application of powder jet deposition, Journal of the Japan Society for Abrasive Technology, 57, 12, (2013) 800 (in Japanese).
7) A. Tomie, C. Kuji, H. Ohisa, K. Shimada, M. Mizutani, K. Sasaki and T. Kuriyagawa: Fabrication of hydroxyapatite film by powder jet deposition. Transaction of the Japan Society of Mechanical Engineers, 81 832 (2015) 15 (in Japanese).
8) A. Tomie, C. Kuji, R. Akatsuka, K. Sasaki, K. Shimada, M. Mizutani and T. Kuriyagawa: Study on particle impact angle in powder jet machining. Transaction of the Japan Society of Mechanical Engineers, 83 856 (2017) 17 (in Japanese).
9) 青木秀希:驚異の生体物質 アパタイト, 医歯薬出版, (1999).
10) K. Izumita, R. Akatsuka, A. Tomie, C. Kuji, T. Kuriyagawa and K. Sasaki: Development of Powder Jet Deposition Technique and New Treatment for Discolored Teeth. Interface Oral Health Science 2016, (2016), 257.
11) 向阪保雄, 遠藤禎行, 堀内貴洋, 新居田亨:気流の加速による凝集粒子の分散, 化学工学論文集, 18 巻(1992)2 号, (1992) 233.
12) 後藤邦彰:粒子分散技術と粉体の付着性に関する一考察, 粉砕, 59 巻, (2016) 51.
13) 水谷公一ほか:微粒子衝突速度が成膜および基板に与える影響—パウダージェットデポジション法によるセラミックス膜創成に関する研究—, 2008 年度精密工学会秋季大会学術講演会講演論文集, (2008) 457.
14) 松尾一泰:圧縮性流体力学—内部流れの理論と解析—, オーム社, (1994).

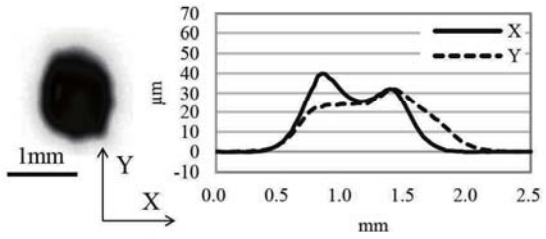

(a) ノズルA

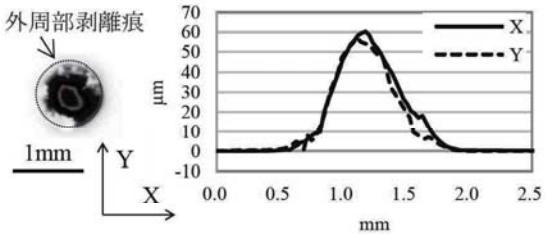

(b) ノズルB

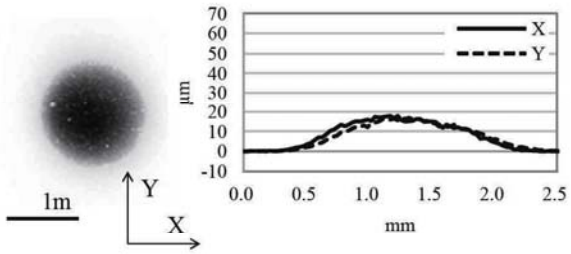

(c) ノズルC

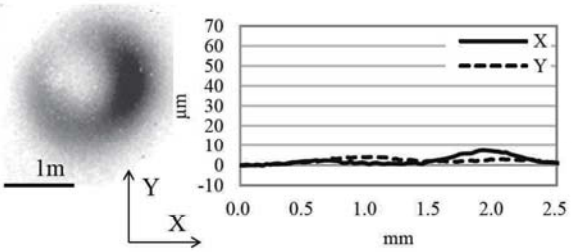

(d) ノズルD

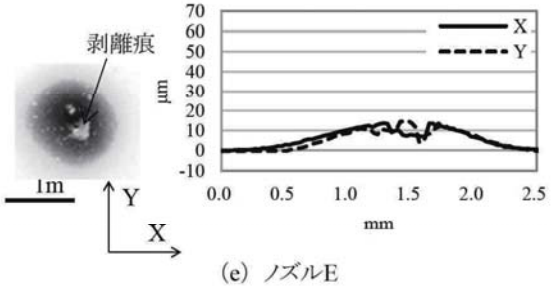

(e) ノズルE

図11 成膜層の形状と断面プロファイル

Paper:

Effect of Ultrafine Bubbles on *Pseudomonas Aeruginosa* and *Staphylococcus Aureus* During Sterilization of Machining Fluid

Hiroko Yamada*,†, Kensuke Konishi, Keita Shimada**, Masayoshi Mizutani**, and Tsunemoto Kuriyagawa***

*Graduate School of Biomedical Engineering, Tohoku University
6-6-01 Aramaki Aza-Aoba, Aoba-ku, Sendai, Miyagi 980-8579, Japan
†Corresponding author, E-mail: hiroko.suzuki.q4@dc.tohoku.ac.jp
**Graduate School of Engineering, Tohoku University, Sendai, Japan
[Received May 29, 2020; accepted November 2, 2020]

Bacterial growth is one of the common causes of putrefaction and deterioration of water-soluble machining fluid. The 16S ribosomal DNA metagenome analysis of the bacterial species composing the microbial flora present in the machining fluid derived after processing demonstrated a high amount of species belonging to the *Pseudomonas* genus. Therefore, we prepared two types of ultrafine bubbles water (gas species: air and CO_2) containing different types of gas and confirmed the bactericidal effect on *Pseudomonas aeruginosa* (ATCC 10145), a typical *Pseudomonas* species. The grinding fluid was prepared using sterile purified water containing ultrafine bubbles (hereafter referred to as UFB) as diluted water, and the *Pseudomonas aeruginosa* was inoculated to obtain 10^6 CFU/mL. The sterilization rate of the number of bacteria was determined immediately after immersion in each fluid and subsequently after two hours. The sterilization rate was determined to be 100% in the test group using the ultrafine bubbles water of CO_2 (CO_2-UFB water). As a comparative control, a similar test was performed on *Staphylococcus aureus* IFO12732, and the sterilization rate was determined as 0%. Fluorescence microscopic observation of bacteria after immersion in the CO_2-UFB water demonstrated damage to the cell wall as the cause of death of the *Pseudomonas aeruginosa*. Therefore, CO_2-UFB demonstrated sterilization of machining fluid by killing *Pseudomonas aeruginosa* in the machining fluid. The bactericidal mechanism of UFB involved the induction of damage in bacterial cell walls. This can be attributed to crushing due to the increase in the particle size of UFB.

Keywords: ultrafine bubbles, sterilization, water-soluble machining fluid, *pseudomonas aeruginosa*

1. Introduction

Water-soluble grinding fluid and cutting fluid (hereafter collectively referred to as machining fluids) are typically used as coolants in the machining process. Both fluids deteriorate due to putrefaction by bacteria and mold after long-term use. In particular, emulsion-type machining fluid is prone to putrefaction, and an unpleasant smell may be generated in factories where room temperature is not controlled. Since the machining fluid is sprayed onto the workpiece at high pressure, it turns into mist and scatters in the workspace. Aerosols of water or fluid with bacterial contamination are closely associated with respiratory infections. For instance, the machining fluid used in factories may be responsible for community-acquired pneumonia [1]. Furthermore, since the machining fluid tends to become aerosol mist during use, the risk of a worker getting infected increases upon contamination with bacteria.

Various types of bacteria have been observed in the machining fluid. Among them, bacterial species belonging to the *Pseudomonas* genus are produced with high frequency in the water-soluble machining fluid during use [2]. In addition, *Pseudomonas aeruginosa* is a type of pathogenic bacterium and a known cause of community-acquired pneumonia [1]. As a measure to prevent the production of such bacteria, a bactericidal agent can be added to the machining fluid. Certain types of fungicides can cause allergic dermatitis [3]. Hence, chemical-free sterilization methods are required to reduce such risks.

To obtain a bactericidal effect without using chemicals, we focused on the technology involving the use of fine bubbles (defined as bubbles with a diameter of 100 μm or less; hereafter referred to as FB). The technology is expected to exhibit various functions such as sterilization by self-crushing, virus inactivation, environmental purification, plant activity, and cleaning depending on the composition (the type of gas), size, and concentration of foam [4–7], the technology has a wide range of applications. FB technology was developed in 1988 for mitigating oyster farming damage. In recent years, its application has been extended to the field of machining [7–9]. Inazawa et al. [8] used oxygen FB to perform the oxide cross-link reaction on the conductive rubber bond and succeeded in hardening the surface of the grinder and reducing the coefficient of friction. In addition, Ninomiya

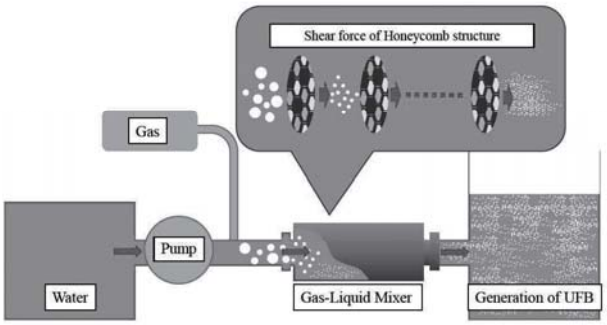

Fig. 1. Principle of the production of ultra-high density ultra-fine bubbles [12].

et al. [9] confirmed the suppression of bacterial growth with grinding fluid in which air with FB was continuously circulated and mixed. Among the FBs, bubbles with a diameter of 1 μm or less are distinguished as ultrafine bubbles (hereafter referred to as UFB) and those with a diameter in the range of 1–100 μm are distinguished as microbubbles (hereafter referred to as MB). These bubbles demonstrate a cleaning and a bioactive effect [4].

The suppression of the growth of bacteria by the bubbles, which is the focus of this study [10], has been reported previously. An advantage of UFB over MB is that it can stay in the fluid for a long period due to its small size, and the effect can be sustained over long intervals [11]. Furthermore, the UFB has a larger specific surface area than the MB obtained by increasing the density, which might be a possible reason for the advantages of UFB over MB. However, the mechanism by which bacterial growth is suppressed by both the UFB and the MB is not yet elucidated.

In this study, we focused on UFB and examined the effect of UFB on the suppression of bacterial growth and growth in the machining fluid. We focused on the effects of air and CO_2 gas contained in UFB. We attempted to elucidate the bactericidal effect of the UFB and its underlying mechanism.

2. Material and Methods

2.1. Production of UFB Water

In this study, water containing high-density UFB (hereafter referred to as UFB water) was prepared using the high-density UFB generator NQ-KP-M1.5 CD-200/60-R3s (manufactured by Nanox Co., Ltd.). The device generated UFB by continuous shearing involved in a complicated fluid path due to the honeycomb structure and was able to produce UFB at a much higher density than other devices. The principle is demonstrated in **Fig. 1**. As shown in **Fig. 1**, the device supplied gas to the raw water. The size of the bubbles was reduced to approximately 100 nm in diameter by the action of shearing force generated by the fluid passing through the honeycomb structure in the gas-liquid mixer under pressure [12]. At the time, it was possible to alter the type of gas in the bubble by changing the type of gas supplied. In this study, we prepared two types of UFB waters using air and CO_2. The UFB water prepared with each gas type was called Air-UFB water and CO_2-UFB water. Sterile purified water was used as the raw water for the preparation of UFB water. The UFB concentration in each type of UFB water was measured with the NanoSight NS300 (manufactured by Malvern Panalytical). The presence of UFB with a diameter of 100 nm or less with 10^7 particles/mL or higher was confirmed.

2.2. Analysis of the Types of Bacteria Present in the Machining Fluid and Their Respective Amounts in the Microbial Flora

The machining fluid after use was collected to confirm the type of bacteria produced in the machining fluid and their amounts in the microbial flora. The number of live cells was measured, and the microbial flora was subjected to metagenome analysis of the 16S ribosomal DNA (16S rDNA). Here, the metagenomic analysis of the 16S rDNA gene was conducted to perform mass parallel base sequence analysis of 16S rDNA gene fragments to determine DNA regions common to bacteria. The type of bacterial species was also determined, and the number of fragments of the same base sequence was measured. As a result, it was possible to confirm the bacterial species present in the microbial flora in the sample and their amounts in the microbial flora.

2.2.1. Collection of the Machining Fluid and the Measurement of the Number of Live Cells

The grinding fluid was used as the machining fluid in this study. Specifically, the grinding fluid (water-soluble chemical type) was diluted to a concentration of 2.5% and collected after three months of use. The number of live cells in the collected machining fluid was measured with a standard agar plate (manufactured by Nissui Pharmaceutical Co., Ltd.).

2.2.2. Metagenome Analysis of 16S rDNA Derived from Bacteria Present in the Machining Fluid

After extracting genomic DNA from 750 μL of the collected machining fluid, the 16S rDNA fragment was amplified by the polymerase chain reaction (PCR). Using this DNA fragment, the flora was examined by performing the metagenome analysis of 16S rDNA using the next-generation sequencer MiSeq system (manufactured by Illumina). The reaction principle involves the sequencing by synthesis (SBS) method [13], which is a modification of the general Sanger method that is commonly used for base sequence analysis. It is possible to perform millions of parallel base sequence analyses with next-generation sequencing. The principle is shown in **Fig. 2**. As shown in panels 1 to 3 of **Fig. 2**, a DNA library was prepared first in which a sequence of adapters was bound to both ends of the 16S rDNA fragment. Next, the DNA library was

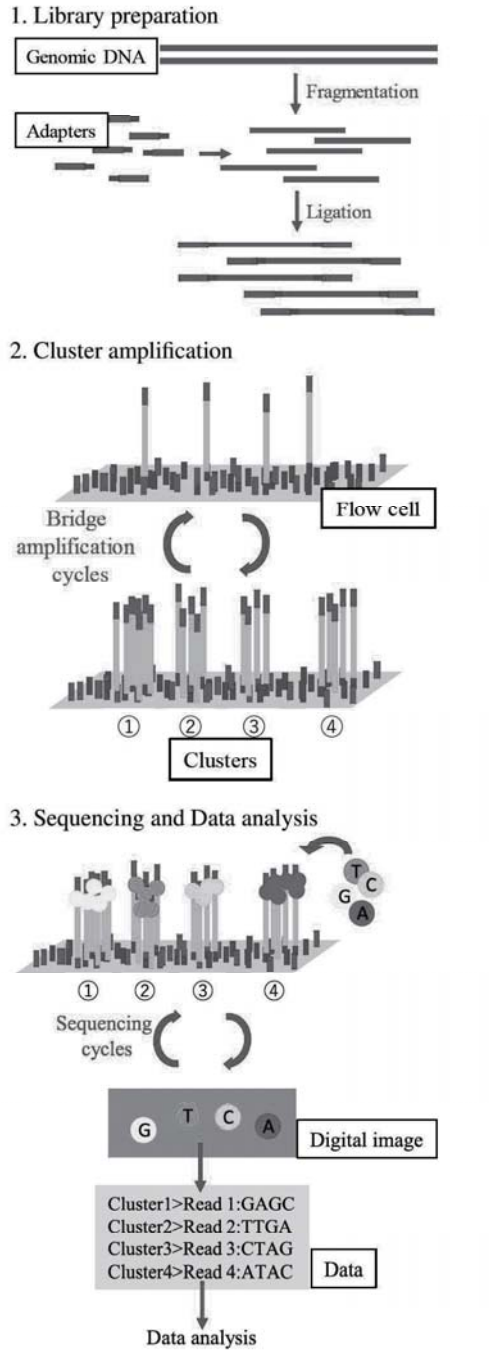

Fig. 2. Principle of 16S rDNA metagenomic analysis [13].

injected into the flow cell. Oligonucleotides that captured the sequence of adapters were bound to the surface of the flow cell at regular intervals. The injected DNA library attached to the oligonucleotide one fragment at a time and was then amplified by bridge PCR cycles to generate a cluster of fragments. Next, upon the addition of a reagent containing a fluorescently labeled base to the flow cell for the sequencing reaction, each cluster absorbed the fluorescently labeled base in the sequence reaction and emitted fluorescence upon excitation. At this time, the base was specified from the flow cell image along with the wavelength and intensity of the excitation light. By repeating this cycle, the base sequence of the DNA fragment was determined, and the number of bacterial species was analyzed from the number of clusters involving the same base sequence. The types of bacteria present in the machining fluid and their respective amounts in the microbial flora were confirmed from the analysis results.

2.3. Check Test of Bactericidal Effect with UFB

2.3.1. Culture of Strains for Sterilization and Preparation of Bacterial Fluid

Bacteria are divided into gram-negative bacteria and positive bacteria based on Gram staining depending on the differences in the structure of a cell wall. The cell wall of gram-negative bacteria is thinner than that of gram-positive bacteria and possesses a characteristic outer membrane [14]. In contrast, the cell wall of gram-positive bacteria is characterized by the presence of multiple peptidoglycan layers [15]. In this study, we focused on *Pseudomonas aeruginosa* produced in the machining fluid, which is a cause of infection among workers. *Pseudomonas aeruginosa* is characterized as gram-negative bacteria. *Staphylococcus aureus*, a widely known gram-positive bacterium, was used as a comparative control. The differences in the outcomes attributed to the difference in bacterial species, especially in the structure of the cell wall, were examined. *Pseudomonas aeruginosa* ATCC10145 and *Staphylococcus aureus* IFO12732 strains were used. Each strain was pre-cultured on a standard agar plate (manufactured by Nissui Pharmaceutical Co., Ltd.), and the generated colonies were dispersed in sterile phosphate-buffered saline to obtain a McFarland standard of 0.5–1. Bacterial fluid with an order of 10^8 CFU/mL was prepared.

2.3.2. Preparation of Machining Fluid for Sterilization Test and the Subsequent Test

Machining fluid for the sterilization test was prepared using each type of UFB water or sterile purified water as diluted water. Diluted water was added with a 2 mL sterile cryovial to prepare grinding fluid (water-soluble chemical type) with a final concentration of 2.5%. Subsequently, the aforementioned bacterial fluid was added to obtain the final concentration of 10^6 CFU/mL. Each vial is kept warm at 23°C for 2 hours in a cool incubator. The initial bacterial concentration and the bacterial concentration 2 hours after the immersion in each fluid were confirmed. This analysis was performed by measuring the number of colonies formed after culturing at 37°C for 24 hours by a serial dilution method using a standard agar plate.

2.4. Fluorescent Staining of Bacteria After Immersion in UFB Water and Observation with Fluorescence Microscope

To directly confirm the life and death of bacteria after immersion in the UFB water and estimate the bactericidal mechanism from the state of dead cells, *Pseudomonas*

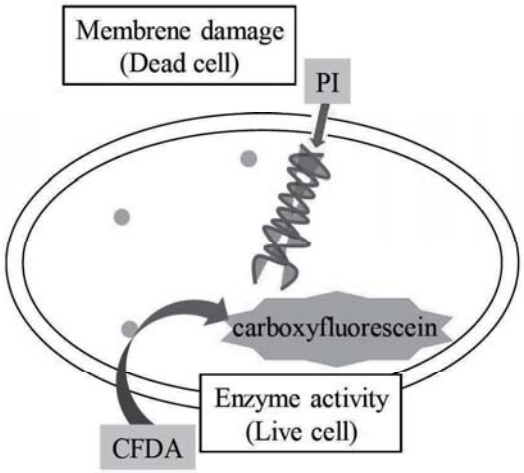

Fig. 3. Principle of the determination of live or dead bacterial cells by fluorescent staining [8].

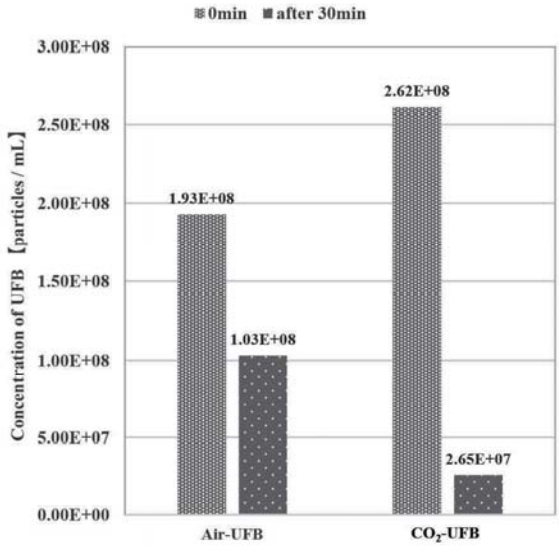

Fig. 4. Time-course changes in UFB concentration in each type of UFB fluid.

aeruginosa and *Staphylococcus aureus* were subjected to fluorescence-double staining with Bacstain CFDA (5(6)-carboxyfluorescein diacetate) and Bacstain PI (propidium iodide) (Dojin Chemical Laboratory) after immersion in each fluid. **Fig. 3** shows the staining principle of each fluorescent staining reagent. Although CDFA in **Fig. 3** does not exhibit fluorescence by itself, it produces fluorescent carboxyfluorescein after decomposition by esterase. Live cells take up CFDA into cells, produce carboxyfluorescein by decomposition with esterase, and emit fluorescence (green) at 515 nm with excitation at 493 nm [16]. In addition, as shown by the figure, the PI does not penetrate the normal cell wall. It only penetrates cells with damaged cell walls for staining nucleic acids. For this reason, PI is used for double staining with fluorescent dyes that demonstrate selectivity for live bacteria, such as CDFA [17]. The PI penetrates the cells that have died due to cell wall damage and emits fluorescence (red) at 620 nm with excitation at 530 nm [16].

After immersion in the UFB water, the bacterial fluid was double-stained with CFDA and PI, and subsequently, observed and photographed with a fluorescence microscope (BZ-9000 (Keyence) or Axiophot (Zeiss)).

3. Result and Discussion

3.1. UFB Concentration, Particle Size, and Concentration Distribution in UFB Water

The UFB concentration of both the Air-UFB water and the CO_2-UFB water was determined to be 10^7 particles/mL or higher. Since it was confirmed that the CO_2-UFB water has a lower UFB concentration than the Air-UFB water, the UFB concentration of each type in UFB water was compared immediately after preparation and 30 minutes after the preparation. The results are demonstrated in **Fig. 4**. As shown in **Fig. 4**, the number of UFBs in the Air-UFB water 30 minutes after preparation was approximately 53% of that observed immediately after preparation. However, in the CO_2-UFB water, the number of UFBs observed 30 minutes after preparation was significantly reduced to approximately 10% of that observed immediately after the preparation.

Figures 5 and **6** show the results of the measurement of UFB particle size and concentration distribution in each type of UFB water immediately after preparation and 30 minutes after preparation. CO_2-UFB demonstrated an average particle size of 160.2 nm (standard deviation 115.8 nm) immediately after preparation and 243.6 nm (standard deviation 152.3 nm) 30 minutes after preparation. Air-UFB showed an average particle size of 90.3 nm immediately after the preparation (standard deviation 33.0 nm) and 85.0 nm (standard deviation 27.3 nm) 30 minutes after preparation. These results indicate that the particle size of CO_2-UFB tends to increase over time compared to that of Air-UFB. Typically, microbubbles with a diameter of 1–100 μm are easily self-crushed [4]. The particle size of bubbles and the ease of self-crushing might be correlated.

The zeta potential used as an index of dispersion stability of colloidal particles with ELSZ-2000ZS manufactured by Otsuka Electronics was measured. The zeta potentials of CO_2-UFB and Air-UFB were -1.3 mV and -25.0 mV, respectively. Typically, colloidal particles tend to aggregate as the zeta potential approaches 0, and the repulsive force between the particles decreases. Hence, CO_2-UFB is more likely to aggregate than Air-UFB.

From the aforementioned results, the particle size of CO_2-UFB is more likely to increase than that of Air-UFB due to aggregation. As a consequence, the bubble collapse becomes easier. However, the mechanism of crushing due to the increase in the particle size of CO_2-UFB is unknown at this time, and detailed analysis will be conducted in the future.

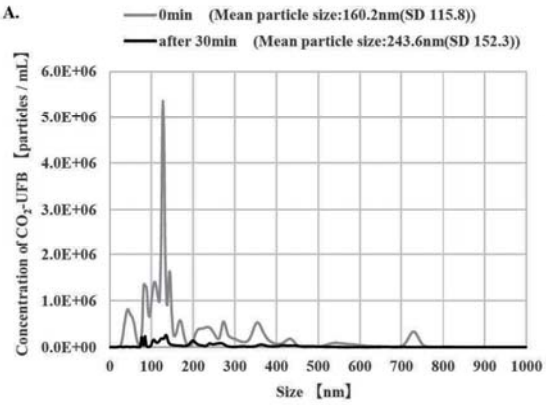

A: Immediately after preparation and 30 minutes later

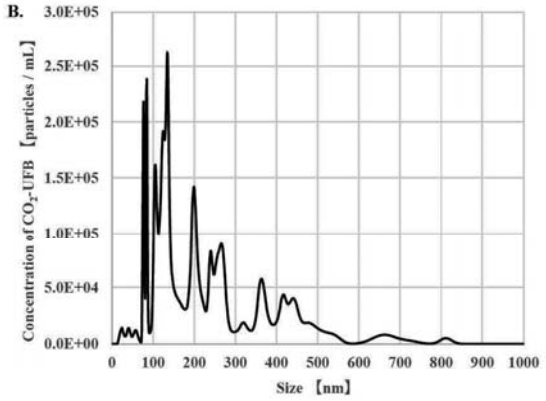

B: 30 minutes after preparation (scale expansion)

Fig. 5. Time-course changes in particle size and concentration distribution (CO_2-UFB).

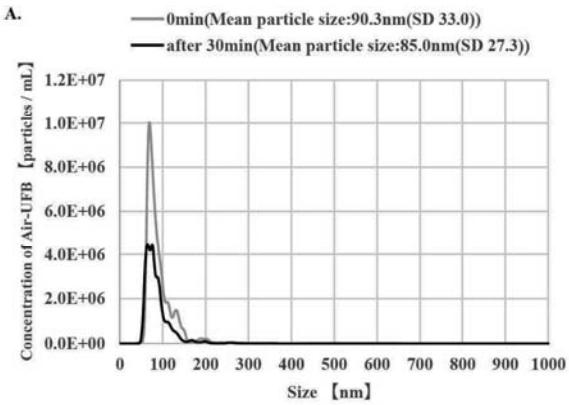

A: Immediately after preparation and 30 minutes later

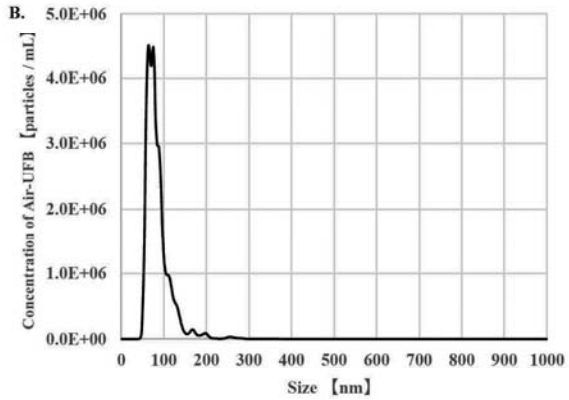

B: 30 minutes after preparation (scale expansion)

Fig. 6. Time-course changes in particle size and concentration distribution (Air-UFB).

3.2. Analysis of the Types of Bacteria Present in Machining Fluid and Their Respective Amounts in Microbial Flora (Analysis Results of 16S rDNA Metagenome)

To confirm the types of bacteria present in the machining fluid and their respective amounts in the microbial flora, the live cell count in the machining fluid was obtained and the flora was analyzed by performing a metagenomic analysis of the 16S rDNA genes. **Table 1** shows the results of the measurement of the number of live cells count observed in each type of machining fluid. Here, the cutting fluid (emulsion type) was diluted to a concentration of 6% for comparison. The cutting fluid was obtained after four months of use. As shown in **Table 1**, the grinding fluid and cutting fluid containing bacterial species with an order of 10^3 CFU/mL or more per mL were used for comparison. A higher amount of bacteria tends to be present in the cutting fluid than that in the grinding fluid. This can be attributed to the fact that the cutting fluid used in this study was the emulsion type, which is typically prone to putrefaction. Hence, bacterial growth is likely to occur.

Next, **Tables 2** and **3** show the results of 16S rDNA metagenome analysis of the grinding fluid and cutting fluid, respectively. As shown in **Tables 2** and **3**, *Pseudomonas diminuta* of the *Pseudomonas* genus occupied 16.23% of the microbial flora in the grinding fluid (**Table 2**). *Pseudomonas mendocina* of the *Pseudomonas* genus occupied 39.69% of the microbial flora in the cutting fluid. Various other *Pseudomonas* species such as *Pseudomonas xanthomarina* and *Pseudomonas panipatensis* were detected (**Table 3**). *Pseudomonas* genus are frequently detected in water-soluble machining fluid [2]. Based on the proportion of *Pseudomonas* genus in the live cells determined by measuring the number of live cells as shown in **Table 1** and the amount of the species belonging to *Pseudomonas* genus in **Tables 2** and **3**, the *Pseudomonas* genus was present with an order of 10^2 CFU/mL in the grinding fluid and the *Pseudomonas* genus with an

Table 1. Number of live cells in each type of machining fluid.

Type of machining fluid	Duration of use	Number of bacteria [CFU/mL]
Grinding fluid	3 month	3.1×10^3
Cutting fluid	4 month	8.6×10^4

Table 2. Results of 16S rDNA metagenome analysis of grinding fluid.

Species classification	%Total reads
Pseudomonas diminuta	16.23
Dyadobacter beijingensis	8.38
Methylobacillus glycogenes	6.05
Thermus thermophilus	4.83
Brevundimonas terrae	3.40
Aminobacter aminovorans	3.16
Comamonas testosteroni	2.68
Unclassified at species level	42.21
Other	13.06

Table 3. Results of 16S rDNA metagenome analysis of cutting fluid.

Species classification	%Total reads
Pseudomonas mendocina	39.69
Aerococcus viridans	3.87
Pseudomonas xanthomarina	2.36
Pseudomonas panipatensis	1.56
Pseudomonas pseudoalcaligenes	1.24
Pseudomonas stutzeri	0.88
Pseudomonas mosselii	0.77
Unclassified at species level	44.69
Other	4.94

Table 4. Grinding fluid sterilization test results (*Pseudomonas aeruginosa*).

Type grinding fluid	Additive rate [%]	Diluent	pH	Initial concentration of *P. aeruginosa* [CFU/mL]	Number of colonies after treatment [CFU/mL]	Sterilization rate [%]
Chemical type	2.5	Air-UFB	7.04	8.0×10^6	$< 8.0 \times 10^6$	0
–	–	Air-UFB	7.04	8.0×10^6	$< 8.0 \times 10^6$	0
Chemical type	2.5	CO_2-UFB	5.03	8.0×10^6	0	100
–	–	CO_2-UFB	5.03	8.0×10^6	0	100
Chemical type	2.5	Purified water	7.35	8.0×10^6	$< 8.0 \times 10^6$	0
–	–	Purified water	7.35	8.0×10^6	$< 8.0 \times 10^6$	0

order of 10^4 CFU/mL was present in the cutting fluid.

The aforementioned results showed that bacteria were present in both the grinding fluid and the cutting fluid, and the microbial flora was predominantly composed of the *Pseudomonas* genus. However, the cutting fluid used in this study also contained a fungicide. The effect of the fungicide is attenuated during long-term use and bacterial growth is likely to occur. However, it might be difficult to identify the factors that affect the increase or decrease of bacteria owing to the influence of the fungicide in short-term indoor experiments. Therefore, in the following sections, the results of the grinding fluid used as the machining fluid will be described.

3.3. Bactericidal Effect of UFB in Machining Fluid

The results described in the previous section showed that the bacteria are present in both the grinding fluid and the cutting fluid, and the *Pseudomonas* genus was present in the highest amount. Hence, we focused on *Pseudomonas aeruginosa* species, which is relatively easy to use in experiments. The bactericidal effect of UFB was examined.

Table 4 shows the results confirming the bactericidal effect of UFB on *Pseudomonas aeruginosa* present in the grinding fluid. A column in **Table 4** in which the type of grinding fluid is described as "–" represents a test group of only the diluent to which the grinding fluid is not added. The number of colonies observed after treatment demonstrated the number of live cells after two hours of immersion in each fluid. The sterilization rate was determined based on the immersion with respect to the initial bacterial count. The rate of decrease in the number of live cells after the immersion was calculated. Based on **Table 4**, the number of bacteria was higher than the initial number in the grinding fluid obtained using the sterilized purified water and Air-UFB water as diluting fluid. The bactericidal effect was not observed on *Pseudomonas aeruginosa*. In contrast, colonies of *Pseudomonas aeruginosa* were not detected in the grinding fluid in which CO_2-UFB water was used as diluting fluid. The sterilization rate was determined as 100%. The effect of metal ions that might have mixed from the UFB generator was considered to be negligible as the bactericidal effect was not confirmed by Air-UFB.

Next, to determine the cause of the bactericidal effect of CO_2-UFB fluid on *Pseudomonas aeruginosa*, the change in pH was examined that was not observed in Air-UFB fluid or sterilized purified water. Specifically, as shown by the results in **Table 4**, the pH of both the Air-UFB fluid and the sterilized purified water was approximately 7. In contrast, the pH of the CO_2-UFB fluid was low, i.e., 5.03. Hence, the difference in pH might be considered as a cause of the bactericidal effect. **Table 5** shows the results of the bactericidal effect of CO_2-UFB fluid and sterilized purified water with a unified pH of approximately 5 on *Pseudomonas aeruginosa*. Based on **Table 5**, the bactericidal effect was confirmed only in the CO_2-UFB fluid even when the pH was set to the same level. Considering

Table 5. Sterilization test results of grinding fluid considering the influence of pH (*Pseudomonas aeruginosa*).

Type grinding fluid	Additive rate [%]	Diluent	pH	Initial concentration of *P. aeruginosa* [CFU/mL]	Number of colonies after treatment [CFU/mL]	Sterilization rate [%]
Chemical type	2.5	CO_2-UFB	5.03	8.0×10^6	0	100
–	–	CO_2-UFB	5.03	8.0×10^6	0	100
Chemical type	2.5	Purified water	5.01	1.8×10^6	$< 1.8 \times 10^6$	0
–	–	Purified water	5.01	1.8×10^6	$< 1.8 \times 10^6$	0

*The pH of purified water (pH 7.35) was adjusted to pH 5.01 the same as that of CO_2-UFB.

Table 6. Grinding fluid sterilization test results (*Staphylococcus aureus*).

Type grinding fluid	Additive rate [%]	Diluent	pH	Initial concentration of *S. aureus* [CFU/mL]	Number of colonies after treatment [CFU/mL]	Sterilization rate [%]
Chemical type	2.5	Air-UFB	7.04	1.4×10^6	$< 1.4 \times 10^6$	0
–	–	Air-UFB	7.04	1.4×10^6	$< 1.4 \times 10^6$	0
Chemical type	2.5	CO_2-UFB	5.03	1.4×10^6	$< 1.4 \times 10^6$	0
–	–	CO_2-UFB	5.03	1.4×10^6	$< 1.4 \times 10^6$	0
Chemical type	2.5	Purified water	7.35	1.4×10^6	$< 1.4 \times 10^6$	0
–	–	Purified water	7.35	1.4×10^6	$< 1.4 \times 10^6$	0

that *Pseudomonas aeruginosa* can normally live in fluid with a pH of 5.0 [18], it is reasonable to assert that no bactericidal effect was observed in the sterilized purified water. Therefore, the bactericidal effect of CO_2-UFB could not be attributed to the pH. The details are outlined in the next section.

3.4. Examination of Factors Responsible for the Bactericidal Effect of CO_2-UFB

In this study, we examined the impact of crushing UFB as a factor responsible for the bactericidal effect of CO_2-UFB. Among FBs, microbubbles with a particle size of 1–100μm can exhibit a bactericidal and disinfecting effect upon self-crushing [4]. The crushing action can also be demonstrated by UFB and might be responsible for the bactericidal effect.

Hence, the differences in the thickness and structure of the bacterial cell wall were examined. The bactericidal effect of UFB on *Staphylococcus aureus* was different from that observed on *Pseudomonas aeruginosa*. **Table 6** shows the results. The findings demonstrate that the amount of *Staphylococcus aureus* increased from the initial number observed in all test groups of CO_2-UFB fluid, Air-UFB fluid, and sterilized purified water; the bactericidal effect was not confirmed. As mentioned above, the variations in cell wall thickness and structure might be the cause of the difference in bactericidal effect on *Pseudomonas aeruginosa* and *Staphylococcus aureus*. The thickness of the cell wall of *Pseudomonas aeruginosa* is 6–10 nm [14] while that of the *Staphylococcus aureus* is 20–40 nm [19]. In addition, the cell wall of the gram-positive bacteria including the *Staphylococcus aureus* is composed of multiple peptidoglycan layers that counteract the internal pressure of the bacterial cells and prevent lysis [15]. Gram-negative bacteria demonstrate a pressure resistance of approximately 5 atm. In contrast, the gram-positive bacteria demonstrate a pressure resistance of approximately 25 atm [20]. *Staphylococcus aureus* demonstrates superior properties compared to *Pseudomonas aeruginosa* with respect to both thickness and structure. It cannot be easily affected by the impact of crushing UFB. As a result, the bactericidal effect of UFB was not observed on *Staphylococcus aureus*.

In addition, the lifespan of the UFB can be related to the difference in the effect attributed to the variations in the gas types present in the UFB. Originally, the UFB remained in the fluid for a long period. However, the zeta potential of CO_2-UFB was closer to 0 compared to that of Air-UFB, and the particles are more likely to aggregate. Based on the results shown in **Figs. 4** and **5**, the CO_2-UFB was more easily crushed as its particle size increased in a short period owing to the aggregation compared to Air-UFB. Therefore, the bactericidal effect of CO_2-UFB was confirmed. It should be noted that the effect can be observed upon long term usage of Air-UFB as well. The control of the bactericidal effect was also examined by measures involving the combination of active crushing of the UFB. Since *Pseudomonas aeruginosa* is an aerobic bacterial species, the effect of dissolved oxygen deficiency was analyzed using UFB (N_2-UFB) containing nitrogen gas. However, N_2-UFB did not demon-

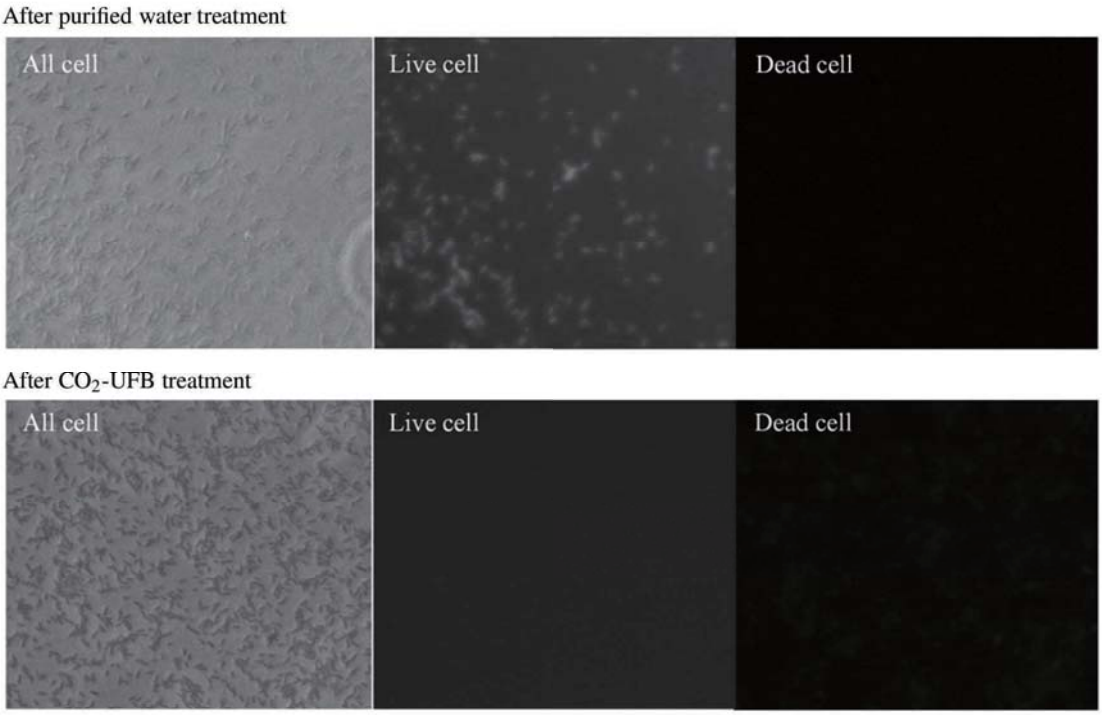

Fig. 7. Fluorescent staining results after immersion in CO_2-UFB fluid and sterile purified water (*Pseudomonas aeruginosa*).

strate a sterilization effect against *Pseudomonas aeruginosa* and *Staphylococcus aureus*. Therefore, the bactericidal effect of CO_2-UFB on *Pseudomonas aeruginosa* was not attributed to the lack of dissolved oxygen.

Next, to confirm that the bactericidal effect of CO_2-UFB is due to the impact of crushing UFB, *Pseudomonas aeruginosa* was directly observed after immersion in the UFB fluid. A live and a dead cells and their cell walls were observed by specific fluorescent staining. The presence or absence of damage was determined. **Fig. 7** shows the results of fluorescence microscopic observation of the *Pseudomonas aeruginosa* after immersion in CO_2-UFB fluid and sterile purified water. The left panel of **Fig. 7** represents an observation image obtained with a phase-contrast microscope that confirms the morphology. The center panel represents the CFDA fluorescence observation image. The live cells are characterized by green fluorescence. The right panel demonstrates a fluorescence observation image of PI. Dead cells with cell wall damage are characterized by red fluorescence. Based on **Fig. 7**, *Pseudomonas aeruginosa* after immersion in the sterile purified water demonstrated green fluorescence, and staining by CFDA was confirmed. However, CFDA-stained bacteria were not observed. *Pseudomonas aeruginosa* demonstrated red fluorescence after immersion in CO_2-UFB fluid owing to the effect of PI. Based on the aforementioned results, the cause of the death of *Pseudomonas aeruginosa* was determined as the cell wall damage caused by CO_2-UFB.

Similarly, *Staphylococcus aureus* that was immune to the bactericidal effect was observed with a fluorescence microscope after immersion in the CO_2-UFB fluid. As shown by **Fig. 8**, for *Staphylococcus aureus*, green fluorescence emitted by CFDA was observed both after immersion in the sterile purified water and the CO_2-UFB fluid; red fluorescence emitted by PI was not observed. Therefore, the cell wall damage caused by CO_2-UFB did not affect *Staphylococcus aureus* to the extent of sterilization.

Based on the aforementioned results, CO_2-UFB was able to kill *Pseudomonas aeruginosa* by inducing cell wall damage.

4. Conclusions

In this study, attempts were made to suppress the growth of bacteria in the machining fluid using UFB containing CO_2 and air. First, the target bacterial species were identified by analyzing the bacterial species generated in the machining fluid and their respective amounts in the microbial flora. Furthermore, the bactericidal effect of each type of UFB on the bacterial species was examined. The following results were obtained.

1) The results of the analysis of microbial flora confirmed that the *Pseudomonas* genus comprises the predominant species in the machining fluid.

2) The bactericidal effect of UFB containing CO_2 and air on *Pseudomonas aeruginosa*, a type of the *Pseudomonas* genus, was examined. As a consequence, a potent bactericidal effect of CO_2-UFB was confirmed.

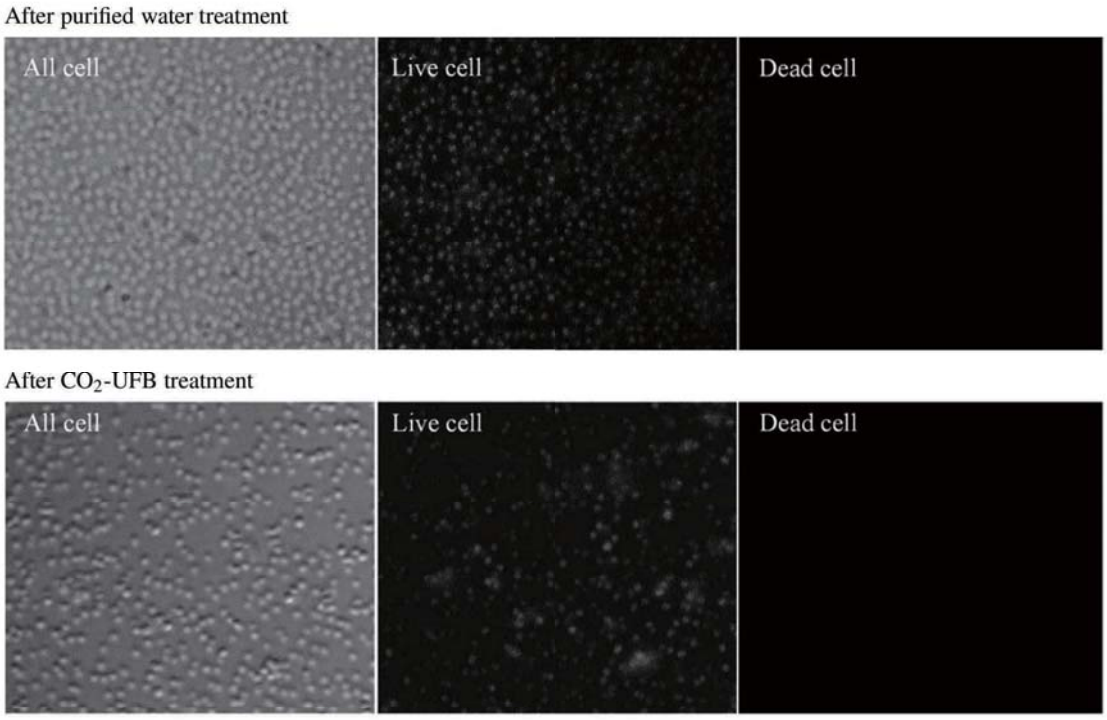

Fig. 8. Fluorescent staining results after immersion in CO_2-UFB fluid and sterile purified water (*Staphylococcus aureus*).

3) The UFBs did not demonstrate a bactericidal effect on *Staphylococcus aureus* used for comparison of the effect on *Pseudomonas aeruginosa*.

4) The bactericidal effect of CO_2-UFB might be attributed to the induction of the damage of bacterial cell walls impacted by the crushing of UFB. This finding was also supported by microscopic observations.

The aforementioned results indicate that CO_2-UFB can sterilize the machining fluid without the use of chemicals by exterminating *Pseudomonas* genus produced in the fluid.

Acknowledgements

A part of this study was supported by JSPS KAKENHI Grant Number 19H00734. We would like to express our gratitude here.

References:

[1] F. P. Ferraz de Campos, A. Felipe-Silva et al., "Community-acquired Pseudomonas aeruginosa-pneumonia in a previously healthy man occupationally exposed to metalworking fluids," Autops Case Rep., Vol.4, No.3, pp. 31-37, 2014.
[2] N. Di Maiuta, A. Rufenacht, and P. Kuenzi, "Assessment of bacteria and archaea in metalworking fluids using massive parallel 16S rRNA gene tag sequencing," Lett. Appl. Microbiol., Vol.65, No.4, pp. 266-273, 2017.
[3] L. E. Maier, H. P. Lampel, T. Bhutani, and S. E. Jacob, "Hand dermatitis: a focus on allergic contact dermatitis to biocides," Dermatol. Clin., Vol.27, pp. 251-264, 2009.
[4] Asahi Research Center report (RS-1007), November 2016 (in Japanese).
[5] M. Takahashi, "Environmental Improvement and Food Safety by Micro-Bubble Technology," Bulletin of the Society of Sea Water Science, Japan, Vol.59, No.1, pp. 17-22, 2005 (in Japanese).
[6] H. Ohnari, "The Characteristics and Possibilities of Micro Bubble Technology," J. of MMIJ, Vol.123, No.3, pp. 89-96, 2007 (in Japanese).
[7] R. Shibuya, "Application of Fine Bubbles," J. of the Surface Finishing Society of Japan, Vol.68, No.6, pp. 335-337, 2017 (in Japanese).
[8] K. Inazawa, H. Ohmori, and N. Itoh, "Effects of O_2 Fine Bubbles on ELID Grinding Using Conductive Rubber Bond Grinding Wheel," Int. J. Automation Technol., Vol.13, No.5, pp. 657-664, 2019.
[9] S. Ninomiya, T. Shimizu, M. Iwai, and K. Suzuki, "Purification effect of micro bubble coolant," J. of Japan Society for Abrasive Technology, Vol.56, No.7, pp. 465-469, 2012 (in Japanese).
[10] T. Q. Luu, P. N. Hong Truong, K. Zitzmann, and K. T. Nguyen, "Effects of Ultrafine Bubbles on Gram-Negative Bacteria: Inhibition or Selection?," Langmuir, Vol.35, No.42, pp. 13761-13768, 2019.
[11] H. Tsuge, "Fundamentals of Microbubbles and Nanobubbles," Bulletin of the Society of Sea Water Science, Japan, Vol.64, No.1, pp. 4-10, 2010 (in Japanese).
[12] http://www.nano-x.co.jp/nanoquick [Accessed May 1, 2020]
[13] https://jp.illumina.com/science/technology/next-generation-sequencing/ngs-vs-sanger-sequencing.html [Accessed May 1, 2020]
[14] A. Yauchi and K. Arima, "Cell wall of bacteria," Bioscience, Biotechnology, and Biochemistry, Vol.2, No.10, pp. 674-682, 1974 (in Japanese).
[15] T. Uehara, "Synthesis of Cell Wall on Bacterial Morphosis," The J. of Biochemistry, Vol.85, No.5, pp. 349-353, 2013 (in Japanese).
[16] https://www.dojindo.co.jp/products/BS03/ [Accessed May 1, 2020]
[17] N. Yamaguchi and M. Nasu, "Flow cytometric analysis of bacterial respiratory enzymatic activity in the natural aquatic environment," J. of Appl. Microbiol., Vol.83, pp. 43-52, 1997.
[18] R. Sakazaki, "Bacteriology of Pseudomonas aeruginosa," Media-Circle, Vol.10, pp. 281-289, 1965 (in Japanese).
[19] T. Higuchi, "New Method for Overcoming Drug Resistance," Shikoku Acta Medica, Vol.58, No.3, pp. 107-121, 2002 (in Japanese).
[20] S. Fukui, "Cell Wall of Bacteria," J. of the Brewing Society of Japan, Vol.66, No.8, pp. 753-758, 1971 (in Japanese).

Name:
Hiroko Yamada

Affiliation:
Graduate School of Biomedical Engineering, Tohoku University

Address:
6-6-01 Aramaki Aza-Aoba, Aoba-ku, Sendai, Miyagi 980-8579, Japan

Brief Biographical History:
1999 Received Master of Agriculture degree from Gifu University
1999-2000 Researcher, Gifu Prefectural International Research Institute for Biotechnology
2000-2003 Chief Researcher, RAKAN Co., Ltd.
2000-2003 External Collaborative Researcher, Graduate School of Medicine, Gifu University
2003-2016 Director / Chief Technology Officer, Contig-i Co., Ltd. (venture company of Gifu University)
2018- President, Symbiotech Labo Co., Ltd.

Main Works:
- Sterilization technology, activation technology of bacteria, detection technology of bacteria

Membership in Academic Societies:
- Japan Society for Abrasive Technology (JSAT)
- Society of Environmental Conservation Engineering (SECE)

Name:
Kensuke Konishi

Affiliation:
Graduate School of Engineering, Tohoku University

Address:
6-6-01 Aramaki Aza-Aoba, Aoba-ku, Sendai, Miyagi 980-8579, Japan

Brief Biographical History:
2019 Received Bachelor of Engineering degree from Tohoku University

Name:
Keita Shimada

Affiliation:
Assistant Professor, Department of Mechanical Systems Engineering, Graduate School of Engineering, Tohoku University

Address:
6-6-01 Aramaki Aza-Aoba, Aoba-ku, Sendai, Miyagi 980-8579, Japan

Brief Biographical History:
2009 Received M.E. from Tohoku University
2012 Received Ph.D. from Tohoku University
2012- Assistant Professor, Department of Mechanical Systems Engineering, Tohoku University

Main Works:
- Micro/meso mechanical manufacturing (M4 process), ultrasonic assisted machining, abrasive process

Membership in Academic Societies:
- Japan Society of Mechanical Engineers (JSME)
- Japan Society for Precision Engineering (JSPE)
- Japan Society for Abrasive Technology (JSAT)

Name:
Masayoshi Mizutani

Affiliation:
Associate Professor, Department of Mechanical Systems Engineering, Graduate School of Engineering, Tohoku University

Address:
6-6-01 Aramaki Aza-Aoba, Aoba-ku, Sendai, Miyagi 980-8579, Japan

Brief Biographical History:
2003 Received M.E. from Integrated Design Engineering, Graduate School of Science and Technology, Keio University
2004- Junior Research Associate, Ohmori Materials Fabrication Laboratory, RIKEN
2006 Received Ph.D. from Integrated Design Engineering, Graduate School of Science and Technology, Keio University
2006- Collaboration Researcher, Advanced Development and Supporting Center, RIKEN
2007- Collaboration Researcher, Ohmori Materials Fabrication Laboratory, RIKEN
2009- Special Postdoctoral Researcher, Ohmori Materials Fabrication Laboratory, RIKEN
2011- External Collaborative Researcher, Sophia University
2012- Collaboration Researcher, Ohmori Materials Fabrication Laboratory, RIKEN
2012- Associate Professor, Department of Mechanical Systems and Design, Tohoku University

Main Works:
- Micro/meso mechanical manufacturing (M4 process), laser process, powder jet deposition (PJD), functional interface, biomaterials, bio-medical applications, biomimetic surface

Membership in Academic Societies:
- Japan Society of Mechanical Engineers (JSME)
- Japan Society for Precision Engineering (JSPE)
- Japan Society for Abrasive Technology (JSAT)

Name:
Tsunemoto Kuriyagawa

Affiliation:
Professor, Bio-Medical Interface Fabrication Laboratory, Graduate School of Biomedical Engineering, Tohoku University

Address:
6-6-01 Aramaki Aza-Aoba, Aoba-ku, Sendai, Miyagi 980-8579, Japan

Brief Biographical History:
1984-1990 Research Associate, Tohoku University
1990-1992 Assistant Professor, Tohoku University
1991-1992 Visiting Professor, University of Connecticut
1992-2002 Associate Professor, Tohoku University
2003- Professor, Tohoku University

Main Works:
- Nano-precision mechanical manufacturing, micro/meso mechanical manufacturing (M4 process), powder jet deposition, and creation of functional interface

Membership in Academic Societies:
- Science Council of Japan (SCJ)
- International Committee for Abrasive Technology (ICAT)
- International Society for Nanomanufacturing (ISNM)
- Japan Society of Mechanical Engineers (JSME)
- Japan Society for Precision Engineering (JSPE)
- Japan Society for Abrasive Technology (JSAT)

Surface & Coatings Technology 408 (2021) 126803

Contents lists available at ScienceDirect

Surface & Coatings Technology

journal homepage: www.elsevier.com/locate/surfcoat

Surface smoothing of bulk metallic glasses by femtosecond laser double-pulse irradiation

Tie Li [a,b], Yang Guo [a], Masayoshi Mizutani [c], Shaolin Xu [a,*]

[a] Department of Mechanical and Energy Engineering, Southern University of Science and Technology, Shenzhen 518055, People's Republic of China
[b] Songshan Lake Materials Laboratory, Dongguan 523808, People's Republic of China
[c] Department of Mechanical Systems Engineering, Graduate School of Engineering, Tohoku University, Sendai 980-8579, Japan

ARTICLE INFO

Keywords:
Femtosecond laser
Double-pulse
Surface smoothing
Bulk metallic glasses

ABSTRACT

Bulk metallic glasses (BMGs) with amorphous structure have excellent mechanical and chemical properties. In polishing process, it is hard but important to maintain amorphous state to keep original properties of BMGs, which are easily crystallized in traditional mechanical polishing and long-pulse laser polishing. In this paper, we first propose to use femtosecond laser double-pulse irradiation to smooth the surface of Zr-based BMG and make it free of laser-induced periodic surface structures and crystallization. Here, the smooth surface with half decreasing in roughness (Sa) to 111 nm is achieved by optimized parameters with laser pulse energy 0.06 μJ of the first pulse, energy ratio 40% of the first to the second pulse and time delay 20 ps. Obvious transition from a coarse surface to a smooth one occurs at near 10 ps time delay and 40% energy ratio. Mobility enhancement of molten materials guarantees the removal of undesirable surface structures through surface tension and gravity. Crystallization is avoided due to rapid heating and cooling under femtosecond laser double-pulse irradiation. A smoothed BMG surface obtained by this method verifies its feasibility in BMGs polishing.

1. Introduction

Bulk metallic glasses (BMGs) , produced by rapid cooling of liquid metallic alloys, are amorphous materials with short-range ordered and long-range disordered characteristics of atoms arrangement [1]. Due to the advantages of high strength and good corrosion resistance, BMGs are very suitable for commercial applications such as sports equipment, electronic products, medical apparatus as well as precision die molds [2]. The performance of BMG components is affected by their surface roughness, and thus further polishing process is generally required after casting process to reduce the surface roughness of BMGs. Since the amorphous state of BMGs is metastable, mechanical polishing may cause crystallization transformation of BMGs [3], which is a phenomenon that should be avoided in the process of polishing. Ion beam polishing has been used to obtain smooth BMG surface without any crystallization [4], while this method requires expensive and sophisticated equipment with a relatively long polishing time. The abrasive water jet method for polishing BMGs has the problems of abrasive pollutant and complexity of influence factors, although polishing precision can be improved by applying micro abrasives [5]. Therefore, how to efficiently obtain a smooth surface without crystallization is an important issue in the polishing of BMGs.

As a commonly used polishing method, laser polishing has proved its effectiveness on the surface of various materials [6–8], and the surface roughness can be controlled below 100 nm. The principle of laser polishing is that the surface layer of material evaporates and melts under laser irradiation, and flows under the action of surface tension and gravity. The valleys of the original rough surface are filled with molten materials, which eventually cool and solidify to form an ideal smooth surface [9]. The advantage of laser polishing is that it can perform flexible polishing on complex geometric shapes [10], and it has good adaptability to a variety of materials. At present, laser polishing technology mainly uses high-power nanosecond laser or continuous laser as the heat source, and the intense thermal effect is conducive to the material remelting process, thereby improving the polishing efficiency. As for bulk metallic glasses, localized heating of laser irradiation may cause crystallization [11]. However, some studies have shown that careful regulation of nanosecond laser parameters can help BMGs maintain their original amorphous state after laser irradiation [12]. Compared with nanosecond lasers, femtosecond lasers irradiation with less thermal effect can keep the amorphous state unchanged under a wider range of irradiation conditions [13,14]. However, the extremely high peak power

* Corresponding author.
E-mail address: xusl@sustech.edu.cn (S. Xu).

https://doi.org/10.1016/j.surfcoat.2020.126803
Received 24 September 2020; Received in revised form 22 December 2020; Accepted 23 December 2020
Available online 2 January 2021

of femtosecond laser may cause ablation and removal of material, and laser induced periodic surface structures (LIPSS) generally appear [15–17], which will increase the surface roughness of metallic glass. Therefore, it is difficult to polish metallic glass using a femtosecond laser directly.

The femtosecond laser double-pulse irradiation method is a kind of pulse shaping technique in the time domain, which has important applications in laser-induced breakdown spectroscopy (LIBS) detection technology [18] and nanoparticle manipulation [19]. In terms of material processing, by changing the time delay (time interval) between two pulses, the second pulse can reach the surface of the material before physical processes triggered by the first pulse finished, which can cause the surface morphology of the target to subject to the coordinated controlling effects of the two pulses. In the literature on double-pulse processing, metal materials such as aluminum, stainless steel, monocrystalline silicon and silicon dioxide can yield improvements in microholes and microgrooves ablation morphology with smoother surface [20–24]. The thickness of the heat affected zone of femtosecond laser irradiation is much thinner than that of nanosecond pulse laser. Therefore, if the femtosecond laser double-pulse irradiation method can be used for BMGs' polishing, the unfavorable results such as recrystallization can be significantly suppressed.

In this paper, we used the time-domain control method of femtosecond laser double-pulse irradiation to achieve surface smoothing of zirconium-based BMGs, and the critical point with and without LIPSS was found in the evolution of time delay and pulse energy ratio between two pulses. X-Ray Diffraction (XRD) test results showed that the amorphous state of metallic glass remains unchanged after the femtosecond laser double-pulse irradiation. This research is expected to promote the practical application of femtosecond laser double-pulse irradiation for polishing of amorphous alloys.

2. Materials and methods

The construction of the femtosecond laser double-pulse irradiation system, which refers to the principle of Mach-Zehnder interferometer, is shown in Fig. 1. The raw laser beam was separated into two different beams (a reference beam and a delayed beam) through a beam splitter. The optical path difference of the two beams was precisely adjusted to obtain specific double-pulse time delay through a precision linear motion control stage (SM-50, Newport) with a step resolution of 1 μm. Before laser processing, the zero point of two pulses in time domain was confirmed experimentally, which means the two pulses achieve workpiece without time delay. Specifically, interference fringes can be observed when two beams combine with a time delay less than two times of pulse duration and without positional deviation by using a laser beam quality analyzer (BGP-LT665, Ophir). The optical path difference of the two beams was adjusted to get the clearest and brightest interference fringes when the two pulses combine without time delay at the zero point. Then, the double-pulse delay time was precisely control by adjusting the linear motion control stage. The neutral density filters were used to change the pulse energy of the reference beam and the delayed beam. A Glan laser polarizer (GLP) and a half-wave plate are combined to adjust the total pulse energy lineraly before pulse delay optical path. A coaxial CCD was used for determining focus position and observing.

A femtosecond laser (Spectra Physics, SpOne-8-SHG) with a central wavelength of 520 nm and pulse width of 300 fs was applied for experiments. The linearly polarized gaussian beam was focused by an objective lens (4×, NA=0.10). The focused laser spot size in our work was estimated by using the method proposed by Liu [25], which is the widely accepted method to determine ablation thresholds of materials. The laser scanning velocity and the repetition frequency were set as 100 μm/s and 1 kHz, respectively. The applied repetition frequency of 1 kHz was referred to amounts of literatures on femtosecond laser machining, and a relatively low scanning velocity was chosen to meet the demand of enough incident pulses per unit area to reveal the ablation. In order to explore the double-pulse effects on the laser processed surface morphology, the double-pulse delay time variables including 0 ps, 1 ps, 2 ps, 4 ps, 10 ps, 20 ps and 40 ps, and the energy ratio of the second pulse to the first one ranging from 0 to 100% were selected. The pulse energy is measured by a calibrated power meter (1919-R, Thorlabs) after the laser transmitting from objective lens. The parameters for femtosecond laser double-pulse irradiation experiments are summarized in Table 1.

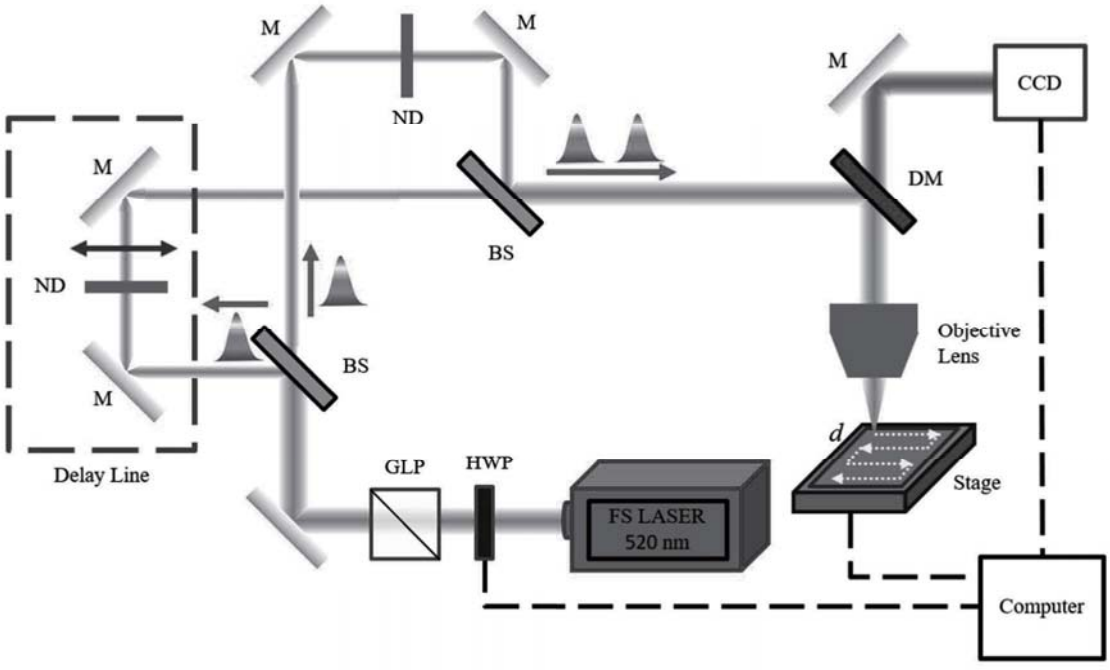

Fig. 1. Schematic of the optical path of the femtosecond laser double-pulse irradiation system. (HWP: half-wave plate; GLP: Glan laser polarizer; BS: beam splitter; M: mirror; ND: neutral density filter; DM: dichroic mirror).

Table 1
Parameters for femtosecond laser double-pulse irradiation experiments.

Parameters	Value
Wavelength (nm)	520
Pulse width (fs)	300
Repetition frequency (kHz)	1
Scanning velocity (μm/s)	100
Spot size (μm)	8.6
Objective lens	4 ×(NA=0.10)
Time delay (ps)	0–40
Energy ratio (%)	0–100

The Zr-based BMG samples used in the experiment were provided by Yi'an Technology Co., Ltd. (Dongguan, China) with the composition of $Zr_{58}Cu_{15}Ni_{12}Al_{10}Nb_3Re_2$. The crystallization temperature of the metallic glass sample is 688 K, and the glass transition temperature is about 313 K. The sample size is 20 mm × 10 mm × 2 mm. Before the femtosecond laser double-pulse irradiation and surface observing processes, the samples were ultrasonically cleaned in ethanol and in deionized water for 10 mins and dried by N_2 gas successively. The testing equipment used in the experiment includes a field-emission scanning electron microscope (SEM, Merlin Gemini II, Zeiss) for observing the surface morphology of samples, a laser scanning confocal microscope (VK-X1000, Keyence) with two kinds of light source (white light and 404 nm violet laser) and four types of objective lens (10×, 20×, 50×, 150×, Olympus Plan) for measuring the processing depth and surface roughness, and an X-ray diffractometer (Smartlab, Rigaku) for characterizing the structures of samples. All the surface measurement conditions are summarized in Table 2.

3. Results and discussions

3.1. Time delay manipulation of double-pulse irradiation

In order to investigate ablation characteristics of metallic glass by femtosecond laser double-pulse irradiation, the scanning morphology with different pulse energy and delay time was observed as shown in Fig. 2. The energy of the first pulse and the second pulse was kept the same. According to morphological characteristics of the experimental groups, the ablation morphology could be divided into four main areas: (1) Coarse zone, corresponding to the upper part of Fig. 2 (0 ps - 4 ps). The common feature was LIPSS in the processing area, and the LIPSS in the processing center area were interrupted by vertical ridge structures. As the laser energy increased to 0.13 μJ, a deeper groove appeared in the processing center area. The shorter the pulse delay time, the less laser energy was required for the grooves to occur. (2) Transition zone, corresponding to the 10 ps time delay group in Fig. 2. In this case, the LIPSS at lower pulse energy disappeared, and the LIPSS at higher energy were inclined and no longer continuous. (3) Smooth zone, corresponding to the lower left corner area in Fig. 2. The LIPSS disappeared completely, and the processing area was very smooth. (4) Wrinkled zone, corresponding to the lower right corner area in Fig. 2. The laser pulse energy used in this area was relatively high, and the processing area remained smooth, but at the same time, some other severe ablation characteristics appeared.

Table 2
Conditions for surface profiles/roughness and XRD measurement.

Items		Value
Surface profiles/ roughness	Objective lens	10×, 20×, 50×, 150×
	Evaluation area	200 μm × 200 μm
	Cut off wavelength	2.5/25 μm
	Scanning mode	Dual scan (white light and laser)
	Analysis software	Keyence Multi-analyzer software (VK-H2J)
	Voltage	45 kV
	Current	200 mA
XRD	Target	CuKα
	Scanning step	0.02°
	Scanning range	10–80°

Fig. 3 shows four types of typical scanning ablation morphology under the same pulse energy (0.11 μJ). The coarse zone, transition zone, smooth zone and wrinkled zone corresponded to 0 ps, 10 ps, 20 ps and 40 ps, respectively. By observing the rough morphology in Fig. 3(a), it was easy to find that a large number of ablative particles were attached to the processing region as well as non-processed areas. LIPSS with various lengths were distributed on the ablation edges, which corresponded to the area with less energy of Gaussian beam. In Fig. 3(b), there were still ablative particles distributed in the processed and non-processed areas, but the number was considerably reduced. Furthermore, there were obvious ablative traces in the form of irregular ablative holes in the processing area In Fig. 3(c), most ablation particles disappear, and there were no ablative traces. The LIPSS disappeared completely, and the processing area was very smooth. In Fig. 3(d), there were ripple-like structures parallel to the laser scanning direction, and their straightness was high. Continuous and dense ablation holes appeared in the center of the processing area. Compared with Fig. 3(c), the ablation phenomenon seems severe. Furthermore, high-spatial frequency LIPSSs (HSFLs) were observed at the side edge of machined region in all the Figs. 3(b)-3(c), which attribute to the increase of the pulse overlap ratio caused by the double-pulse irradiation processes.

By analyzing the evolution of the microgrooves morphology with the increase of delay time in Fig. 3, the changes could be summarized from four aspects as follows: (1) The reduction of ablative particles. The deposition of ablative particles was a typical feature of the phase explosion in laser ablation, and the characteristic time of phase explosion is between picosecond and nanosecond after the laser reaching the material surface [26]. According to the fact that the ablative particles in the non-processed area could not be covered by the second pulse, it can be inferred that when the second pulse reaches the material surface, the physical process of phase explosion caused by the first pulse has not yet occurred. The introduction of the second pulse after a certain delay time inhibits the phase explosion process of the material under laser irradiation. (2) The surface smoothing of the micro-grooves. We believe that femtosecond laser double-pulse irradiation method with suitable delay time can suppress the generation of phase explosion, and convert the materials removal process to liquid layer spallation, leading to a smooth surface with materials melting and flowing. The previous study [27] has shown that there are two materials removal mechanisms in the strong ablation regime of ultrafast laser, including phase explosion and spallation. In the case of the phase explosion mechanism, vapor and small clusters of materials eject from surface in a very violent way less likely to melt and flow. As for the spallation mechanism, the removal of materials occurs in a mild way accompanied with melting and flowing. Then, due to the superior mobility of molten metallic glass [21], the surface valleys can be filled with molten materials under the control of surface tension and gravity, which helps to form a smooth surface eventually. Fig. 4 shows the different surface formation mechanisms under femtosecond laser single-pulse irradiation and double-pulse irradiation. Based on the results in Fig. 2, it can be inferred that the smoothing effect of this double-pulse irradiation starts at a delay time between 4 ps and 10 ps, when ablative traces can be observed in rough areas. It reached a stable state at around 20 ps, and the entire processing area almost completely changed into a smooth surface. (3) The evolution of ripple structures. Perpendicular to the laser polarization direction, the ripple structures in Fig. 3(a) appeared in the edge region with low energy density, which confirmed to the typical characteristics of LIPSS in the regime of weak ablation. The direction of the ripple structures in Fig. 3(d) was parallel to the laser scanning direction as well as the polarization direction, and it was more obvious in the central region with higher energy, but gradually disappeared on both sides with lower energy. In Fig. 2, such

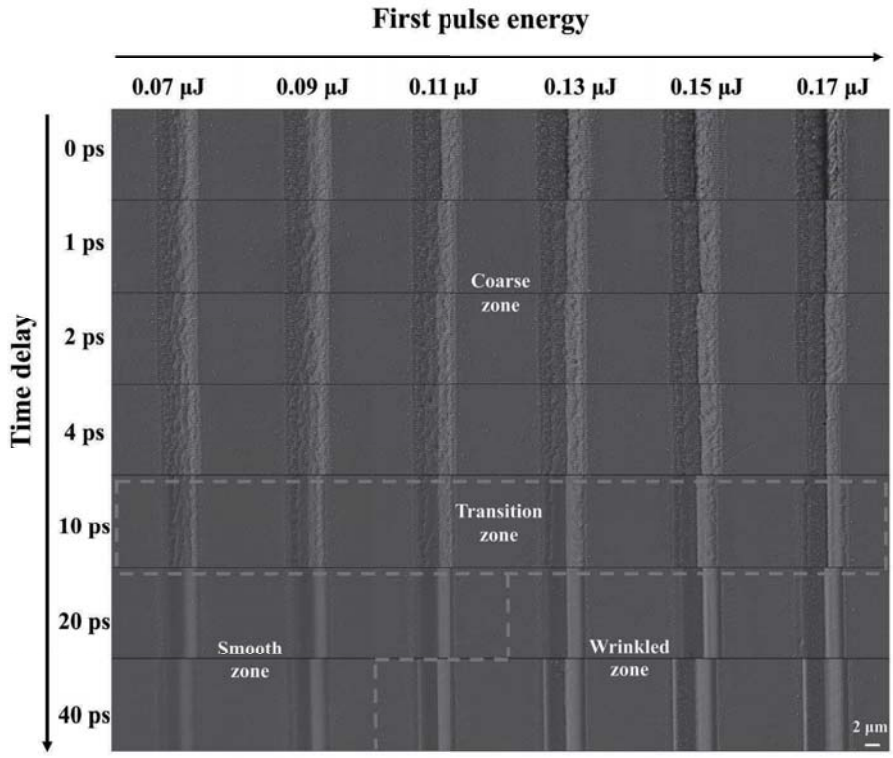

Fig. 2. Evolution of surface morphology with different double-pulse time delay and single pulse energy under femtosecond laser double-pulse irradiation. (the pulse energy of double pulses keeps consistent).

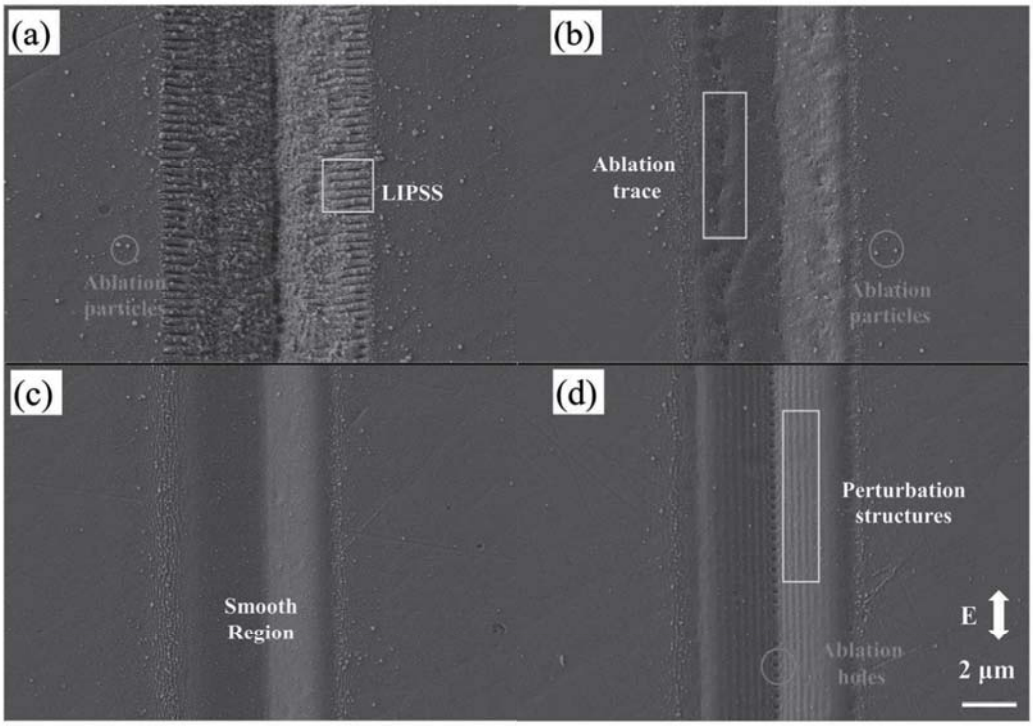

Fig. 3. Four typical ablation morphology with different time delay of (a) 0 ps, (b) 10 ps, (c) 20 ps and (d) 40 ps. (The pulse energy is 0.11 μJ, the arrow indicates the polarization direction).

structures of the wrinkled region only appeared in the experimental group with higher pulse energy, which did not conform to the typical characteristics of LIPSS in the case of weak ablation. Such corrugated structures may be the result of surface stress waves disturbing the liquid layer when the laser pulse energy is high [28]. (4) Ablative holes with regular arrangement appeared along the center line of the microgrooves.

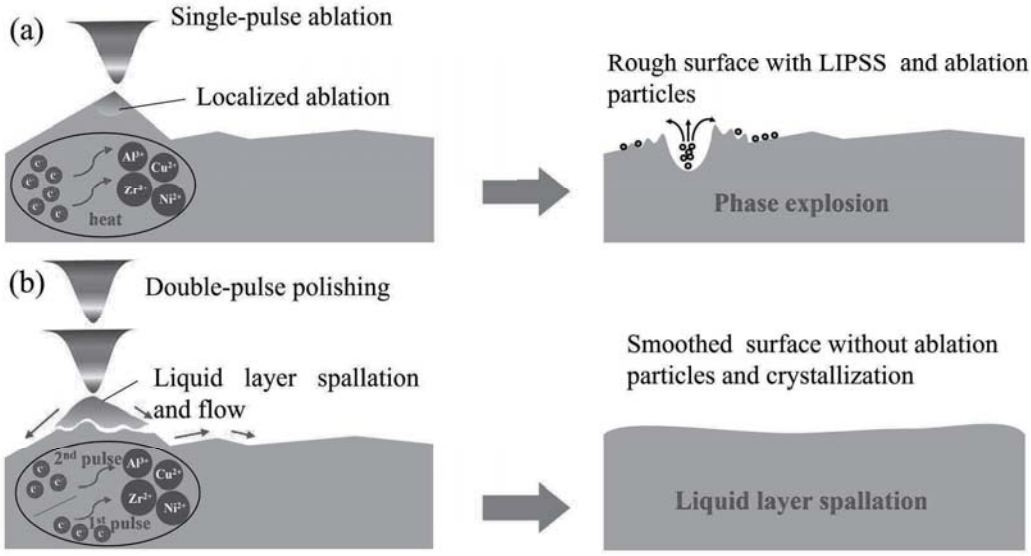

Fig. 4. Schematic diagram of the surface formation mechanisms under femtosecond laser (a) single-pulse irradiation and (b) double-pulse irradiation.

When the energy density and pulse overlap rate are appropriate, the incubation effect of multiple pulses may cause such ablative holes [29].

The ablation depth of each experimental group in Fig. 2 was measured as shown in Fig. 5 (the results were obtained by taking the average value of 5 measurements). For the low energy groups of 0.07 μJ, 0.09 μJ and 0.11 μJ, the ablation depth decreased significantly in the 0–4 ps delay period but slowly in the 10–40 ps delay period. As for higher energy of 0.13 μJ, 0.15 μJ and 0.17 μJ group, at 0 to 4 ps delay time, the ablation depth also showed a decrease, but when time delay ranged from 10 to 30 ps, there were ablation enhancement phenomena due to the ablation holes in the machining center area. Ablation holes were found in 10 to 30 ps group, while weakened in 40 ps group. Hence the microgroove depth increases first, then the trend was weakened. As the delay time of 0–40 ps increased, the double-pulse irradiation reduced the ablation efficiency of Zr-based bulk metallic glass. A reduced material-removal rate is also seen in titanium and silver under femtosecond laser double-pulse treatment [30,31]. Possible explanation for this phenomenon can be attributed to shock waves (including compression wave and rarefaction wave): as the compression wave propagation speed is larger than the rarefaction wave propagation velocity, at a certain delay time, compression wave and rarefaction wave will produce an offset effect, which influences the material removal process [32,33]. Some other explanations for the reduction of material removal rate include shielding effects of excited plasma triggered by the first pulse [34].

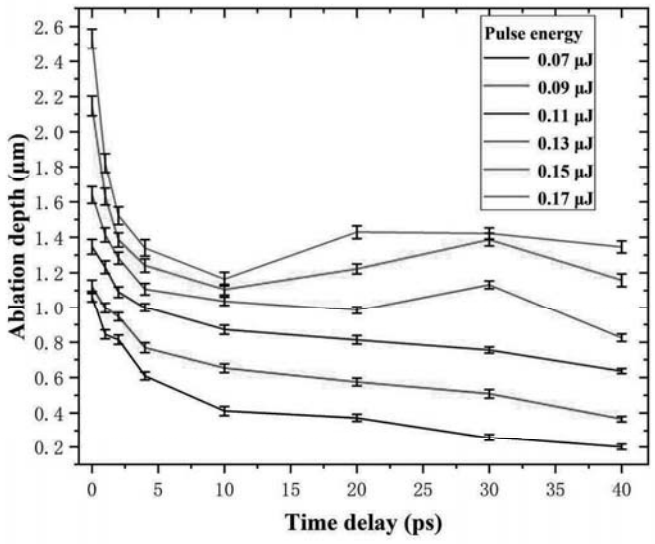

Fig. 5. Ablation depth with manipulation of pulse energy and time delay.

3.2. Pulse energy ratio manipulation of double-pulse irradiation

In order to explore the regulation effect of the energy difference between two pulses on the surface morphology, the second pulse energy was changed. Fig. 6 shows the surface morphology evolution under various pulse energy ratio. The energy of the second pulse was designed as to be adjustable, while the first pulse energy was fixed. The pulse delay time was 20 ps. When the second pulse did not exist (the pulse energy ratio is 0%), the ablative morphology presented as a staggered arrangement state of LIPSS and ridge structures, with many ablative particles and poor surface quality. When a second pulse with only 1% energy of the first pulse was introduced, the ablative process of the first pulse was inhibited, and the ablative width and particles were reduced. The ablative morphology obtained by 10% pulse energy ratio was similar to that of 1% experimental group. When the pulse energy ratio increased to 20%, LIPSS at the edge of the processing area disappeared, and the continuity of structure on the ridged surface weakened, showing a trend of morphology transformation. When the pulse energy ratio increased to 40%, ridge structures disappeared, and the corresponding region was in a smooth state. When the second pulse energy continued to increase to 60%, 80% and 100%, the traces of grooves gradually appeared in the center of the processing area, and the processing depth increased.

Fig. 7 shows the variation of ablation depths at different pulse energy ratios. When the second pulse went from 0 to 1%, the ablation depth decreased sharply. When the pulse energy ratio increased from 1% to 40%, the ablation depth continued to decrease monotonically, but the ablation depth decreased at different rates in different experimental groups. It was easy to find that when the pulse energy ratio was 40%, the ablation depth of each experimental group reached the minimum value. It could be found from Fig. 6 that the double-pulse irradiation had the least influence on the ablation morphology in this case. The ablative depth increased monotonically when increasing the second pulse energy with the energy ratio bigger than 60%, which was in line with the general law that the total energy of two pulses increased and the ablative

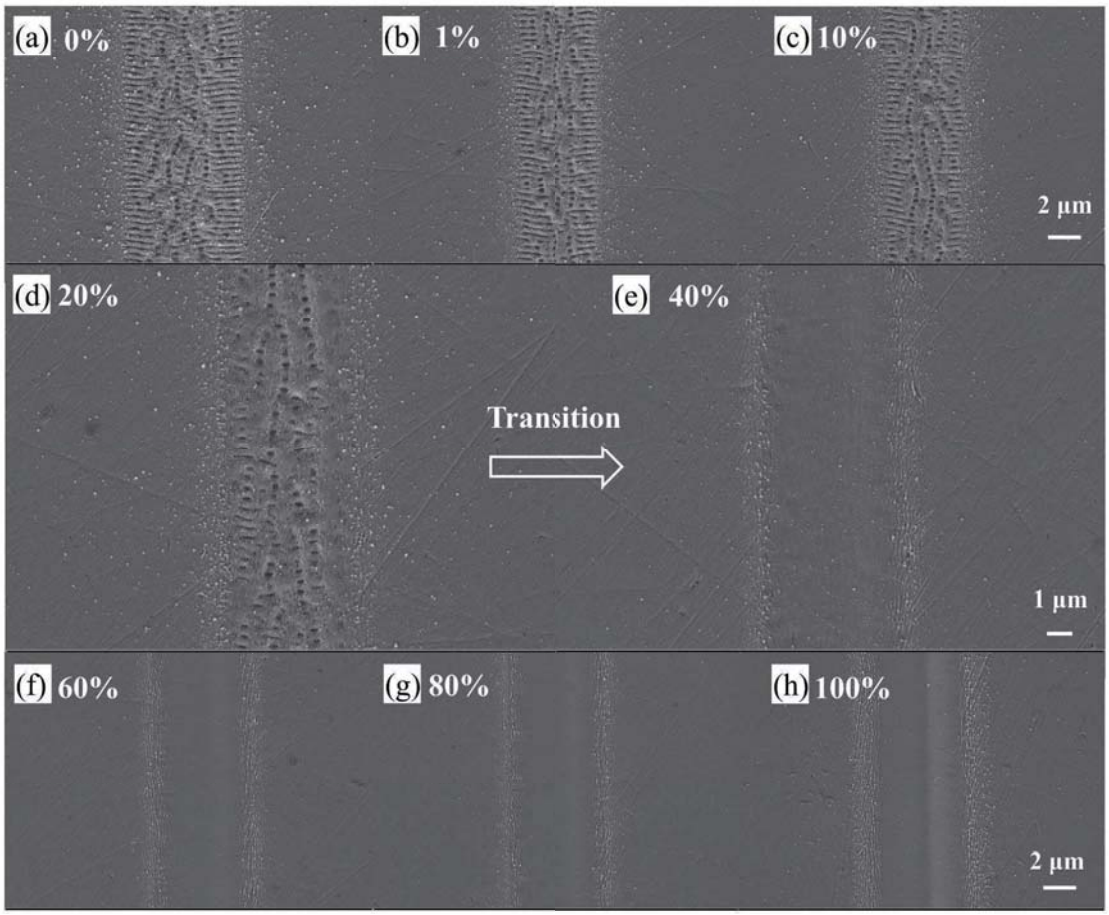

Fig. 6. Evolution of surface morphology with different pulse energy ratios of (a) 0%, (b) 1%, (c) 10%, (d) 20%, (e) 40%, (f) 60%, (g) 80% and (h) 100%. The pulse energy is 0.08 μJ.

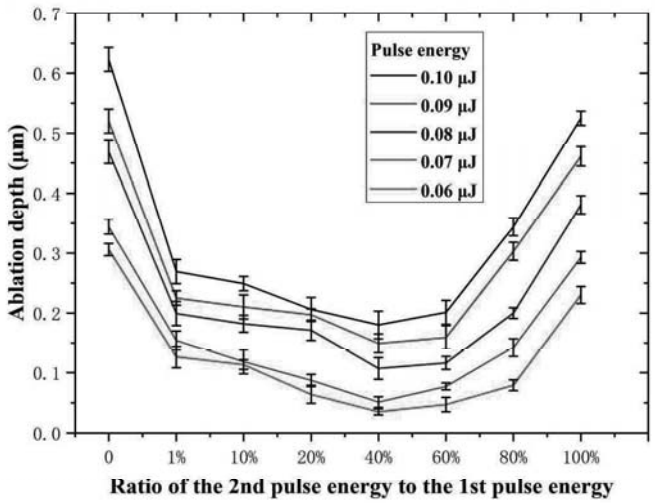

Fig. 7. The pulse energy ratio dependence of ablation depth under the time delay of 20 ps.

depth increased. By comparing the 0% and 100% experimental groups, it could be seen that the introduction of a second pulse with the same energy would lead to a decrease in the ablation depth of single pulse, which confirmed the above analysis on the ablation depth under double-pulse irradiation.

3.3. Smoothing of coarse surfaces by double-pulse irradiation

The experimental results above showed that femtosecond laser double-pulse irradiation method has great potential in producing smooth surfaces of BMGs. We further verified its adaptability in polishing BMGs in a relative large rough surface fabricated by laser ablation. The rough area was repaired by femtosecond laser double-pulsed method with fluence of 0.45 J/cm^2 and pulse-delay time of 20 ps. According to the 3D surface profile and SEM images as shown in Fig. 8, the original roughed surface and the double-pulse treated smooth surface have obvious differences. The disappearance of LIPSS and decrease of ablative particles on the original rough surface area proved the surface flattening effect of femtosecond laser double-pulse irradiation. The original ablated surface has a larger fluctuation in height comparing to the smoothed surface. The roughness (Sa) of the original and smoothed surfaces were measured to be 206 nm and 111 nm, respectively. However, due to the nonuniform energy distribution of Gaussian beam and the interval of each laser scan, there would be depth fluctuations perpendicular to the scanning direction. Therefore, smooth grooves with intervals approximately equal to 2.5 μm between the two adjacent scans appeared on the surface after the femtosecond laser double-pulse processing. In future study, a more homogeneous line-shaped laser beam with uniform energy distribution can be used to improve the polishing efficiency and further decrease surface roughness by femtosecond laser double-pulse method. Fig. 9 shows the XRD results measured after the femtosecond laser double-pulse and single-pulse treatments of metallic glasses. By comparing with the amorphous characteristic peak of the untreated samples, neither femtosecond laser double-pulse nor single-

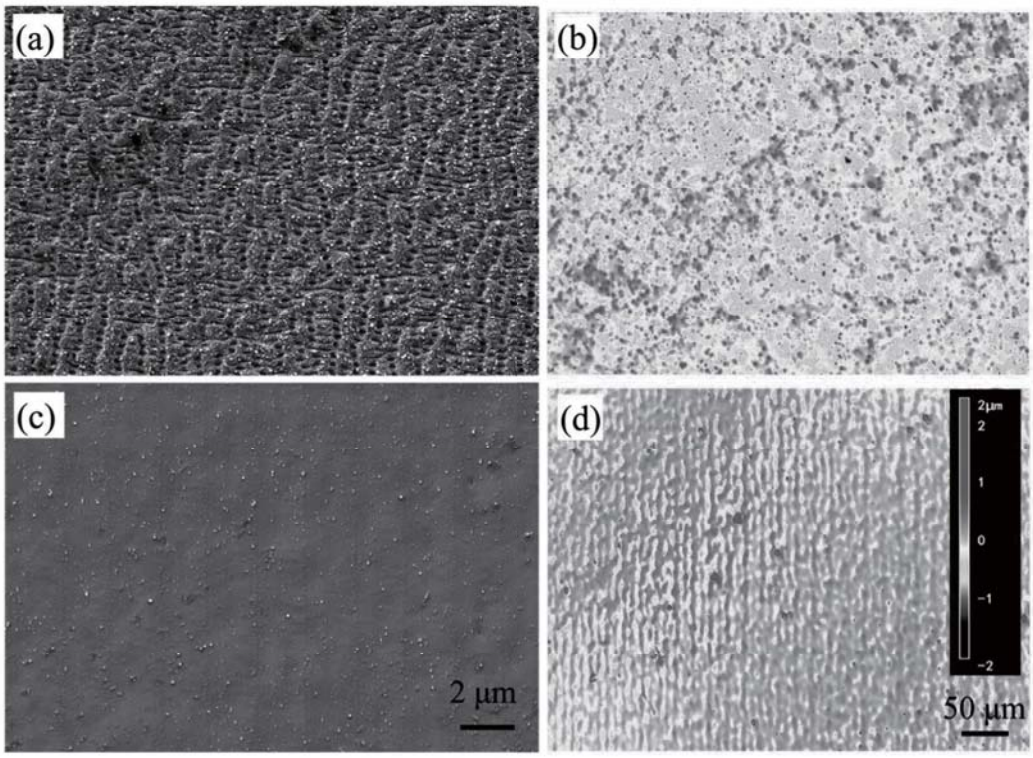

Fig. 8. Comparison of surface morphology and 3D profiles obtained by (a-b) femtosecond laser ablation (0.45 J/cm^2) and (c-d) after femtosecond laser double-pulse smoothing (0.45 J/cm^2).

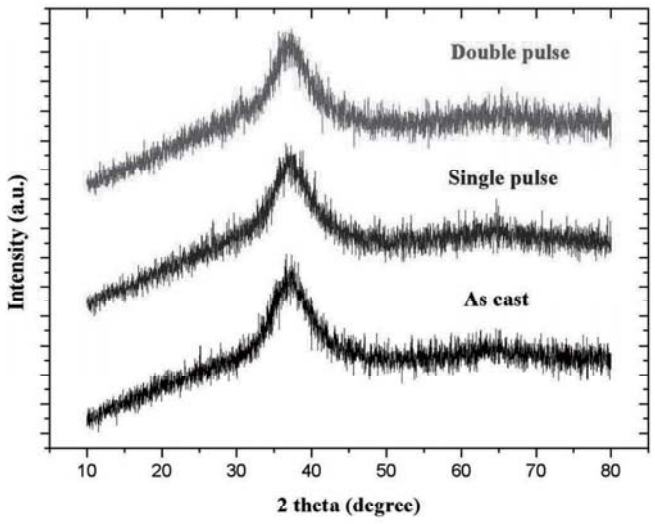

Fig. 9. XRD results of samples as cast, after femtosecond laser single-pulse and double-pulse irradiation.

pulse treatment caused the crystallization of the metallic glass samples. The amorphous state of metallic glass material was preserved owing to the relatively short interaction time between the femtosecond laser and the targets less than the general electron-phonon relaxation time. Specifically, after irradiation with a femtosecond laser, the heating and cooling rate of metallic glass is higher than the critical cooling rate in a BMG 's formation, which makes the molten liquid material solidify before it can nucleate and grow up.

4. Conclusions

In this study, ablation characteristics of metallic glass under femtosecond laser double-pulse irradiation were investigated, and we found that delay time, pulse energy and energy ratio of two pulses have a decisive influence on the ablated surface morphology. A transition from a rough surface to a smooth one occurred around 10 ps of the double-pulse delay time. The ablation efficiency with a double-pulse energy ratio around 40% reached the minimum value, which is the critical point of smoothing effect of the femtosecond laser double-pulse method. Smooth surface can be obtained via femtosecond laser double-pulse irradiation and the surface roughness (Sa) decreases to near 100 nm without laser induced periodic surface structures. Here, the smoothing effect could be explained by the molten materials flowing from surface tension and gravity which helps to flat the surface undulation. Furthermore, the amorphous state of Zr-based bulk metallic glass remained unchanged after the femtosecond double-pulse smoothing process. It is valuable to discuss the adoption of the double-pulse process for high-efficient large-area polishing of BMGs by such as galvanometer and cylindrical lens in the future study.

CRediT authorship contribution statement

Tie Li: Methodology, Investigation, Data Curation, Formal analysis, Writing - Original draft. Yang Guo: Data Curation, Writing - Original draft. Masayoshi Mizutani: Writing - Reviewing and Editing. Shaolin Xu: Conceptualization, Supervision, Writing - Reviewing and Editing, Funding acquisition.

Declaration of competing interest

The authors declare that they have no known competing financial interests or personal relationships that could have appeared to influence the work reported in this paper.

Acknowledgements

This work was supported by the National Natural Science Foundation of China (Grant No. 51705233) and the Shenzhen Science and Technology Programs (Grant No. GJHZ20190820151801786, KQTD20170810110250357).

References

[1] E. Williams, N. Lavery, Laser processing of bulk metallic glass: a review, J. Mater. Process. Technol. 247 (2017) 73–91. https://doi.org/10.1016/j.jmatprotec.2017.03.034.
[2] M.M. Khan, A. Nemati, Z.U. Rahman, U.H. Shah, H. Asgar, W. Haider, Recent advancements in bulk metallic glasses and their applications: a review, Crit. Rev. Solid State Mater. Sci. 43 (2018) 233–268. https://doi.org/10.1080/10408436.2017.1358149.
[3] L. Shao, D. Chen, M. Myers, J. Wang, B. Tilakaratne, D. Wijesundera, W.K. Chu, G. Xie, A. Zare, D.A. Lucca, Smoothing metallic glasses without introducing crystallization by gas cluster ion beam, Appl. Phys. Lett. 102 (2013) 1–6. https://doi.org/10.1063/1.4794540.
[4] S.G. Mayr, R.S. Averback, Surface smoothing of rough amorphous films by irradiation-induced viscous flow, Phys. Rev. Lett. 87 (2001) 1–4. https://doi.org/10.1103/PhysRevLett.87.196106.
[5] F.J. Shiou, P.H. Loc, N.H. Dang, Surface finish of bulk metallic glass using sequential abrasive jet polishing and annealing processes, Int. J. Adv. Manuf. Technol. 66 (2013) 1523–1533. https://doi.org/10.1007/s00170-012-4436-1.
[6] X. Zhang, L. Ji, L. Zhang, W. Wang, T. Yan, Polishing of alumina ceramic to submicrometer surface roughness by picosecond laser. Surface and Coatings Technology, 397 (2020). 125962.https://doi.org/ 10.1016/j.surfcoat.2020.125962.
[7] A. Lamikiz, J.A. Sanchez, L.N. Lopez de Lacalle, D. del Pozo, J.M. Etayo, J.M. López, Laser polishing techniques for roughness improvement on metallic surfaces, Int. J. Nanomanuf. 1 (2007) 490–498. https://doi.org/10.1504/IJNM.2007.014568.
[8] K.W. Guo, Effect of polishing parameters on morphology of DF2 (AISI-O 1) steel surface polished by Nd:YAG laser, Surf. Eng. 25 (2009) 187–195. https://doi.org/10.1179/026708408X336382.
[9] E. V. Bordatchev, A.M.K. Hafiz, O.R. Tutunea-Fatan, Performance of laser polishing in finishing of metallic surfaces, Int. J. Adv. Manuf. Technol. 73 (2014) 35–52. https://doi.org/10.1007/s00170-014-5761-3.
[10] K. Niitsu, Y. Tayama, T. Kato, J. Yan, Laser recovery of grinding-induced subsurface damage in the edge and notch of a single-crystal silicon wafer, Surf. Topogr. Metrol. Prop. 7 (2019). https://doi.org/10.1088/2051-672X/aafe3c.
[11] C. Dold, M. Kachel, D. Wortmann, V. Wessels, A. Dohrn, A. Bruinink, F. Pude, J.F. Loeffler, R. Poprawe, K. Wegener, Surface structuring of zirconium-based bulk metallic glasses using ultrashort laser pulses, Laser Appl. Microelectron. Optoelectron. Manuf. XIX. 8967 (2014) 89670V. https://doi.org/10.1117/12.2035383.
[12] E. Williams, E.B. Brousseau, Nanosecond laser processing of Zr41.2Ti13.8Cu12.5Ni10Be22.5 with single pulses, Journal of Materials Processing Technology. 253 (2016) 34–42. https://doi.org/10.1016/j.jmatprotec.2016.01.023.
[13] W. Jia, Z. Peng, Z. Wang, X. Ni, C. Yue Wang, The effect of femtosecond laser micromachining on the surface characteristics and subsurface microstructure of amorphous FeCuNbSiB alloy, Appl. Surf. Sci. 253 (2006) 1299–1303. https://doi.org/10.1016/j.apsusc.2006.02.003.
[14] X. Wang, P. Lu, N. Dai, Y. Li, C. Liao, Q. Zheng, L. Liu, Noncrystalline micromachining of amorphous alloys using femtosecond laser pulses, Mater. Lett. 61 (2007) 4290–4293. https://doi.org/10.1016/j.matlet.2007.01.089.
[15] C. Li, H. Zhang, G. Cheng, N. Faure, D. Jamon, J.P. Initial cumulative effects in femtosecond pulsed laser-induced periodic surface structures on bulk metallic glasses, J. Laser Micro Nanoeng. 11 (2016) 357–365. https://doi.org/10.2961/jlmn.2016.03.0014.
[16] W. Zhang, G. Cheng, X.D. Hui, Q. Feng, Abnormal ripple patterns with enhanced regularity and continuity in a bulk metallic glass induced by femtosecond laser irradiation, Appl. Phys. A Mater. Sci. Process. 115 (2014) 1451–1455. https://doi.org/10.1007/s00339-013-8062-z.
[17] L. Ran, S. Qu, Femtosecond laser induced surface structures on amorphous alloys, 2011 Acad. Int. Symp. Optoelectron. Microelectron. Technol. AISOMT 2011. (2011) 134–137. https://doi.org/10.1109/AISMOT.2011.6159336.
[18] M. López-Claros, M. Dell Aglio, R. Gaudiuso, A. Santagata, A. De Giacomo, F.J. Fortes, J.J. Laserna, Double pulse laser induced breakdown spectroscopy of a solid in water: effect of hydrostatic pressure on laser induced plasma, cavitation bubble and emission spectra, Spectrochim. Acta - Part B At. Spectrosc. 133 (2017) 63–71. https://doi.org/10.1016/j.sab.2017.02.010.
[19] M. Dell'Aglio, R. Gaudiuso, R. Elrashedy, O. De Pascale, G. Palazzo, A. De Giacomo, Collinear double pulse laser ablation in water for the production of silver nanoparticles, Phys. Chem. Chem. Phys. 15 (2013) 20868–20875. https://doi.org/10.1039/c3cp54194k.
[20] A. Semerok, C. Dutouquet, Ultrashort double pulse laser ablation of metals, Thin Solid Films. 453–454 (2004) 501–505. https://doi.org/10.1016/j.tsf.2003.11.115.
[21] Y. Lei, N. Zhang, J. Yang, C. Guo, Femtosecond laser eraser for controllable removing periodic microstructures on Fe-based metallic glass surfaces, Opt. Express. 26 (2018) 5102. https://doi.org/10.1364/oe.26.005102.
[22] N. Leng, L. Jiang, X. Li, C. Xu, P. Liu, Y. Lu, Femtosecond laser processing of fused silica and aluminum based on electron dynamics control by shaping pulse trains, Appl. Phys. A Mater. Sci. Process. 109 (2012) 679–684. https://doi.org/10.1007/s00339-012-7098-9.
[23] J. Schille, L. Schneider, S. Kraft, L. Hartwig, U. Loeschner, Experimental study on double-pulse laser ablation of steel upon multiple parallel-polarized ultrashort-pulse irradiations, Appl. Phys. A Mater. Sci. Process. 122 (2016) 1–11. https://doi.org/10.1007/s00339-016-0169-6.
[24] G.D. Förster, L.J. Lewis, Numerical study of double-pulse laser ablation of Al, Phys. Rev. B. 97 (2018) 1–17. https://doi.org/10.1103/PhysRevB.97.224301.
[25] J. M. Liu, "Simple technique for measurements of pulsed Gaussian-beam spot sizes," Opt. Lett. 7, 196-198 (1982). https://doi.org/10.1364/OL.7.000196.
[26] A.Y. Vorobyev, C. Guo, Direct femtosecond laser surface nano/microstructuring and its applications, Laser Photonics Rev. 7 (2013) 385–407. https://doi.org/10.1002/lpor.201200017.
[27] Wu C, Zhigilei L V. Microscopic mechanisms of laser spallation and ablation of metal targets from large-scale molecular dynamics simulations. Applied Physics A, 2014, 114(1): 11-32.https://doi.org/10.1007/s00339-013-8086-4.
[28] F. Ma, J. Yang, XiaonongZhu, C. Liang, H. Wang, Femtosecond laser-induced concentric ring microstructures on Zr-based metallic glass, Appl. Surf. Sci. 256 (2010) 3653–3660. https://doi.org/10.1016/j.apsusc.2010.01.003.
[29] H. Liu, W. Lin, Z. Liu, L. Ji, M. Hong, Self-organized periodic microholes array formation on aluminum surface via femtosecond laser ablation induced incubation effect, Adv. Funct. Mater. 29 (2019) 1–7. https://doi.org/10.1002/adfm.201903576.
[30] D.E. Roberts, A. du Plessis, L.R. Botha, Femtosecond laser ablation of silver foil with single and double pulses, Appl. Surf. Sci. 256 (2010) 1784–1792. https://doi.org/10.1016/j.apsusc.2009.10.004.
[31] Y. Furukawa, R. Sakata, K. Konishi, K. Ono, S. Matsuoka, K. Watanabe, S. Inoue, M. Hashida, S. Sakabe, Demonstration of periodic nanostructure formation with less ablation by double-pulse laser irradiation on titanium, Appl. Phys. Lett. 108 (2016) 1–5. https://doi.org/10.1063/1.4955035.
[32] J. Roth, A. Krauß, J. Lotze, H.R. Trebin, Simulation of laser ablation in aluminum: the effectivity of double pulses, Appl. Phys. A Mater. Sci. Process. 117 (2014) 2207–2216. https://doi.org/10.1007/s00339-014-8647-1.
[33] M.E. Povarnitsyn, T.E. Itina, P.R. Levashov, K. V. Khishchenko, Simulation of ultrashort double-pulse laser ablation, Appl. Surf. Sci. 257 (2011) 5168–5171. https://doi.org/10.1016/j.apsusc.2010.11.158.
[34] D.J. Forster, S. Faas, Shielding effects and re-deposition of material during processing of metals with bursts of ultra-short laser pulses, Appl. Surf. Sci. 440 (2018) 926-931. https://doi.org/10.1016/j.apsusc.2018.01.297.

【解説記事・紹介記事】

◇ 特集 造形技術と精密加工が支える医療の発展 ◇

人生 100 年時代のための新しい歯科治療

New Dental Treatments for 100-year Life Society

厨川常元*
Tsunemoto KURIYAGAWA

Key words: biomedical, powder jet processing, abrasive jet machining, powder jet deposition, dental treatment

1. 緒　言

皆さんは，日本の人口が現在，減少しはじめているということをどれだけ深刻に捉えているだろうか？**図1**は日本の人口推移予想[1)2)]を示したものである．この図からわかるように，国の予測では2050年には1億人を切り，2100年には4800万人になるといわれている．しかもその1/3以上が65歳以上の老年人口である．我々はこのような超高齢社会の到来に向けて，健康で豊かな生活を送るためには何が必要か，また解決すべき技術課題は何かを，今のうちから考えていかなければならない．

その答えの1つが医工学分野における基礎研究と，応用研究の充実である．医工学は，工学の基礎理論・知識の集積や実践的技術，並びに医学・歯学・生物学の基盤的知識と臨床における専門的技術を駆使して，生命体の構造と機能を解明する比較的新しい学問分野である．そして医療という“サービス”を具現化するための診断装置，治療装置の開発を工学のシーズを駆使して製品化していくことが要求されている．しかしながら，日本のお家芸である“ものづくり”の技術は，こと医療分野においては欧米諸国に大きく後れをとっているのが現状である．この発展には総合的な工学の知見が必要不可欠であるが，とくに精密加工技術によるところが大きいものと考えられる．

本特集では，3次元造形技術や噴射加工技術など，最新の造形技術と精密加工技術にフォーカスし，医療分野への貢献に関して特集を企画した．本稿では特に歯科治療への応用展開に着目し，その最新技術に関して紹介する．

2. これからの歯科治療

政府は2017年，人生100年時代構想会議を発足させ，将来の超長寿社会の教育，雇用，社会保障のあり方に関しての議論を始めた．このような状況の中，高齢者が最後まで自分の口で食事を楽しむために，口腔環境の改善は極めて重要である．例えば，1989年より厚生省（当時）と日本歯科医師会により始められた「80歳になっても20本以上自分の歯を保とう」という，いわゆる8020運動が効果を現している．これは歯と口の健康への関心が高まり，口腔環境が改善したためと考えられている．今後は超高齢社会の到来に伴い，8020運動から9028運動に発展させ，歯の健康寿命を延伸する試みも必要になると考えられている．そのためには，これまでの「歯科治療型」から，口腔機能の低下を予測しその維持・向上を図る「健康予測管理型」に変革していかなくてはならない．すなわち口腔機能低下の主原因である齲蝕（うしょく：虫歯）と歯周病の2大疾患を新規予防法で激減させ，高度歯科医療を簡便化することによって口腔保健と全身保健の両立を図っていかなくてはならない．

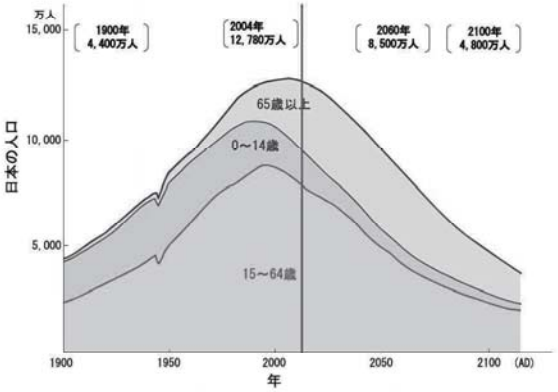

図 1　日本の人口動態

そのため筆者らは下記の3つの検討を，医歯工連携のもとで始めている．①齲蝕と歯周病の根絶（近未来の齲蝕予防は細菌叢（さいきんそう：微生物の集団）コントロールと炎症コントロールになると予想），②予防歯科・審美歯科によるQoL（Quality of Life）の向上（パウダージェットデポジションによる歯質の再構築技術），③機能性歯科インプラントの実現（自然歯に近い機能を実現する立体構造や結晶構造の設計，ならびにその製造技術開発）である．以下，CAD/CAM（Computer-aided design/Computer-aided manufacturing）システムによる機械加工と噴射加工による歯科治療について紹介する．

3. 歯科用 CAD/CAM システムによるセラミック修復治療

研削でセラミック製のインレー（詰め物）を製作し，歯科治療を行う歯科用CAD/CAMシステムを用いたセラミック修復治療が普及している[3)]．

一般に，工学の世界ではCAD/CAMは一般的な技術として，製品設計，製造の分野で広く普及している．このシステムを歯科分野における補綴（ほてつ）治療（歯冠や歯の欠損を，義歯，インレー，クラウン，ブリッジなどの人工物を用いて修復すること）に応用した場合，治療時間の大幅な短縮，修復物の残存日数の増加などの利点がある．本システムでは**図2**に示すように3Dスキャナで口腔内を3次元計測し，そのデータを用いてコンピュータで修復物を設計，小径クイル砥石を用いたミリング-マ

* 東北大学大学院医工学研究科：〒980-8579 宮城県仙台市青葉区荒巻字青葉6-6-01

〈学会受付日：2020年 1月17日〉

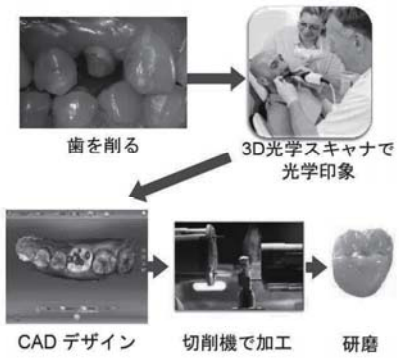

図 2 歯科用 CAD/CAM システムによる修復物作製[4]

シンでセラミックブロックを研削しインレーを作製する. したがって従来のような歯型を取る必要がなく, 早い場合は1回の通院で治療が完了する画期的なものである.

このようなセラミック治療は, 審美的に良好であるだけではなく, 従来の補綴治療と異なり, 修復物の製作・セットが完了するまで必要だった仮歯が不要となり, 唾液などの汚染が少なくなるため, 長期的な歯の予後(詰め物の残存率)が良好であることも大きな特長である.

4. 噴射加工による新しい歯科治療

高速に加速した固体粒子を工作物に衝突させ, その衝撃力により材料の除去あるいは表面改質を行う加工を総称して噴射加工(blasting)といわれている. このプロセスは固体粒子の有する運動エネルギーを工作物に投入し, 塑性変形あるいは脆性破壊を生じさせるもので, 古くから行われている. 通常は噴射加工といえば材料除去法として捉えられてきたが, 近年では逆に噴射粒子を工作物表面に付着させることもできるようになってきた. そこで本報では, 粒子を高速で噴射衝突させる加工法全体を粒子噴射加工法(powder jet processing)と定義し, そのなかで材料除去を行う加工法をアブレイシブジェット加工(abrasive jet machining, 以下 AJM と略記, **図 3** 左図参照), 材料付着を行う加工法をパウダージェットデポジション(powder jet deposition, 以下 PJD と略記, 図 3 右図参照)と区別することにする. そしてこれら 2 つの加工法の歯科治療への応用事例に関して紹介する.

4. 1 AJM による齲蝕の選択的除去[5)~7)]

近年, 接着性レジン材料の高性能化により, 虫歯の修復処置法は, より歯質保存的な修復法へと変貌を遂げた. すなわち, 窩洞(かどう)形成に関して保持形態が不要になったことなどにより, 修復処置に関して健全歯質を削除して犠牲にする必要性がなくなってきた. これにより窩洞形成に際しては齲蝕罹患歯質の除去のみを必要とする症例が増えつつある. こうした接着性レジン修復法の一般的な手法としては, エアータービンによる齲窩の開拡, 電気エンジンを用いた齲蝕除去, そして窩縁部の整理後, 修復操作が行われる. 齲蝕除去に関しては, 細菌侵入の見られる齲蝕象牙質第一層のみを除去するために, 齲蝕検知液を併用し, 染色と除去を繰り返す方法が最も有効的とされているが, 比較的面倒な作業の 1 つとなっている.

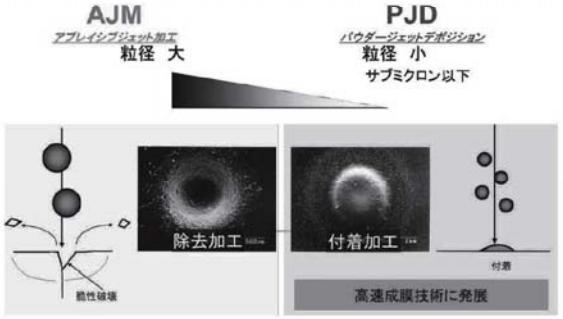

図 3 噴射加工における除去から付着への遷移

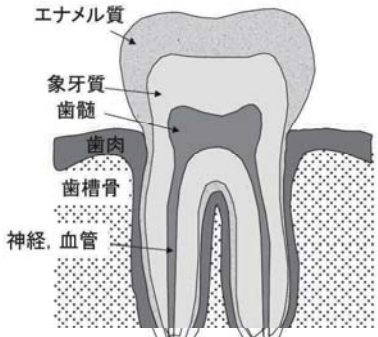

図 4 歯の構造

ここで歯の構造について説明する. **図4**に示すように, 歯は大きく3つに分けることができ, 表面の部分はエナメル質と呼ばれ, 非常に硬く摩耗しにくくなっている. その内側には, 象牙質があり, その中には象牙細管というストロー状の管が歯髄より放射状にのびており, 歯に養分を供給している. さらに内側には歯髄があり, 神経および血管が通っている. 齲蝕というのは, 口腔に常在する細菌の発酵作用により含水炭素から乳酸が作られ, この乳酸により歯牙硬組織の石灰を脱却(脱灰)させ, 有機成分は蛋白質を溶解する細菌の作用により破壊されて起こるものである.

虫歯治療においては, 除去作用が齲蝕象牙質のみに限定され, 健全な組織には全く影響を及ぼさないことが理想的である. 一般に, 工作物にスクラッチ溝を形成させるためには, 工具の硬さは工作物の約 1.2 倍以上必要とされている. したがって齲蝕象牙質より硬く, 正常な歯質よりは軟らかい砥粒を用いて AJM を行えば, 選択的除去が可能になると考えられる.

そこでまずヒト抜去歯の硬度分布を測定した. 測定はダイナミック超微小硬度計を用いて行い, ダイナミック硬度DHVで評価した. DHV硬度とはビッカース圧子を測定材料に押し込んだとき, その押し込み深さより硬度を評価したものである. 図からわかるように齲蝕象牙質部では非常に軟らかくDHV硬度で1以下となっており, 正常象牙質では約20～50と齲蝕象牙質と比較するとかなりの差が見られ, さらにエナメル質部分では700～1000と非常に硬くなっていることがわかる.

一方, 砥粒材質として齲蝕象牙質よりは硬く正常象牙質よりは軟らかいもしくは同程度の硬度を有するプラスチック TPL (Polycarbonate resin, HV=40～55, DHV＝7～10)を選定し

た．この TPL 砥粒は齲蝕象牙質と正常部の中間の硬度を有し，選択的除去が可能になるものと考えた．

次に齲蝕象牙質を有するヒト抜去歯をダイヤモンド内周刃切断機により切断し，厚さ2mmの試料を作成した．最初に齲蝕検知液により齲蝕象牙質を染色し，**図5**(a)に示すように齲蝕象牙質部を視認できるようにした．そのときの写真中の線に沿って，齲蝕象牙質領域から正常象牙質領域までの硬度分布と染色濃度分布を測定した．ここで染色濃度は切断試料面の画像をコンピュータに取り込み画像処理を行ったもので，この値が大きいほど染色濃度（細菌侵入度）が高いことを示す．

齲蝕象牙質の除去例と除去領域と硬度，濃度分布を対応させ示したものを図5(b)に示す．図よりTPL#80砥粒では硬度がDHV=5付近まで除去が行われており，染色部もほとんど取り除かれているのがわかる．また噴射時間は約30sと十分長くとったが，全く正常象牙歯質には除去が進展しておらず，齲蝕象牙質の選択的除去が行われていることが確認できた．

4．2　パウダージェットデポジションによる歯質の再構築[8)~11)]

前節は除去作用による歯科治療であったが，ここでは付着作用を用いた全く新しい歯科治療を紹介する．これは噴射加工によりセラミックス厚膜を成膜することにより歯質の再構築を行おうとするもので，世界で初めての治療法である．

最初にその付着メカニズムについて説明する．噴射粒子は約250～350m/sの速度で対象物に衝突する．この衝突した粒子は約数nm～数10nmの微小片に破砕される．このような破砕片表面は非常に活性であるため，直ちに再結合し膜が形成される．この反応は数nsの微小時間内に完了する．この過程を可視化するために，マイクロレベルでは**図6**に示すように平滑化粒子法（Smoothed Particle Hydrodynamics，以下SPH法）により，またアトミックレベルでは**図7**に示すように量子分子動力学法（Quantum Molecular Dynamics，以下MD法）によりシミュレーションを行った．図6から明らかなように粒子は数nsの短い時間で数nmの粒子に破砕されている．さらに図7の結果より，MD法により，ハイドロキシアパタイト（Hydroxyapatite：HA）粒子はHA基板に原子結合により固着していることがわかる．本プロセスは常温大気圧環境下で行うことが可能で，他の成膜プロセスと比較して成膜装置，コストの点で大きな優位性を示す．**図8**はPJDによりヒト歯表面のエナメル質上に成膜したHA膜の断面写真である．(a)は成膜界面のSEM（Scanning Electron Microscope）写真，(b)と(c)はTEM（Transmission Electron Microscope）写真である．これらの写真より，成膜されたHA膜は粉砕された約10nm程度の微粒子で構成されており，エナメル質表面上に密着していることがわかる．

現在，知覚過敏症の治療の臨床試験が終了し，本格的な治療応用への道が開けてきた．さらには現在，**図9**に示すようにHA粒子とジルコニアセラミックス粒子の複合粒子により歯面を白くする審美歯科への応用や，抗菌性のHA粒子を用いた予防歯科への応用も研究開発が始まっている．また本手法によりTi製インプラント表面へのHA膜の成膜など，医学分野への応用展開も始まっている．

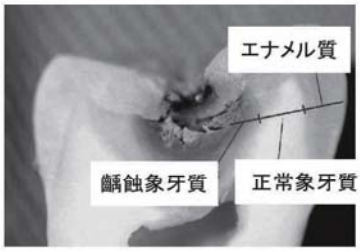

(a)　ヒト抜去歯断面（齲蝕部が着色されている）

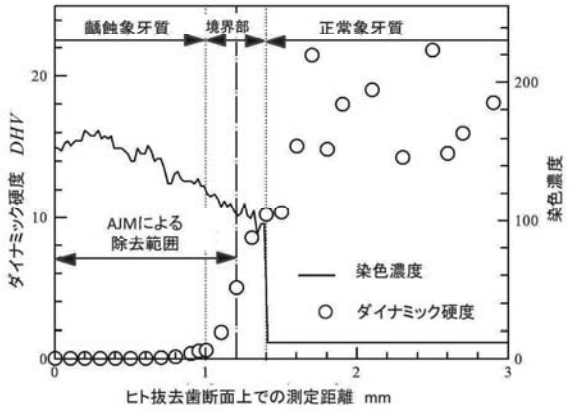

(b)　染色濃度と硬度の分布

図 5　歯の齲蝕部と正常部分の相違

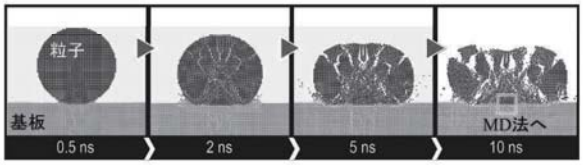

図 6　SPH 法を用いた粒子衝突時の挙動解析

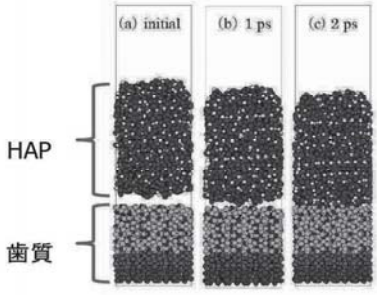

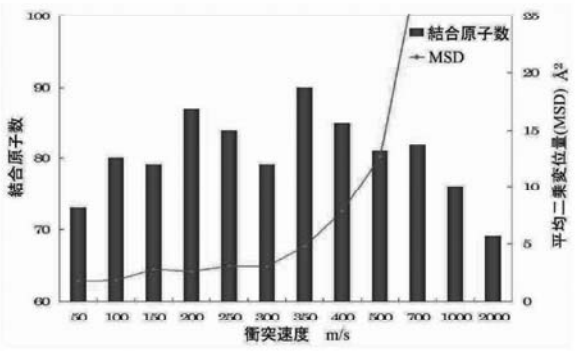

図 7　量子分子動力学法による衝突界面での原子挙動

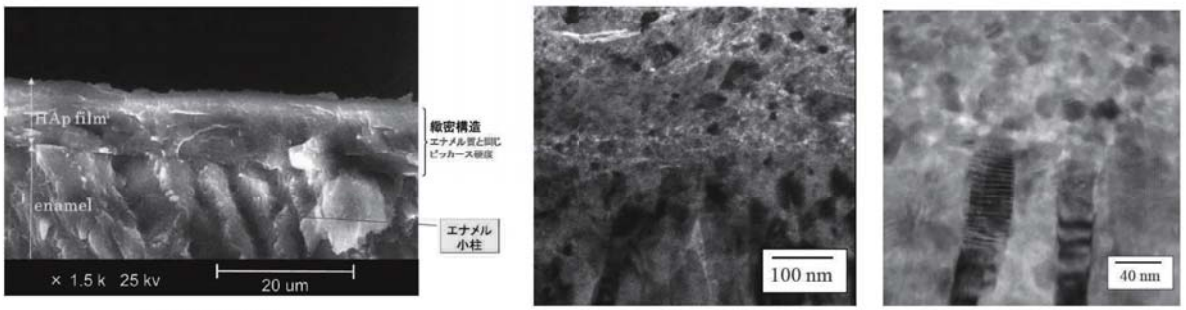

(a) SEM 写真　(b) TEM 写真　(c) TEM 写真(高倍率)

図 8 パウダージェットデポジションにより成膜されたハイドロキシアパタイト厚膜断面

図 9 パウダージェットデポジションによる歯科治療の未来

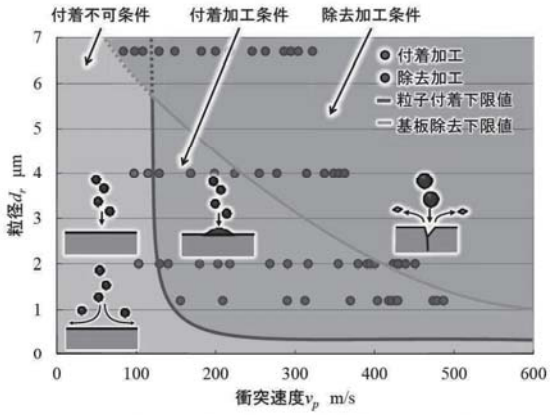

図 10 除去作用と付着作用の遷移

4．3 付着現象と除去現象

4.1と4.2で説明した噴射現象は全く異なるプロセスではなく，噴射砥粒の粒径と噴射速度を適当に選ぶことにより，その加工作用を選択することができる．**図10**は粒径と噴射速度との関係をまとめたものである．青い部分が付着領域，赤い部分が除去領域，灰色の部分は何も起こらない領域である．このプロセスマッピングをうまく利用すれば，同じ粒子径のHA砥粒を使って，最初に目的領域を除去したあと，噴射条件を変更し，その部分に新しいHA膜を成膜することも可能となる．

5．おわりに

本報では噴射加工の歯科治療への応用事例を中心に紹介した．医療機器商品開発において，装置の開発，その後の臨床研究，臨床試験，さらに薬事承認まで完了するためには，長い年月と高額の費用が必要となる．研究成果の社会実装における種々の困難，いわゆる「魔の川」，「死の谷」，「ダーウィンの海」をいかに飛び越えるか．そのためにはニーズ調査・市場調査・企画・ビジネスプラン・薬事戦略など，周囲の情勢が変化していくなかで機敏に対応していかなければならない．そのためには，これからの“ものづくり”，“ことづくり”を考えるとき，将来何が求められているのか，何が売れるのかを十分予想し，バックキャスト的発想で，そのための技術は何か，今解決すべき技術課題は何かを常に考えていかなければならない．

さらに若手研究者にとくに期待するのは，未知の領域に飛び込んでいくアントレプレナーシップの醸成と実行である．これからの開発研究の進展が，非常に楽しみである．

6．参考文献

1) 加藤康司．エネルギー自立自然共生のロハスの家(復興と百年の計)．日本機械学会誌，115, 1126 (2012) 664.
2) 日本の将来推計人口報告書(WEB版)，国立社会保障・人口問題研究所(平成18年12月推計)
http://www.ipss.go.jp/syoushika/tohkei/suikei07/index.asp
3) 野地美代子，新素材とCAD/CAMは低侵襲をもたらすか？(その可能性と課題)，補綴臨床，49, 6(2016)11.
4) 厨川常元，砥粒加工の医療への応用，砥粒加工学会誌，63, 2 (2019) 67.
5) 堀口尚司，二階堂徹，大槻昌幸，田上順次，佐野英彦，猪越重久，厨川常元，山田敏元：回転切削器具からの脱却(Air Abrasive法を用いた選択的齲蝕除去の可能性)，日本接着歯学会誌，16-2 (1998) 55-62.
6) T.Kuriyagawa, O.Kinbara, S.Horiguchi, J.Tagami, T.Yamada and K.Syoji: Selective Removal Process of Carious Dentine with Micro Abrasive Jet Technology, Key Engineering Materials, 238 (2003) 405.
7) 堀口尚司，山田敏元，杉崎順平，小松えりな，二階堂徹，田上順次，厨川常元：Air-powder Abrasive Systemに結晶性セルロースを用いた新しい歯面清掃法の開発，日本歯科保存学会誌，42-3 (1999) 536-544.
8) 水谷正義ら，パウダージェットデポジション(PJD) における粒子破砕挙動と成膜メカニズムに関する研究，砥粒加工学会誌，61, 1 (2017) 28.
9) Chihiro Nishikawa, Naohide Mizukuchi, Akihiko Tomie, Keita Shimada, Masayoshi Mizutani, and Tsunemoto Kuriyagawa: Characteristics of Thick Film Deposition in Powder Jet Machining, Int. J. of Automation Technology, 7, 6 (2013)630.
10) 冨江瑛彦，久慈千栄子，水口直秀，西川智弘，嶋田慶太，泉田一賢，赤塚亮，佐々木啓一，水谷正義，厨川常元：窩洞へのハイドロキシアパタイト膜形成高速粒子衝突による付着現象の歯科治療への適用，砥粒加工学会誌，57, 12 (2013)800.
11) 佐藤慧，西川智弘，萩原隆行，嶋田慶太，堀内渉，松村賢，赤塚亮，佐々木啓一，石崎勉，荒川正嘉，太田一史，水谷正義，厨川常元：パウダージェットデポジション法によるエナメル質へのハイドロキシアパタイト成膜，日本機械学会論文集(C 編)，79, 808 (2013)109.

2020年度（第16回）精密工学会賞受賞業績の紹介

厨　川　常　元

厨川常元氏は長きにわたり，機械加工を礎としつつ，「機能創成」という新しい視点からピコ精度・ナノ精度の機能性加工に取り組み，ものづくりに新たな研究分野を開拓し，それを実現するための加工装置を産学官連携の下で開発・実用化してこられました．関連する研究は加工特性と機能特性の両面を考慮してアプローチしていることが大きな特徴であり，かつ M^4 プロセス（Micro/Meso Mechanical Manufacturing）と呼ばれる分野の体系化に貢献されてこられました．

近年は，精密加工への適用が難しいと言われてきたパウダージェット加工を歯科治療などの分野で実用化する研究に注力して，医工学の連携として異分野融合研究も先導し，その功績は極めて大きいものであります．

また，厨川氏は，精密工学会の活動に対して，ナノ精度機械加工専門委員会の委員長をはじめ，東北支部長，理事，副会長として，長年にわたり多大なる貢献をしています．同様に，日本学術会議会員，精密工学会フェロー，日本機械学会フェロー，砥粒加工学会会長，The International Society for NanoManufacturing フェロー，国際砥粒加工委員会（ICAT）委員長として，これらの学協会団体の活動と発展に対しても大きく寄与してこられました．

以上のとおり，厨川常元氏は精密工学，特にものづくりの分野の加工技術の研究・開発に多大な貢献をされてこられました．ここにその功績を称え，精密工学会賞を贈賞いたします．

略　歴

1984年　東北大学大学院工学研究科（精密工学専攻）博士課程後期3年の課程退学
（期間満了）（1987年　同修了）
東北大学助手工学部に採用
1990年　東北大学講師工学部に昇任
1992年　東北大学助教授工学部に昇任
2003年　東北大学教授大学院工学研究科に昇任
2014年　東北大学教授大学院医工学研究科に異動（工学研究科兼担）
2015年　東北大学未来科学技術共同研究センター（NICHe）教授（兼担）
2017年　東北大学大学院医工学研究科研究科長・教授
2020年　東北大学大学院医工学研究科教授
精密工学会フェロー（2011年度）
日本学術会議・会員，日本機械学会フェロー，高エネルギー加速器研究機構・客員教授

高能率加工から超精密加工、そして機能創成加工へ

東北大学　大学院医工学研究科　厨川常元

1．はじめに

この度は、栄えある2020年度精密工学会賞にお選びいただき、誠にありがとうございます。この表彰は、私にとって身に余る栄誉であるだけでなく、精密工学会にお世話になってきたこの30年を振り返る良い機会となりました。本稿では、私が学生だった頃からの加工に関する研究に関して振り返ってみたいと思います(図1参照)。

2．高能率研削；クリープフィード研削

私が4年生で研究室に配属になったときに与えられた卒業論文テーマは“ラップ焼けに関する研究”であった。ラッピング、ポリッシングにより金属材料を鏡面研磨していくと、黒光りしていく、いわゆる“ラップ焼け”を解決せよというものであった。その現象解明と対策を明らかにするために、その当時は導入したばかりの蛍光X線分析装置を使い加工面の表面分析を行った。その結果、黒光りの主な原因は微小な切り屑の物理的な埋め込みであり、加工液に界面活性剤を添加することにより大幅に減少させられることが分かった。

その後大学院に進学したが、そのときのテーマは“クリープフィード研削に関する研究”であった。その当時はクリープフィード研削は一般的でなく、ほとんど文献もなかったが、どうも研削送り速度を極端に小さくし、切込みを大きくして研削する高能率研削であるということだけが分かった。しかし、研究室には汎用研削盤しかなかったため、低速送りがかけられない、したがって汎用研削盤のテーブルの上に自作の低速送りテーブルを固定し、実験を始めた。その結果、クリープフィード研削においては，全体の研削抵抗は大きいが、砥粒切れ刃1個に作用する力は逆に小さくなることが分かった。そして、砥石は目つぶれ気味となること、それを改善するためには極軟砥石を使用することが重要であることが分かった。

学位取得後、1991～92年にかけて米国のコネチカット州立大学の研削研究所に留学する機会を得て、そこでジェットエンジンのタービンブレードのクリープフィード研削の研究を続けた。

3．米国留学

留学生活では大学の雑務から解放されていたため、比較的自由な時間が持てた。そこで、帰国後の研究テーマを探すために、米国内の大学や企業をなるべく多く訪問した。テキサス州にあるブラスト関係の企業を訪問したとき、始めてAJM (Abrasive Jet Machining)という言葉を知って、“これだ！”と直感した。日本の先生がたには、“今更ブラストの研究なんて、50年前にすでにやられているよ”、といわれたが、私にとっては、妙に気になって、頭から離れない。そこで日本に帰国してから、本格的に始めることとした。しかしすぐには研究成果は出ないだろうと考え、研削の研究の2本立てでいくことにした。

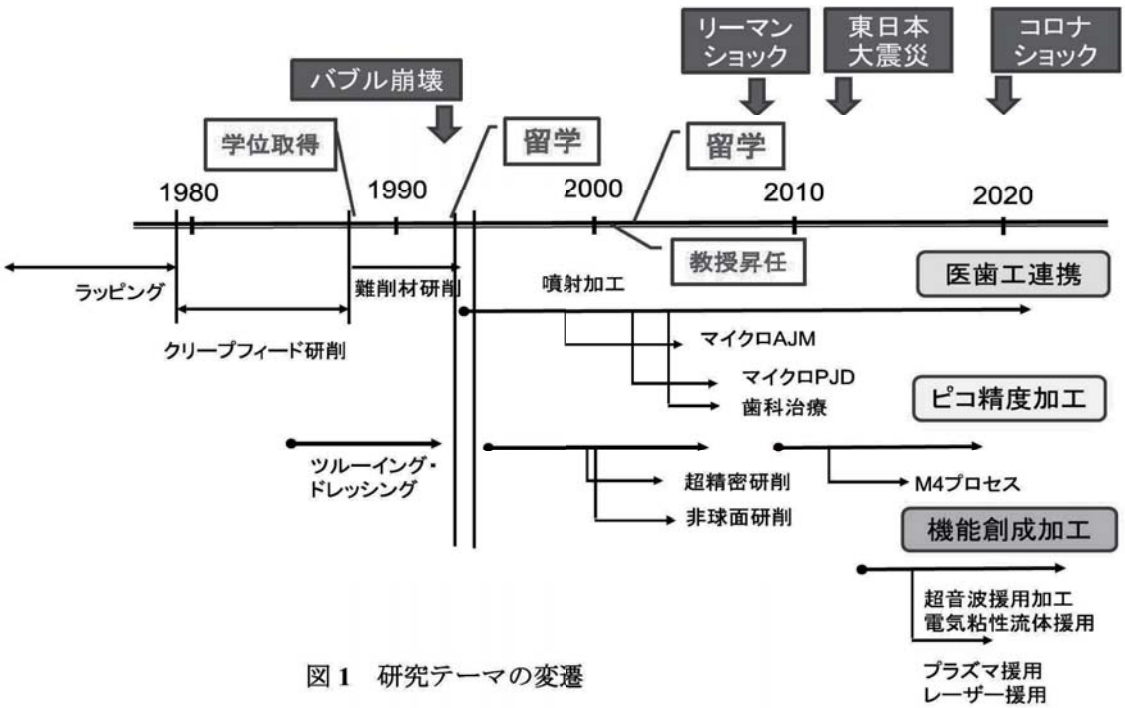

図1　研究テーマの変遷

4．アブレイシブジェット加工

AJMは小径ノズル（内径0.5～2.0mm）から砥粒(直径10～20μm)を、亜音速まで加速、噴射させて、硬脆材料等を微細加工する方法である。これはイオンビーム加工や電子ビーム加工と同じように、一種の粒子ビーム加工であるから、もし噴射砥粒の個数と速度、噴射領域を制御することができれば、精密加工に使用できると考えた。そこで光学メーカや砥粒メーカと共同研究を始め、デジタル制御方式のAJM装置を開発した。さらに、インクジェットプリンタのインク粒子の代わりに砥粒を複数ノズルから噴射し、ガラス等の表面を機械的にパターンエッチングすることのできるアブレイシブジェットプリンタを開発した。この時に開発した、粒子を精密に噴射させる技術は、後のPJD(Powder Jet Deposition)の開発へと繋がることになる。

5．超精密研削；非球面研削

一方で、ダイヤモンド砥石を使ってセラミックス材料をクリープフィード研削するために、ダイヤモンド砥石の超精密ツルーイング・ドレッシングの研究を行っていた。その研究の延長で、砥石断面を円弧にツルーイングし、セラミックスベアリングのレース面の研削を行っていた。しかし適用事例がそれだけでは満足がいかなかったので、高精度にツルーイングした円弧断面を別のものに応用しようと考えた。それが非球面研削であった。すなわち、砥石の円弧断面で任意の非球面形状を包絡創成しようとするものである。この“円弧包絡研削法”の開発は、研削点が常に移動するため、砥石摩耗が分散され、その結果として非球面形状の大幅な形状精度向上が達成された。その後に、研削面粗さを極端に小さくすることのできる“パラレル研削法”や、非球面形状のムラを減少させる“超安定研削法”を開発した。研究が佳境を迎えた2000年はじめは、ちょうどデジタルカメラへの変革が始まった時期と重なり、複数の光学メーカから採用された。

6．パウダージェットデポジション

AJMの研究から派生した技術として、PJDがあげられる。前述したようにAJMは粒子ビーム加工の一種で、粒子の運動エネルギを被削材の脆性破壊エネルギに変換するプロセスと考えることができる。したがってAJMは除去加工であるが、粒子のサイズが異なれば付着加工にもなるのではないかと、想像していた。研究の結果、粒子のサイズ、噴射速度を変えることにより、除去から付着に遷移することを明らかにした。このPJDを歯科治療に応用し、エナメル質の再構築に成功した。現在では臨床試験も終了し、知覚過敏等の治療に適用されはじめている。さらに将来的には審美歯科や予防歯科に適用を拡大しようとしている。

7．現在、これからの研究テーマ

非球面加工の研究テーマも2010年頃には少なくなってきた。その頃リーマンショックとも重なり、経済も低迷状況となった。私も次の研究テーマ設定に悩んでいたが、その時に始めたのが、高付加価値加工を目指した機能創成加工とピコ精度加工である。現在ではその応用対象は工業分野のみならず、現在では医学、歯学、薬学、農学等に及んでいる。**図2**にその一部を紹介する。

8．最後に

これまで私は、仕事や様々な付き合いの場で数え切れないほど多くの人たちと出会ってきました。上司や先輩の諸氏、同輩や後輩、学生の皆さん、そして企業の研究者、技術者の方々、現場の技能者の方々。たくさんの人たちから多くのことを教わり、さまざまな経験をさせてもらいました。今の自分があるのは、その人たちのお蔭だと思っております。その中でも特に、異分野、異業種の方々との議論や助言が研究テーマ開拓に有益でありました。

本稿が若い研究者たちの参考になれば幸いです。特に異分野の方々とのネットワーク構築とブレーンストーミングを重ね、新しい学術領域、産業分野を開拓してください。皆様方の大いなる発展を期待しております。

図2　ピコテクノロジー基盤高付加価値ものづくり
（日本学術会議マスタープラン2020）

微細構造解析分野

集束イオンビーム加工装置（Focused Ion Beam）

デバイスの小型化や複合化が急速に進む中、局所領域からのサンプリングやナノレベルでの修飾加工のニーズは高まる一方で、集束イオンビーム加工（FIB）装置は材料・製品の研究開発に欠かせない存在となっています。当センターでも2台のFIB装置がほぼフル稼働の状態です。TEM観察用の薄片試料作製では、従来、主流であった金属・酸化物に加え、生体・高分子材料、さらにこれらの複合材料への加工が増えつつあります。また、物性発現を目的としたパターニングや数100枚にも及ぶ連続スライス＆ビューによる材料内部の三次元解析など、支援内容も急速に多様化しています。ここでは微粒子の断面観察と金薄膜へのパターニングの例を紹介いたします。　（兒玉裕美子・竹中佳生）

●微粒子状の生体材料の薄片化加工と断面観察

歯科治療を目的としたバイオセラミックス粒子の開発では、粒子内部の結晶性の評価だけでなく、組成や大きさの異なる2種類の粒子の結合・分散状態の観察が必要です。そのため私たちは、形態を崩さないよう樹脂に粒子を分散固化させ、FIBによる薄片化を行っています（a）。 たとえば、写真は造粒後の粒子や基板への衝突後の粒子から得られたものです（b, c）。 また、導電性がなく、異素材である樹脂と粒子から成る試料でも薄片化可能でバイオ粒子周囲に小さな酸化物粒子が付着する様子が確認できています。さらに、複合粒子を堆積させた膜のFIB断面加工・TEM観察から数ミクロンオーダーでの堆積組織が認められ（d）、 FIBを用いたスライス＆ビューによる内部の立体的な構造解析を進めています 。

（東北大学厨川常元研究室）

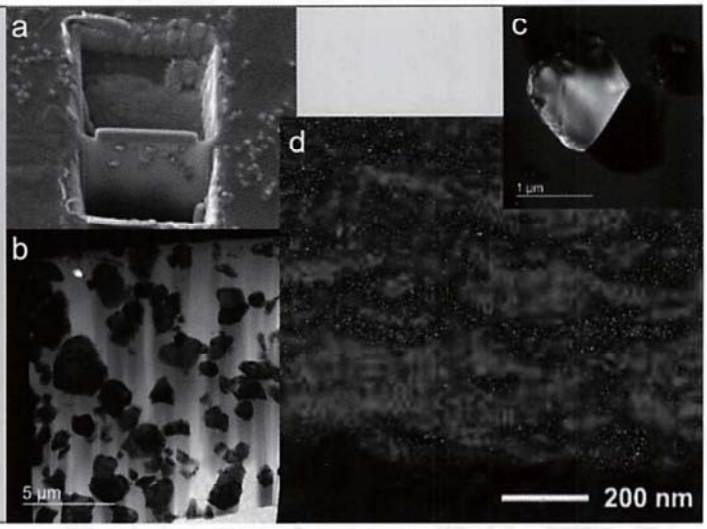

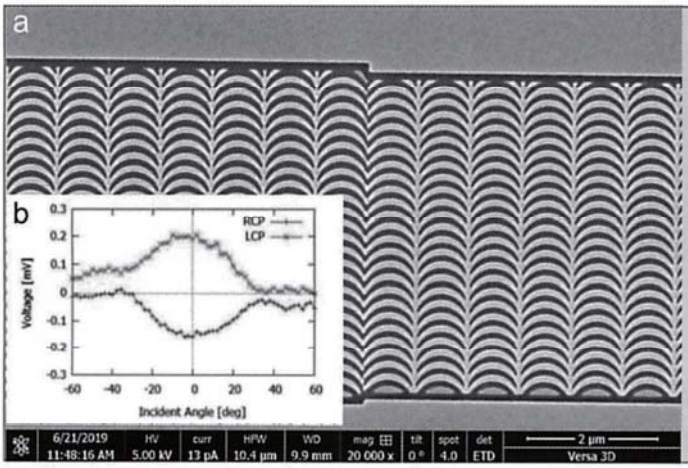

●金薄膜へのパターニングと非線形光学効果

反転対称性が破れた系においては光照射によって直流起電力が発生することが知られており（2次の非線形光学効果）、波長より小さな構造では、この効果が飛躍的に大きくなる可能性があります。当センターの FIBにより作製した金薄膜パターン（a）とパルスレーザにより発生した起電力の入射角度依存性（b）を示します。円偏光したレーザーでは垂直入射近傍でも起電力が発生し、その符号は偏光の向きによって反転します。電磁場計算によると、右回り円偏光（RCP）の場合には表面に局在した電場が入射角度に依らず、写真の右方向に伝搬すると予測され、この電磁場が金属中の自由電子を引きずることで起電力が発生すると考えられます。（東北大学石原照也研究室）

核磁気共鳴分光装置（Nuclear Magnetic Resonance）

透過電子顕微鏡は結晶の構造を決定するのに強力な手段ですが、電子線の散乱現象に基づく手法のため、限界も存在します。たとえば、水素などの軽元素の結合状態を調べる場合です。一方、核磁気共鳴（NMR）分光法は有機化合物などの構造決定に有用な手段です。

原子番号あるいは質量数が奇数の原子核は、自転をすることにより磁気を有し、小さな磁石とみなすことができます。一方、勢いよくまわるコマが傾きだすと、コマの軸の先はゆっくりと旋回しますが、この現象は重力と回転運動の相互作用によるもので歳差運動と呼ばれます。原子核という磁石も同様です。重力の代わりに磁場の中に置かれると首をもたげながら回転します。このとき、この回転速度と同じ周波数で回転する磁場（電磁波）を横方向からかけると、電磁波の吸収あるいは放出が起こります。この共鳴現象が核磁気共鳴（NMR）です。

原子核の共鳴周波数は化学結合によって変化するので（化学シフト）、電磁波の周波数を連続的に変化させて得られた共鳴スペクトル（a）から、原子が置かれた化学状態を知ることができるのです。　（權 垠相・今野豊彦）

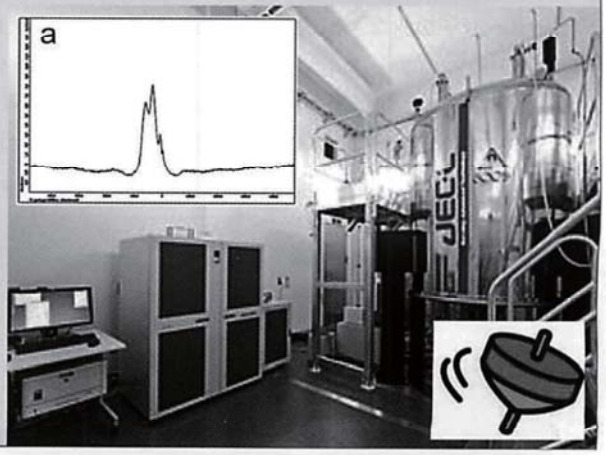

【国際発表】

Future of High Value Manufacturing
(Introduction of Bio-Medical Applications for the Super Aging Society)

Tsunemoto Kuriyagawa

Tohoku University, 6-6-01 Aramaki Aoba, Aoba-ku, Sendai 980-8579

We aim to promote innovations of pico- & nano-precision Micro/Meso Mechanical Manufacturing (M4 process) at the frontier of manufacturing technology, including ultra-precision mechanical manufacturing technologies for various shapes, nano-precision fabrication for 3D microstructures, atom/molecule manipulation for nanostructures and so on. Our goal is not only to create high-precision shapes, but also to generate functional structures on the shape by controlling the micro textures. Today, I will introduce an unique technology, which is powder jet deposition (PJD). The deposition mechanism of PJD was studied with smoothed particle hydrodynamics (SPH) and molecule dynamics (MD) simulations. The deformation of a particle and a substrate by impact was successfully simulated. From the result, a thick film is generated due to the repetition of the deposition of the stagnation areas. The blasting experiments were also conducted to study the machining mechanism at transition condition. The machining surface was analyzed with SEM and TEM. It was that found from these results, the removal process of the substrate material and deposition process of particles onto the substrate occur concurrently under the transition conditions. Utilizing the PJD, a hydroxyapatite film has been successfully deposited on a human tooth as a new dental treatment.

[1] M. Mizutani, C. Kuji, H. Ohisa, S. Nishimura, K. Mizutani, R. Akatsuka, K. Sasaki, S. Xu, K. Shimada, and T. Kuriyagawa, Particle fracture behavior and deposition mechanism in powder jet deposition (PJD), J. of JSAT, 61 (1), 28-33 (2017).

Fig. 1. Developed dental PJD unit and deposited HA film on human enamel.

2021.1.19, ELyTMaX webinar

New Technology for Bio-Medical Interface Creation Utilizing Powder Jet Deposition

Nano-Precision Mechanical Fabrication Lab.

Prof. Tsunemoto KURIYAGAWA

Graduate School of Biomedical Engineering
Tohoku University
Japan

TOHOKU UNIVERSITY

High-Efficiency Machining

1980-1992
Airplane

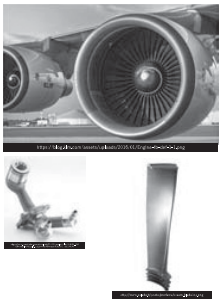

Ultra-Precision Machining

1992-2008
Aspherical lens

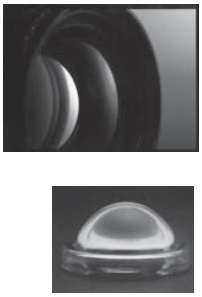

? ? ?

2008-
What should be the next?

TOHOKU

High Value Manufacturing

1. Pico precision machining
2. Function generation machining

Oral Health Science

1. Powder Jet Deposition; PJD
2. Generation of Bio-Functional Interface

3

Oral Health Science

Demographics of Japan

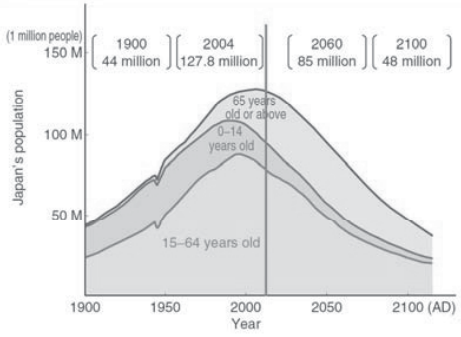

5

Eat delicious food and live longer

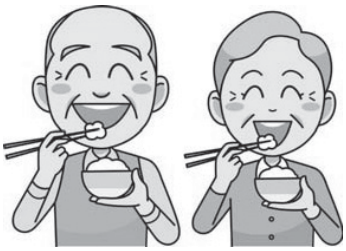

6

8020

Maintain 20 teeth or more of their own even at age 80 !!

Changes in percentage of people having 20 teeth

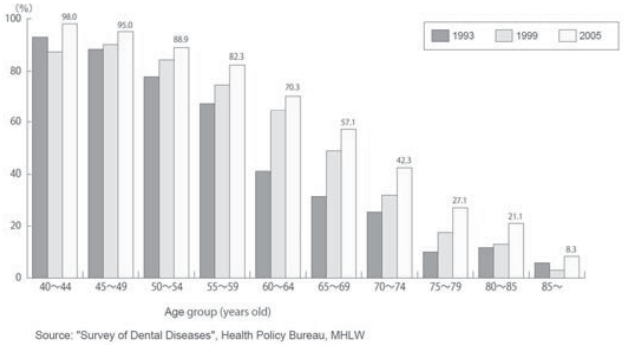

Source: "Survey of Dental Diseases", Health Policy Bureau, MHLW

9028

for super aging society over 100 years old !!

PJD

Powder Jet Deposition

Generation of Bio-Functional Interface

Principle of powder jet process

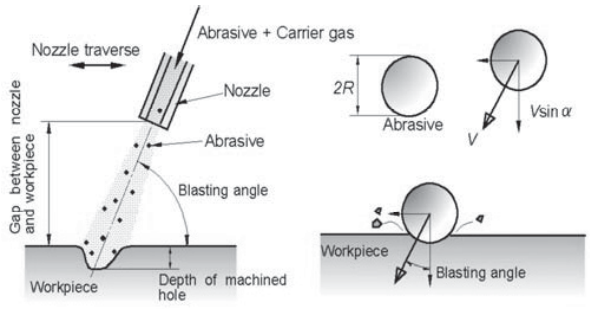

Powder jet machining

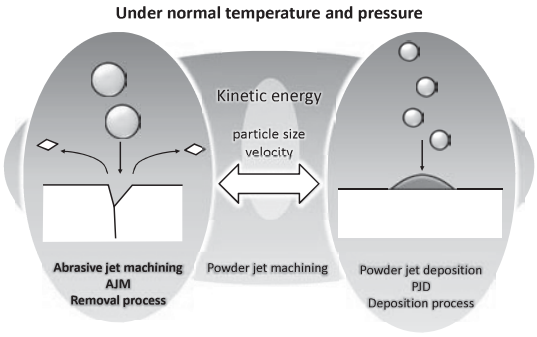

Simulation of powder jet deposition

Smoothed particle hydrodynamics　　Molecular dynamics

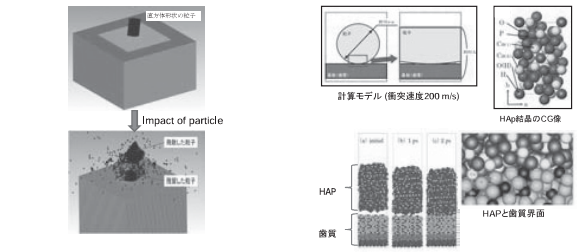

Fracture of particle and substrate
Physical phenomena

Atomic force in interfacial surface
Chemical phenomena

14

Impact of spherical particle

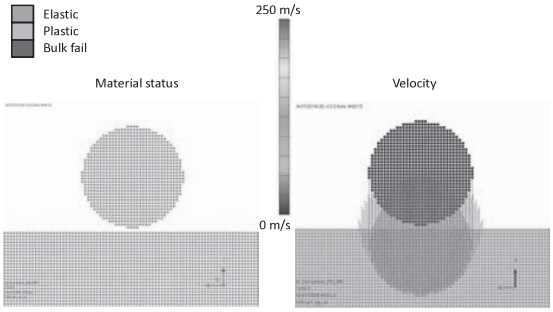

15

Impact of cubic particle

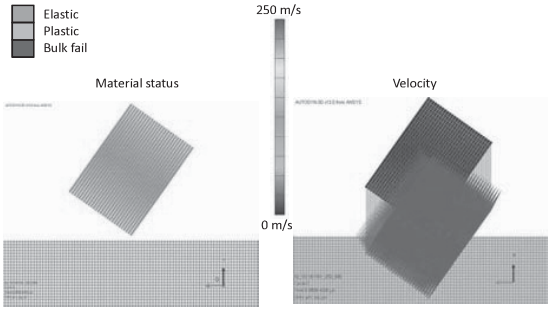

16

Simulation of particle impact

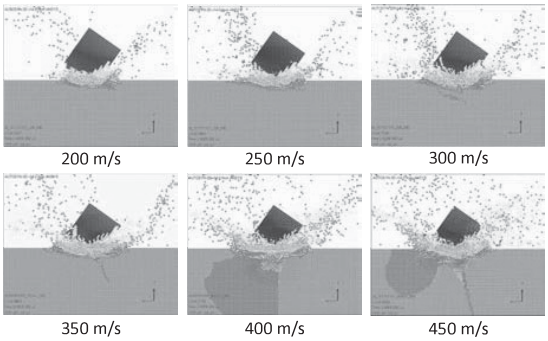

Simulation of powder jet deposition

Smoothed particle hydrodynamics　　Molecular dynamics

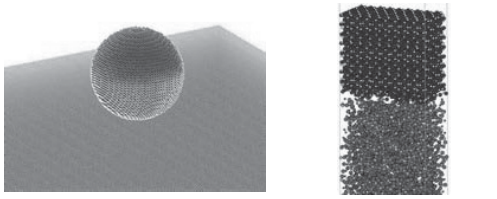

Fracture of particle and substrate
Physical phenomena

Atomic force in interfacial surface
Chemical phenomena

18

Simulation of particle impact using MD

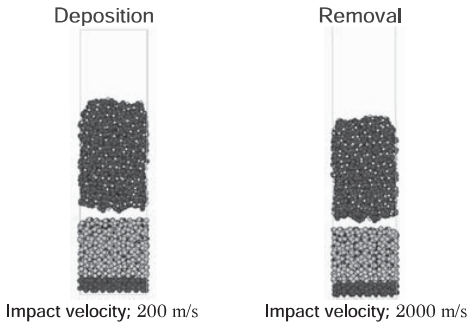

Optimum impact velocity

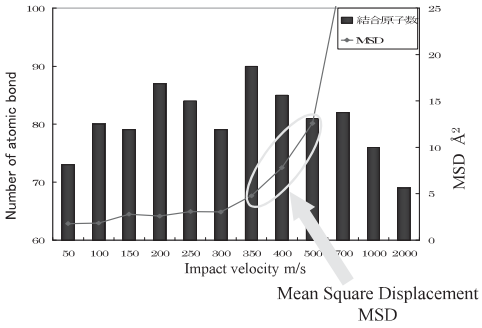

Process mapping

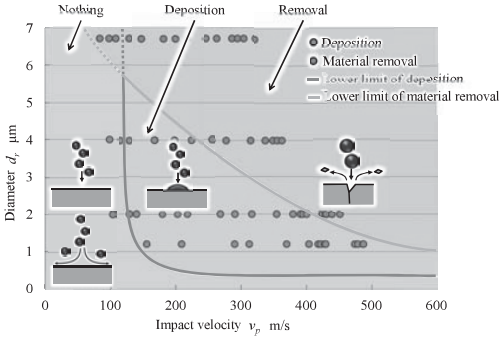

Tooth anatomy

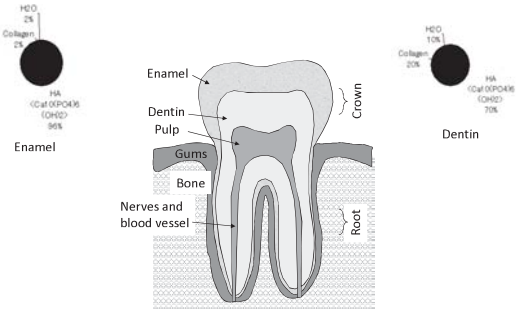

Tooth decay

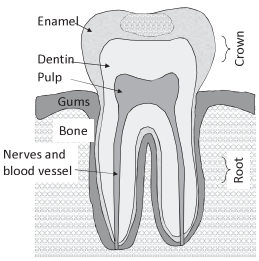

Conventional restorative dentistry

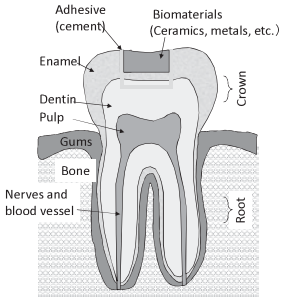

Advantages of the PJD

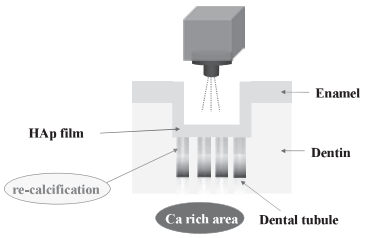

Very strong adhesion

Dental PJD

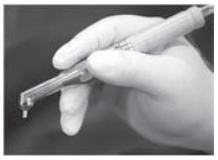

Dental PJD hand piece

micro-particles of hydroxyapatite (HA)

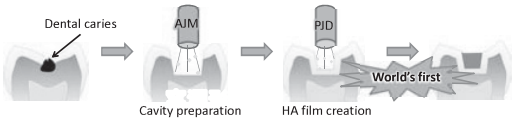

Cavity preparation HA film creation

26

Developed Dental PJD Unit

Forming Thick HA Film on Tooth by Powder Jet Deposition

Clinical Indication
- Discoloration Teeth
- Hypersensitivity
- Linear for Cavity
- Sealant for Fissure/Pit

Lining of Cavity

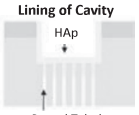

Discoloration

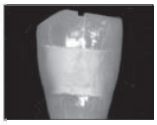

Critical test

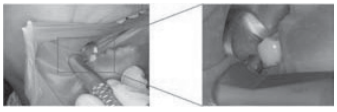

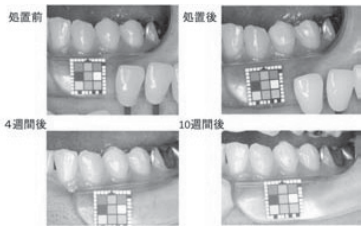

HA film with PJD

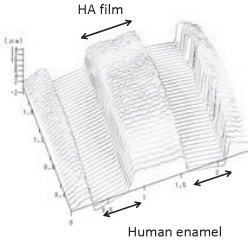

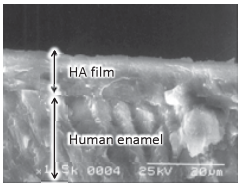

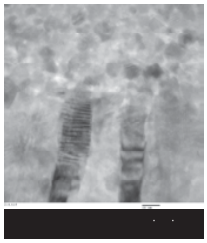

30

New dental applications

Cavity protection

⇒Rebuild enamel by PJD, recalcification after caries removal.

Cosmetic dentistry

⇒Whitening for the white and transparent teeth.

Preventive dentistry

⇒Prevention of Periodontal disease using antibacterial HAp.
HA+F
HA+TiO_2

Thank you very much.

Tsunemoto Kuriyagawa, Dr.

Professor:
Bio-Medical Interface Fabrication Laboratory
Nano-Precision Mechanical Fabrication Laboratory

Tohoku University

Tel: +81-22-795-6948
Fax: +81-22-795-7027
Aramaki Aoba 6-6-01, Aoba-ku,
Sendai 980-8579, Japan
http://www.pm.mech.tohoku.ac.jp
e-mail: tkuri@tohoku.ac.jp

【国内発表】

熱処理を援用した軟磁性アモルファス薄帯の加工手法の開発
Development of machining method for soft-magnetic amorphous sheets with optimum heat-treatment

久慈千栄子[1,2]、嶋田慶太[2]、水谷正義[2]、厨川常元[3]、竹中佳生[4]、今野豊彦[4]
[1]公益財団法人いわて産業振興センター, [2]東北大学大学院工学研究科,
[3]東北大学大学院医工学研究科, [4]東北大学金属材料研究所
*Chieko Kuji[1,2], Keita Shimada[2], Masayoshi Mizutani[2], Tsunemoto Kuriyagawa[3], Kana Takenaka[4] and Toyohiko Konno[4]
[1]Iwate Industrial Promotion Center, Morioka 020-0857, Japan, [2]Graduate School of Engineering, Tohoku Univ., Sendai 980-8579, Japan, [3]Graduate School of Biomedical Engineering, Tohoku Univ., Sendai 980-8579, Japan, [4]Institute for Materials Research, Tohoku Univ., Sendai 980-8577, Japan

1. 緒言

アモルファス合金は、原子配列が並進対称性を持たない金属であり、その構造に起因して特異な物性を発現する[1]。特にFe基アモルファス合金は、低鉄損などの優れた軟磁気特性を持ち、磁心材料としての活用が期待される。一方機械的な性質は、強靭性などの優れた特徴ゆえに、加工は非常に困難である。そこで筆者らは、レーザーによる局所的な熱処理を援用した新たな加工手法を提案している。アモルファス合金は加熱に伴い、構造緩和と呼ばれる原子の再配列を起こし、その後、核生成・成長機構により結晶化する[2]。この構造変化を局所的に制御する事で、被加工領域のみを変質させ、加工性の向上を目指す。本研究では、局所加熱を援用した加工手法開発の前段階として、アモルファス合金に対して均一な熱処理を行い、材料構造と機械的特性の関係を明らかにした。

2. 結果および考察

試料には、日立金属（株）製のFe基アモルファス薄帯Metglas 2605S-3A（$Fe_{77}B_{16}Cr_2Si_5$）を用いた。熱処理は還元雰囲気中（0.998%H_2-Arガス）で室温から673K～1073Kまで加熱した。示差走査熱量測定および、X線回折測定から、結晶化の初期段階（753K～763K）でα-Feが析出し、その後（773K～873K）準安定相であるFe_3Bが析出することがわかった。さらに、高温（1073K）の熱処理により、準安定相は安定相であるFe_2Bへと成長し、Cr由来の安定相である$Fe_{23}B_6$も析出した。透過型電子顕微鏡を用いて、Fig.1の通り内部構造の観察を行った。表層の不均一核生成（Fig.1(b)）の後、内部で均一核生成（Fig.1(c)）が生じ、温度の上昇により結晶粒は隣接するほど成長した（Fig.1(d)）。内部構造の異なる試料に対し、マイクロビッカース硬さの評価を行った（Fig.2）。構造緩和（673K～733K）から初期の結晶生成（～773K）の間は線形的に硬さが上昇した。このことから、構造緩和の時点で機械的特性は変化し、結晶粒が点在する状態では、アモルファス相の変形が支配的であると推測された。さらに、結晶粒が隣接（873K）した時点で急激に硬度が上昇したことから、結晶金属特有の転位の移動による変形へ移行したと考えられる。一方、高温（1073K）の熱処理条件での硬度低下は、結晶粒の粗大化に伴うHall-Petch効果によるものと考えられる。

3. 結言

熱処理による構造変化を調査し、構造緩和および結晶化に伴う機械的特性への影響を調査した。結晶粒の成長によるアモルファス相の消滅と結晶粒界の生成により、転位機構による変形が主体となる事がわかった。

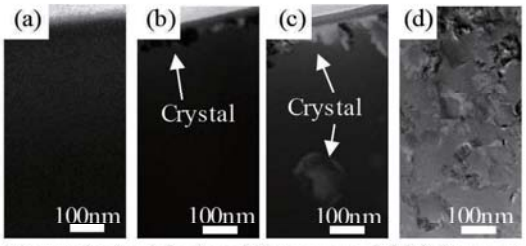

Fig 1. Transmission Electron Microscope (TEM) images: (a) As-received sample, (b) Annealed to 753K sample, (c) Annealed to 773K sample and (d) Annealed to 873K sample.

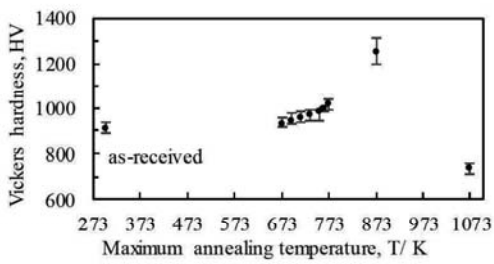

Fig 2. Vickers hardness of amorphous alloy. Samples were annealed from 673K to 1073K.

[1] Masayuki Wakamiya, J. Soc. Mat. Sci., Japan, **Vol. 42, No. 478**, pp.771-779 (1993).
[2] Yoshihiro Takahara et al., J.Japan Inst. Metals, **Vol. 51, No. 2**, pp.95-101 (1987).

謝辞

本研究の一部は文部科学省ナノテクノロジープラットフォーム事業（東北大学微細構造解析プラットフォーム）の支援（JPMX09A20TU0017）および、岩手県工業技術センターの研修生制度支援を受けて実施されました。

【修士論文】

Study on Ultrafine-Bubble

Kensuke Konishi

Abstract

A bubble is air surrounded by liquid and has been used in various fields for a long time such as cleaning, cosmetics, food, and pharmaceuticals. Recently, nanometer-order bubbles, called ultrafine bubbles (UFBs), has been applied practically in a wide range of fields using their unique characteristics. As application fields, engineering is no longer an exception: it has been reported that machining fluid containing the UFBs reduces wear and improves surface texture in grinding and polishing. However, the principles and mechanisms of their effects are still unclear since the scale of phenomena related to the UFB is below the diffraction limit. To promote the practical applications of the UFB more widely, it is urgent to understand the basic characteristics of the UFB and to control the phenomena related to the UFB.

This study mainly consists of two investigation subjects: the effect of the electrical characteristics on the stabilization of the UFB and the effect of a combination of the UFB and an external force. The electric repulsion between bubbles is one of the stability mechanisms which prevent the coalescence; however, only few examples quantitatively evaluated the contribution of the electrical characteristics to the stability through numerical calculations or experiments. Therefore, this study investigates the stabilizing effect of the electrical characteristics on the UFB through numerical calculations and experiments.

Regarding a combination of the UFB and the external force, physical and chemical effects are observed when bubbles shrink rapidly in liquid: the physical effect is the generation of microjet, and the chemical effect is the generation of hydroxyl radicals (OH radicals). Since these functions are completely different, it is necessary to investigate the phenomena that a combination of the external force and the bubbles cause. Therefore, this study investigates the effect of a combination of the UFB and the external force.

Chapter 1 introduces the background and objectives of this thesis.

In Chapter 2, the contribution of the electrical characteristics to the stability of the UFB was evaluated by the Derjaguin–Landau–Verway–Overbeek (DLVO) theory, which can evaluate the dispersion stability of colloidal dispersion systems. The potential curves of the O_2 and CO_2 UFB suggest that O_2 UFB has high dispersion stability while CO_2 UFB easily aggregates. This numerical calculation agreed with the experimental results. Furthermore, experiments with different acidity/basicity UFB-dispersed solutions were conducted to clarify the effect of the acidity/basicity and the electrical characteristics on the aggregation. After adjusting the original O_2 and CO_2 UFB-dispersed water to acidic and basic using HCl and NaOH, the UFB concentration and the zeta potential were compared. The comparison shows acidity/basicity and the zeta potential affect the dispersion stability of UFB. It was also confirmed that the numerical calculation results of the DLVO theory and the experimental results have same tendency. This suggests that the DLVO theory could calculate the dispersion stability of UFB.

Chapter 3 demonstrates the temporal change of the radius of the UFB under 28/40 kHz and 1 MHz ultrasonic irradiation using Noltingk–Neppiras equation. The calculation results suggest that the UFB may vibrate but is unlikely to collapse. Additionally, to investigate the phenomena of UFB under ultrasonic irradiation, three types of experiments were conducted to investigate the sound pressure change, bubble collapses, and OH radical generation.

The sound pressure was measured to estimate the phenomena occurring under ultrasonic irradiation with UFB. The kHz ultrasonic irradiation brought no significant difference in the frequency responses between purified water (PW) and UFB-dispersed water (UFB water). The results also indicate the generation of cavitation bubbles and the collapses with or without the UFBs. The megahertz ultrasonic irradiation oscillated the bubbles more in UFB water than in PW.

The bubble collapse was evaluated by comparing the erosion of an aluminum foil. The kilohertz ultrasonic irradiation brought collapses in both PW and UFB water. The intensive erosion was not observed in the UFB water, suggesting that the UFB can suppress the intensive erosion due to the ultrasonic irradiation. Contrastingly, the megahertz ultrasonic irradiation provided no collapse.

The OH radical generation was measured by electron spin resonance (ESR) using 5,5dimethyl-1-pyrroline-N-oxide (DMPO) for trapping the OH radicals. The kilohertz ultrasonic irradiation did not contribute to the OH radical generation in either PW or UFB water. On the other hand, the megahertz ultrasonic irradiation generated the OH radicals in both liquids, especially in the UFB water.

These results suggest that the bubble collapse does not always link to the OH radical generation detected out of bubbles.

In Chapter 4, the general conclusions of this study are summarized.

Development of High Functionality of Cutting Tool by Hybrid Texturing

Yusuke Sakairi

Abstract

High-efficiency cutting has increasingly been demanded high-mix low-volume production; however, the tool life is a bottleneck for realizing more efficient manufacturing because the cutting tools are exposed in a severe environment of high temperature and high pressure in high cutting speed, which can extensively raise the wear rate. To protect the tools from wear, surface treatment technology is applied on the surface to form wear-proof layers. Conventional surface treatment technologies include chemical vapor deposition and physical vapor deposition and their disadvantages are the low adhesion of the coating and the thickness nonuniformity in applying to the complex surfaces. Plasma shot (PS) treatment is supposed to solve these disadvantages. In this process, arc discharges occur between the workpiece and the electrode, and the electrode partially melts and transfers to the workpiece surface during the discharge. The PS treatment can give various surface characteristics by using an appropriate electrode material, e.g., a previous study reports that a modified layer with a high hardness was successfully formed on iron-based materials by using a TiC electrode; however, the PS treatment has the disadvantage of occurring shape deterioration called "sagging" when this treatment is applied to the cutting edge of tools. Thus, this thesis introduces a hybrid texturing method that combines other surface treatments to solve the problems of the PS. Three methods are introduced: one is to remove the convexity of the PS modified surface with a nanosecond pulse laser, another is to create LIPSS (Laser-induced periodic surface structures) with a picosecond pulse laser, and the other is to control the modification position by creating structure before PS modification. After clarifying the modification characteristics of hybrid texturing and evaluating the functionality by contact angle measurement, hardness test, and friction test. Cutting experiments were then carried out for evaluating the effectiveness of the microstructure on the high-speed steel (HSS) tools in the cutting process. This thesis is composed of five chapters.

Chapter 1 is the introduction of this study. The mechanism and feature of the PS treatment were explained. Moreover, three hybrid texturing methods were proposed: one is to remove the convexity of the PS modified surface with a nanosecond pulse laser, another is to create LIPSS (Laser-induced periodic surface structures) with a picosecond pulse laser, the other is to control the modification position by creating structure before PS modification. Finally, the objectives of this thesis and the organization of this thesis were described.

In Chapter 2, the PS treatment was applied to HSS surfaces using a TiC electrode to confirm the effect of the discharge current (I_p) on forming a single dimple and evaluate the modified layer. The diameter of a single dimple increased by the increase of I_p. The roughness of the modified layer increased when I_p and pulse duration (T_{on}) increased.

Irradiation of the nanosecond laser (NL) improved the roughness of the PS modified surface and reduced both the depth of the molten pool and the height of the convexity, suggesting that the entire surface was planarized. The feature of LIPSS changed around the convexity. The result suggests that the feature of the LIPSS depends on the

texture of the irradiated object. By creating the structure before the PS treatment, the modification position was controlled and cracks were suppressed.

Chapter 3 demonstrates the evaluation of the functionalities of the hybrid textured surface. The evaluated items were the contact angle, hardness test, and friction characteristics.

The contact angle measurement evaluated the wettability by each single surface treatment and the hybrid texturing. The difference of the contact angles between the PS-treated and non-treated surfaces was within the range of error. The NL-irradiated surface and the LIPSS-fabricated surface became hydrophilic while the LIPSS-fabricated and PS-treated surface became hydrophobic. These results suggest that the wetting mode of a droplet on the flat surface with the LIPSS is the Wenzel mode while that on the PS surface with LIPSS is the Cassie–Baxter mode; water may fill the microscopic gaps of the LIPSS on the flat surface but may not fill those on the concave structures created by the PS.

The Vickers hardness test confirmed the surface hardening by the plasma shot and examined the change of the hardness by changing the treatment conditions. Additionally, the change of hardness by the hybrid texturing was evaluated. The hardness test confirmed that the hardness increased as I_p and T_{on} increased. Moreover, it found that the surface was hardened by the NL irradiation.

The friction tests confirmed how much the roughnesses of the PS modified surface and the NL-irradiated surface affected the coefficient of friction (COF) and evaluated how effectively the LIPSS reduced the COF, and investigated the change in the COF by the hybrid texturing. The fiction tests showed that the COFs of the PS-modified surfaces were higher at I_p = 3 A and lower at I_p = 10, 21, and 51 A than that of the non-treated surface. The COF of the PS + NL surface increased. It contributes the reduction of the molten pool. The COF reduction effect of LIPSS depended on the surface roughness before creation, and the COF of the LIPSS surface was greatly reduced.

Chapter 4 elucidates the cutting experiments using the tool treated with the hybrid texturing proposed in Chapters 2 and 3. The tools are named depending on their surface treatment: the tool whose surface is modified with the PS and then irradiated with the NL to remove the convexity is named "LaPS" (laser after PS), the tool whose surface is irradiated by the NL to control the position of the PS modification and modified with the PS is named "LbPS" (laser before PS). The tools with LIPSS are distinguished by the direction of the LIPSS: the tool whose LIPSS is parallel and perpendicular to the workpiece are called $LIPSS_{\parallel}$, and $LIPSS_{\perp}$, respectively. The prepared HSS tools were these nine types: (a) non-treated (i.e., as-received), (b) $LIPSS_{\parallel}$, (c) $LIPSS_{\perp}$, (d) PS, (e) PS+$LIPSS_{\parallel}$, (f) PS+$LIPSS_{\perp}$, (g) LaPS, (h) LaPS+$LIPSS_{\parallel}$, (i) LbPS. Cutting experiments were carried out under wet conditions. Formation of the crater wear were recognized at the edge of the tip of the non-treated tool after cutting, but the wear on the PS tool was reduced, brought by the hardening effect of the PS modification. In the PS tool, the cutting area increased due to the sagging of the edge and the cutting resistance increased, and the cutting resistance decreased by removing the convex parts with the NL. The LIPSS tool promoted chip-flow and reduced the surface roughness of the work material. The LaPS + LIPSS tools suppressed the tool wear and adhesion and improved surface roughness of the workpiece. The hybrid texturing improved the functionality of cutting tool.

In Chapter 5, the general conclusions of this study are summarized.

Development of the highly functional implant with rhizoid porous structure

Masataka Chuzenji

Abstract

Metallic medical implants are rapidly spreading as effective countermeasures against motor disorders and oral disorders. Therefore, they play an important role in the elderly patient prolongation of healthy life expectancy and improvement in the quality of life. The demand for them is expected to grow in developed countries with an aging population; however, they have several problems to be overcome. "Stress shielding" is caused by the difference in elastic modulus between biological metal materials and bones. One way to reduce the elastic modulus is to introduce pores in the metal, such kind of metals are called porous metals. The porous structure can also provide strong retention ability between bones and implants because porous structure promotes bone growth into the pores.

Many methods for making porous metals have been proposed so far, and metal additive manufacturing (MAM) has been gathering attention in recent years. This method can realize a complex porous structure like a lattice structure with high design flexibility. However, such structures require complicated procedures, and it is necessary to consider the reproducible minimum dimension as a design restriction. Therefore, in order to disseminate the porous implants manufactured by MAM, a simple and size-independent method is necessary.

Thus, the author has proposed a "rhizoid porous structure (RPS)" utilizing vacancy defects contained in the objects produced by selective laser melting (SLM), which is one of the representative MAM methods. The RPS has tens to hundreds of micrometers of pores and the pores connect complicatedly like the root of a plant. Because the shaping conditions can control the porosity of the RPS, it is expected to develop highly functional implants with multiple functions by deriving the optimum shaping conditions from functional or dynamical designs. This thesis aims to show the feasibility of the highly functional implant. The thesis consists of following the five chapters.

Chapter 1 introduces the background and the objectives of this thesis.

Chapter 2 investigates the controllable range of RPS porosity and the effect of modeling conditions on pore formation. The samples were fabricated with various scanning speeds, widths, and laser powers. Subsequently, an X-ray CT scan obtained the internal information of the samples. The information was then processed to visualize the internal pores and calculate the porosity of the samples. The calculation results showed that the porosities of the samples were about 0% to 45%. The porosity increased as the scanning speed increased. This trend might be introduced by the surface roughness; the higher scanning speed generates the rougher surface. The output energy hardly affected the porosity and pore orientation. A larger scanning width than the diameter of the laser spot significantly affect pore generation.

Chapter 3 demonstrates the evaluation of the mechanical properties of the RPS material, specifically, the compressive strength and fatigue strength. The compression tests showed that maximum compressive stress and elastic modulus decreased as the porosity increased. These results might be linked to the decrease of the

effective sectional area due to the increase of the pores. The elastic modulus was about 15 GPa to 25 GPa that was close to the bone, expected to solve the stress shielding phenomenon. On the other hand, the bending fatigue test revealed that the fatigue strength of the RPS material became lower than that of the bulk material due to the stress concentration on the pores. These results clarified that the RPS could achieve a low elastic modulus, while its fatigue strength requires to be improved.

Chapter 4 focuses on the dental implant with the RPS. The internal structure of the highly functional implant using the RPS was proposed and the graded structure was built by the SLM. Design areas of the model were divided at a regular interval along the radial direction, and different laser scanning speeds were assigned to each area to vary the porosity. This method then realized the samples with a gradational porosity along each radial direction, and two types of graded structures were fabricated: one is a dense-center and coarse-circumference structure (hereafter, simply referred to as the dense-center structure), and the other is a coarse-center and dense-circumference structure (hereafter, simply referred to as the coarse-center structure). The maximum compressive stresses of the dense-center structure and the coarse-center structure were about the same as the test piece of the scanning speed (SS) 430 mm/s, and that of SS 240 mm/s, respectively, and the elastic moduli of them were about the same as the test piece of the SS 430 mm/s and that of the SS 150 mm/s test piece, respectively. And fatigue test results showed fatigue strength was similar to the result obtained in Chapter 3.

The cell culture experiments demonstrated the RPS sample with specific porosities equal to those of non-porous materials. Furthermore, the results confirmed that the cells entered the pores and formed networks with each other. These results suggests that the RPS implants may achieve strong bonding with bones because their pores advance bone growth and retention ability.

In Chapter 5, summarized the results and conclusions of this thesis. Additionally, engineering and industrial significations of this study were stated.

Study on Micro-Textured Surface Generated by Ultrasonic Vibration-Assisted Cutting

Fu Tiqiang

Abstract

Commonly, a surface is described as the outer boundary of an object regardless of the depth of textures on the surface; however, the micro- and nanostructures of plant and animal surfaces in nature have a great influence on their attributes as interfaces, such as transport barrier, surface wettability, anti-adhesive and self-cleaning properties, signaling, optical properties, mechanical properties and reduction of surface temperature, etc. The functions are also meaningful for industrial applications, therefore, nowadays a large area of biomimetic research deals with the functional micro- and nanostructures and the transmission of biological principles and functional structures. This research mainly focuses on surface wettability.

Surface wettability is related to many industrial applications like lubrication, painting, liquid coating, spray quenching, soldering, jet-printing, etc., so surface wettability has received strong interest in theoretical research and practical applications over the past years. Until now, researchers have proposed several modes to explain the wetting process. The Wenzel and Cassie–Baxter modes are the classical modes that can explain a part of the wetting phenomenon; however, there is still a long way to go before these theories can be used to design and predict surface wettability completely. In terms of practical research, previous research has proved that there are two methods to change surface wettability: changing surface chemical properties and fabricating structures on the surface. Surface chemistry is related to Young's contact angle, and surface textures influence the contact mode between liquid and solid.

The development of material and machining technology makes designing wettability feasible. Some materials themselves are hydrophilicity or hydrophilicity, and they also can coat on the surfaces of other materials to confer excellent wettability. Additionally, many machining processes are applied to fabricate the micro- and nanostructures on the surface to control the wettability, e.g., electrical discharge machining (EDM), micromilling, etching, ion beam texturing, and ultrasonic vibration-assisted cutting (UVAC). They have their own characteristics and none of them is perfect.

In this research, a mixed mode that includes the Wenzel and Cassie–Baxter modes by adjusting the penetration depth of liquid into microstructures is proposed to explain the wetting process. In terms of the experiment, the UVAC process combining ultrasonic vibration with conventional machining is used to fabricate the micro-textured surfaces due to its excellent features including low resistance force, reduction of tool wear, relatively high surface quality, and high dimensional precision. Additionally, laser irradiation and water-repellent coating were applied to change surface chemistry. The laser irradiation influences the surface chemistry by the thermal effect, which can result in the oxidization of the surface and decomposition of CO_2. The water-repellent changes the material directly, and the applied coating material was a commercial solvent (Ultra-Ever Dry SE 7.6.110).

This thesis is composed of five chapters.

Chapter 1 is the introduction. It mainly describes the background, some functional surfaces discovered in nature, and surface wettability. Additionally, several machining processes usually applied to fabricate micro- and nanostructures are introduced.

Chapter 2 demonstrates an analysis of the wettability of the micro-textured surface. This chapter explains the wetting process by thermodynamic contact theory and introduces some fundamental equations like Young's equation, the Wenzel equation, and Cassie–Baxter equation. Finally, a mixed mode is proposed to explain some experimental phenomenon. The mixed mode introduces a variable called the penetration depth and by adjusting

it, different states from the Wenzel state to the Cassie–Baxter state are obtained.

Chapter 3 describes the experiment fabricating the micro-textures surface by changing the pitch, cutting depth, and tool angle. By changing both pitch and cutting, different scales of pyramid structures were obtained. Different square frustums were created by only changing the pitch. Besides, changing the tool angle also provided different square frustums, where their slope angles of the sidewall were different. The surfaces were observed by scanning electron microscope, and the contact angles (CAs) of them were measured to assess the wettability.

Chapter 4 proposes two hybrid machining processes to change both surface chemistry and surface textures. One is the UVAC process and laser irradiation. The laser process changed the micro-textured surfaces and elemental composition due to oxidization and the decomposition of CO_2. Because the laser-processed surface is chemically active after processing and requires a certain time to become chemically stable, the CAs were measured over days. Additionally, ethylene glycol was also applied to assess wettability when the surfaces were stable. The other was the UVAC process and water-repellent coating. By adjusting the order of process, surfaces covered with the coating material completely or partly could be obtained and their CAs were measured.

Chapter 5 concludes this thesis: the general conclusion, engineering significance, and industrial significance of this thesis are described.

This study proposes the mixed mode to explain the wetting process and clarifies the relationship among the wettability, surface textures, and surface chemistry. The mixed mode can calculate the droplet state partly with a low error. Surface textures fabricated by the UVAC process can control the CA from 75° to 120°. Laser irradiation is another method to control the CA, however, the CA $\theta > 120°$ or $\theta < 75°$ is not obtained. Additionally, Water-repellent coating can obtain superhydrophobic surfaces whose CAs were around 150°. It is difficult or impossible that fabricate the micro-textures on the coating material because it is soft and easy to be destroyed.

Study on Restorative Treatment of Discolored Tooth by Powder Jet Deposition

Nami HONGO

Abstract

In the field of dentistry, demand for aesthetic dental treatment has been increasing in addition to recovery and improvement of biological functions. This thesis defines the "aesthetic dental treatment" limitedly as follows: a treatment restoring the discolored tooth and preserving the natural tooth color. The existing aesthetic dental treatment generally restores the discolored teeth by coating them with a dental restoration material such as aesthetic composite resins or ceramics by adhesive materials. However, these materials possess quite different chemical compositions and mechanical properties from the those of tooth, which can give rise to different mechanical, thermal, or chemical stresses in the oral environment and can lead to clinical problems such as fatigue breakage, drop off from the tooth by the deterioration of the adhesive agent. Therefore, a new aesthetic dental treatment should possess such features that (1) the chemical, compositional, and mechanical properties of the restorative material correspond to the human tooth, and (2) the material can adhere to the tooth directly without adhesive materials. In this regard, powder jet deposition (PJD) is a promising method for a new aesthetic dental treatment. The PJD is a film-formation technique by colliding the high-speed particles on the target material, and it can perform at room temperature and under atmospheric pressure; these characteristics enable the PJD to create hydroxyapatite (HA) film on human teeth. Clinical trials have demonstrated the clinical effectiveness of the PJD-formed HA film in the field of prosthodontics and preventive dentistry. On the other hand, the PJD has not been applied to aesthetic dental treatment because the HA film hardly conceals the base color due to its transparency. Therefore, HA particles covered with ZrO_2 small particles were employed in the PJD to create an aesthetic composite film on the tooth. This thesis demonstrates the results of a feasibility study aiming at realizing an innovative aesthetic dental treatment in which the composite particles are deposited on the discolored tooth by the PJD.

Chapter 1 introduces this thesis. The background of this study, epidemiology in aesthetic dentistry, and problems on present aesthetic dental treatment, the proposal of an innovative aesthetic dental treatment method using dental bioceramics and PJD, and the objectives of this study are described.

Chapter 2 establishes a method for quantitatively evaluating the aesthetics of the PJD-formed film with the brightness. The brightness corresponds with a colorimetric parameter L* in the CIELAB color space and is regarded as the most important factor in existing restorative treatment for discolored tooth. This proposed method demonstrated that the aesthetics of ZrO_2 film was effectively higher than that of HA film; however, the thickness of the former film was lower than the latter one. To complement the disadvantages of the ZrO_2 and HA particles with each other, the composite particles merging those two bioceramic particles were designed to

apply to the PJD aesthetic dental treatment, and the following two composite methods successfully developed the composite particles: one is the mechanochemical (MC) technique that combines particles strongly via mechanochemical reaction, and the other is the nozzle-dispersion (ND) technique that aerosolizes the particles by a dispersion nozzle to aggregate the particles to each other loosely via weak forces like van der Waals force.

Chapter 3 demonstrates the evaluation of the film-forming effectiveness of the two composite particles developed in the previous chapter and the aesthetics of their films, and the analysis of the film structure. The experiment with the composite particles clarified that the composite particles maintained the high film-forming effectiveness of HA particles, and its film effectively reflects the high aesthetics of ZrO_2 particles. Comparing the two combining methods, the MC-type film is brighter per unit thickness while the ND-type film is thicker; judging comprehensively, the aesthetics of the ND-type film was better than the other film. Scanning electron microscopy (SEM) revealed that the surface of the ND-type film included ZrO_2-concentrated minute convexes, and its cross-section was a lamellar structure where both HA and ZrO_2 layers are alternately present. The ZrO_2 area ratio in an arbitrary area of the cross-section was stable regardless of the size of the convex part on the surface, and the average area ratio of ZrO_2 increased in proportion to the increase in the ZrO_2 composite rate of the ND-type particles. Finally, the three-dimensional structural analysis of the ND-type film clarified that the lamellar structure inside the film was composed of the HA, ZrO_2, and crack layers generated parallelly to the surface, and that no local bias existed in each tissue component.

Chapter 4 investigates the aesthetic effect of the film by controlling the parameters related to the color tone of the composite film: the ZrO_2 composite rate of the composite particles, film thickness, and brightness of the background color. Firstly, the PJD method used ND-type particles with 0–20% ZrO_2 to form films on glass substrates. The investigation on the obtained films clarified that the two parameters, the ZrO_2 composite rate of the particles and the film thickness, positively correlated with the ZrO_2 concentration on the film surface and the film brightness. On the other hand, the parameters negatively correlated with the film transmittance, which means the larger amount of ZrO_2 in the film provides the higher concealing ability. Particularly, the film with a high concealing ability showed its color unaffectedly by the background color ($12.4 \leq L^* \leq 95.9$). Considering the concealing ability depended on the two parameters, a protocol was proposed by assuming that the formation of an ND-type-10, 15% film with more than 5 μm thickness could provide discolored teeth with the brightness around the upper limit of this method, $L^* = 50–75$. Following this protocol, the PJD successfully formed ND-type-10, 15% films with 20–30 μm thickness on the extracted teeth with caries, and the films gave the aesthetics as bright as $L^* = 75$ to the discolored teeth. Additionally, the adjustment of the film thickness could control the degree of the aesthetic effect. These results demonstrated that the protocol proposed in this thesis could be used practically as aesthetic dental treatment with the PJD.

In Chapter 5, the general conclusions of this study are summarized.

英文 Abstract

Title: Behavior at the Interface between Microstructured Metals and Biological Tissues
Author: Shuya KANEKO
Supervisor: Tsunemoto KURIYAGAWA

Demand for minimally invasive medical devices has recently been increasing to extend the healthy life expectancy and improve the quality of life. One of the methods minimizing invasion risk is to control friction of medical devices using surface microstructures, and the short-pulsed laser including the picosecond laser (PL) is a promising method for creating microstructures; however, friction with soft materials such as biological tissues is still unclear. This study, therefore, employed a PL to fabricate functional microstructures on the surface of stainless steel and evaluated the friction between the microstructured surface and polyurethane elastomer (PUE) gel, which is a pseudo biomaterial, to assess the invasion. The wettability of the microstructured surfaces depended on their original roughness; the PL irradiation hydrophilized the fine-polished surfaces, while hydrophobized the rough-polished ones. The sliding resistance between the fine-polished and PL-irradiated surface and PUE gel decreased under a low load and lubricated condition. Additionally, the pull-out resistance from the PUE gel decreased on the microstructured needle compared with the as-received one. The results of this study demonstrate that an appropriate combination of surface polishing and PL irradiation can control the wettability and frictional properties of the surface of medical devices, thereby achieving minimally invasive procedures.

和文アブストラクト

論文題目： 微細構造を有する金属と生体組織との界面で生じる挙動解析
提出者氏名： 兼子 周也
指導教員： 厨川 常元

国民の健康寿命の延伸及びQOLの向上のために医療器具の低侵襲化に対する需要が高まっている．その低侵襲性を達成する策のひとつに表面微細構造による医療器具の摩擦制御があるが，生体組織のようなソフトマテリアルとの摩擦は不明な点が多い．そこで本研究では，パルスレーザにより微細構造創成法を医療器具材料のステンレス鋼に創成し，生体組織のようなソフトマテリアルとの摩擦特性を検証することにより，低侵襲化の可能性を検討した．粗さの異なるステンレス基材上にピコ秒パルスレーザによる微細構造を創成した試料の濡れ性試験から，基材の元の粗さがレーザ処理後の試料の濡れ性にも影響を与えることを見出した．#2000 研磨面にピコ秒パルスレーザを照射することで表面が親水化し，疑似生体組織であるウレタンゲルと基材の界面の低荷重，潤滑状態での摩擦係数が減少することを示した．また，ピコ秒レーザにより微細構造を創成した注射針では抜針抵抗が減少することを明らかにした．
本研究の成果は，医療器具を研磨し適切な表面性状にしたのちピコ秒レーザを照射することで，濡れ性および摩擦特性を制御し，低侵襲化を達成できる可能性を示すものである．

【令和２年度卒業生】

	氏名	研究テーマ	所属先・勤務先
学部生	大越広夢	ウルトラファインバブルの基本特性に関する研究	進学（工学研究科）
	湯田健太郎	放電加工の最適ジャンプパラメータに関する研究	進学（工学研究科）
大学院博士課程前期	小西健介	ウルトラファインバブルに関する研究	東京ガス株式会社
	坂入勇輔	ハイブリッドテクスチャによる高機能切削工具の開発	株式会社ブリヂストン
	中善寺優昂	根状多孔質構造体を有する高機能インプラントの開発	株式会社島津製作所
	本郷那美	パウダージェットデポジションによる歯冠色修復に関する研究	株式会社島津製作所
	付　体強	Study on Micro-Textured Surface Generated by Ultrasonic Vibration-assisted Cutting	未定
	兼子周也	微細構造を有する金属と生体組織との界面で生じる挙動解析	NGB 株式会社
教員	嶋田慶太	濡れ性勾配のワンパス加工を実現する超音波援用切削法および 3 次元接触角解析法の開発	大学共同利用機関法人 高エネルギー加速器研究機構

【研究室だより】

昨年の冬は寒さがひときわ身に染みる厳しいものとなりましたが，最近ではすっかり暖かくなり，日ごとに春の訪れを感じるようになりました．一方で昨年度より猛威を振るっている新型コロナウイルスの勢いはいまだ衰えず，二密を避ける新しい生活様式ももはや日常になりつつあります．

厨川先生は４月１日より医工学研究科から工学研究科に配置換え（医工学研究科は兼担）になりました．水谷先生は研究や学生に対する指導，鞭撻など忙しい日々を送っております．藤田事務補佐員には事務手続きなどの研究室の仕事をサポートしていただいております．また助教として研究室のために長年ご尽力された嶋田先生がつくば市の高エネルギー加速器研究機構に移られました．新天地でのご活躍をお祈り申し上げます．

研究室では，昨年 10 月に社会人ドクターが４名，中国からの留学生２名が加わり，博士課程後期学生は全員で 14 名になりました．また博士課程前期（修士）学生は２年生が４名，１年生が２名の計６名，４年生は IMAC の１名を含め全員で５名となっております．

今年度も私たち厨川/水谷研究室一同は，健康に気を配りつつ勉学や研究をはじめあらゆる活動に励み，有意義な一年を過ごしていきたいと考えております．

令和３年４月

博士課程前期１年　大越　広夢